Simulation of Electrohydrodynamic Distortion Relevant to Liquid Metal Ion Sources

Thesis by
Cheolmin Im

In Partial Fulfillment of the Requirements for the
Degree of
Doctor of Philosophy

CALIFORNIA INSTITUTE OF TECHNOLOGY
Pasadena, California

2025
Defended May 23, 2025

Cheolmin Im
ORCID: 0000-0003-4063-2312

ACKNOWLEDGEMENTS

To begin, I would like to express my utmost gratitude to my advisor and mentor, Prof. Sandra M. Troian. The amount of intellectual and emotional support I received in forms of timely, precise critique and encouragement of the research forays, unwavering patience and belief, warm kindness and impeccable sense of humor, and just the sheer amount of time and effort devoted are beyond what anyone could have hoped for from an advisor and a mentor. No amount of words can adequately describe the appreciation and admiration I hold for her as a scientist and a human being in my heart. I can only hope to apply myself in the career and life that follows as well as she has done unto hers. Prof. Troian, thank you for all that you have done to support my graduate studies at Caltech.

I would also like to thank the rest of my thesis committee, Prof. Kenneth G. Libbrecht, Prof. Paul M. Bellan and Prof. Keith C. Schwab for their insightful comments and inspiring conversations derived from perspectives and knowledge outside of my field.

I would also like to thank Dr. Eric D. Black and Prof. Kenneth G. Libbrecht again, and Dr. Alireza Ghaffari for extending me teaching assistantships in the Caltech Senior Physics Laboratory (Ph 77) and Introduction to the Micro/Nanofabrication Lab (APh/EE 109), respectively. I sincerely appreciate all the assistance I received to be able to successfully lead the students of my tracks and many inspiring and often humorous conversations we had throughout the terms. It was all a very valuable experience. I would also like to acknowledge all of the students who made the experience further enjoyable through their excitement and curiosity.

I also thank my fellow labmates, Dillon Chang and Hiroki Kaifu, for the interesting discussions and good laughs we shared during the lunch meetings and also at the 2024 APS March Meeting in Minneapolis. I would also like to extend a special acknowledgement to the system administrator of our lab, Dr. Peter A. Thompson, who devoted so much of his time to maintain the computer hardware and software, promptly diagnose and fix all IT issues and provide assistance on expediting the countless simulations I ran on the computing cluster. It is not an understatement to claim that the research conducted would simply have been impossible without his help.

To my friends here at Caltech and also scattered across the continent, thank you for sharing all the years of our friendships with me. I would like to especially acknowledge Carlos Cabrera, Robert Piacenti, Christopher Koch, Jeffrey Tan, Anthony Kim, Huws Landsburger, Bragan Kelly, Nathan Kim, Ruben Santana, Cameron Chaffey, Chin Yi Tan, Arjun Savel, Vishnu

Iyer, Youngjoon Han and members of the "Apple Core" (Sara Anjum, Andrew Charbonneau, Ian Foo and Hannah Manetsch), who shared so many laughs with me at various ages and settings and on discussions on widely ranging topics from simple harmonic oscillators to baseball management games. I am extremely thankful to have cultivated such friendships with you all.

It would be remiss of me not to express gratitude to the mentors I was fortunate to have met before my time at Caltech. To Mr. B, Mrs. Arana and Mrs. Godoy, I am so thankful to have had your guidance and warmth during my formative years right after I had just moved to the United States. Out of everything you did, I will never forget the 8th grade trip to Washington D.C., which was only made possible for me from your support. To Mr. Greenberg, you gave me the first introduction to physics in a classroom setting. I truly appreciate the lengths you took to teach the subject in an intellectually whetting and enjoyable way. To Mr. Starodub, you gave me the first glimpses of what scientific research involves. I thank you for your guidance and for providing me the opportunity to present the research in wider settings. To Ms. Chaiyont, you gave all of the math club geeks a place to call home in our high school. I am grateful to have been in your ever radiating, warm presence in your statistics class and many lunchtime math club sessions. Prof. Richard T. Scalettar, thank you for making the COSMOS summer program intellectually enjoyable and giving me a chance to conduct my first physics research on classical spin models with you after the program had ended. Dr. Arjun S. Gambhir, thank you for extending me a great opportunity to conduct research on Lattice QCD with you even though you were very busy yourself trying to settle in at Berkeley. I truly appreciate the intellectual and emotional support you provided in our time together.

To all of my uncles, aunts, cousins and family friends back in Korea, thank you for providing encouragement to me and my family throughout all these years. I miss you all and soon hope to take regular visits to Korea to see you. I would like to especially express my gratitude to my maternal grandparents, Yonggil Park and Sasoon Moon, and my late paternal grandparents, Daeyoung Im and Yoosim Goh for their unconditional love that they bestowed unto me, which still rings from the back of my heart like the sound of cicadas propagating through the starry country nights spent in their homes.

And how could I forget my family? To my dad, Dr. Hongsik Im, my appreciation and admiration for you as an engineer and a dad grow with each passing moment. I still cannot fathom the courage and drive it must have taken to give up the world you have known and instead pursue your long harbored dreams that started with pursuing a Ph.D. at the age of 38 and culminated in founding your own company for expert analysis and simulation of

turbomachinery systems. The mere thought of your strong and steady presence has provided me countless emotional comfort and consolation, not to mention your actual words of advice and wisdom. To my mom, Gyeongsuk Park, I also cannot fathom the courage it must have taken to also give up the world you have known in order to provide unwavering support of our family's pursuits. You are the mighty engine that has kept our family humming along, especially with your always warm meals, words of advice and humor. My appreciation and admiration for you also grow with each passing moment. To my sister, Hoyeon Im, you provided the "yin" to my "yang" in the household with many of your positive qualities that I lack. I was always secretly envious of you because you were always so adorable and now I have additionally cultivated an admiration of your confidence and initiative. You don't need my encouragement but nevertheless, I am confident that you will become the Nightingale to many patients who will receive your care. To my dad, my mom and my sister, I love you all so much.

ABSTRACT

The free surface of a liquid metal film in vacuum subject to an imbalance of destabilizing Maxwell (electric) and stabilizing capillary forces can undergo rapidly accelerating electrohydrodynamic (EHD) distortion which culminates in formation of protrusions from whose tips highly energetic ion beams are emitted. Such a phenomenon has been successfully leveraged into liquid metal ion sources (LMIS) which are fundamental to the operation of focused ion beam systems used for micro- and nanofabrication and even microarray devices actuating space micropropulsion. In this thesis, we have conducted a series of computational simulations using the arbitrary Lagrangian Eulerian finite element method designed to track the pre-emission EHD liquid distortion for realistic LMIS geometries characterizing a slender microemitter with a sharp (highly curved) tip positioned beneath an apertured extractor in vacuum.

The simulations unveil various stable and unstable configurations whose protrusions can occur along the liquid surface. The particular configurations are found to correlate with the Reynolds number and electric Weber number based on a handful of initial values, namely the applied electric potential, microemitter apex curvature radius and initial liquid thickness. For the parameter space explored, spectral analysis of the unstable configuration yields a dominant wavenumber in close agreement to that predicted from linear stability analysis of the flat liquid layer. This can be traced to the fact that a key aspect ratio indicates that the dynamics are in the flat liquid limit. Examination of the late stage dynamical behavior of the evolving protrusions reveals self-similar growth for all configurations examined. Values of the exponents extracted from the simulations are found to cluster neatly when plotted against Reynolds number and electric Weber number.

TABLE OF CONTENTS

LIST OF ILLUSTRATIONS

Number *Page*

LIST OF TABLES

NOMENCLATURE

This section lists the symbols used throughout the entire thesis. The symbols are grouped in physical variables, initial state variables, material constants of liquid film, constant of vacuum layer, simulation specific variables and referenced quantities.

Physical variables

t	Time.
r	Axisymmetric radial coordinate.
z	Axisymmetric vertical coordinate.
$z = h(r,t)$	Coordinate of the liquid-vacuum free surface.
$\vec{u}(r,z,t) = u\,\hat{r} + w\,\hat{z}$	Liquid velocity.
$p(r,z,t)$	Liquid pressure.
$\mathcal{K}_{em}(r,t)$	Mean curvature of the microemitter surface.
$\mathcal{K}_h(r,t)$	Mean curvature of the liquid free surface.
$R(r,t) = 1/\mathcal{K}_h(r,t)$	Curvature radius of the liquid free surface.
$\phi(r,z,t)$	Vacuum electric potential.
$\vec{E}(r,z,t) = E_r\hat{r} + E_z\hat{z}$	Vacuum electric field.
$\theta(r,t) = -\tan^{-1}\left[(\partial h/\partial r)^{-1}\right]$	Local half angle of liquid free surface.
$p_M(r,t)$	Electric (Maxwell) pressure on liquid-vacuum free surface.
$p_C(r,t)$	Capillary pressure on liquid-vacuum free surface.
$p_V(r,t)$	Viscous pressure on liquid-vacuum free surface.

Initial state variables

r_s	Value of constant radius of curvature of microemitter apex at $r = 0$.
h_o	Value of constant initial liquid thickness.

$r_s + h_o$	Value of constant radius of curvature of initial liquid apex at $r = 0$.
ϕ_o	Electric potential applied to the microemitter.

Material constants of liquid film

ρ	Liquid density.
γ	Liquid surface tension.
μ	Liquid viscosity.

Constant of vacuum layer

$\varepsilon_o = 8.85 \times 10^{-12}$ F/m	Vacuum permittivity.

Simulation specific variables

$t_o = 10^{-12}$	Simulation ramp up time of ϕ_o.
t_f	Simulation final termination time when maximum electric field on the liquid surface is approximately equal to 5 GV/m.

Referenced quantities

$\mathsf{Re} = \sqrt{\frac{\rho\varepsilon_o}{2}}\frac{\phi_o}{\mu}\frac{h_o}{r_s + h_o}$	Reynolds number.
$\mathsf{We} = \frac{\varepsilon_o \phi_o^2}{2\gamma h_o}$	Electric Weber number.
θ_f	Local $\theta(r, t = t_f)$ minimum closest to $r = 0$.
r_θ	r at which θ_f is extracted.

Chapter 1

INTRODUCTION

1.1 Liquid metal ion source: description and history

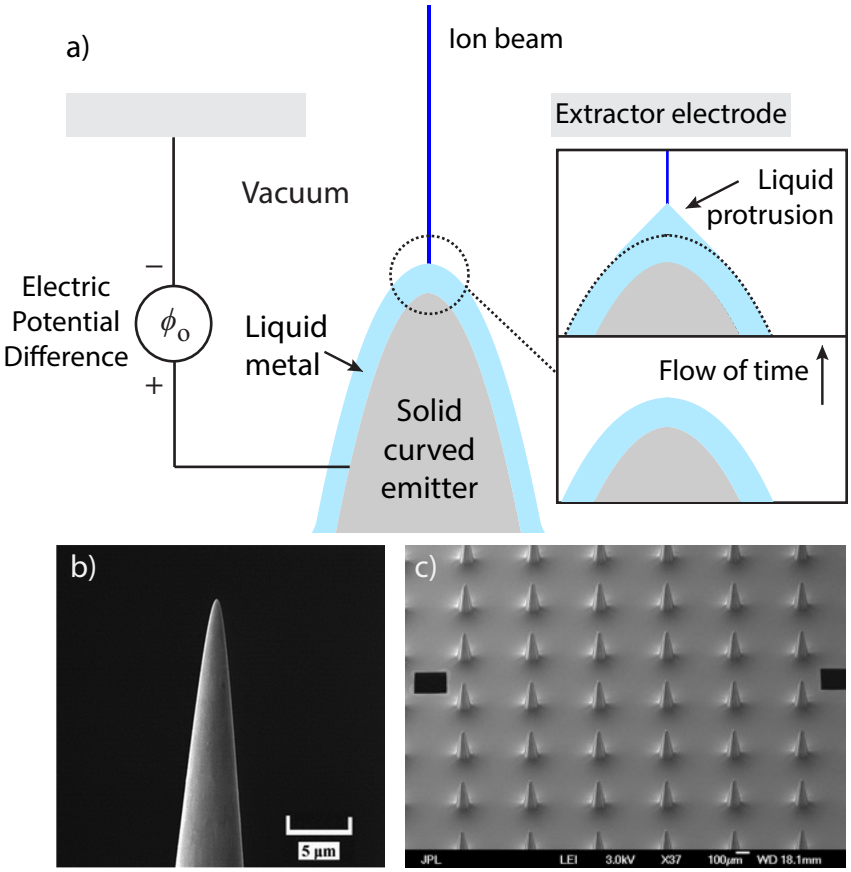

Figure 1.1: Schematic diagram of the liquid metal ion source (LMIS). (a) A liquid metal layer is externally wetted to the solid, curved emitter surface and placed under an apertured extractor. Applying an electric potential difference between the emitter and extractor deforms the liquid at the emitter tip into a protrusion as shown in the inset, from the apex of which an ion beam is emitted. (b) Scanning electron micrograph of a LMIS emitter tip made from an electrochemically etched tungsten wire. The apex curvature radius is 0.47 μm. Reproduced with permission from Fig. 2(a) of Ref. [57]. (c) Example of a LMIS microemitter array with 500 μm pitch. Reproduced with permission from Fig. 4 of Ref. [98].

One of the most significant technologies that has been developed in the past half century is the liquid metal ion source (LMIS). Shown in Fig. 1.1(a) is a schematic diagram of the essential system design and operation. The setup typically consists of a solid, curved

emitter electrode that is externally wetted with a molten liquid metal layer (typically gallium Ga) that serves as the source of the to be emitted ions. The liquid metal is known to be well approximated as a perfectly conducting material due to the charge relaxation timescale being instantaneous in comparison to flow time scales. The emitter is typically $O(100\ \mu\text{m})$ tall and possesses $O(1\ \mu\text{m})$ apex curvature radius. Fig. 1.1(b) shows an example emitter profile near its apex, which possesses strong curvature owing to the electrochemical etching [68] typically used for fabrication. The emitter electrode externally wetted with a liquid metal film is placed under an apertured extractor counterelectrode and subject to a strong electric potential difference of $O(1-10\ \text{kV})$, which generates strong electric fields locally enhanced in the vicinity of the curved emitter apex. The resulting imbalance of electric (Maxwell) and capillary pressures generated at the electrified liquid surface induces a significant liquid distortion that ultimately culminates in the formation of a small liquid protrusion, which emits a highly energetic, positive ion beam from field evaporation [45, 105] if its apex electric field exceeds $O(10\ \text{GV/m})$. The system can also be induced to emit negative ions [38, 59] if the polarity of the applied potential is reversed. It is known experimentally that the potential bias can lead to ions or electrons. In this thesis, we positively biased the emitter and liquid metal with respect to the extractor and ceiling. However, since the Maxwell pressure is proportional to the magnitude squared of the electric field, the analysis holds irrespective of the bias. The entire system is actuated just from minimal volume of liquid metal in the microscale. Singular microemitters (i.e. emitter heights of $O(100\ \mu\text{m})$) can also be placed in an array-like structure as shown in Fig. 1.1(c) for applications requiring high throughput.

The earliest attempt at technologically leveraging such electrohydrodynamic (EHD) phenomenon was made by Krohn [78] in 1961, who documented charged droplet and ion emission suitable for space micropropulsion from eutectic liquid metal alloys (such as Wood's metal of Bi-Pb-Sn-Cd) extracted from small capillary tubes. A decade later, Krohn and Ringo [79] additionally realized the potential to leverage the phenomenon for developing ion sources suitable for probes, machining and implantation [80–82]. Around the same time, Clampitt *et al.* [22] developed the first prototypes of the externally wetted LMIS design outlined in Fig. 1.1. This was soon successfully coupled with charged particle optics by Seliger *et al.* [126, 127] in 1979 to result in the first ever LMIS based focused ion beam (FIB) system. The technology began the era of fabricating, modifying and characterizing matter at the micro and nano-scale as originally envisioned by Feynman [42] two decades earlier without any *a priori*. The current commercial FIB systems can readily generate ion beams with brightness of $O(10^{10}\text{A m}^{-2}\ \text{sr}^{-1})$, currents up to $O(100\ \mu\text{A})$, current densities more than $O(10^{11}\text{A m}^{-2})$ and spot diameters of $O(1\ \text{nm})$ [108] allowing imaging [33],

maskless ion implantation [83] and etching [75], milling [155], mask defect repair [61], doping [121], chemical vapor deposition [99], mass spectroscopy [88], ion microscopy [89] and many more applications. The interested reader can consult books [108, 117] and review articles [50, 63, 101, 109] and references therein for a comprehensive overview of the technology and applications. Outside of micro and nanotechnological applications, the system has also been applied to inertial fusion confinement [114–116] and for microemitter array space micropropulsion devices [97, 98, 103, 138, 139] as originally pursued by Krohn.

1.2 Note on liquid metals as perfect conductors versus leaky dielectrics

Table 1.1: Comparison of physical properties between liquid metals and leaky dielectrics. Liquid metal species considered are gallium and indium, whereas leaky dielectrics considered are water and corn oil. Presented quantities are density ρ, surface tension γ, viscosity μ, melting point T_{melt}, electrical conductivity σ, relative permittivity ε_r and charge relaxation timescale $\tau_\sigma = \varepsilon_r \varepsilon_o / \sigma$. Water and corn oil σ and ε_r are those at $T = 298$ K.

Liquid	ρ (kg/m^3)	γ (N/m)	μ (mPa s)	T_{melt} (K)	σ (S/m)	ε_r	τ_σ (s)
Gallium [69]	6100	0.720	1.94	303	3.9×10^6 [112]	1	2.3×10^{-18}
Indium [69]	7030	0.556	1.80	430	3.2×10^6 [142]	1	2.8×10^{-18}
Water	1000	0.076	1.79	273	5.5×10^{-6} [143]	78.3 [95]	1.3×10^{-4}
Corn Oil [120]	915	0.032	59.2	253 [65]	4.0×10^{-11} [25]	3.34 [25]	7.4×10^{-1}

Liquid metals are known to be well modeled as a perfectly conducting liquid in which charge relaxation [100] is instantaneous in comparison to flow time scales. There are also liquids of the "leaky dielectric" type that are characterized by a finite electrical conductivity [123] in which the relaxation time can be substantial. The physical properties and the charge relaxation times for selected liquid metals (gallium and indium) and leaky dielectrics (water and corn oil) are shown in Table 1.1, where indeed the charge relaxation in liquid metals can be considered to be effectively instantaneous. This difference was shown by simulations conducted by Collins *et al.* [24] to lead to differences in the tip shapes between leaky dielectrics and perfect conductors. Leaky dielectrics exhibit EHD tip streaming in which the tip elongates to a slender filament that can subsequently undergo capillary breakup into progeny droplets from surface tangent electric stresses generated by charge transport which occur on time scales comparable to the liquid flow. In contrast, perfect conductors only support tip sharpening as they can only sustain surface normal electric fields. Therefore, while there exists a wealth of analytical [48], experimental [23] and computational [111] literature on the EHD distortion of leaky dielectrics of relevance to "ionic liquid ion sources", their results are not quite applicable and are thus omitted from the discussion that follows.

1.3 EHD LMIS behavior prior to ion emission

Although the LMIS is a mature technology with the general physical principles of operation known, it remains difficult to access the details of the EHD liquid metal distortion prior to ion emission due to the difficulties faced by analytical and experimental approaches.

1.3.1 Liquid metal EHD distortion in the LMIS geometry

One of the difficult details to access is how the liquid metal wetted to the LMIS actually spatiotemporally evolves prior to ion emission. This has yet to be extensively documented experimentally due to the difficulty of accessing the nano-microscale lengths and times involved prior to ion emission. Early attempts at observing the distorted profile were made by rapidly cooling and freezing the operating system that enabled scanning electron microscopy micrographs [153] of the solidified liquid at the emitter apex region. However, the images of the solidified structure did not accurately reflect the *in-situ* profiles due to significant blunting of highly curved regions that occurred during solidification. The *in-situ* studies were later successfully conducted using high vacuum transmission electron microscopy (HV-TEM), which resulted in stunning images of emitting liquid protrusions as sampled in Fig. 1.2(b) and various instabilities like globule formation, spatiotemporally transient protrusion development and multiple protrusion formations. These were conducted by Ben Assayag *et al.* [12, 13], Driesel *et al.* [34–39, 62, 113] and Van es *et al.* [149] for various single species and eutectic alloys. However, the temporal resolution of just $O(0.1\text{ s})$ afforded by the charge coupled device cameras utilized for the studies precluded meaningful extraction of the temporal information as they could only image the liquid tip prior to protrusion development (as sampled in Fig. 1.2(a)) or after protrusions had already begun emission (as sampled in Fig. 1.2(b)). The extreme $O(10\text{ GV/m})$ electric fields generated at the emitting protrusion apex also causes significant deviations of the imaging electron trajectories, which forced application of very high electron acceleration voltages of $O(1\text{ MV})$. These studies were also unable to access the liquid bulk flow patterns as liquid metals are opaque, which renders many optical techniques based on particle seeding [56, 122] or lasers [159] inapplicable, not to mention the difficulties of achieving sufficient resolution. Non-optical imaging methods, such as probes [67] and ultrasonic imaging [140], possess similar problems with their invasiveness and insufficient resolution. As such, much of the available literature has instead focused on characterizing just the ion emission properties of LMIS systems.

It is not difficult to see the immense difficulty analytical approaches are faced with solving for the spatiotemporal fluid and electrostatic field solutions from the highly coupled, nonlinear system of equations with boundary conditions presented by the curved emitter electrode and

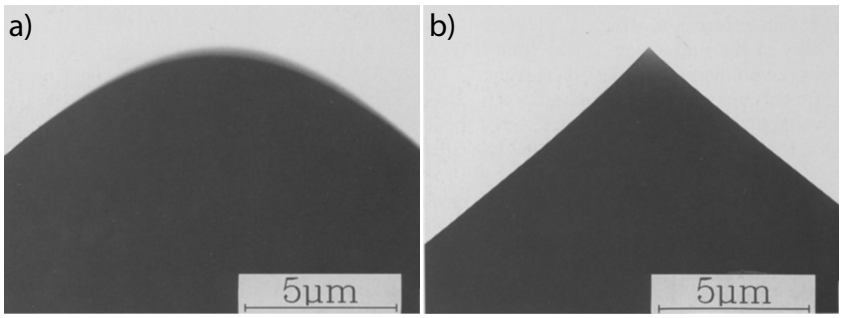

Figure 1.2: HV-TEM micrographs of a gallium LMIS liquid tip (a) prior and (b) post emission ignition with 33 μA current. Reproduced with permission from Fig. 5(a) and (c) of Ref. [38].

the extractor aperture. Much of the available analysis has also focused on characterizing the ion emission mechanism from steady state emitting liquid shapes. The specific shape that served as the basis of many such analyses is the "Taylor cone" [141]. Taylor was aware from experimental observations that date back to Gilbert [51] in 1600 that the distortion of an electrically conducting liquid under influence of strong electric fields typically leads to formation of conical protrusion profiles from whose apex emission occurs. He then sought to find the geometric profile of an infinite mass of a perfectly conducting liquid that results in a static equilibrium between the negative Maxwell and positive capillary pressure all along its free surface. Taylor's analysis is most easily seen by considering a conical conductor that possesses a polar angle $\theta = \theta_o$ in the spherical coordinate system $(\mathsf{r}, \varphi, \theta)$ (where φ is the azimuthal angle) whose origin is defined as the conical apex. For calculating the mean curvature $\mathcal{K}$, it is best to invoke the cylindrical coordinates (r, φ, z) in which $r = \mathsf{r}\sin\theta$, $z = \mathsf{r}\cos\theta$ and $\varphi = \varphi$ as the cone is rotationally symmetric about the azimuth. The conical surface h is then given by

$$z = h(r) = r\cot\theta_o \tag{1.1}$$

where $\cot\theta_o$ is a constant specifying the cone angle. The mean curvature $\mathcal{K}$ for an axisymmetric surface $h(r)$ is

$$\mathcal{K} = \frac{1}{2}\left(\frac{1}{[1+(dh/dr)^2]^{3/2}}\frac{\partial^2 h}{\partial r^2} + \frac{1}{r}\frac{1}{[1+(dh/dr)^2]^{1/2}}\frac{\partial h}{\partial r}\right) \tag{1.2}$$

such that $\mathcal{K} \sim r^{-1}$. Since the capillary pressure $p_C \sim \mathcal{K}$, it also scales as $p_C \sim r^{-1}$. It can be immediately seen that the capillary pressure should also scale as $p_C \sim \mathsf{r}^{-1}$ in spherical coordinates. The Laplace equation describing the rotationally symmetric vacuum electric potential $\phi(\mathsf{r}, \theta)$ back in spherical coordinates is

$$\frac{1}{\mathsf{r}^2}\frac{\partial}{\partial \mathsf{r}}\left(\mathsf{r}^2\frac{\partial\phi}{\partial \mathsf{r}}\right) + \frac{1}{\mathsf{r}^2\sin\theta}\frac{\partial}{\partial\theta}\left(\sin\theta\frac{\partial\phi}{\partial\theta}\right) = 0 \tag{1.3}$$

where the solution has the general form [70]

$$\phi = A\mathsf{r}^n P_n(\cos\theta) \tag{1.4}$$

where A is an undetermined constant representing the scale of local field strength and $P_n(\cdot)$ is the Legendre polynomial of order n. Evaluating the electric field $\vec{E} = -\nabla\phi$ on the conic surface $\theta = \theta_o$ yields

$$E_\mathsf{r} = -\frac{\partial\phi}{\partial\mathsf{r}} = -An\mathsf{r}^{n-1}P_n(\cos\theta_o) = 0 \tag{1.5}$$

$$E_\theta = -\frac{1}{\mathsf{r}}\frac{\partial\phi}{\partial\theta} = -A\mathsf{r}^{n-1}\frac{\partial}{\partial\theta}\left[P_n(\cos\theta)\right]_{\theta=\theta_o} \tag{1.6}$$

where $P_n(\cos\theta_o) = 0$ arises from the conic surface being an equipotential. It can be seen that the Maxwell pressure scales as $p_M \sim \left|\vec{E}\right|^2 \sim \mathsf{r}^{2(n-1)}$. For the two pressures p_C and p_M to balance, n must equal $1/2$, which immediately yields the conic surface interior half angle from the unique root of $P_{1/2}(\cos\theta_o) = 0$ to be $\pi - \theta_o = 49.3°$ known as the "Taylor cone" angle.

However, the Taylor cone cannot in fact be used to describe a state of stable equilibrium as the Maxwell and capillary pressures diverge to infinity at the conical apex, which renders the solution as a state of metastable or unstable equilibrium. As ion emission occurs from the apical region, this issue alone makes application of the Taylor cone to analysis of ion emission very problematic. Some have tried to circumvent this issue by considering that possessing a rounded apex [52] or that stitched with a liquid sphere [154], an elongated cuspidal [46, 74, 93] or columnar jet [71] but these models are phenomenologically motivated at best. The solution also requires the extractor to have the shape of one of the family of electrostatic equipotentials to which the cone surface itself belongs, which is a very specific condition that is not met in practice. The solution also only applies to the static situation with no liquid flow and thereby neglects the strong dynamic response exhibited by the liquid to the applied electric fields. Despite these issues and the availability of *in-situ* observations that clearly present dynamic protrusion shapes, the solution has been used as the basis for many analyses of emission characteristics [10, 94, 151] and numerical simulations of emitted ion trajectories [104, 154], and also taken as the standard nomenclature in the greater LMIS and FIB community [150] even through some modern literature. Since the shape of the emission site controls all ion emission properties from the onset voltage to the emitted current to the beam divergence angle, it is critical to establish the correct dynamical liquid profiles and accompanying physical fields that serve as the precursors to ion emission.

1.3.2 Influence of key LMIS operating conditions on the ensuing EHD liquid distortion

As a consequence of the limitations inherent to experimental and analytical approaches, the available literature has also been unable to probe in detail how key LMIS operating conditions influence the ensuing EHD liquid distortion. There have been many previous analyses that treat the early stage distortion as an EHD surface instability. Tonks [145] provided the first treatment using a mechanical approach in which he was able to find the critical electric field strength required for accelerated distortion of the perfectly conducing, flat liquid surface into protrusions. Frenkel [47] provided the first hydrodynamic treatment using the inviscid surface Bernoulli equation shortly after Tonks and recovered the critical field strength as calculated by Tonks. Landau and Lifshitz [85] provided the first dispersion relation relating the growth rate and wavenumber of perturbative modes in the inviscid, infinitely thick liquid limit. Efforts on probing the influence of finite liquid viscosity on the instability growth were later carried out by Nevrovskii [107] on introducing corrections to the inviscid results, Chu *et al.* [21] from the perspectives of a dissipative harmonic oscillator and He *et al.* [60] and Miskovsky *et al.* [102] from treatment of the full Navier Stokes equation and associated boundary conditions. However, it was de Surgy *et al.* [131, 132] who conducted the comprehensive linear stability analysis that culminated in the correct dispersion relation applicable for perfectly conducting, flat liquids possessing arbitrary thickness and viscosity and placed under an arbitrarily thick vacuum. However, all of these analyses assume the basic system of a perfectly conducting liquid supported on a smooth, flat substrate and placed under a smooth, flat extractor. The geometry and the resultant electric field distribution are vastly different to those found in real LMIS systems possessing a curved emitter and an apertured extractor. It is therefore unknown how the stability of the deforming liquid metal may be influenced by the two geometric components.

The late time dynamical behavior of the electrified liquid metal tip prior to ion emission has also been analyzed in the literature. Such behavior was first noted by Tonks [145] in the same analysis to be a self-similar process leading to a runaway growth. The observation was later followed by a pioneering asymptotic analysis by Zubarev [165] who established that the late stage dynamics of the perfectly conducting, inviscid liquid protrusion tip undergoing field self enhancement and sharpening is indeed driven by self-similar growth leading to finite time blowup. Zhou and Troian [164] later improved upon the analysis to highlight the strong influence of inertia during self-similar growth, which revealed a multiplicity of inertial self-similar solutions. Zubarev [166] has also recently found self-similar growth of the viscous liquid protrusion tips. Again, however, there is not much that can be said for how might the introduction of realistic LMIS geometric components influence such

predicted late stage dynamical behavior. The small spatiotemporal timescales associated with both the instability development and late time self-similar dynamics make it especially challenging to study the two physical phenomena in real LMIS systems.

The handful of experimental studies that vary some operating parameters like the emitter apex curvature [9, 10, 152] only report the response of current-voltage curves with no information on the response of the liquid distortion. Though the aforementioned *in-situ* studies did capture the dynamical response of emitting protrusions to changes in the ion current, no such response was cataloged for the distortion prior to ion emission. The studies also often operated with a specific emitter and extractor configuration kept fixed throughout the investigation. Limited data on the operating conditions themselves, especially on the liquid thicknesses wetted to the emitters, make it difficult to reproduce the observed distortion and extract correlations.

As such, there exists little protocol available in the literature on how the LMIS system should be designed and operated for desirable performance. One of the problems that plague the long term stability and performance is the underspray [17, 77] of emitted ions to the extractor underside, which leads to a build up of residue that can eventually block the aperture and lead to short circuiting resulting in catastrophic device failure. Another phenomenon that has yet to be sufficiently correlated to operating conditions is the appearance of multiple emission sites [9] from a single LMIS emitter. Though there exists some *in-situ* observations of multiple, parasitic protrusions that arise for high operating currents, data needed to correlate such distortion to various operating parameters remain minimal. Extracting such correlations would potentially enable control over the ion emission characteristics desirable for various applications.

It is evident that the currently available experimental techniques and analytical approaches are inadequate to accurately capture the spatiotemporal liquid distortion and the response of such distortion to changes in key operating conditions presented by LMIS systems. These issues have hindered the ability of researchers to predictively design systems specifically targeted for desired applications.

1.4 Previous computational simulations of EHD liquid metal distortion

The advent of advanced computational techniques provides a viable alternative to experimental and analytical approaches to finally study the details of the LMIS flow and stability prior to ion emission through simulations that accurately and stably track the spatiotemporal evolution of the liquid metal free surface. Such simulations were first conducted by Cui and Tong [26], who implemented the marker and cell method [58] to track the spatiotemporal

evolution of a perfectly conducting, viscous electrified liquid emerging out of a cylindrical tube and wetted to a needle emitter tip. They reported liquid distortion into protrusions with interior half angles different from the Taylor cone angle, though the details provided were brief.

The development of an axially symmetric protrusion from an initially flat liquid metal layer was first conducted by Suvorov and coworkers [134–136], who utilized the marker and cell method [58] with adaptive grid generation [11] allowing for preferential grid compression in the vicinity of the rapidly sharpening protrusion tip for smooth and stable spatiotemporal evolution of the liquid free surface. Their simulations yielded dynamic protrusion growth accompanied by runaway behavior of the protrusion apex electric field, mean curvature and velocity. This behavior was shown to be self-similar as previously predicted by Zubarev [165]. Collins *et al.* [24] instead utilized a finite element method with elliptic mesh generation and adaptive time integration to simulate the distortion for electrified liquids of varying conductivity. They concluded from their results that the primary mechanism for the inception of EHD tip streaming leading to the elongation of the tip into a thin jet and subsequent breakup into droplets observed for leaky dielectrics is the development of large electric shear stresses from charge relaxation comparable to the relevant flow timescales. As perfectly conducting liquids cannot support internal and surface tangent electric fields due to instantaneous charge relaxation, the protrusion tips can only undergo tip sharpening accompanied by field self enhancement. Albertson and Troian [5] used the arbitrary Lagrangian Eulerian finite element method [32] with adaptive mesh generation and time integration to confirm self-similar growth of such protrusions regardless of the Reynolds number, whereas Zhou and Troian [164] instead utilized a boundary integral patching technique to extract numerical solutions of liquid formations describing a multiplicity of inertial self-similar protrusion shapes. The distortion of a perfectly conducting droplet has also been simulated for the viscous droplet suspended in a surrounding liquid by Betelu *et al.* [14] and Fontelos *et al.* [44] using the Euler model and for the inviscid droplet suspended in vacuum by Burton and Taborek [18] and Garzon *et al.* [49] using the inviscid Bernoulli model. These simulations showed the formation of self sharpening tips at the ends of the droplet marked by self-similar power law growths of the surface charge density and apex curvature. As for geometries relevant to real LMIS systems, there have been previous research conducted by the {LIS^{2}T} group at Caltech (Albertson [4], Zhou [163] and White [156]) on computationally modeling the EHD distortion for such geometries and developing the mathematical formalism for flow on curved and topologically patterned substrates also found for such systems. The work described in this thesis extends the previous research on computationally modeling the EHD distortion in a realistic LMIS geometry.

1.5 Overview of the thesis

The work described in this thesis simulates the spatiotemporal evolution of the electrified liquid metal surface in a realistic LMIS geometry, uncovering the effects of the curved microemitter and apertured extractor on the EHD phenomenon and presenting rules of thumb applicable to LMIS design and operation. The simulations are conducted using the arbitrary Lagrangian Eulerian finite element method [32], which is a method optimal for tracking the spatiotemporal evolution of a rapidly accelerating liquid free surface. The contents of this thesis are as follows.

In Chapter 2, we provide the basic hydrodynamic theory that ultimately introduces the definitions of the Reynolds and electric Weber numbers invoked throughout the thesis. We also provide the linear stability analysis of the arbitrarily thick and viscous flat liquid metal layer under a normal electric field used as predictions for results discussed in Chapter 4. The original analysis has already been conducted by de Surgy *et al.* [131, 132] in Cartesian coordinates using gravity dependent scalings. The analysis shown here accounts for the axisymmetric and gravityless domains used for our computational simulations.

In Chapter 3, we simulate the EHD liquid metal distortion in a realistic LMIS geometry prior to ion emission using finite element simulations. We find a rich multiplicity of possible EHD modes categorized by the existence, location and number of protrusions that develop from the evolving liquid free surface. We construct a mode diagram that correlates the final mode outcomes to the Reynolds and electric Weber numbers dominantly scaled by key initial conditions in the initial liquid thickness, microemitter apex curvature radius and applied electric potential. We discuss the rules of thumb found for generating an axially symmetric protrusion in the modeled geometry and observations on the confined development of protrusions to within the initial liquid apex curvature radius no matter the mode or applied initial conditions.

In Chapter 4, we examine the influence of extractor aperture and microemitter curvature on the EHD instability development. The effects exerted by each component are extracted by conducting simulations in the three systems: the base flat liquid layer and flat apertureless extractor, flat liquid layer and flat apertured extractor, and curved microemitter and flat apertured extractor (i.e. LMIS) geometry. The initial liquid surface, which is modeled to be perfectly smooth for simulations in Ch. 3 and 5, is additionally imbued with a small degree of random noise. The simulations reveal the stabilizing effects of the two components on the evolving liquid surface that ultimately confine the instability development within the initial liquid apex curvature radius of the symmetry axis in the LMIS geometry. Despite the stabilizing mechanisms, however, we extract a strong correlation between the dominant

instability wavenumbers extracted from the LMIS geometry and those predicted by previous linear stability analyses conducted by de Surgy *et al.* [131, 132] of the base system for an arbitrarily thick and viscous liquid. This correlation is expected to potentially provide researchers with the ability to control the generated instability wavelength for applications where such formations are desirable.

In Chapter 5, we examine the late time dynamical behavior of EHD modes that arise in the modeled LMIS geometry. The simulations reveal that the protrusion tips indeed undergo self-similar development marked by power law growths irrespective of the generated EHD mode. The axial EHD mode self-similar exponents for the protrusion apex Maxwell and capillary pressures are found to exhibit collapse in the Reynolds and electric Weber number parameter space. Examination of exponents across the axial, coronal and instability EHD modes reveal a separation of extracted values arising out of the axial/non-axialness of the analyzed protrusion. The results indicate a strong robustness of late stage self-similar dynamics to changes in the protrusion axialness, symmetry and number.

The data tables possessing key results for all conducted simulations can be found in Sec. 3.10 for Ch. 3, Sec. 4.11 for Ch. 4 and Sec. 5.9 for Ch. 5. The convergence tests on the protrusion apex coordinates and self-similar exponents of select examples can also be found in Sec. 3.9 and Sec. 5.8, respectively. The numbering convention of the sections, tables, figures and equations is such that the first number always refers to the chapter number in which the components reside. Every variable with a subscript f refers to the quantity evaluated at the most prominent protrusion apex at the simulation final termination time.

Chapter 2

BASIC HYDRODYNAMIC THEORY AND LINEAR STABILITY ANALYSIS

This section reviews the basic hydrodynamic theory and linear stability analysis pertaining to the well known arbitrarily thick and viscous flat, electrified liquid metal layer under a normal electric field. The purpose of this section is first to address the specific choices of characteristic scales used to nondimensionalize the governing equations and boundary conditions. The nondimensionalization results in construction of key nondimensional numbers that are used to characterize the EHD distortion simulated in the modeled LMIS geometry. The nondimensionalization procedure presented here relies on known techniques which have been covered in standard texts [29, 123]. The linear stability analysis presented in this chapter follows the general procedure taken by de Surgy *et al.* [131, 132], who were the first to correctly conduct the analysis for the described flat liquid system.

The description of the system goes as follows. It is set in the axisymmetric coordinate system (r, z) without gravity. A perfectly conducting liquid layer whose undisturbed surface lies on $z = h_o$ is wetted on a flat substrate at $z = 0$ and placed under a flat, apertureless extractor at $z = b + h_o$ with a vacuum in between the liquid and the extractor. The vertical gap distance between the liquid and extractor is designated as b. A constant electric potential $\phi = \phi_o$ is applied to the liquid surface. The extractor is grounded to $\phi = 0$.

The structure of the chapter goes as follows. Sec. 2.1 presents the governing equations and boundary conditions applicable for the described flat liquid system. Sec. 2.2 introduces the symbols and notation for the characteristic scales and nondimensionalized versions of the physical variables. Sec. 2.3 presents the nondimensionalization of the equations and boundary conditions guided by choices made on the characteristic scales, which leads to the definitions of the Reynolds Re and electric Weber We numbers invoked in the succeeding chapters. Sec. 2.4 to 2.7 then provide the details of the linear stability analysis of the described flat liquid system. This culminates in the extraction of the gravity independent nondimensional dispersion relation [131] and recovery of the dimensional dispersion relation [132] that describe the growth rate of surface perturbations.

2.1 Governing equations and boundary conditions

The liquid metal flow is modeled by the continuity and Navier-Stokes equation for an incompressible, isothermal Newtonian fluid where the velocity $\vec{u}(r,z,t) = u\ \hat{r} + w\ \hat{z}$ and pressure $p(r,z,t)$ satisfy

$$\nabla \cdot \vec{u} = 0 \quad \text{in } \Omega_{liq} \tag{2.1}$$

$$\begin{aligned} \rho\frac{\partial u}{\partial t} + \rho u\frac{\partial u}{\partial r} + \rho w\frac{\partial u}{\partial z} &= -\frac{\partial p}{\partial r} + \mu\left(\frac{\partial}{\partial r}\left[\frac{1}{r}\frac{\partial}{\partial r}(ru)\right] + \frac{\partial^2 u}{\partial z^2}\right) \text{ in liquid} \\ \rho\frac{\partial w}{\partial t} + \rho u\frac{\partial w}{\partial r} + \rho w\frac{\partial w}{\partial z} &= -\frac{\partial p}{\partial z} + \mu\left(\frac{1}{r}\frac{\partial}{\partial r}\left[r\frac{\partial w}{\partial r}\right] + \frac{\partial^2 w}{\partial z^2}\right) \text{ in liquid} \end{aligned} \tag{2.2}$$

where ρ and μ are the liquid metal density and viscosity defined as material constants, respectively.

The liquid metal is modeled as a perfectly conducting fluid such that the electrostatic approximation is valid in the vacuum. The electric potential $\phi(r,z,t)$ satisfies the Laplace equation

$$\nabla^2\phi = 0 \text{ in vacuum} \tag{2.3}$$

where the electric field can be found by taking the gradient of ϕ

$$\vec{E}(r,z,t) = -\nabla\phi = \left(-\frac{\partial\phi}{\partial r}\right)\hat{r} + \left(-\frac{\partial\phi}{\partial z}\right)\hat{z} = E_r(r,z,t)\hat{r} + E_z(r,z,t)\hat{z} \tag{2.4}$$

The boundary conditions go as follows. Defining the liquid surface to be $z = h(r,t)$, the normal stress boundary condition governs the pressure on the liquid surface

$$p = -\frac{1}{2}\varepsilon_o E^2 - 2\gamma\mathcal{K}_h + \hat{n}\cdot\left\{\mu\left[\nabla\vec{u} + (\nabla\vec{u})^T\right]\right\}\cdot\hat{n} \quad \text{on } z = h(r,t) \tag{2.5}$$

with the components defined as the Maxwell pressure p_M, capillary pressure p_C and normal viscous pressure p_V

$$p = p_M + p_C + p_V \quad \text{on } z = h(r,t) \tag{2.6}$$

where the sign convention is such that p_M is always negative and pulls the liquid into the vacuum. The variable γ is the constant liquid metal surface tension, ε_o is the vacuum permittivity, and E is the $h(r,t)$ electric field magnitude defined as

$$E = \left|\vec{E}\right| = \sqrt{\left(-\frac{\partial\phi}{\partial r}\right)^2 + \left(-\frac{\partial\phi}{\partial z}\right)^2} \tag{2.7}$$

The surface normal vector $\hat{n}$ is

$$\hat{n} = \frac{1}{\sqrt{1 + (\partial h/\partial r)^2}}\left(-\frac{\partial h}{\partial r}\hat{r} + \hat{z}\right) \tag{2.8}$$

The surface mean curvature $\mathcal{K}_h$ is

$$\mathcal{K}_h = -\frac{1}{2}(\nabla \cdot \hat{n}) = \frac{1}{2}\left(\frac{\partial^2 h/\partial r^2}{[1+(\partial h/\partial r)^2]^{3/2}} + \frac{\partial h/\partial r}{r[1+(\partial h/\partial r)^2]^{1/2}}\right) \tag{2.9}$$

The deviatoric stress tensor is

$$\overleftrightarrow{K} = \mu(\nabla\vec{u} + (\nabla\vec{u})^T) = \mu\begin{bmatrix} 2\dfrac{\partial u}{\partial r} & \dfrac{\partial u}{\partial z} + \dfrac{\partial w}{\partial r} \\ \dfrac{\partial u}{\partial z} + \dfrac{\partial w}{\partial r} & 2\dfrac{\partial w}{\partial z} \end{bmatrix} \tag{2.10}$$

such that the viscous pressure evaluates to

$$\hat{n} \cdot \overleftrightarrow{K} \cdot \hat{n} = \frac{2\mu}{(1+(\partial h/\partial r)^2)}\left(\left[\frac{\partial h}{\partial r}\right]^2 \frac{\partial u}{\partial r} - \frac{\partial h}{\partial r}\frac{\partial u}{\partial z} - \frac{\partial h}{\partial r}\frac{\partial w}{\partial r} + \frac{\partial w}{\partial z}\right) \tag{2.11}$$

Substituting the expressions into Eq. 2.5 gives

$$p = -\frac{1}{2}\varepsilon_o E^2 - \gamma\left(\frac{\partial^2 h/\partial r^2}{[1+(\partial h/\partial r)^2]^{3/2}} + \frac{\partial h/\partial r}{r[1+(\partial h/\partial r)^2]^{1/2}}\right)$$
$$+\frac{2\mu}{(1+(\partial h/\partial r)^2)}\left(\left[\frac{\partial h}{\partial r}\right]^2 \frac{\partial u}{\partial r} - \frac{\partial h}{\partial r}\frac{\partial u}{\partial z} - \frac{\partial h}{\partial r}\frac{\partial w}{\partial r} + \frac{\partial w}{\partial z}\right) \quad \text{on } z = h(r,t) \tag{2.12}$$

The shear stress boundary condition specifies a vanishing shear viscous stress on the $h(r,t)$

$$\hat{n} \cdot \left\{\mu\left[\nabla\vec{u} + (\nabla\vec{u})^T\right]\right\} \cdot \hat{t} = 0 \quad \text{on } z = h(r,t) \tag{2.13}$$

where $\hat{t}$ is the surface tangent

$$\hat{t} = \frac{1}{\sqrt{1+(\partial h/\partial r)^2}}\left(\hat{r} + \frac{\partial h}{\partial r}\hat{z}\right) \tag{2.14}$$

such that the evaluated and simplified form is

$$\frac{\mu}{(1+(\partial h/\partial r)^2)}\left(2\left[\frac{\partial h}{\partial r}\frac{\partial w}{\partial z} - \frac{\partial h}{\partial r}\frac{\partial u}{\partial r}\right] + \left[1-\left(\frac{\partial h}{\partial r}\right)^2\right]\left[\frac{\partial u}{\partial z} + \frac{\partial w}{\partial r}\right]\right) = 0 \tag{2.15}$$

which simply yields the following condition

$$2\left[\frac{\partial h}{\partial r}\frac{\partial w}{\partial z} - \frac{\partial h}{\partial r}\frac{\partial u}{\partial r}\right] = -\left[1-\left(\frac{\partial h}{\partial r}\right)^2\right]\left[\frac{\partial u}{\partial z} + \frac{\partial w}{\partial r}\right] \quad \text{on } z = h(r,t) \tag{2.16}$$

The kinematic boundary condition relates the motion of the liquid surface to the velocity at the liquid surface

$$\frac{\partial h}{\partial t} + u\frac{\partial h}{\partial r} = w \quad \text{on } z = h(r,t) \tag{2.17}$$

A constant electric potential is applied to the liquid surface

$$\phi = \phi_o \quad \text{on } z = h(r,t) \tag{2.18}$$

At the symmetry axis $r = 0$, the flux is set to zero

$$u = 0, \ \frac{\partial w}{\partial r} = 0 \quad \text{at } r = 0 \tag{2.19}$$

At the bottom electrode serving as the domain floor $z = 0$, the no slip and no penetration conditions are set

$$u = 0, \ w = 0 \quad \text{on } z = 0 \tag{2.20}$$

At the top electrode serving as the extractor surface $z = b + h_o$, the electric potential is set to be grounded to $\phi = 0$.

$$\phi = 0 \quad \text{on } z = b + h_o \tag{2.21}$$

2.2 Characteristic scales

The nondimensional versions of physical variables are defined with the characteristic scales yet to be determined. The scales will be shown to be naturally extracted from the nondimensionalization of the governing equations and boundary conditions themselves. The subscripts c define the dimensional scales for the physical variables and the capitalized variables define the nondimensional versions of the physical variables.

$$R = \frac{r}{r_c}, \ r_c \text{ is some characteristic length scale in the } r \text{ direction} \tag{2.22}$$

$$Z = \frac{z}{z_c}, \ z_c \text{ is some characteristic length scale in the } z \text{ direction} \tag{2.23}$$

$$H = \frac{h}{h_o}, \ \text{since the initial state has an average thickness of } h_o \tag{2.24}$$

$$P = \frac{p}{p_c}, \ p_c \text{ is some characteristic fluid pressure} \tag{2.25}$$

$$\Phi = \frac{\phi}{\phi_c}, \ \phi_c \text{ is some characteristic electric potential} \tag{2.26}$$

$$\vec{\mathcal{E}} = \frac{\vec{E}}{E_c}, \ E_c \text{ is the characteristic electric field magnitude} \tag{2.27}$$

$$U = u/u_c, \ u_c \text{ is some characteristic fluid speed along the } r \text{ direction} \tag{2.28}$$

$$W = w/w_c, \ w_c \text{ is some characteristic fluid speed along the } z \text{ direction} \tag{2.29}$$

$$T = \frac{t}{t_c}, \ t_c \text{ is some characteristic time} \tag{2.30}$$

2.3 Nondimensionalization

This section presents the nondimensionalization of the governing equations and boundary conditions presented in Sec. 2.1.

Substituting nondimensional variables into the continuity equation Eq. 2.1

$$\frac{1}{r}\frac{\partial}{\partial r}(ru) + \frac{\partial w}{\partial z} = 0 \tag{2.31}$$

$$\frac{u_c}{r_c}\frac{1}{R}\frac{\partial}{\partial R}(RU) + \frac{w_c}{z_c}\frac{\partial W}{\partial Z} = 0 \tag{2.32}$$

The velocity scales u_c and w_c are set to be related by

$$u_c = w_c\frac{r_c}{z_c} \tag{2.33}$$

which yields

$$\frac{1}{R}\frac{\partial}{\partial R}(RU) + \frac{\partial W}{\partial Z} = 0 \quad \text{in liquid} \tag{2.34}$$

Substituting nondimensional variables into the Navier-Stokes equation Eq. 2.2 gives

$$\begin{aligned}
\frac{\rho u_c}{t_c}\frac{\partial U}{\partial T} + \frac{\rho u_c^2}{r_c}U\frac{\partial U}{\partial R} + \frac{\rho u_c w_c}{z_c}W\frac{\partial U}{\partial Z} &= -\frac{p_c}{r_c}\frac{\partial P}{\partial R} + \mu\left(\frac{u_c}{r_c^2}\frac{\partial}{\partial R}\left[\frac{1}{R}\frac{\partial}{\partial R}(RU)\right] + \frac{u_c}{z_c^2}\frac{\partial^2 U}{\partial Z^2}\right) \\
\frac{\rho w_c}{t_c}\frac{\partial W}{\partial T} + \frac{\rho u_c w_c}{r_c}U\frac{\partial W}{\partial R} + \frac{\rho w_c^2}{z_c}W\frac{\partial W}{\partial Z} &= -\frac{p_c}{z_c}\frac{\partial P}{\partial Z} + \mu\left(\frac{w_c}{r_c^2}\frac{1}{R}\frac{\partial}{\partial R}\left[R\frac{\partial W}{\partial R}\right] + \frac{w_c}{z_c^2}\frac{\partial^2 W}{\partial Z^2}\right)
\end{aligned} \tag{2.35}$$

Substituting $u_c = w_c r_c/z_c$ wherever possible leads to

$$\begin{aligned}
\frac{\rho w_c^2 r_c}{z_c^2}\left(\frac{z_c}{t_c w_c}\frac{\partial U}{\partial T} + U\frac{\partial U}{\partial R} + W\frac{\partial U}{\partial Z}\right) &= -\frac{p_c}{r_c}\frac{\partial P}{\partial R} + \mu\left(\frac{w_c}{r_c z_c}\frac{\partial}{\partial R}\left[\frac{1}{R}\frac{\partial}{\partial R}(RU)\right] + \frac{w_c r_c}{z_c^3}\frac{\partial^2 U}{\partial Z^2}\right) \\
\frac{\rho w_c^2}{z_c}\left(\frac{z_c}{t_c w_c}\frac{\partial W}{\partial T} + U\frac{\partial W}{\partial R} + W\frac{\partial W}{\partial Z}\right) &= -\frac{p_c}{z_c}\frac{\partial P}{\partial Z} + \mu\left(\frac{w_c}{r_c^2}\frac{1}{R}\frac{\partial}{\partial R}\left[R\frac{\partial W}{\partial R}\right] + \frac{w_c}{z_c^2}\frac{\partial^2 W}{\partial Z^2}\right)
\end{aligned} \tag{2.36}$$

where the characteristic timescale t_c can then be determined to be that from the dominant vertical liquid motion

$$t_c = \frac{z_c}{w_c} \tag{2.37}$$

such that

$$\begin{aligned}
\frac{\rho w_c^2 r_c}{z_c^2}\left(\frac{\partial U}{\partial T} + U\frac{\partial U}{\partial R} + W\frac{\partial U}{\partial Z}\right) &= -\frac{p_c}{r_c}\frac{\partial P}{\partial R} + \mu\left(\frac{w_c}{r_c z_c}\frac{\partial}{\partial R}\left[\frac{1}{R}\frac{\partial}{\partial R}(RU)\right] + \frac{w_c r_c}{z_c^3}\frac{\partial^2 U}{\partial Z^2}\right) \\
\frac{\rho w_c^2}{z_c}\left(\frac{\partial W}{\partial T} + U\frac{\partial W}{\partial R} + W\frac{\partial W}{\partial Z}\right) &= -\frac{p_c}{z_c}\frac{\partial P}{\partial Z} + \mu\left(\frac{w_c}{r_c^2}\frac{1}{R}\frac{\partial}{\partial R}\left[R\frac{\partial W}{\partial R}\right] + \frac{w_c}{z_c^2}\frac{\partial^2 W}{\partial Z^2}\right)
\end{aligned} \tag{2.38}$$

Dividing through by the factor $\rho w_c^2/z_c$ for both components

$$\begin{aligned}\frac{r_c}{z_c}\left(\frac{\partial U}{\partial T}+U\frac{\partial U}{\partial R}+W\frac{\partial U}{\partial Z}\right) &= -\frac{p_c z_c}{\rho w_c^2 r_c}\frac{\partial P}{\partial R}+\frac{\mu z_c}{\rho w_c^2}\left(\frac{w_c}{r_c z_c}\frac{\partial}{\partial R}\left[\frac{1}{R}\frac{\partial}{\partial R}(RU)\right]+\frac{w_c r_c}{z_c^3}\frac{\partial^2 U}{\partial Z^2}\right)\\ \frac{\partial W}{\partial T}+U\frac{\partial W}{\partial R}+W\frac{\partial W}{\partial Z} &= -\frac{p_c}{\rho w_c^2}\frac{\partial P}{\partial Z}+\frac{\mu z_c}{\rho w_c^2}\left(\frac{w_c}{r_c^2}\frac{1}{R}\frac{\partial}{\partial R}\left[R\frac{\partial W}{\partial R}\right]+\frac{w_c}{z_c^2}\frac{\partial^2 W}{\partial Z^2}\right)\end{aligned} \tag{2.39}$$

and taking out the factor $w_c r_c/z_c^3$ from R component viscous term and w_c/z_c^2 from Z component viscous term

$$\begin{aligned}\frac{r_c}{z_c}\left(\frac{\partial U}{\partial T}+U\frac{\partial U}{\partial R}+W\frac{\partial U}{\partial Z}\right) &= -\frac{p_c z_c}{\rho w_c^2 r_c}\frac{\partial P}{\partial R}+\frac{\mu r_c}{\rho w_c z_c^2}\left(\frac{z_c^2}{r_c^2}\frac{\partial}{\partial R}\left[\frac{1}{R}\frac{\partial}{\partial R}(RU)\right]+\frac{\partial^2 U}{\partial Z^2}\right)\\ \frac{\partial W}{\partial T}+U\frac{\partial W}{\partial R}+W\frac{\partial W}{\partial Z} &= -\frac{p_c}{\rho w_c^2}\frac{\partial P}{\partial Z}+\frac{\mu}{\rho w_c z_c}\left(\frac{z_c^2}{r_c^2}\frac{1}{R}\frac{\partial}{\partial R}\left[R\frac{\partial W}{\partial R}\right]+\frac{\partial^2 W}{\partial Z^2}\right)\end{aligned} \tag{2.40}$$

and multiplying the R component equation by r_c/z_c in order to set the pressure gradient factors in both components the same gives

$$\begin{aligned}\frac{r_c^2}{z_c^2}\left(\frac{\partial U}{\partial T}+U\frac{\partial U}{\partial R}+W\frac{\partial U}{\partial Z}\right) &= -\frac{p_c}{\rho w_c^2}\frac{\partial P}{\partial R}+\frac{\mu r_c^2}{\rho w_c z_c^3}\left(\frac{z_c^2}{r_c^2}\frac{\partial}{\partial R}\left[\frac{1}{R}\frac{\partial}{\partial R}(RU)\right]+\frac{\partial^2 U}{\partial Z^2}\right)\\ \frac{\partial W}{\partial T}+U\frac{\partial W}{\partial R}+W\frac{\partial W}{\partial Z} &= -\frac{p_c}{\rho w_c^2}\frac{\partial P}{\partial Z}+\frac{\mu}{\rho w_c z_c}\left(\frac{z_c^2}{r_c^2}\frac{1}{R}\frac{\partial}{\partial R}\left[R\frac{\partial W}{\partial R}\right]+\frac{\partial^2 W}{\partial Z^2}\right)\end{aligned} \tag{2.41}$$

The Reynolds number can then be extracted as

$$\mathsf{Re}=\frac{\rho w_c z_c}{\mu} \tag{2.42}$$

which is dependent on the vertical velocity w_c and length z_c scales. The dependence has been chosen due to the known dominance of the vertical motion over the lateral motion, which will be shown in Sec. 3 in further detail. The current form of the nondimensionalized Navier Stokes equation is then

$$\begin{aligned}\frac{r_c^2}{z_c^2}\left(\frac{\partial U}{\partial T}+U\frac{\partial U}{\partial R}+W\frac{\partial U}{\partial Z}\right) &= -\frac{p_c}{\rho w_c^2}\frac{\partial P}{\partial R}+\frac{1}{\mathsf{Re}}\frac{r_c^2}{z_c^2}\left(\frac{z_c^2}{r_c^2}\frac{\partial}{\partial R}\left[\frac{1}{R}\frac{\partial}{\partial R}(RU)\right]+\frac{\partial^2 U}{\partial Z^2}\right)\\ \frac{\partial W}{\partial T}+U\frac{\partial W}{\partial R}+W\frac{\partial W}{\partial Z} &= -\frac{p_c}{\rho w_c^2}\frac{\partial P}{\partial Z}+\frac{1}{\mathsf{Re}}\left(\frac{z_c^2}{r_c^2}\frac{1}{R}\frac{\partial}{\partial R}\left[R\frac{\partial W}{\partial R}\right]+\frac{\partial^2 W}{\partial Z^2}\right)\end{aligned} \tag{2.43}$$

in liquid

where further simplification will arise from the nondimensionalization of the normal stress boundary condition applied to $z=h(r,t)$.

At the liquid surface, note that

$$Zz_c = H(R,T)h_o \rightarrow Z = H(R,T)\frac{z_c}{h_o} \tag{2.44}$$

which indicates that the appropriate scaling for z_c is

$$z_c = h_o \tag{2.45}$$

At the liquid surface $Z = H$, the normal stress boundary condition Eq. 2.12 becomes

$$p_c\ P|_{Z=H} = -\frac{1}{2}\varepsilon_o E_c^2 \mathcal{E}^2 - \frac{\gamma z_c}{r_c^2}\left(\frac{\partial^2 H/\partial R^2}{\left[1+\frac{z_c^2}{r_c^2}\left(\frac{\partial H}{\partial R}\right)^2\right]^{3/2}} + \frac{\partial H/\partial R}{R\left[1+\frac{z_c^2}{r_c^2}\left(\frac{\partial H}{\partial R}\right)^2\right]^{1/2}}\right)$$
$$+\frac{2\mu}{1+\frac{z_c^2}{r_c^2}\left(\frac{\partial H}{\partial R}\right)^2}\left(\frac{z_c^2 u_c}{r_c^3}\left[\frac{\partial H}{\partial R}\right]^2\frac{\partial U}{\partial R} - \frac{u_c}{r_c}\frac{\partial H}{\partial R}\frac{\partial U}{\partial Z} - \frac{z_c w_c}{r_c^2}\frac{\partial H}{\partial R}\frac{\partial W}{\partial R} + \frac{w_c}{z_c}\frac{\partial W}{\partial Z}\right) \tag{2.46}$$

Substituting $u_c = w_c r_c / z_c$ wherever possible

$$p_c\ P|_{Z=H} = -\frac{1}{2}\varepsilon_o E_c^2 \mathcal{E}^2 - \frac{\gamma z_c}{r_c^2}\left(\frac{\partial^2 H/\partial R^2}{\left[1+\frac{z_c^2}{r_c^2}\left(\frac{\partial H}{\partial R}\right)^2\right]^{3/2}} + \frac{\partial H/\partial R}{R\left[1+\frac{z_c^2}{r_c^2}\left(\frac{\partial H}{\partial R}\right)^2\right]^{1/2}}\right)$$
$$+\frac{2\mu}{1+\frac{z_c^2}{r_c^2}\left(\frac{\partial H}{\partial R}\right)^2}\left(\frac{z_c w_c}{r_c^2}\left[\frac{\partial H}{\partial R}\right]^2\frac{\partial U}{\partial R} - \frac{w_c}{z_c}\frac{\partial H}{\partial R}\frac{\partial U}{\partial Z} - \frac{z_c w_c}{r_c^2}\frac{\partial H}{\partial R}\frac{\partial W}{\partial R} + \frac{w_c}{z_c}\frac{\partial W}{\partial Z}\right) \tag{2.47}$$

and bringing out a factor of w_c/z_c from the viscous pressure term leads to

$$p_c\ P|_{Z=H} = -\frac{1}{2}\varepsilon_o E_c^2 \mathcal{E}^2 - \frac{\gamma z_c}{r_c^2}\left(\frac{\partial^2 H/\partial R^2}{\left[1+\frac{z_c^2}{r_c^2}\left(\frac{\partial H}{\partial R}\right)^2\right]^{3/2}} + \frac{\partial H/\partial R}{R\left[1+\frac{z_c^2}{r_c^2}\left(\frac{\partial H}{\partial R}\right)^2\right]^{1/2}}\right)$$
$$+\frac{2}{1+\frac{z_c^2}{r_c^2}\left(\frac{\partial H}{\partial R}\right)^2}\frac{\mu w_c}{z_c}\left(\frac{z_c^2}{r_c^2}\left[\frac{\partial H}{\partial R}\right]^2\frac{\partial U}{\partial R} - \frac{\partial H}{\partial R}\frac{\partial U}{\partial Z} - \frac{z_c^2}{r_c^2}\frac{\partial H}{\partial R}\frac{\partial W}{\partial R} + \frac{\partial W}{\partial Z}\right) \tag{2.48}$$

Dividing through by p_c leads to

$$P|_{Z=H} = -\frac{\varepsilon_o E_c^2}{2p_c}\mathcal{E}^2 - \frac{\gamma z_c}{p_c r_c^2}\left(\frac{\partial^2 H/\partial R^2}{\left[1+\frac{z_c^2}{r_c^2}\left(\frac{\partial H}{\partial R}\right)^2\right]^{3/2}} + \frac{\partial H/\partial R}{R\left[1+\frac{z_c^2}{r_c^2}\left(\frac{\partial H}{\partial R}\right)^2\right]^{1/2}}\right)$$
$$+\frac{2}{1+\frac{z_c^2}{r_c^2}\left(\frac{\partial H}{\partial R}\right)^2}\frac{\mu w_c}{p_c z_c}\left(\frac{z_c^2}{r_c^2}\left[\frac{\partial H}{\partial R}\right]^2\frac{\partial U}{\partial R} - \frac{\partial H}{\partial R}\frac{\partial U}{\partial Z} - \frac{z_c^2}{r_c^2}\frac{\partial H}{\partial R}\frac{\partial W}{\partial R} + \frac{\partial W}{\partial Z}\right) \tag{2.49}$$

where the characteristic pressure p_c can be set as the Maxwell pressure that is also known to be the dominant contribution necessary for destabilization of the liquid surface and subsequent liquid growth and protrusion development

$$p_c = \frac{1}{2}\varepsilon_o E_c^2 \tag{2.50}$$

such that when $p_c = \varepsilon_o E_c^2/2$ is substituted back, it yields

$$P|_{Z=H} = -\mathcal{E}^2 - \frac{2\gamma z_c}{\varepsilon_o E_c^2 r_c^2}\left(\frac{\partial^2 H/\partial R^2}{\left[1+\frac{z_c^2}{r_c^2}\left(\frac{\partial H}{\partial R}\right)^2\right]^{3/2}} + \frac{\partial H/\partial R}{R\left[1+\frac{z_c^2}{r_c^2}\left(\frac{\partial H}{\partial R}\right)^2\right]^{1/2}}\right)$$
$$+\frac{2}{1+\frac{z_c^2}{r_c^2}\left(\frac{\partial H}{\partial R}\right)^2}\frac{2\mu w_c}{\varepsilon_o E_c^2 z_c}\left(\frac{z_c^2}{r_c^2}\left[\frac{\partial H}{\partial R}\right]^2\frac{\partial U}{\partial R} - \frac{\partial H}{\partial R}\frac{\partial U}{\partial Z} - \frac{z_c^2}{r_c^2}\frac{\partial H}{\partial R}\frac{\partial W}{\partial R} + \frac{\partial W}{\partial Z}\right) \tag{2.51}$$

The electric Weber number measuring the ratio between the destabilizing Maxwell pressure scaled by p_c and stabilizing capillary pressure scaled by $\gamma z_c/r_c^2$ can then be extracted as

$$\mathsf{We} = \frac{p_c r_c^2}{\gamma z_c} = \frac{\varepsilon_o E_c^2 r_c^2}{2\gamma z_c} \tag{2.52}$$

such that

$$P|_{Z=H} = -\mathcal{E}^2 - \frac{1}{\mathsf{We}}\left(\frac{\partial^2 H/\partial R^2}{\left[1+\frac{z_c^2}{r_c^2}\left(\frac{\partial H}{\partial R}\right)^2\right]^{3/2}} + \frac{\partial H/\partial R}{R\left[1+\frac{z_c^2}{r_c^2}\left(\frac{\partial H}{\partial R}\right)^2\right]^{1/2}}\right)$$
$$+\frac{2}{1+\frac{z_c^2}{r_c^2}\left(\frac{\partial H}{\partial R}\right)^2}\frac{2\mu w_c}{\varepsilon_o E_c^2 z_c}\left(\frac{z_c^2}{r_c^2}\left[\frac{\partial H}{\partial R}\right]^2\frac{\partial U}{\partial R} - \frac{\partial H}{\partial R}\frac{\partial U}{\partial Z} - \frac{z_c^2}{r_c^2}\frac{\partial H}{\partial R}\frac{\partial W}{\partial R} + \frac{\partial W}{\partial Z}\right) \tag{2.53}$$

As for the factor in the viscous pressure term, notice that from the current nondimensionalized form of the Navier-Stokes equation in Eq. 2.43

$$\begin{aligned}\frac{r_c^2}{z_c^2}\left(\frac{\partial U}{\partial T}+U\frac{\partial U}{\partial R}+W\frac{\partial U}{\partial Z}\right) &= -\frac{p_c}{\rho w_c^2}\frac{\partial P}{\partial R}+\frac{1}{\mathsf{Re}}\frac{r_c^2}{z_c^2}\left(\frac{z_c^2}{r_c^2}\frac{\partial}{\partial R}\left[\frac{1}{R}\frac{\partial}{\partial R}(RU)\right]+\frac{\partial^2 U}{\partial Z^2}\right)\\ \frac{\partial W}{\partial T}+U\frac{\partial W}{\partial R}+W\frac{\partial W}{\partial Z} &= -\frac{p_c}{\rho w_c^2}\frac{\partial P}{\partial Z}+\frac{1}{\mathsf{Re}}\left(\frac{z_c^2}{r_c^2}\frac{1}{R}\frac{\partial}{\partial R}\left[R\frac{\partial W}{\partial R}\right]+\frac{\partial^2 W}{\partial Z^2}\right)\end{aligned} \tag{2.54}$$

the characteristic velocity scale w_c can be defined by equating the inertia scale ρw_c^2 to the characteristic pressure p_c as the Maxwell pressure is also known to generate the inertia that ultimately leads to liquid distortion and protrusion development.

$$\rho w_c^2 = p_c \rightarrow w_c = \sqrt{\frac{p_c}{\rho}} = \sqrt{\frac{\varepsilon_o}{2\rho}}E_c \tag{2.55}$$

The Navier-Stokes equation then takes the finalized form

$$\begin{aligned}\frac{r_c^2}{z_c^2}\left(\frac{\partial U}{\partial T}+U\frac{\partial U}{\partial R}+W\frac{\partial U}{\partial Z}\right) &= -\frac{\partial P}{\partial R}+\frac{1}{\mathsf{Re}}\frac{r_c^2}{z_c^2}\left(\frac{z_c^2}{r_c^2}\frac{\partial}{\partial R}\left[\frac{1}{R}\frac{\partial}{\partial R}(RU)\right]+\frac{\partial^2 U}{\partial Z^2}\right)\\ \frac{\partial W}{\partial T}+U\frac{\partial W}{\partial R}+W\frac{\partial W}{\partial Z} &= -\frac{\partial P}{\partial Z}+\frac{1}{\mathsf{Re}}\left(\frac{z_c^2}{r_c^2}\frac{1}{R}\frac{\partial}{\partial R}\left[R\frac{\partial W}{\partial R}\right]+\frac{\partial^2 W}{\partial Z^2}\right)\end{aligned} \tag{2.56}$$

in liquid

where the Reynolds number Re can now be defined as a function of the characteristic electric field scale E_c

$$\mathsf{Re} = \frac{\rho w_c z_c}{\mu} = \sqrt{\frac{\rho\varepsilon_o}{2\mu^2}}E_c z_c \tag{2.57}$$

The prefactor for the viscous pressure in the normal stress boundary condition can then be substituted with $w_c = \sqrt{\varepsilon_o/2\rho}E_c$ such that

$$P|_{Z=H} = -\mathcal{E}^2 - \frac{1}{\mathsf{We}}\left(\frac{\partial^2 H/\partial R^2}{\left[1+\frac{z_c^2}{r_c^2}\left(\frac{\partial H}{\partial R}\right)^2\right]^{3/2}} + \frac{\partial H/\partial R}{R\left[1+\frac{z_c^2}{r_c^2}\left(\frac{\partial H}{\partial R}\right)^2\right]^{1/2}}\right)$$
$$+\frac{2}{1+\frac{z_c^2}{r_c^2}\left(\frac{\partial H}{\partial R}\right)^2}\frac{\mu\sqrt{2}}{\sqrt{\varepsilon_o\rho}E_c z_c}\left(\frac{z_c^2}{r_c^2}\left[\frac{\partial H}{\partial R}\right]^2\frac{\partial U}{\partial R} - \frac{\partial H}{\partial R}\frac{\partial U}{\partial Z} - \frac{z_c^2}{r_c^2}\frac{\partial H}{\partial R}\frac{\partial W}{\partial R} + \frac{\partial W}{\partial Z}\right) \tag{2.58}$$

where the Reynolds number $\mathsf{Re} = \sqrt{\varepsilon_o\rho/2\mu^2}E_c z_c$ can indeed be recognized to give the final form of the normal stress boundary condition

$$P|_{Z=H} = -\mathcal{E}^2 - \frac{1}{\mathsf{We}}\left(\frac{\partial^2 H/\partial R^2}{\left[1+\frac{z_c^2}{r_c^2}\left(\frac{\partial H}{\partial R}\right)^2\right]^{3/2}} + \frac{\partial H/\partial R}{R\left[1+\frac{z_c^2}{r_c^2}\left(\frac{\partial H}{\partial R}\right)^2\right]^{1/2}}\right)$$
$$+\frac{2}{1+\frac{z_c^2}{r_c^2}\left(\frac{\partial H}{\partial R}\right)^2}\frac{1}{\mathsf{Re}}\left(\frac{z_c^2}{r_c^2}\left[\frac{\partial H}{\partial R}\right]^2\frac{\partial U}{\partial R} - \frac{\partial H}{\partial R}\frac{\partial U}{\partial Z} - \frac{z_c^2}{r_c^2}\frac{\partial H}{\partial R}\frac{\partial W}{\partial R} + \frac{\partial W}{\partial Z}\right) \tag{2.59}$$

At the liquid surface $Z = H$, the shear stress boundary condition Eq. 2.16 becomes

$$2\left[\frac{w_c}{r_c}\frac{\partial H}{\partial R}\frac{\partial W}{\partial Z} - \frac{u_c z_c}{r_c^2}\frac{\partial H}{\partial R}\frac{\partial U}{\partial R}\right] = -\left[1-\frac{z_c^2}{r_c^2}\left(\frac{\partial H}{\partial R}\right)^2\right]\left[\frac{u_c}{z_c}\frac{\partial U}{\partial Z} + \frac{w_c}{r_c}\frac{\partial W}{\partial R}\right] \tag{2.60}$$

where substituting $u_c = w_c r_c/z_c$ and canceling common factors of w_c/r_c result in

$$2\left[\frac{\partial H}{\partial R}\frac{\partial W}{\partial Z} - \frac{\partial H}{\partial R}\frac{\partial U}{\partial R}\right] = -\left[1-\frac{z_c^2}{r_c^2}\left(\frac{\partial H}{\partial R}\right)^2\right]\left[\frac{r_c^2}{z_c^2}\frac{\partial U}{\partial Z} + \frac{\partial W}{\partial R}\right] \quad \text{at } Z = H \tag{2.61}$$

At the liquid surface $Z = H$, the kinematic boundary condition Eq. 2.17 becomes

$$\frac{z_c}{t_c}\frac{\partial H}{\partial T} + \frac{u_c z_c}{r_c}U\frac{\partial H}{\partial R} = w_c W \quad \text{at } Z = H \tag{2.62}$$

where substituting $u_c = w_c r_c/z_c$ and $t_c = z_c/w_c$ simply yields

$$\frac{\partial H}{\partial T} + U\frac{\partial H}{\partial R} = W \quad \text{at } Z = H \tag{2.63}$$

On the bottom electrode $Z = 0$, the nondimensionalized no slip and no penetration condition (Eq. 2.20) become

$$U = 0,\ W = 0 \quad \text{on } Z = 0 \tag{2.64}$$

At the symmetry axis $R = 0$, the nondimensionalized no flux conditions (Eq. 2.19) become

$$U = 0,\ \partial W/\partial R = 0 \quad \text{on } R = 0 \tag{2.65}$$

In the vacuum, the Laplace equation Eq. 2.3 becomes

$$\frac{\phi_c}{r_c^2}\frac{\partial^2\Phi}{\partial R^2} + \frac{\phi_c}{r_c^2}\frac{\partial\Phi}{\partial R} + \frac{\phi_c}{z_c^2}\frac{\partial^2\Phi}{\partial Z^2} = 0 \tag{2.66}$$

and results in

$$\left(\frac{\partial^2\Phi}{\partial R^2} + \frac{1}{R}\frac{\partial\Phi}{\partial R}\right) + \frac{r_c^2}{z_c^2}\frac{\partial^2\Phi}{\partial Z^2} = 0 \quad \text{in vacuum} \tag{2.67}$$

with the nondimensionalized electric field

$$E_c\vec{\mathcal{E}} = \frac{\phi_c}{r_c}\left(-\frac{\partial\Phi}{\partial R}\right)\hat{R} + \frac{\phi_c}{z_c}\left(-\frac{\partial\Phi}{\partial Z}\right)\hat{Z} \tag{2.68}$$

At the top electrode $Z = (b + h_o)/h_o$, the nondimensionalized potential ground Eq. 2.21 becomes

$$\Phi = 0 \ \text{ at } Z = (b + h_o)/h_o \tag{2.69}$$

The characteristic electric potential scale ϕ_c is simply set as

$$\phi_c = \phi_o \tag{2.70}$$

which gives the nondimensionalized applied constant electric potential (Eq. 2.18) applied to the liquid surface $Z = H$

$$\Phi = \frac{\phi_o}{\phi_c} = 1 \ \text{ at } Z = H \tag{2.71}$$

and also leads to

$$E_c\vec{\mathcal{E}} = \frac{\phi_o}{r_c}\left(-\frac{\partial\Phi}{\partial R}\right)\hat{R} + \frac{\phi_o}{z_c}\left(-\frac{\partial\Phi}{\partial Z}\right)\hat{Z} \tag{2.72}$$

Emphasis will now be given to the choice of the characteristic electric field scale E_c. The scale used for the thesis chapters Ch. 3 to Ch. 6 has been deliberately chosen as

$$E_c = \frac{\phi_c}{r_c} = \frac{\phi_o}{r_c} \tag{2.73}$$

which has been motivated by how the maximum initial electric field value for the simulated LMIS geometry is found at the initial liquid apex and scales dominantly on the initial liquid

apex curvature radius $\sim \phi_o/(r_s + h_o)$. This quality of the initial field is highlighted in Sec. 3.3. This length scale indeed sets the characteristic lateral scale r_c as

$$r_c = r_s + h_o \tag{2.74}$$

such that

$$\vec{\mathcal{E}} = \left(-\frac{\partial \Phi}{\partial R}\right)\hat{R} + \frac{r_c}{z_c}\left(-\frac{\partial \Phi}{\partial Z}\right)\hat{Z} \tag{2.75}$$

The scalings extracted from and chosen during the nondimensionalization of governing equations and boundary conditions go as

$$z_c = h_o \tag{2.76}$$

$$r_c = r_s + h_o \tag{2.77}$$

$$\phi_c = \phi_o \tag{2.78}$$

$$E_c = \frac{\phi_c}{r_c} = \frac{\phi_o}{r_s + h_o} \tag{2.79}$$

$$p_c = \frac{\varepsilon_o E_c^2}{2} = \frac{\varepsilon_o \phi_o^2}{2(r_s + h_o)^2} \tag{2.80}$$

$$w_c = \sqrt{\frac{p_c}{\rho}} = \sqrt{\frac{\varepsilon_o}{2\rho}}\frac{\phi_o}{r_s + h_o} \tag{2.81}$$

$$u_c = w_c\frac{r_c}{z_c} = \sqrt{\frac{\varepsilon_o}{2\rho}}\frac{\phi_o}{h_o} \tag{2.82}$$

$$t_c = \frac{z_c}{w_c} = \sqrt{\frac{2\rho}{\varepsilon_o}}\frac{h_o(r_s + h_o)}{\phi_o} \tag{2.83}$$

with the key nondimensional numbers having been identified as the Reynolds number Re and electric Weber number We possessing the forms

$$\mathsf{Re} = \frac{\rho w_c z_c}{\mu} = \frac{\rho h_o}{\mu}\sqrt{\frac{p_c}{\rho}} = \frac{\rho h_o}{\mu}\sqrt{\frac{\varepsilon_o}{2\rho}}E_c = \boxed{\sqrt{\frac{\varepsilon_o \rho}{2}}\frac{\phi_o}{\mu}\frac{h_o}{r_s + h_o}} \tag{2.84}$$

$$\mathsf{We} = \frac{p_c r_c^2}{\gamma z_c} = \frac{\varepsilon_o E_c^2}{2}\frac{(r_s + h_o)^2}{\gamma h_o} = \frac{\varepsilon_o \phi_o^2}{2(r_s + h_o)^2}\frac{(r_s + h_o)^2}{\gamma h_o} = \boxed{\frac{\varepsilon_o \phi_o^2}{2\gamma h_o}} \tag{2.85}$$

It should be noted that the nondimensional quantity z_c/r_c that measures the ratio between the characteristic vertical ($z_c = h_o$) and lateral ($r_c = r_s + h_o$) length scales is found in the definition of the Re such that it need not be considered as a separate nondimensional number. The current definitions of Re and We will be used for the rest of the document. Note that the electric Weber number We has also been referred as the electric capillary number in other similar studies [5].

2.4 Linear stability analysis: linearization

The following sections in the current chapter are strictly focused on the linear stability of the previously described arbitrarily thick and viscous flat liquid layer under a normal electric field. Though linear stability analysis of the described system has been conducted by de Surgy *et al.* [131, 132], the original dimensionless analysis [131] invoked characteristic scalings dependent on gravity. This makes it difficult to directly apply their dimensionless results into gravityless environments that have been taken for this thesis. The analysis was also conducted in Cartesian coordinates (x, z) instead of axisymmetric coordinates (r, z) taken for our simulations. Therefore, while the general procedure of the analysis presented in this chapter is the same, the details will differ.

For these sections, a different characteristic electric field $E_{c,LS}$ is defined as

$$E_{c,LS} = \frac{\phi_c}{b} = \frac{\phi_o}{b} \tag{2.86}$$

which was used by de Surgy *et al.* analysis [131, 132] and is motivated by the fact that the electric field value applied to the flat liquid surface is exactly ϕ_o/b. This is different from the scaling $E_c = \phi_o/r_c$ used elsewhere throughout the text that better will reflect the microemitter curvature generated field enhancement found in the LMIS geometry. Substituting this back into the nondimensionalized electric field expression gives

$$\vec{\mathcal{E}} = \frac{b}{r_c}\left(-\frac{\partial \Phi}{\partial R}\right)\hat{R} + \frac{b}{z_c}\left(-\frac{\partial \Phi}{\partial Z}\right)\hat{Z} \tag{2.87}$$

The Reynolds Re_{LS} and electric Weber We_{LS} numbers for the linear stability analysis then become

$$\mathsf{Re}_{LS} = \frac{\rho w_c z_c}{\mu} = \frac{\rho h_o}{\mu}\sqrt{\frac{p_c}{\rho}} = \frac{\rho h_o}{\mu}\sqrt{\frac{\varepsilon_o}{2\rho}}E_{c,LS} = \sqrt{\frac{\varepsilon_o \rho}{2}}\frac{\phi_o}{\mu}\frac{h_o}{b} \tag{2.88}$$

$$\mathsf{We}_{LS} = \frac{p_c r_c^2}{\gamma z_c} = \frac{\varepsilon_o E_{c,LS}^2}{2}\frac{r_c^2}{\gamma h_o} = \frac{\varepsilon_o \phi_o^2}{2b^2}\frac{r_c^2}{\gamma h_o} = \frac{\varepsilon_o \phi_o^2 r_c^2}{2\gamma b^2 h_o} \tag{2.89}$$

where the underlying definition of the Reynolds $\rho w_c z_c/\mu$ and electric Weber $p_c r_c^2/\gamma z_c$ numbers are the same. The difference only arises when the characteristic electric field value is explicitly substituted into the numbers. Thus, factors of Re and We that appear in the nondimensionalized equations and boundary conditions can be substituted with Re_{LS} and We_{LS} for the ensuing linear stability analysis.

The de Surgy *et al.* analysis [131, 132] also took the bottom electrode to be placed at $z = -h_o$ instead of $z = 0$, the unperturbed liquid surface at $z = 0$ instead of $z = h_o$ and the top electrode at $z = b$ instead of $z = b + h_o$ taken for the preceding sections. The analysis

to be shown for the rest of the chapter is set in the coordinates taken by de Surgy *et al.* for consistency. For clarity, variables for the redefined liquid and vacuum domains to be used in the analysis are introduced here. The dimensional liquid and vacuum domains are defined as

$$\Omega_{liq} : \{r \in [0, \infty), z \in [-h_o, h]\} \tag{2.90}$$

$$\Omega_{vac} : \{r \in [0, \infty), z \in [h, b]\} \tag{2.91}$$

The nondimensionalized liquid and vacuum domains then become

$$\tilde{\Omega}_{liq} : \{R \in [0, \infty), Z \in [-h_o/z_c, H]\} \tag{2.92}$$

$$\tilde{\Omega}_{vac} : \{R \in [0, \infty), Z \in [H, b/z_c]\} \tag{2.93}$$

The zeroth order solutions for the base state of a flat, unperturbed liquid surface in the current system are

$$H^0 = 0 \tag{2.94}$$

$$P^0 = -1 \text{ in } \tilde{\Omega}_{liq} \tag{2.95}$$

$$\Phi^0 = 1 - \frac{h_o}{b} Z \text{ in } \tilde{\Omega}_{vac} \tag{2.96}$$

$$U^0 = 0 \text{ in } \tilde{\Omega}_{liq} \tag{2.97}$$

$$W^0 = 0 \text{ in } \tilde{\Omega}_{liq} \tag{2.98}$$

The perturbed system will now add small first order corrections to the zeroth order solutions. These are labeled with the (1) script.

$$H = H_{(1)} \tag{2.99}$$

$$P = -1 + P^{(1)} \text{ in } \tilde{\Omega}_{liq} \tag{2.100}$$

$$\Phi = \left(1 - \frac{h_o}{b} Z\right) + \Phi^{(1)} \text{ in } \tilde{\Omega}_{vac} \tag{2.101}$$

$$U = U^{(1)} \text{ in } \tilde{\Omega}_{liq} \tag{2.102}$$

$$W = W^{(1)} \text{ in } \tilde{\Omega}_{liq} \tag{2.103}$$

Substituting the above forms of the nondimensionalized variables into the nondimensionalized equations and boundary conditions and keeping contributions up to the first order leads to the following forms.

The nondimensionalized continuity equation (Eq. 2.34) is reduced to

$$\frac{\partial U^{(1)}}{\partial R} + \frac{U^{(1)}}{R} + \frac{\partial W^{(1)}}{\partial Z} = 0 \quad \text{in } \tilde{\Omega}_{liq} \tag{2.104}$$

and the nondimensionalized Navier-Stokes equation (Eq. 2.56) is reduced to

$$\begin{aligned}\frac{r_c^2}{h_o^2}\left(\frac{\partial U^{(1)}}{\partial T}\right) &= -\frac{\partial P^{(1)}}{\partial R} + \frac{1}{\mathrm{Re}_{LS}}\frac{r_c^2}{h_o^2}\left(\frac{h_o^2}{r_c^2}\left[-\frac{U^{(1)}}{R^2} + \frac{1}{R}\frac{\partial U^{(1)}}{\partial R} + \frac{\partial^2 U^{(1)}}{\partial R^2}\right] + \frac{\partial^2 U^{(1)}}{\partial Z^2}\right) \text{ in } \tilde{\Omega}_{liq} \\ \frac{\partial W^{(1)}}{\partial T} &= -\frac{\partial P^{(1)}}{\partial Z} + \frac{1}{\mathrm{Re}_{LS}}\left(\frac{h_o^2}{r_c^2}\left[\frac{1}{R}\frac{\partial W^{(1)}}{\partial R} + \frac{\partial^2 W^{(1)}}{\partial R^2}\right] + \frac{\partial^2 W^{(1)}}{\partial Z^2}\right) \text{ in } \tilde{\Omega}_{liq}\end{aligned} \tag{2.105}$$

In the vacuum, the nondimensionalized Laplace equation (Eq. 2.67) is still

$$\frac{h_o^2}{r_c^2}\left(\frac{\partial^2 \Phi^{(1)}}{\partial R^2} + \frac{1}{R}\frac{\partial \Phi^{(1)}}{\partial R}\right) + \frac{\partial^2 \Phi^{(1)}}{\partial Z^2} = 0 \quad \text{in } \tilde{\Omega}_{vac} \tag{2.106}$$

At the surface $Z = H_{(1)}$, the nondimensionalized normal pressure boundary condition (Eq. 2.59) is reduced to

$$P^{(0)} + P^{(1)} = -\frac{b^2}{h_o^2}\left(-\frac{\partial \Phi}{\partial Z}\right)^2 - \frac{1}{\mathrm{We}_{LS}}\left(\frac{\partial^2 H_{(1)}}{\partial R^2} + \frac{\partial H_{(1)}}{\partial R}\right) + \frac{2}{\mathrm{Re}_{LS}}\frac{\partial W}{\partial Z} \quad \text{at } Z = H \tag{2.107}$$

where the surviving terms from $(-\partial\Phi/\partial Z)^2$ are

$$\begin{aligned}\left(-\frac{\partial \Phi}{\partial Z}\right)^2 &= \left(-\frac{\partial \Phi^{(0)}}{\partial Z}\right)^2 + 2\left(-\frac{\partial \Phi^{(0)}}{\partial Z}\right)\left(-\frac{\partial \Phi^{(1)}}{\partial Z}\right) + \left(-\frac{\partial \Phi^{(1)}}{\partial Z}\right)^2 \\ &= \frac{h_o^2}{b^2} - \frac{2h_o}{b}\frac{\partial \Phi^{(1)}}{\partial Z}\end{aligned} \tag{2.108}$$

such that after some algebra

$$P^{(1)} = \frac{2b}{h_o}\frac{\partial \Phi^{(1)}}{\partial Z} - \frac{1}{\mathrm{We}_{LS}}\left(\frac{\partial^2 H_{(1)}}{\partial R^2} + \frac{\partial H_{(1)}}{\partial R}\right) + \frac{2}{\mathrm{Re}_{LS}}\frac{\partial W}{\partial Z} \quad \text{at } Z = H \tag{2.109}$$

At the surface $Z = H_{(1)}$, the shear stress boundary condition is reduced to

$$\frac{\partial U^{(1)}}{\partial Z} + \frac{h_o^2}{r_c^2}\frac{\partial W^{(1)}}{\partial R} = 0 \quad \text{on } Z = H \tag{2.110}$$

At the liquid surface $Z = H_{(1)}$, the kinematic condition is

$$\frac{\partial H_{(1)}}{\partial T} = W_{(1)} \quad \text{at } Z = H \tag{2.111}$$

At the liquid surface $Z = H_{(1)}$, the constant electric potential applied yields requires

$$\Phi^{(0)} + \Phi^{(1)} = \left(1 - \frac{h_o}{b}H_{(1)}\right) + \Phi^{(1)} \quad \text{on } Z = H \tag{2.112}$$

or

$$\Phi^{(1)} = \frac{h_o}{b} H_{(1)} \quad \text{on } Z = H \tag{2.113}$$

At the bottom electrode $Z = -1$, the no slip and no penetration boundary conditions require

$$U^{(1)} = 0,\ W^{(1)} = 0 \quad \text{on } Z = -1 \tag{2.114}$$

At the top electrode $Z = b/h_o$, the potential ground requires

$$\Phi^{(1)} = 0 \quad \text{on } Z = b/h_o \tag{2.115}$$

At the symmetry axis $R = 0$, the no flux condition becomes

$$U^{(1)} = 0, \quad \frac{\partial W^{(1)}}{\partial R} = 0 \quad \text{on } R = 0 \tag{2.116}$$

2.5 Linear stability analysis: algebraic reduction

The solutions for the perturbative terms are sought using the ansatz written below

$$H_{(1)} = \text{Real}[\delta_H(Z)\exp(\beta T)J_0(KR)] \tag{2.117}$$
$$P^{(1)} = \text{Real}[\delta_P(Z)\exp(\beta T)J_0(KR)] \tag{2.118}$$
$$\Phi^{(1)} = \text{Real}[\delta_\Phi(Z)\exp(\beta T)J_0(KR)] \tag{2.119}$$
$$U^{(1)} = \text{Real}[\delta_U(Z)\exp(\beta T)J_1(KR)] \tag{2.120}$$
$$W^{(1)} = \text{Real}[\delta_W(Z)\exp(\beta T)J_0(KR)] \tag{2.121}$$

where the Bessel functions of the first kind $J_0(KR)$ of order 0 are now prescribed due to axisymmetry [30, 130], except for the $J_1(KR)$ for $U^{(1)}$. Bessel functions of the second kind are omitted as they blow up at $R = 0$. The radial dependence of the radial velocity $U^{(1)}$ is set to $J_1(KR)$ due to the no flux condition at $R = 0$. The introduced K will correspond to the nondimensional wavenumber of the perturbation, whereas β will correspond to the nondimensional growth rate. The algebraic nondimensional equations and boundary conditions then take the following forms.

In the liquid, the algebraic linearized nondimensional continuity (Eq. 2.104) and Navier-Stokes equations (Eq. 2.105) become

$$K\delta_U + \frac{\partial \delta_W}{\partial Z} = 0 \quad \text{in } \tilde{\Omega}_{liq} \tag{2.122}$$

$$\begin{aligned} \frac{r_c^2}{h_o^2}\beta\delta_U &= K\delta_P + \frac{1}{\text{Re}_{LS}}\frac{r_c^2}{h_o^2}\left(-\frac{h_o^2}{r_c^2}K^2\delta_U + \frac{\partial^2\delta_U}{\partial Z^2}\right) \quad \text{in } \tilde{\Omega}_{liq} \\ \beta\delta_W &= -\frac{\partial\delta_P}{\partial Z} + \frac{1}{\text{Re}_{LS}}\left(-\frac{h_o^2}{r_c^2}K^2\delta_W + \frac{\partial^2\delta_W}{\partial Z^2}\right) \quad \text{in } \tilde{\Omega}_{liq} \end{aligned} \tag{2.123}$$

In the vacuum, the algebraic nondimensional Laplace (Eq. 2.106) becomes

$$-\frac{h_o^2}{r_c^2}K^2\delta_\Phi + \frac{\partial^2\delta_\Phi}{\partial Z^2} = 0 \quad \text{in } \tilde{\Omega}_{vac} \tag{2.124}$$

At the liquid surface $Z = H_{(1)}$, the algebraic linearized nondimensional normal pressure boundary condition (Eq. 2.109) becomes

$$\delta_P = \frac{2b}{h_o}\frac{\partial\delta_\Phi}{\partial Z} + \frac{1}{\mathsf{We}_{LS}}K^2\delta_H + \frac{2}{\mathsf{Re}_{LS}}\frac{\partial\delta_W}{\partial Z} \quad \text{at } Z = H \tag{2.125}$$

At the liquid surface $Z = H_{(1)}$, the algebraic linearized nondimensional shear stress condition (Eq. 2.110) becomes

$$\frac{\partial\delta_U}{\partial Z} - \frac{h_o^2}{r_c^2}K\delta_W = 0 \quad \text{on } Z = H \tag{2.126}$$

At the liquid surface $Z = H_{(1)}$, the algebraic linearized kinematic condition (Eq. 2.111) becomes

$$\delta_H = \delta_W \quad \text{at } Z = H \tag{2.127}$$

At the liquid surface $Z = H_{(1)}$, the algebraic linearized first order correction to the nondimensional potential (Eq. 2.113) becomes

$$\delta_\Phi = \frac{h_o}{b}\delta_H \quad \text{on } Z = H \tag{2.128}$$

At the bottom electrode $Z = -1$, the no slip and no penetration boundary conditions (Eq. 2.114) still require

$$\delta_U = 0,\ \delta_W = 0 \quad \text{on } Z = -1 \tag{2.129}$$

At the top electrode $Z = b/h_o$, the potential ground (Eq. 2.115) still requires

$$\delta_\Phi = 0 \quad \text{on } Z = b/h_o \tag{2.130}$$

At the symmetry axis $R = 0$, the no flux condition (Eq. 2.116) is already satisfied from the Bessel function dependence as the $U = 0$ is already satisfied from $J_0(0) = 0$ and the $\partial W/\partial R = 0$ is also already satisfied as $\partial J_0(KR)/\partial R = -KJ_1(KR)$ which is equal to zero at $R = 0$.

2.6 Linear stability analysis: solutions for perturbative terms

The transformation of the differential governing equations into algebraic form now permits solving for the unknown $\delta(Z)$ dependence of the perturbations in terms of K and β. For the electric potential δ_Φ term, the relevant equations are

$$\frac{\partial^2 \delta_\Phi}{\partial Z^2} = \frac{h_o^2}{r_c^2} K^2 \delta_\Phi \quad \text{in } \tilde{\Omega}_{vac} \tag{2.131}$$

$$\delta_\Phi = \frac{h_o}{b} \delta_H \quad \text{on } Z = H \tag{2.132}$$

$$\delta_\Phi = 0 \quad \text{on } Z = b/h_o \tag{2.133}$$

where it can easily be seen that the solution takes the form

$$\delta_\Phi = A_\Phi \sinh\left(\frac{h_o}{r_c} K \left[Z - \frac{b}{h_o}\right]\right) \tag{2.134}$$

where A_Φ is some unknown coefficient.

The relevant equations used for δ_U, δ_W and δ_P are

$$\frac{r_c^2}{h_o^2}\beta\delta_U = K\delta_P + \frac{1}{\mathsf{Re}_{LS}}\frac{r_c^2}{h_o^2}\left(-\frac{h_o^2}{r_c^2}K^2\delta_U + \frac{\partial^2 \delta_U}{\partial Z^2}\right) \quad \text{in } \tilde{\Omega}_{liq} \tag{2.135}$$

$$\beta\delta_W = -\frac{\partial \delta_P}{\partial Z} + \frac{1}{\mathsf{Re}_{LS}}\left(-\frac{h_o^2}{r_c^2}K^2\delta_W + \frac{\partial^2 \delta_W}{\partial Z^2}\right) \quad \text{in } \tilde{\Omega}_{liq} \tag{2.136}$$

$$K\delta_U + \frac{\partial \delta_W}{\partial Z} = 0 \quad \text{in } \tilde{\Omega}_{liq} \tag{2.137}$$

$$\delta_U = 0,\ \delta_W = 0 \quad \text{on } Z = -1 \tag{2.138}$$

where solving for one of the δ terms will naturally lead to solutions for the other two terms. Solving for δ_W first requires isolating δ_P from the R component momentum equation

$$\delta_P = \frac{1}{K}\left(\frac{r_c^2}{h_o^2}\beta\delta_U + \frac{1}{\mathsf{Re}_{LS}}K^2\delta_U - \frac{1}{\mathsf{Re}_{LS}}\frac{r_c^2}{h_o^2}\frac{\partial^2 \delta_U}{\partial Z^2}\right) \tag{2.139}$$

from where δ_U can be turned into δ_W through the continuity equation

$$\delta_P = -\frac{1}{K^2}\left(\frac{r_c^2}{h_o^2}\beta\frac{\partial \delta_W}{\partial Z} + \frac{1}{\mathsf{Re}_{LS}}K^2\frac{\partial \delta_W}{\partial Z} - \frac{1}{\mathsf{Re}_{LS}}\frac{r_c^2}{h_o^2}\frac{\partial^3 \delta_W}{\partial Z^3}\right) \tag{2.140}$$

such that the Z component Navier-Stokes equation becomes after some algebra

$$-\left[\mathsf{Re}_{LS}\beta - \left(\frac{\partial^2}{\partial Z^2} - \frac{h_o^2}{r_c^2}K^2\right)\right]\left(\frac{\partial^2}{\partial Z^2} - \frac{h_o^2}{r_c^2}K^2\right)\delta_W = 0 \tag{2.141}$$

where the solution to the above equation with the no penetration boundary condition $\delta_W = 0$ on $Z = -1$ is

$$\delta_W = B_1 \sinh\left(\frac{h_o}{r_c}K[Z+1]\right) + B_2 \sinh\left(\frac{h_o}{r_c}KZ\right) + B_3 \sinh\left(Q[Z+1]\right) + B_4 \sinh\left(QZ\right) \tag{2.142}$$

with a new variable Q has been defined for conciseness

$$Q = \sqrt{\frac{h_o^2}{r_c^2}K^2 + \mathsf{Re}_{LS}\beta} \tag{2.143}$$

The delta term δ_U can be easily recovered from the continuity equation to be

$$\begin{aligned}\delta_U = -\frac{1}{K}\Bigg\{&B_1\frac{h_o}{r_c}K\cosh\left(\frac{h_o}{r_c}K[Z+1]\right) + B_2\frac{h_o}{r_c}K\cosh\left(\frac{h_o}{r_c}KZ\right)\\ &+B_3Q\cosh\left(Q[Z+1]\right) + B_4Q\cosh\left(QZ\right)\Bigg\}\end{aligned} \tag{2.144}$$

and the delta term δ_P is also easily recovered from the solution to δ_U to be

$$\delta_P = -\frac{r_c}{h_o}\frac{\beta}{K}\left[B_1\cosh\left(\frac{h_o}{r_c}K[Z+1]\right) + B_2\cosh\left(\frac{h_o}{r_c}KZ\right)\right] \tag{2.145}$$

2.7 Linear stability analysis: dispersion relation

There remain six unknowns in the solutions for the perturbative terms: five coefficients A_Φ, B_1, B_2, B_3 and B_4 plus the δ_H yet to be solved for, meaning there must be six equations that relate the unknowns to one another. These can be found from the algebraic linearized boundary conditions.

At the surface $Z = H_{(1)}$, substituting δ_U and δ_P into the algebraic linearized shear stress boundary condition (Eq. 2.126) leads to

$$B_1\left[2\frac{h_o^2}{r_c^2}K\sinh\left(\frac{h_o}{r_c}K\right)\right] + B_3\left[\frac{Q^2 + h_o^2K^2/r_c^2}{K}\sinh(Q)\right] = 0 \tag{2.146}$$

At the surface $Z = H_{(1)}$, substituting δ_W into the algebraic linearized kinematic condition (Eq. 2.127) leads to

$$B_1\sinh\left(\frac{h_o}{r_c}K\right) + B_3\sinh(Q) - \beta\delta_H = 0 \tag{2.147}$$

At the liquid surface $Z = H_{(1)}$, substituting δ_Φ into the algebraic linearized constant surface electric potential condition (Eq. 2.128) leads to

$$A_\Phi\sinh\left(\frac{b}{r_c}K\right) + \frac{h_o}{b}\delta_H = 0 \tag{2.148}$$

At the bottom electrode $Z = -1$, substituting δ_U and δ_W into the algebraic linearized no slip and no penetration boundary conditions (Eq. 2.129) leads to

$$B_2 \sinh\left(\frac{h_o}{r_c}K\right) + B_4 \sinh\left(Q\right) = 0 \tag{2.149}$$

$$B_1 \frac{h_o}{r_c}K + B_2 \frac{h_o}{r_c}K \cosh\left(\frac{h_o}{r_c}K\right) + B_3 Q + B_4 Q \cosh\left(Q\right) = 0 \tag{2.150}$$

At the surface $Z = H_{(1)}$, substituting δ_P, δ_Φ and δ_W into the algebraic linearized normal stress boundary condition (Eq. 2.125) leads after some algebra

$$A_\Phi \frac{2b}{r_c}\frac{h_o}{r_c}\mathsf{Re}_{LS}K\cosh\left(\frac{b}{r_c}K\right) + B_1\frac{Q^2 + \frac{h_o^2}{r_c^2}K^2}{K}\cosh\left(\frac{h_o}{r_c}K\right) + B_2\frac{Q^2 + \frac{h_o^2}{r_c^2}K^2}{K}$$
$$+2B_3\frac{h_o}{r_c}Q\cosh\left(Q\right) + 2B_4\frac{h_o}{r_c}Q + \frac{\mathsf{Re}_{LS}}{\mathsf{We}_{LS}}\frac{h_o}{r_c}K^2\delta_H = 0 \tag{2.151}$$

Thus, the problem possesses six linear homogeneous equations for the six unknowns. Nontrivial solutions are found by setting the determinant of the coefficients to zero, which

yields

$$
\begin{bmatrix}
0 & \frac{h_o^2}{2\frac{r_c^2}{K}\sinh\left(\frac{h_o}{r_c}K\right)} & 0 & \frac{h_o^2}{r_c^2}K^2 \\
\sinh\left(\frac{b}{r_c}K\right) & 0 & \frac{h_o}{r_c}K\cosh\left(\frac{h_o}{r_c}K\right) & Q \\
0 & \frac{h_o}{r_c}K & 0 & \sinh\left(\frac{h_o}{r_c}K\right) \\
\frac{2bh_o\mathsf{Re}_{LS}K}{r_c^2}\cosh\left(\frac{b}{r_c}K\right) & \frac{Q^2+\frac{h_o^2}{r_c^2}K^2}{K}\cosh\left(\frac{h_o}{r_c}K\right) & \frac{Q^2+\frac{h_o^2}{r_c^2}K^2}{K} & \frac{h_o}{r_c}2Q\cosh(Q)
\end{bmatrix}
\begin{bmatrix}
0 \\ -\beta \\ \frac{h_o}{b} \\ 0 \\ 0 \\ \frac{\mathsf{Re}_{LS}}{\mathsf{We}_{LS}}\frac{h_oK^2}{r_c}
\end{bmatrix}
=
\begin{bmatrix}
\frac{h_o^2}{r_c^2}K^2 \\ \overline{K}\sinh(Q) \\ 0 \\ \sinh(Q) \\ Q\cosh(Q) \\ \frac{h_o}{r_c}2Q
\end{bmatrix}
\tag{2.152}
$$

Evaluating Eq. 2.152 and conducting some tedious algebra indeed results in the nondimen-

sional dispersion relation

$$
\begin{aligned}
&4QK^3\frac{h_o^3}{r_c^3}\left[Q - K\frac{h_o}{r_c}\coth(Q)\coth\left(K\frac{h_o}{r_c}\right)\right] \\
&-\left(Q^2 + K^2\frac{h_o^2}{r_c^2}\right)^2\left[Q\coth(Q)\coth\left(K\frac{h_o}{r_c}\right) - K\frac{h_o}{r_c}\right] + \frac{4QK^2\frac{h_o^2}{r_c^2}\left(Q^2 + K^2\frac{h_o^2}{r_c^2}\right)}{\sinh(Q)\sinh\left(K\frac{h_o}{r_c}\right)} \\
&= \mathsf{Re}_{LS}^2\left[\frac{\frac{h_o}{r_c}K^3}{\mathsf{We}_{LS}} - 2K^2\frac{h_o^2}{r_c^2}\coth(\alpha K)\right]\left[Q\coth(Q) - K\frac{h_o}{r_c}\coth\left(K\frac{h_o}{r_c}\right)\right]
\end{aligned}
\tag{2.153}
$$

which is independent of gravity dependent scalings.

The dimensional version of quantity K, which is now understood to be the dimensionless radial wavenumber of the surface perturbation, is defined as

$$
k = Kk_c = \frac{K}{r_c} \tag{2.154}
$$

whereas the dimensional version of quantity β, which is now understood to be the dimensionless growth rate of the surface perturbation, is defined as

$$
s = \beta s_c = \frac{\beta}{t_c} = \beta\frac{w_c}{h_o} \tag{2.155}
$$

whereas the dimensional version of quantity Q is

$$
q = Qq_c = \frac{Q}{h_o} = \sqrt{k^2 + \frac{\rho s}{\mu}} \tag{2.156}
$$

such that the dimensional dispersion relation can indeed be found as

$$
\begin{aligned}
&4qk^3\left[q - k\coth(qh_o)\coth(kh_o)\right] - (q^2 + k^2)^2\left[q\coth(qh_o)\coth(kh_o) - k\right] \\
&+\frac{4qk^2\left(q^2 + k^2\right)}{\sinh(qh_o)\sinh(kh_o)} = \frac{\rho}{\mu^2}\left[\gamma k^3 - \varepsilon_o E_a k^2\coth(kb)\right]\left[q\coth(qh_o) - k\coth(kh_o)\right]
\end{aligned}
\tag{2.157}
$$

where $E_a = \phi_o/b$ is the electric field value applied to the unperturbed liquid surface and also equal to the characteristic electric field value $E_{c,LS}$ chosen for the analysis conducted. This is the same dimensional dispersion relation (minus the gravitational term excluded in our system) as found by de Surgy *et al.* [132] in Cartesian coordinates (x, z). The agreement arises as expected as a consequence of the rotational symmetry also utilized by de Surgy *et al.* in reducing the coordinate system from (x, y, z) to (x, z). The dispersion

relations in the asymptotic limits of the thin ($kh_o \ll 1$) or thick ($kh_o \gg 1$) and inviscid ($\rho s/\mu \gg \max(k^2, 1/h_o^2)$) and viscous ($\rho s/\mu \ll \max(k^2, 1/h_o^2)$) liquid as defined by de Surgy *et al.* [132] take the forms found in Table 2.1, where the classical Landau and Lifshitz [85] result for a thick, inviscid liquid under a thick vacuum without gravity is recovered as $b \to \infty$ in Eq. 2.158.

Table 2.1: Table of thick/thin and inviscid/viscous liquid limits as defined by de Surgy *et al.* [131, 132] and the corresponding dispersion relations without gravity. The material constants are vacuum permittivity ε_o and liquid density ρ, surface tension γ and viscosity μ. The system variables are liquid thickness h_o, vacuum thickness b and electric field applied to the unperturbed liquid surface E_a. The growth rate s for the instability mode of wavenumber k in the asymptotic limits can be found by evaluating the dispersion relations.

Thick/Thin liquid limit	Inviscid/Viscous liquid limit	Dispersion relation	
Thick $kh_o \gg 1$	Inviscid $\rho s/\mu \gg \max(k^2, 1/h_o^2)$	$\rho s^2 = -\gamma k^3 + \varepsilon_o E_a^2 k^2 \coth(kb)$	(2.158)
Thin $kh_o \ll 1$	Inviscid $\rho s/\mu \gg \max(k^2, 1/h_o^2)$	$\rho s^2 = h_o \left[-\gamma k^4 + \varepsilon_o E_a^2 k^3 \coth(kb)\right]$	(2.159)
Thick $kh_o \gg 1$	Viscous $\rho s/\mu \ll \max(k^2, 1/h_o^2)$	$s = \frac{1}{2\mu}\left[-\gamma k + \varepsilon_o E_a^2 \coth(kb)\right]$	(2.160)
Thin $kh_o \ll 1$	Viscous $\rho s/\mu \ll \max(k^2, 1/h_o^2)$	$s = \frac{h_o^3}{3\mu}\left[-\gamma k^4 + \varepsilon_o E_a^2 k^3 \coth(kb)\right]$	(2.161)

Chapter 3

ELECTROHYDRODYNAMIC MODES OF RELEVANCE TO LIQUID METAL ION SOURCES

3.1 Introduction

Ever since Krohn's discovery of ion emission from an electrified liquid metal droplet [78] in the early 1960s, there has been great interest in developing small scale systems that emit highly energetic ion beams. Such beams are emitted from protrusions that develop from a liquid metal film subject to an imbalance of Maxwell (electric) and capillary stresses. These systems known as liquid metal ion sources (LMIS) [22] have since become fundamental to the operation of focused ion beam systems [108] used for nanofabrication and microarray devices actuating space micropropulsion [103].

Although the general physical principles of LMIS operation are known, it remains difficult to access the details of the underlying electrohydrodynamic (EHD) flow and stability. While there exists a wealth of literature on the electrospray of leaky dielectric liquids [123] (i.e. non-perfectly conducting) dating back to investigations by Zeleny [160–162], the findings are not directly applicable to the LMIS due to significant differences in charge relaxation timescales [100]. Non-perfectly conducting liquids allow charge relaxation on time scales comparable to the flow [100], which in turn generates internal bulk and surface tangential electric fields that lead to EHD tip streaming [24]. This is a process where the protrusion tip elongates into a slender filament susceptible to capillary breakup and droplet detachment. Liquid metals are instead well modeled as perfectly conducting liquids possessing instantaneous charge relaxation. They can only generate surface normal electric fields, which just leads to the development of a sharpening tip [24] from whose apex an ion beam is emitted.

One of the difficult details to access is the spatiotemporal evolution of EHD modes generated in a realistic LMIS geometry. This has yet to be extensively documented due to the difficulty of experimentally accessing the nano-microscale lengths and times involved prior to ion emission. Indeed, the *in-situ* LMIS investigations conducted by Ben Assayag *et al.* [12, 13], Driesel *et al.* [35, 38, 39, 113] and Van Es *et al.* [149] using high vacuum transmission electron microscopy could only image already emitting protrusions and were subject to imaging electron path distortion from $\mathcal{O}(10\,\mathrm{GV/m})$ apex fields realized during field evaporation [108]. The opacity of liquid metals also prevents visualizing the liquid

bulk flow using conventional optical methods.

Elegant asymptotic analysis conducted by Zubarev [165] unveiled the late time dynamical behavior of protrusions to undergo self-similar growth leading to a runaway process and finite time blowup of the apex Maxwell and capillary pressures. The analysis was made without reference to any particular electrode geometry as self-similar processes require the prevalence of local, not global, conditions in the region of interest. However, the analysis on the growth prior to the onset of self-similarity in a realistic geometry and how might that be influenced by initial conditions remains elusive due to the difficulties presented by an apertured extractor and curved emitter when solving the highly coupled and nonlinear equations.

The advent of advanced computational techniques such as finite element simulations offers a clear path forward to investigate the full spatiotemporal evolution. Such simulations of a flat, electrified liquid metal layer under a flat, apertureless extractor have already been able to demonstrate the difference between liquid metal and leaky dielectric protrusion EHD tip development [24] and self-similar growth of protrusions [134–136] irrespective of the Reynolds number [5]. Despite the availability of such techniques, however, there still remains the difficulty of accurately, stably and convergently solving the governing equations in a realistic LMIS geometry with the required spatiotemporal resolution.

This study presents results from computational simulations that model the EHD mode development in a realistic LMIS geometry where a liquid metal layer is externally wetted to a smooth, parabolic microemitter and held at a constant electric potential to a flat, apertured extractor electrode. The system dimensions are made comparable to those found in microarray LMIS/electrospray space micropropulsion devices. The arbitrary Lagrangian Eulerian finite element method [32] is used to track the spatiotemporal evolution of the rapidly accelerating liquid free surface. The computational details are outlined in Sec. 3.2. The behavior of initial vacuum electric field in the realistic geometry is described in Sec. 3.3. The results reveal a multiplicity of EHD modes categorized as the drainage, axial, coronal, instability and dual mode that all develop within the liquid tip region defined by the initial liquid apex curvature radius and possess desirable final time electric field line collimation. Each mode is characterized in Sec. 3.4 and Sec. 3.5 using the spatiotemporal surface evolution, final time snapshots of the velocity and pressure fields and temporal evolution of key protrusion apex quantities for selected examples. Sec. 3.6 presents a mode diagram that correlates the mode outcomes to the Reynolds Re and electric Weber We numbers dominantly scaled by the initial liquid thickness, microemitter apex curvature radius and applied electric potential. Discussion on the importance of the initial liquid thickness,

rules of thumb for axial mode generation, additional signatures of mode confinement and consequences of chosen algorithmic and geometric details are offered in Sec. 3.7 before the key findings are summarized in Sec. 3.8.

3.2 Methods

This section presents details on the computational geometry, governing equations and boundary conditions and computational algorithm utilized for the simulations.

3.2.1 Computational geometry

Shown in Fig. 3.1(a) is the axisymmetric computational domain (r, z) of a realistic LMIS geometry in a vacuum without gravity. A solid, smooth parabolic microemitter surface with apex curvature radius r_s is externally wetted with a liquid metal layer of constant initial thickness h_o, which has been simply assumed for simplicity of modeling. The initial liquid surface $z = h(r, t = 0)$ is modeled as an "offset surface" [41, 110] to the parabolic microemitter surface. The microemitter surface can be expressed as a paraboloidal surface of revolution

$$z = f_{em}(r) = -\frac{r^2}{2r_s} \tag{3.1}$$

and also in the implicit form

$$g_{em}(r, z) = z - f_{em}(r) = z + \frac{r^2}{2r_s} = 0 \tag{3.2}$$

and in the parameterized form with a parameter a

$$\vec{r}_{em}(a) = (r(a), z(a)) = \left(a, -\frac{a^2}{2r_s}\right) \tag{3.3}$$

where a for the microemitter directly corresponds to the radial coordinate. The implicit form will be used to define the microemitter surface unit normal vector $\hat{n}_{em}$ used to define the offset initial liquid surface. The parametric form will be used to be express the offset initial liquid surface in terms of the microemitter surface.

The mean $\mathcal{K}$ and Gaussian $\mathcal{G}$ curvatures of the microemitter surface are

$$\begin{aligned}\mathcal{K}_{em}(r) &= \frac{1}{2}\left(\frac{\frac{\partial^2 f_{em}}{\partial r^2}}{\left[1 + \left(\frac{\partial f_{em}}{\partial r}\right)^2\right]^{3/2}} + \frac{\frac{\partial f_{em}}{\partial r}}{r\left[1 + \left(\frac{\partial f_{em}}{\partial r}\right)^2\right]^{1/2}}\right) = \frac{\kappa_1 + \kappa_2}{2} \\ &= -\frac{1}{2r_s}\left(\frac{1}{\left[1 + (r/r_s)^2\right]^{3/2}} + \frac{1}{\left[1 + (r/r_s)^2\right]^{1/2}}\right)\end{aligned} \tag{3.4}$$

Table 3.1: Definitions of physical and initial state variables, and quantities referenced in the results and Tables 3.10-3.17.

Physical Variables	Symbol
Axisymmetric coordinates	(r,z)
Time	t
Coordinate of liquid free surface	$z = h(r,t)$
Liquid velocity	$\vec{u}(r,z,t) = u\,\hat{r} + w\,\hat{z}$
Liquid pressure	$p(r,z,t)$
$h(r,t)$ mean curvature	$\mathcal{K}_h(r,t)$
$h(r,t)$ curvature radius	$R(r,t) = 1/\mathcal{K}_h(r,t)$
Vacuum electric potential	$\phi(r,z,t)$
Vacuum electric field	$\vec{E}(r,z,t) = E_r\hat{r} + E_z\hat{z}$
Vacuum electric field magnitude	$E = \lvert\vec{E}\rvert$
Local half angle of $h(r,t)$	$\theta(r,t) = -\tan^{-1}\left[(\partial h/\partial r)^{-1}\right]$
$h(r,t)$ Maxwell pressure	$p_M(r,t)$
$h(r,t)$ capillary pressure	$p_C(r,t)$
$h(r,t)$ viscous pressure	$p_V(r,t)$
Constant initial state variables	**Symbol**
Microemitter apex curvature radius	r_s
Initial liquid thickness	h_o
Initial liquid apex curvature radius	$r_s + h_o$
Applied electric potential	ϕ_o
Evaluation location	**Script**
At evolving protrusion apex	$apex$
Referenced quantities	**Symbol**
Shown $h(r,t)$ sampling time	Δt
Aspect ratio squared	$[h_o/(r_s + h_o)]^2$
$E(r = 0, z = h_o, t = t_o)$	E_o
Reynolds number	$\mathsf{Re} = \sqrt{\rho\varepsilon_o/2}\,\phi_o h_o/\mu(r_s + h_o)$
Electric Weber number	$\mathsf{We} = \varepsilon_o\phi_o^2/2\gamma h_o$
Simulation final termination time	$t_f = \arg\,[E^{apex}(t) \geq 5\ \text{GV/m}]$
r^{apex} at $t = t_f$	r_f
z^{apex} at $t = t_f$	z_f
R^{apex} at $t = t_f$	R_f
$\lvert\vec{u}\rvert^{apex}$ at $t = t_f$	$\lvert\vec{u}\rvert_f$
p^{apex} at $t = t_f$	p_f
Local minimum in θ at $t = t_f$ closest to $r = 0$	θ_f
r at which θ_f is extracted	r_θ

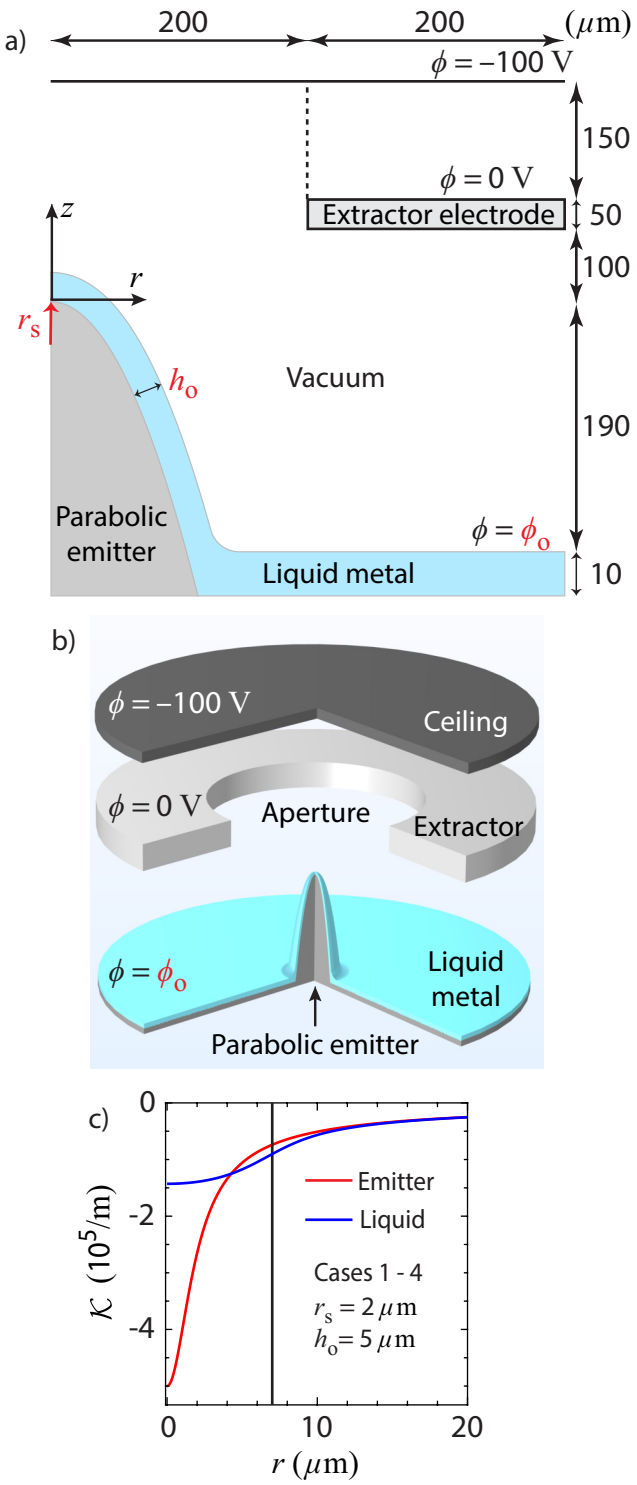

Figure 3.1: Details of computational geometry. Only h_o, r_s and ϕ_o are varied across simulations. (a) Details of the axisymmetric computational domain, (b) sketch of the domain partially revolved about $r = 0$ with a 90° vertical slice and (c) $\mathcal{K}$ for the microemitter Eq. 3.4 and $h(r, 0)$ Eq. 3.11 for "Cases 1-4" in Table 3.3 with vertical line denoting $r = r_s + h_o$.

and

$$\mathcal{G}_{em}(r) = \kappa_1\kappa_2 = \frac{\dfrac{\partial^2 f_{em}}{\partial r^2}\dfrac{\partial f_{em}}{\partial r}}{r\left[1+\left(\dfrac{\partial f_{em}}{\partial r}\right)^2\right]^2} = \frac{1}{r_s^2\left[1+(r/r_s)^2\right]^2} \tag{3.5}$$

where κ_1 and κ_2 are the two principal curvatures of the microemitter surface. The convention taken by the derivation of the differential properties of offset surfaces [110] is that κ_1 and κ_2 are positive if the associated centers of curvature is opposite to the direction of the surface normal. Since the κ_1 and κ_2 as defined by Eq. 3.4 are negative at all r, it means that the centers of curvature should be same as the direction of the surface normal. Since the centers of curvature lie inside the microemitter, $\hat{n}_{em}$ used to define the offset surface should point into the microemitter or

$$\hat{n}_{em}(r) = -\frac{\nabla g_{em}}{|\nabla g_{em}|} = -\frac{(r/r_s, 1)}{\sqrt{1+(r/r_s)^2}} \tag{3.6}$$

The initial liquid surface offset to the microemitter surface by a distance d everywhere in the direction of $\hat{n}_{em}$ can then be defined [41] as

$$\vec{r}_{h(r,0)}(a) = \vec{r}_{em}(a) + \hat{n}_{em}(a)d \tag{3.7}$$

where d is positive if the offset is taken in the same direction as $\hat{n}_{em}$ and negative if taken opposite. The microemitter surface unit surface normal in parametric form $\hat{n}_{em}(a)$ is the same as $\hat{n}_{em}(r)$ with the radial coordinate r swapped for the parameter a as the two are equal for the microemitter surface. Since the liquid is to be wetted on top of the microemitter surface, the offset distance is taken to be $d = -h_o$ such that the initial liquid surface $h(r, t = 0)$ is

$$\vec{r}_{h(r,0)}(a) = \left(a + \frac{ah_o}{r_s\sqrt{1+(a/r_s)^2}}, -\frac{a^2}{2r_s} + \frac{h_o}{\sqrt{1+(a/r_s)^2}}\right) \tag{3.8}$$

where it is evident that the initial liquid surface is not a paraboloid [129] unlike the paraboloidal microemitter surface. The parameter a is also no longer equal to the radial coordinate r for the offset surface. This is because the offset surface is constructed and expressed in terms of the normal projections of each point on the microemitter. The unit surface normal of the initial liquid surface [41] is related to that of paraboloid by

$$\hat{n}_{h(r,0)} = \Gamma\hat{n}_{em} \text{ where } \Gamma = \frac{1+2\mathcal{K}_{em}d+\mathcal{G}_{em}d^2}{\left|1+2\mathcal{K}_{em}d+\mathcal{G}_{em}d^2\right|} = \pm 1 \tag{3.9}$$

Since $d = -h_o$ and $\mathcal{K}_{em} < 0$ and $\mathcal{G}_{em} > 0$ for all r, $\Gamma = 1$ for the offset, meaning the normals are oriented in the same direction. The mean curvature of the surface offsets [41] is given by

$$\mathcal{K}_{\text{offset}} = \Gamma \frac{\mathcal{K} + \mathcal{G}d}{1 + 2\mathcal{K}d + \mathcal{G}d^2} \tag{3.10}$$

which, after substituting for $d = -h_o$ and expressions for $\mathcal{K}$ (Eq. 3.4) and $\mathcal{G}$ (Eq. 3.5), yields

$$\mathcal{K}_{h(r,t=0)}(a) = -\frac{1}{2r_s}\left(\frac{1}{\left[1 + (a/r_s)^2\right]^{3/2} + h_o/r_s} + \frac{1}{\sqrt{1 + (a/r_s)^2} + h_o/r_s}\right) \tag{3.11}$$

where at the initial liquid apex located at $a = 0$, it yields

$$\mathcal{K}_{h(r,t=0)}(0) = -\frac{1}{r_s + h_o} \tag{3.12}$$

giving the initial liquid apex curvature radius as $r_s + h_o$, which is indeed that of the microemitter apex curvature radius r_s augmented by the initial liquid thickness h_o. The mean curvatures are negative, nonuniform and smooth as sampled in Fig. 3.1(c).

The bottom of the microemitter is submerged in a liquid metal reservoir. The junction between the liquid wetted to the microemitter and the reservoir is smoothed with a fillet possessing a radius 20 μm.

Fig. 3.1(b) shows a sketch of the simulated geometry that has been partially revolved about the axis of symmetry. The geometry has been sampled for $h_o = 5$ μm and $r_s = 5$ μm that are the largest values simulated for this study. A 90° vertical slice has been taken to reveal the solid parabolic microemitter externally wetted with the liquid metal layer. All dimensions are to scale except for the domain floor and ceiling, which have been thickened for better visibility. The sketch clearly shows the sharpness of the curved microemitter and the wetted liquid profile.

3.2.2 Governing equations and boundary conditions

The key dimensional governing equations and boundary conditions of the EHD distortion have been presented in Sec. 2.1. Slight modifications and additions to the boundary conditions arise from the details of the computational geometry. The extractor surface and domain ceiling are set with constant potentials at $\phi = 0$ and $\phi = -100$ V, respectively. Along the symmetry axis $r = 0$ and rightmost domain wall, the electric flux is set to zero by $\partial\phi/\partial r = 0$. The no slip and no penetration conditions (Eq. 2.20) are imposed on the microemitter surface, reservoir floor and rightmost domain wall.

3.2.3 Computational algorithm

Finite element simulations that calculate the spatiotemporal $h(r,t)$ evolution in the modeled geometry have been conducted using the commercial software package COMSOL Multiphysics with Microfluidics [3]. The choices made for the computational algorithm are found to allow the EHD distortion to be tracked across length scales spanning $O(100\ \mu\text{m})$ to $O(1\ \text{nm})$ and time scales spanning $O(1\ \mu\text{s})$ to $O(1\ \text{ps})$.

3.2.3.1 Finite element triangular mesh generation and update

The finite element meshing scheme generates a nonuniform mesh where element side lengths can be made as small as 5 nm in regions of high local interface curvature to resolve the protrusion tip development. The arbitrary Lagrangian Eulerian finite element method [32] is employed to track the spatiotemporally rapidly accelerating $h(r,t)$ with a moving mesh. The Laplace method [1] is used to smoothly update the displacements of elements placed away from $h(r,t)$. The entire mesh is regenerated whenever the minimum of the chosen element quality metric falls below a specified threshold. The chosen metric is based on the quotient of the element area and the radius of the circumscribed circle, which is highly sensitive to small and large angles and element anisotropy. The number of elements ranges from roughly 25,300 to 274,000. Systems with the thinnest h_o are generally meshed with the largest number of elements as thin liquids require meshing with smaller element sizes.

3.2.3.2 Physical field discretization and time stepping scheme

The implemented discretization orders are cubic Lagrange for the mesh, quadratic Lagrange and linear Lagrange for $\vec{u}$ and p fields and quadratic Lagrange for ϕ to ensure consistency of discretization orders in the governing equations and boundary conditions. The time stepping algorithm used is the implicit backward differentiation formula (BDF) method [16]. The integration order and time step size adaptively vary during the time stepping for numerical stability. The COMSOL input "relative tolerance" controlling the relative uncertainty in the computed solution is set to 10^{-5}. At each time step, all physical quantities are simultaneously updated using the iteratively damped Newton's method [31]. At each iteration, the direct solver PARDISO [124] is used to solve the linearized system of equations. The potentials $\phi = \phi_o$ on $h(r,t)$ and $\phi = -100$ V on the domain ceiling are ramped from zero over a small timescale $t_o = 10^{-12}$ s using a step function with continuous second derivatives to expedite the initial time stepping.

3.2.3.3 Tracking the most prominent protrusion tip

The evolving most prominent protrusion apex coordinate r^{apex} is tracked by tracking the r coordinate of the global minimum in the Maxwell pressure $p_M(r,t)$, which corresponds to the coordinate possessing the largest electric field value on $h(r,t)$. Although the capillary pressure p_C is a quantity which explicitly depends on the first and second derivatives of $h(r,t)$, p_M has been chosen as it always dominates p_C to drive the EHD mode development and protrusion tip sharpening. Spurious numerical fluctuations in p_C that could hide the true protrusion signatures were also found right after remeshing events due to the complete regeneration of the surface mesh. Such fluctuations were not observed for p_M, which demonstrates its robustness and applicability in tracking r^{apex}. All other quantities at the apex can then be readily extracted at r^{apex} at each instance in time.

3.2.3.4 Simulation termination criterion

Each simulation is terminated at $t = t_f$ when the most prominent protrusion apex electric field $E^{apex} \approx 5$ GV/m, a value of similar order to liquid metal ion field evaporation values of $O(10$ GV/m) [108]. The actual values depend on the liquid metal and operating conditions: for instance, Ga ion emission has been reported at values as low as 5 GV/m [27]. The protrusion apex curvature radius R^{apex} at t_f was found to be at least three times larger than the minimum mesh size employed.

There were a handful of systems that possessed $E_o \geq 5$ GV/m. For completeness in reporting the mode outcome, such systems were advanced until $E^{apex} \approx 10$ GV/m to document only the generated mode type in Tables 3.10-3.17.

3.2.3.5 Simulation stability and convergence

Mesh and relative tolerance convergence tests of selected "axial" and "coronal" mode cases were conducted to determine the optimal values of minimum mesh size (5 nm) and relative tolerance (10^{-5}) for numerical stability and computational efficiency. The axial z_f and coronal (r_f, z_f) were stable with $O(10$ nm) variation for mesh size and relative tolerance smaller than those employed. For the "EHD instability" mode, the calculated protrusion wavelengths were also found to be comparable to those of surface EHD instabilities [131, 132] known to occur for a flat liquid layer. The connection is explored further in Ch. 4. The minimum mesh size is also 19 times larger than the empirical Ga atomic diameter (2.60 nm [128]) such that the continuum approximation [118] remains valid for each finite element.

3.2.3.6 Plotting

Snapshots of $\phi(t_o)$ contours and $\vec{E}(t_o)$ field lines shown in Sec. 3.3 and $\vec{u}$ and p fields in Sec. 3.4 have been obtained from COMSOL internal graphics utilities. All other plots have been generated using in-house MATLAB [2] plotting routines.

3.2.3.7 Key simulation parameters

Table 3.2: Material constants used for liquid metal gallium (Ga) at the melting point [69] and vacuum permittivity, values for key initial variables and ranges of key parameters.

Material constants	Symbol	Value
Ga density	ρ	6100 kg/m^3
Ga surface tension	γ	0.718 N/m
Ga shear viscosity	μ	1.94×10^{-3} Pa s
Vacuum permittivity	ε_o	8.85×10^{-12} F/m
Key initial variables		**Values**
h_o		0.1, 0.2, 0.5, 1.0, 2.0, 5.0 μm
r_s		0.1, 0.2, 0.5, 1.0, 2.0, 5.0 μm
ϕ_o		2.5, 5.0, 7.5, 10.0 kV (Tables 3.10-3.15)
		1.5 - 20.0 kV (Tables 3.16-3.17)
Key parameter ranges		
$3.84 \times 10^{-4} \leq [h_o/(h_o + r_s)]^2 \leq 9.61 \times 10^{-1}$		
$4 \leq \mathsf{Re} \leq 1250$		
$5 \leq \mathsf{We} \leq 24700$		
0.12 GV/m $\leq E_o \leq$ 8.13 GV/m		
$0 \leq r_f/(r_s + h_o) \leq 0.93$		
$E_f \approx 5$ GV/m for $E_o < 5$ GV/m		

The choices for key simulation parameters are provided in Table 3.2. The modeled liquid metal species is gallium (Ga) of constant density ρ, surface tension γ and viscosity μ provided in the table. Only h_o, r_s and ϕ_o were varied across the simulations. The chosen ranges for r_s and ϕ_o were made comparable to those found in the available experimental literature. The range for h_o, a quantity difficult to measure due to the liquid metal opacity and microemitter curvature, was made the same as r_s to access a wide range of the aspect ratio squared $[h_o/(h_o+r_s)]^2$. All other system parameters explicitly provided in Fig. 3.1(a)

were fixed with the order of magnitudes motivated from the microarray electrospray/liquid metal space micropropulsion [6, 28, 55, 86, 90, 97, 98, 106, 111] literature. A comparison is provided in Table 3.8. The values were further motivated from simulations that tracked the initial electric field response to changes in the fixed parameters. These results are to be discussed in Sec. 3.3.

3.3 Behavior of initial vacuum electric field in realistic geometry

This section describes the behavior of the initial vacuum $\vec{E}(r, z, t_o)$ generated for the modeled geometry. The results are taken from "Case 2" as listed in Table 3.3. The response of E_o as fixed system parameters are changed can be found in Table 3.9. The qualitative behavior described has been found to be general from checks conducted for limiting cases of r_s, h_o and ϕ_o combinations.

3.3.1 Initial $\vec{E}$ distribution

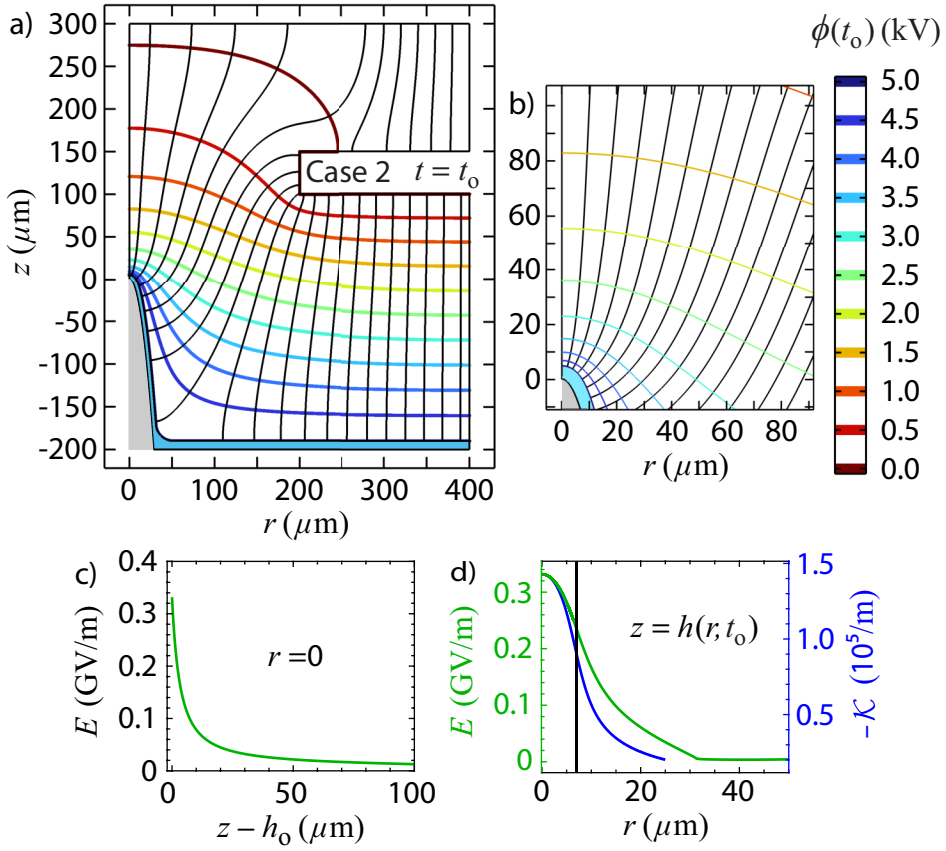

Figure 3.2: Initial $\vec{E}$ distribution with vacuum ϕ contours (colored lines) and $\vec{E}$ field lines (black lines) over (a) full and (b) inset view, (c) E on symmetry axis $r = 0$ and (d) E (green) and $\mathcal{K}$ (blue) on $h(r, t_o)$ with $r = r_s + h_o$ (vertical line) denoted.

Fig. 3.2(a)-(b) show an example of the generated initial vacuum $\vec{E}(t_o)$ field lines and $\phi(t_o)$ contours. The leftmost field line in Fig. 3.2(a) and first three field lines in Fig. 3.2(b) emanating from within the liquid tip region $r \leq r_s + h_o$ exhibits desirable collimation. Field lines generated away from the region become less collimated and eventually terminate on the extractor surface. The maximum initial E is always found at the initial liquid apex $h(0, t_o)$ regardless of h_o, r_s and ϕ_o. The field is only strongly enhanced near the apex as shown for E probed along the $r = 0$ symmetry axis (Fig. 3.2(c)) and $h(r, t_o)$ (Fig. 3.2(d)). The field distribution on $h(r, t_o)$ tracks the $\mathcal{K}$ distribution especially within $r \leq r_s + h_o$, which confirms that the E enhancement is generated by the $\mathcal{K}$ enhancement. The fillet possesses minimum E on $h(r, t_o)$ due its convex curvature and distances to the apex and extractor.

3.3.2 Effect of varying fixed system parameters on initial electric field on liquid surface $E(r, h, t_o)$

The effect of varying fixed system parameters on the initial electric field on liquid surface $E(r, z = h, t = t_o)$ has been tracked through simulations that calculate the initial electrostatic fields in the vacuum. The response of the initial liquid apex electric field E_o to changes in each parameter is shown in Table 3.9. Varying the aperture radius, microemitter height and microemitter apex to extractor underside gap distance were found to induce significant E_o response as shown in Fig. 3.3(a)-(f). Fig. 3.3(b) shows that E_o increases at a strongly linear rate as the aperture radius decreases before approaching an asymptote at radii smaller than the chosen microemitter apex to extractor gap distance, whereas Fig. 3.3(d) shows that it increases towards an asymptote as the microemitter height becomes larger than the chosen aperture radius and gap distance. These responses were surprisingly obtained even though E_o was strictly measured at the initial liquid apex at $r = 0$ and far from the flat liquid reservoir. In addition, Fig. 3.3(e) shows that increasing the microemitter apex to extractor gap distance decreases E_o at a linear rate for small gaps as intuit before the rate becomes smaller for gaps larger than the chosen microemitter height. Fig. 3.3(a), (c) and (e) further show that the respective responses occur all along the liquid surface wetted to the microemitter.

3.3.3 Scaling of initial liquid apex electric field E_o on $\phi_o/(r_s + h_o)$

These responses of E_o to the aperture and microemitter height and also the offset nature of $h(r, t_o)$ profile preclude analytic estimates of E_o derived from existing electrostatic analyses of simpler geometries like the hyperbola-to-plane [40, 84, 91], parabola-to-parabola [8] and line charge-to-plane [19]. Nevertheless, it is known [84] from these analyses that E_o is

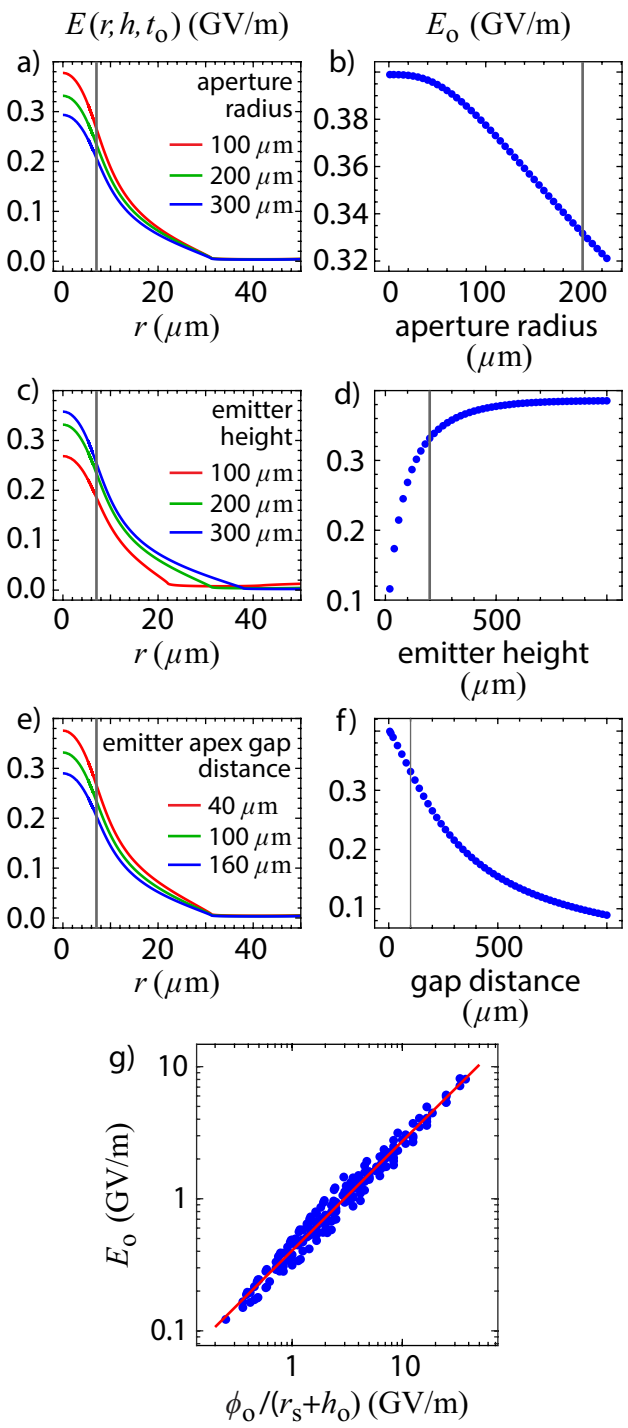

Figure 3.3: Dependence of initial electric field on liquid surface $E(r, z = h, t = t_o)$ and initial liquid apex electric field $E_o = E(r = 0, z = h_o, t = t_o)$ on (a)-(b) aperture radius, (c)-(d) microemitter height and (e)-(f) microemitter apex to extractor underside gap distance. The vertical lines in (a), (c) and (e) denote where $r = r_s + h_o$, whereas those in (b), (d) and (f) denote the employed value for simulations. Comparison between E_o and $\phi_o/(r_s + h_o)$ (markers) is made in (g) with a log-log fit (red) of slope 0.823 ± 0.100.

expected to dominantly scale as $\phi_o/(r_s + h_o)$ regardless of the detailed configuration as long as the initial liquid surface is thin and its apex radius $r_s + h_o$ is small compared to the liquid apex to extractor spacing. Such scaling is known to hold even with space charge effects [52] that have not been modeled in the simulations. The two conditions are synonymous for the current geometry and are satisfied as the maximum $r_s + h_o = 10$ μm simulated is still around an order of magnitude less than the minimum gap distance 100 μm - $h_o = 95$ μm. Indeed, Fig. 3.3(g) shows strong correspondence between E_o and $\phi_o/(r_s + h_o)$ with a log-log fit slope of 0.823 ± 0.100, which is not exactly linear due to the aperture and finite microemitter height effects but nevertheless confirms the prevalence of the local $r_s + h_o$ in determining E_o.

3.4 EHD mode characterization

This section presents results characterizing the EHD modes found from the simulations. Each mode is characterized using examples listed in Table 3.3. The broad characteristics described for each mode have been found to be general from checks conducted for limiting cases of r_s, h_o and ϕ_o. Measurements of key physical quantities can be found in Tables 3.10-3.17.

3.4.1 EHD modes revolved around symmetry axis

Fig. 3.4 shows the snapshots of the distorted liquid profile at $t = t_f$ partially revolved about $r = 0$ with a 90° vertical slice for the protrusion developing EHD modes to be described in this section. The regions highlighted in red corresponds to the most prominent protrusion apex location in the axisymmetric view. Fig. 3.4(a) shows an example (case 2) for the axial mode resulting in the development of a single protrusion along the symmetry axis $r = 0$. Fig. 3.4(b) shows an example (case 3) for the coronal mode resulting in the development of a single ring. Fig. 3.4(c)-(d) show examples for the thick (case 4) and thin (case 5) instability mode resulting in multiple rings. The examples also happen develop an axial protrusion as part of the instability. Other instances of the instability that do not develop an axial protrusion have been observed. Fig. 3.4(e) shows an example (case 6) for the dual mode resulting in simultaneous development of the coronal and instability mode. The subsequent figures used to describe the modes present the profiles in the (r, z) cut such that the rings will manifest as non-axial protrusions. It should be noted that issues related to additional instabilities leading to capillary breakup of such rings have not been considered in the simulations due to the axisymmetry of the computational domain.

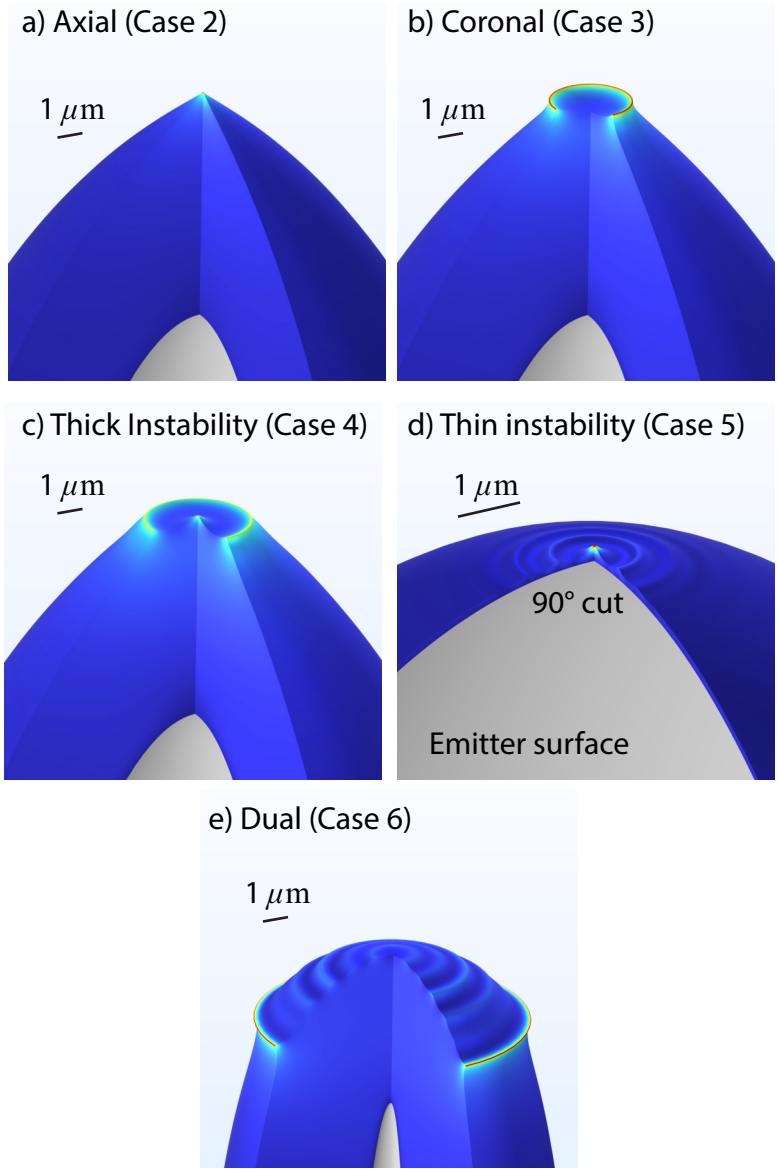

Figure 3.4: View of the liquid profile at $t = t_f$ partially revolved about $r = 0$ with a 90° vertical slice for (a) axial, (b) coronal, (c) thick instability, (d) thin instability and (e) dual mode examples. The microemitter is colored in grey whereas the liquid bulk possesses a color gradient corresponding to the velocity magnitude. The scale bar in each panel corresponds to a distance of 1 μm.

Table 3.3: Label, mode outcome, key initial variables, termination time and key nondimensional numbers for examples used in Sec. 3.4 to characterize the EHD modes found in the simulations. Sec. 3.4.2 characterizes the drainage mode, Sec. 3.4.3 characterizes the axial mode, Sec. 3.4.4 characterizes the coronal mode, Sec. 3.4.5 characterizes the thick instability mode and Sec. 3.4.6 characterizes the thin instability mode and the dual mode. Measurements of key physical quantities at $t = t_f$ for all simulated systems (182 in total) can be found in Tables 3.10-3.17.

Label	Mode	h_o (μm)	r_s (μm)	ϕ_o (kV)	t_f (s)
Case 1	Drainage	5.0	2.0	2.5	
Case 2	Axial	5.0	2.0	5.0	7.57×10^{-7}
Case 3	Coronal	5.0	2.0	7.5	4.73×10^{-7}
Case 4	Thick Inst.	5.0	2.0	10.0	3.26×10^{-7}
Case 5	Thin Inst.	0.1	5.0	17.5	7.07×10^{-8}
Case 6	Dual	5.0	0.1	10.0	1.28×10^{-7}

Label	Re	We
Case 1	151	8
Case 2	303	31
Case 3	454	69
Case 4	605	123
Case 5	29	18900
Case 6	830	123

3.4.2 Drainage mode characteristics

This section describes the "drainage" mode characterized by the drainage of liquid wetted to the microemitter surface without any protrusion development.

3.4.2.1 Spatiotemporal drainage mode $h(r,t)$ evolution

Shown in Fig. 3.5 is the $h(r,t)$ evolution of the "drainage" mode example. It occurs despite the absence of gravity and a nonzero ϕ_o that still generates a negative Maxwell pressure p_M acting to pull the liquid into the vacuum. It is overcome by the positive capillary pressure p_C that acts to flatten the curved free surface. The capillary pressure is generated by the negative, nonuniform parabolic microemitter curvature that rapidly decreases when probed away from the microemitter apex. The resultant curvature gradient generates the forcing that induces the liquid to thin at the concave microemitter apex (Fig. 3.5(b)) and thicken at the positively curved, convex fillet (Fig. 3.5(c)), consistent with known physical observations

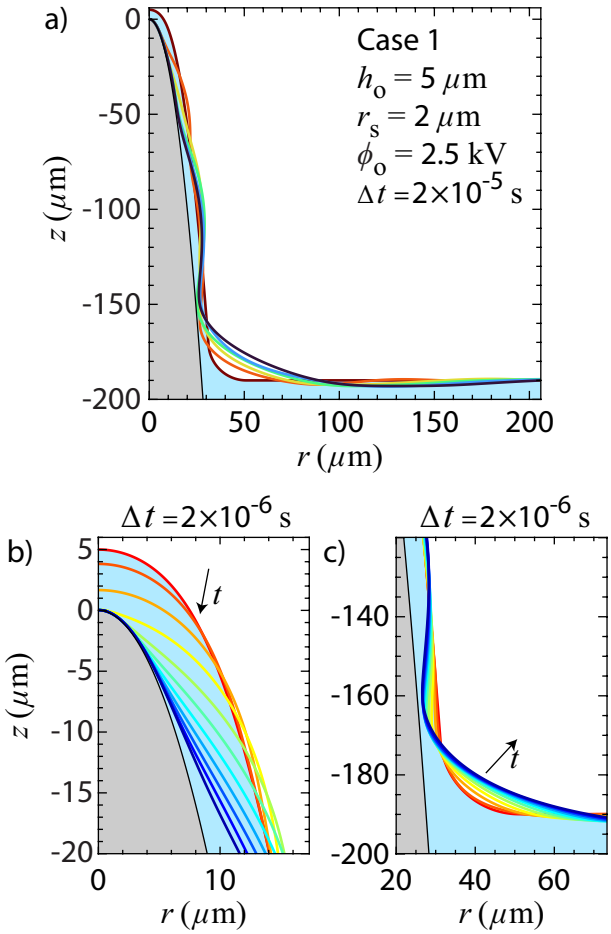

Figure 3.5: Spatiotemporal drainage evolution with $h(r,t)$ (colored lines) uniformly sampled at Δt, initial liquid bulk (blue) and microemitter (grey). Note the difference in Δt between (a) far and inset views at the (b) tip and (c) fillet.

[76] and simulations in the lubrication limit [125] for liquids wetted to positively and negatively curved surfaces. The draining liquid coalesces into an advancing bulge that eventually drains into the reservoir. A still thinning layer of $O(10\text{ nm})$ remains wetted to the microemitter surface as the bulge drains.

3.4.2.2 Distribution of drainage $\vec{u}$ and p at early time

Shown in Fig. 3.6 are velocity $\vec{u}$ and pressure p distributions sampled at the beginning of the liquid drainage. The largest speeds are found around $r = 0$ tip surface, confirming that the thinning occurs the fastest at the most sharply curved location. The pressure is positive along shown $h(r,t)$ as p_C prevails over p_M and decreases away from the tip as $\mathcal{K}_h$ is reduced, which weakens both p_C and p_M. The resultant $-\nabla p$ generates the draining flow of wetted liquid down the microemitter surface as shown by the velocity arrows. The

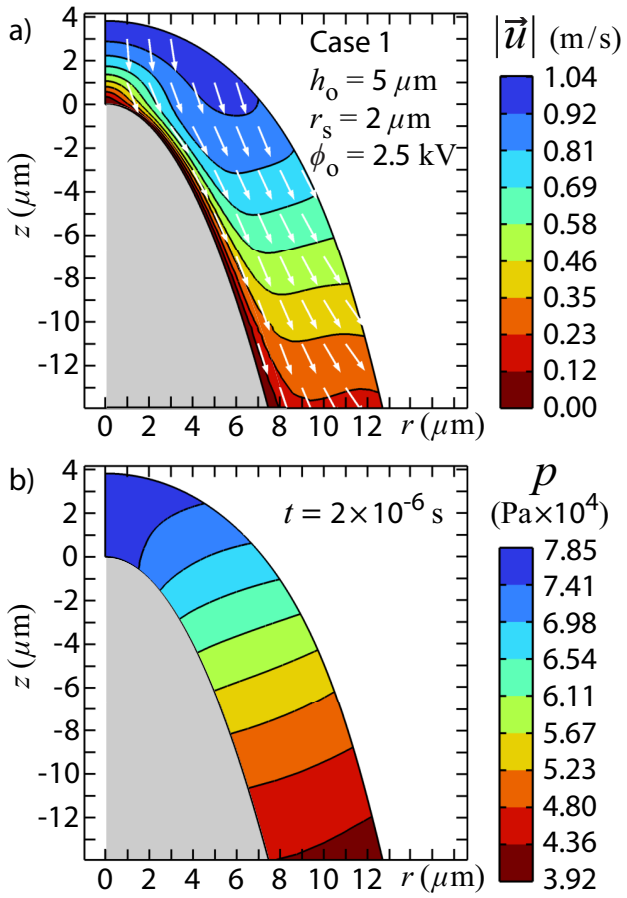

Figure 3.6: Drainage early time (a) velocity and (b) pressure of the tip bulk. Values for $|\vec{u}|$ and p contours (black lines) are linearly sampled. All $\vec{u}$ arrow (white) lengths are normalized.

viscous pressure p_V at the surface and shear viscous stress contributions in the bulk resisting the liquid motion were found to be an order of magnitude smaller than the found p_C and p_M. Although the $\vec{u}$ gradients can be significant as seen from the $|\vec{u}|$ contour distribution, the small Ga viscosity of 1.94×10^{-3} Pa s suppresses the viscous contributions to the flow.

3.4.3 Axial mode characteristics

This section describes the "axial" mode that develops a single protrusion located on the $r = 0$ symmetry axis.

3.4.3.1 Spatiotemporal axial mode $h(r,t)$ evolution

Fig. 3.7 displays the $h(r,t)$ evolution of the "axial" mode example. Fig. 3.7(a)-(b) show that $h(r,t)$ away from the liquid tip exhibits very little deformation. The point where $h(r,t_f) \leq h(r,0)$ is marked by a cross in Fig. 3.7(b). This location was found to be stable

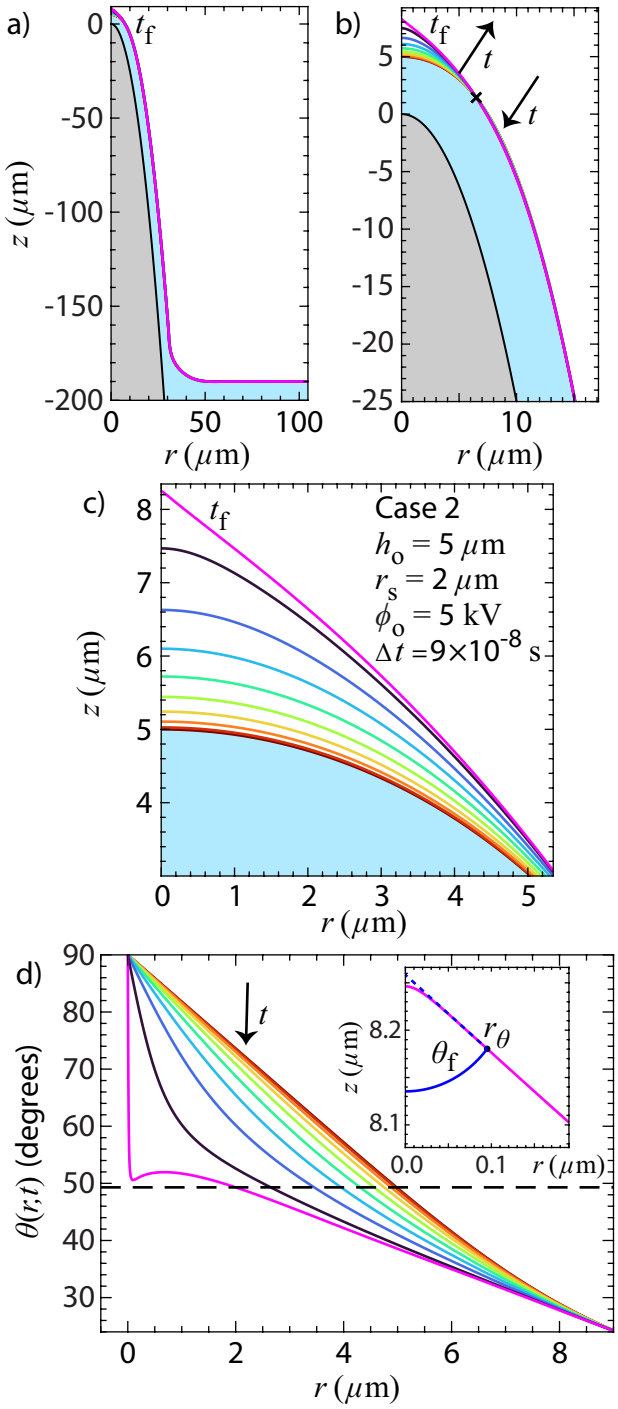

Figure 3.7: Spatiotemporal axial mode example evolution with nine $h(r,t)$ uniformly sampled at Δt (colored lines), final $h(r,t_f)$ (pink line), initial liquid bulk (blue) and microemitter (grey) for the (a) far, (b) intermediate and (c) tip view. Black cross in (b) marks where $h(r,t_f) \leq h(r,0)$. (d) Half angle $\theta(r,t)$ evolution with the Taylor cone [141] angle 49.3° (dashed line) denoted. Inset shows how θ_f and r_θ are calculated.

in t for the provided view and thereby indicates the width of the mode developing liquid tip region, which is found to be enclosed within the initial liquid apex radius $r \leq r_s + h_o$. The supporting liquid supply is drawn from the bulk past the point, where the drainage into the developing mode may be small but occurs all along the wetted liquid and around the azimuth to comprise a tremendous amount of supply. Fig. 3.7(c) shows the rapid spatiotemporal $h(r,t)$ acceleration which culminates in the development of a single axial protrusion. The protrusion apices at the termination times $t = t_f$ were found to be rounded with R_{apex} of $O(10\text{ nm})$ as cataloged in Tables 3.10-3.17. The times t_f are also all of $O(10^{-9} - 10^{-5}\text{ s})$ and generally inversely scales as E_o. These are orders of magnitudes less than the imaging rates used for *in-situ* investigations.

Fig. 3.7(d) presents the local surface half angle $\theta(r,t)$ evolution in $r \leq r_s + h_o$. The quantity $\theta(r,t) = -tan^{-1}[(\partial h/\partial r)^{-1}]$ measures the angle between $r = 0$ and the surface tangent evaluated at the $h(r,t)$ mesh nodes. The slope $\partial h/\partial r$ at each node is approximated by the central difference method evaluated using the nearest neighboring nodes. The half angle $\theta(r,t)$ decreases in t and ultimately culminates in a local minimum close to $r = 0$ as shown at $t = t_f$, which indicates a change in $\mathcal{K}_h$ character from concave to convex induced by the axial protrusion development. The value and corresponding r coordinate at t_f have been designated as θ_f and r_θ. The minimum was found to develop over Δt much smaller than that sampled and decrease in θ_f and r_θ once it develops. Though the sampled θ_f is close to the "Taylor cone" [141] value of 49.3°, those found for other axial systems were found to vary between 42 and 65° as cataloged in Tables 3.10-3.17, confirming the dynamic development [5, 135, 136, 164] of axial protrusions. In fact, increasing E_o was generally found to increase θ_f, as protrusions need not be as sharpened to satisfy the termination criterion, and decrease r_θ, which demonstrates the ability of stronger p_M to more tightly focus protrusion development.

3.4.3.2 Axial $\vec{u}$ and p at $t = t_f$

Shown in Fig. 3.8 and 3.9 are the velocity $\vec{u}$ and pressure p distributions sampled at $t = t_f$ for the axial example. The contour maps confirm that the late time flow is concentrated around the accelerating apex possessing the magnitudes $|\vec{u}| = |\vec{u}|_f$ of $O(100\text{ m/s})$ and $p = p_f$ of $O(10^7\text{ Pa})$ as cataloged in Tables 3.10-3.17. The p values are now negative as p_M prevails over p_C to have developed the protrusion. The viscous contributions are still found to be an order of magnitude smaller than p_M and p_C due to small Ga viscosity. The velocity arrows superimposed on the liquid domain in Fig. 3.8 additionally indicate that the flow is strongly vertical. The arrows nearby the apex are also not purely radial

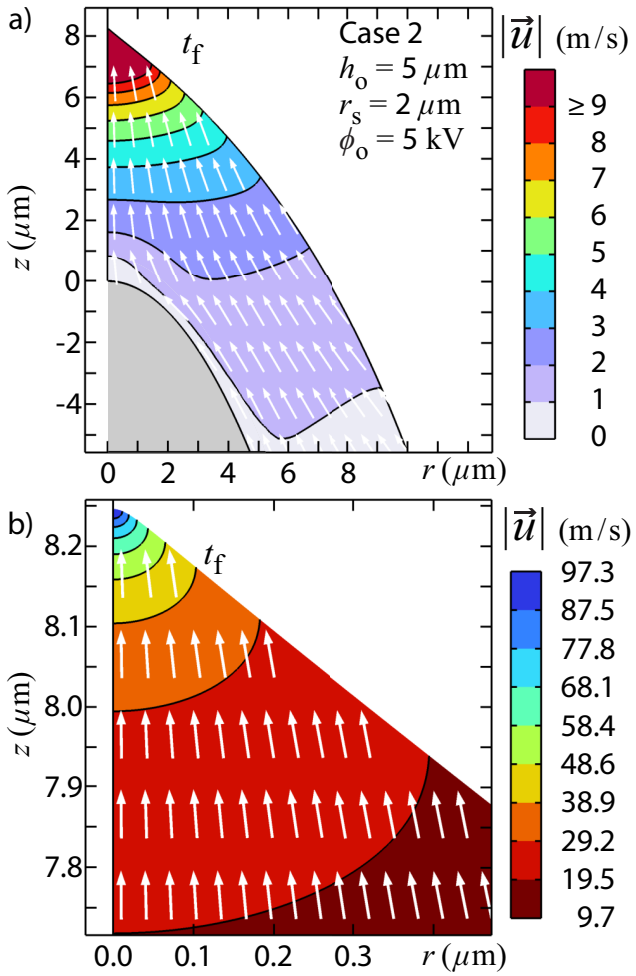

Figure 3.8: Axial mode example velocity at $t = t_f$ with $|\vec{u}|$ contours (black lines) linearly sampled for the (a) bulk and (b) tip view. All $\vec{u}$ arrow (white) lengths are normalized.

towards the apex. This is a feature also shared by the $|\vec{u}|$ and p contours as they attach non perpendicularly to $h(r,t)$; p contours are especially flattened along the r coordinate. These angular dependencies are in contrast to the radial sink flow towards the apex as predicted by Zubarev's original self-similar analysis [165] for a perfectly conducting, inviscid liquid. The angular dependence was recovered for the subsequent analysis [136, 164] that retained inertial effects to contribute to the same order as Maxwell and capillary effects.

3.4.4 Coronal mode characteristics

This section describes the "coronal" mode that develops a single protrusion located away from $r = 0$ symmetry axis.

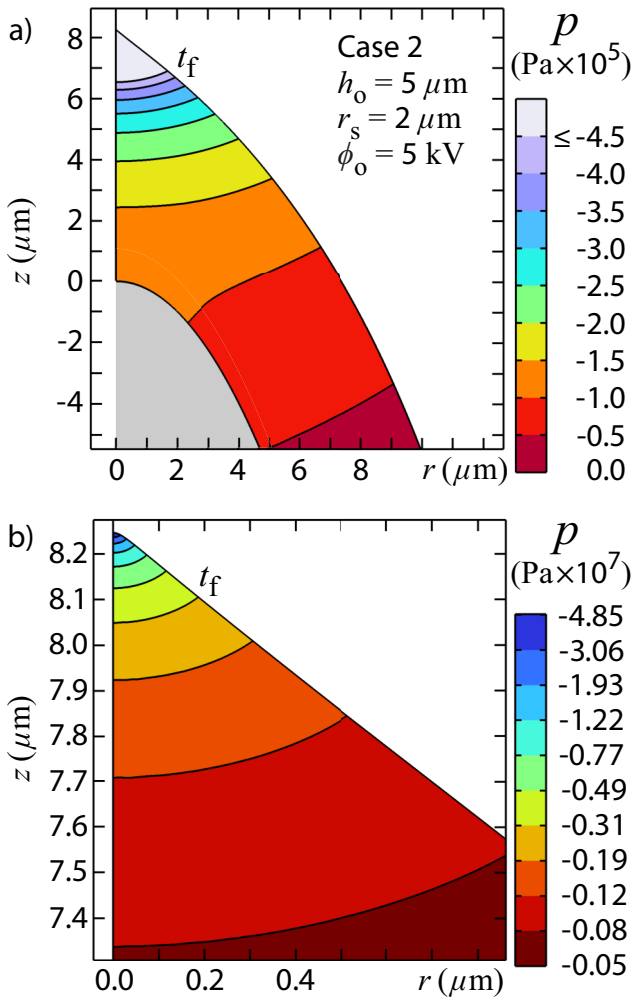

Figure 3.9: Axial mode example pressure at $t = t_f$ with p contours (black lines) linearly sampled for the (a) bulk view and logarithmically for the (b) tip view.

3.4.4.1 Spatiotemporal coronal mode $h(r,t)$ evolution

Shown in Fig. 3.10 is the $h(r,t)$ evolution of the "coronal" mode example where a single but non-axially located protrusion develops. It forms non-axially despite the smoothness of the initial surface and its $\mathcal{K}_h$ and the strongest initial E found at $h(0,t_o)$. Fig. 3.10(c) shows that the protrusion develops from a region that becomes increasingly flattened to either side to form a bulge. It protrudes at an angle that generally increases with increasing r_f but does not project normally outwards from the microemitter or the initial liquid surface. It is also asymmetric due to the unequal liquid supply available to either side, precluding θ_f measurement. Despite the non-axial development, all mode generating activity still occurs within $r \leq r_s + h_o$ as shown in Fig. 3.10(a)-(b) and demonstrated by $r_f/(r_s + h_o) < 1$ cataloged in Tables 3.10-3.17 for all coronal systems. The logged t_f and R_f are also

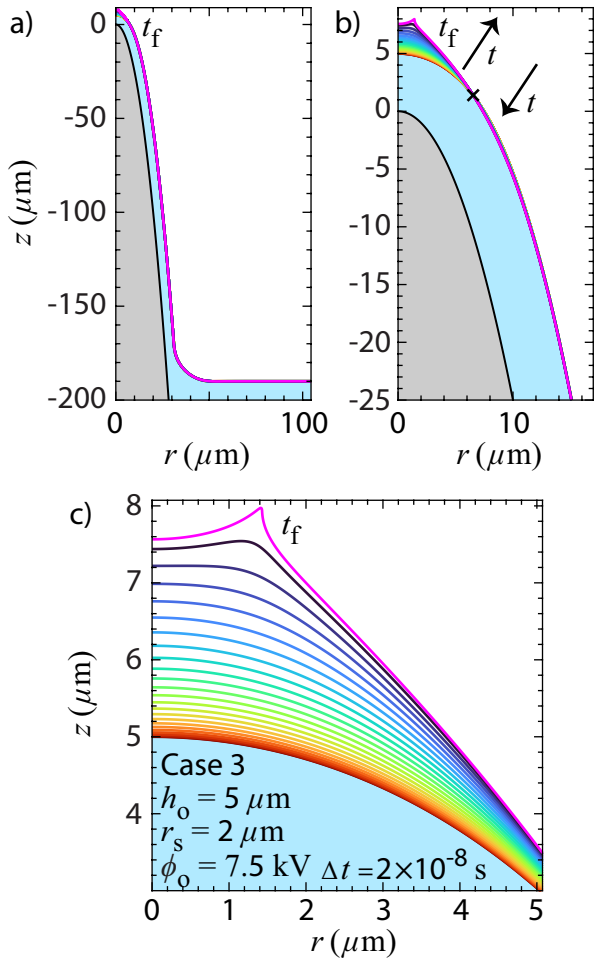

Figure 3.10: Spatiotemporal coronal mode example evolution with twenty four $h(r,t)$ uniformly sampled at Δt (colored lines), final $h(r,t_f)$ (pink line), initial liquid bulk (blue) and microemitter (grey) for the (a) far, (b) intermediate and (c) tip view. Black cross in (b) marks where $h(r,t_f) \leq h(r,0)$.

comparable to those found for the axial mode.

3.4.4.2 Coronal $\vec{u}$ and p at $t = t_f$

Shown in Fig. 3.11 and 3.12 are the velocity $\vec{u}$ and pressure p distributions sampled at $t = t_f$ for the coronal example. Despite the non-axial location, the flow fields share all characteristics found for the axial mode counterparts back in Sec. 3.4.3.2 except for the following differences. The fields now additionally possess asymmetry about the apex derived from the asymmetric protrusion profile derived from unequal flow. It is interesting to note that the p contours in Fig. 3.12(b) are much more symmetric than the $|\vec{u}|$ contours in Fig. 3.11(b) and still retain the flatness about the protrusion apex as found for the axial

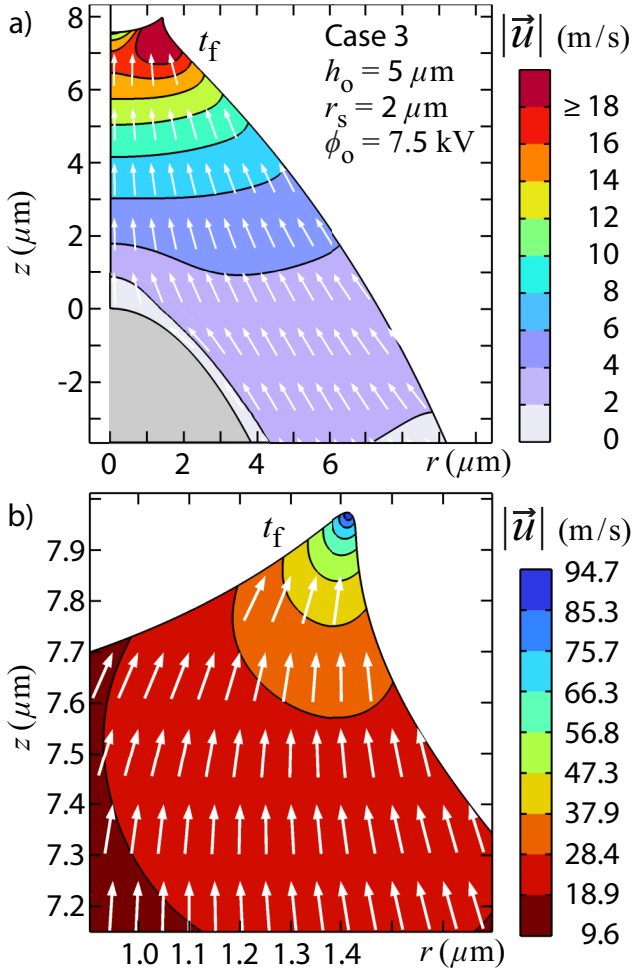

Figure 3.11: Coronal mode example velocity at $t = t_f$ with $|\vec{u}|$ contours (black lines) linearly sampled for the (a) bulk and (b) tip view. All $\vec{u}$ arrow (white) lengths are normalized.

mode. The capillary pressure p_C, which is always positive along the mode developing $h(r,t)$ for the axial mode, was found to be able to take negatively signed values away from the still rounded protrusion apex due to the strongly convex protrusion $\mathcal{K}_h$ as evident in the apex views. The negative p_C aids the still negative p_M to direct further supply into the developing protrusion.

3.4.5 EHD instability mode characteristics

This section describes the "EHD instability" mode that develops multiple, regularly spaced protrusions along the liquid surface.

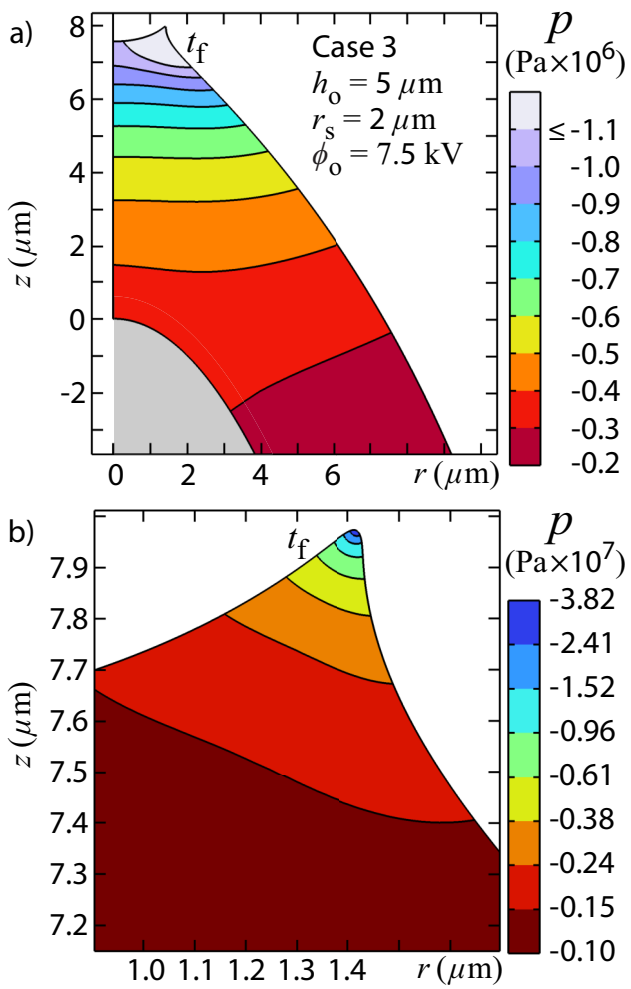

Figure 3.12: Coronal mode example pressure at $t = t_f$ with p contours (black lines) linearly sampled for the (a) bulk view and logarithmically for the (b) tip view.

3.4.5.1 Spatiotemporal EHD instability mode $h(r,t)$ evolution

Shown in Fig. 3.13 is the $h(r,t)$ evolution of the "EHD instability" mode example culminating in the simultaneous development of multiple protrusions along the liquid surface. Much like the axial and coronal modes, Fig. 3.13(a)-(b) show that the mode development is still confined within $r \leq r_s + h_o$. The apex radii R_f are also comparable but t_f are generally smaller as E_o needed to excite the instability was generally larger. Fig. 3.13(c) shows that the protrusions simultaneously protrude from $h(r,t)$ from the view provided. However, they develop at different rates as only a single protrusion apex is found to possess $E^{apex} \geq 5$ GV/m at t_f regardless of the number of protrusions. Though this protrusion apex protrudes from $r = 0$ for this example, it does not necessarily develop at $r = 0$ nor closest to $r = 0$. The surface can also develop multiple protrusions that are all entirely

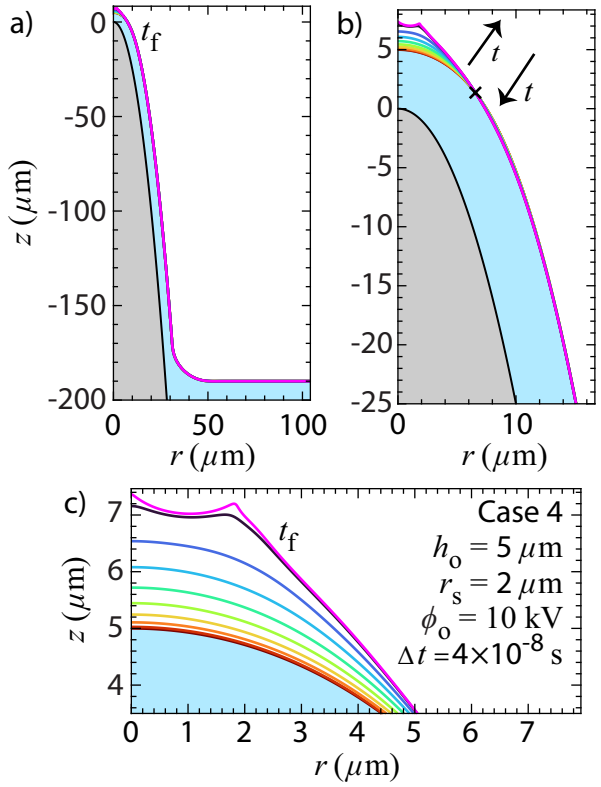

Figure 3.13: Spatiotemporal instability mode example evolution with nine $h(r,t)$ uniformly sampled at Δt (colored lines), final $h(r,t_f)$ (pink line), initial liquid bulk (blue) and microemitter (grey) for the (a) far, (b) intermediate and (c) tip view. Black cross in (b) marks where $h(r,t_f) \leq h(r,0)$.

non-axial. The protrusions also do not travel along the surface [34, 39, 62, 113] and do not coalesce or retract into the surface [34, 38, 39] during the development simulated like multiple protrusion formations imaged during *in-situ* LMIS and alloy LMAIS investigations conducted by Driesel and co-workers.

These characteristics suggest that it is similar not to convective instabilities but rather to surface EHD instabilities [131, 132] known to occur from a flat liquid metal layer under a flat, apertureless extractor. A comparison was made between the lateral protrusion apex to apex spacing observed in Fig. 3.13(c) and the maximally unstable wavelength obtained from the known flat layer dispersion relation [132] by substituting h_o for liquid thickness and E_o for the characteristic electric field. The wavelength was calculated to be 1.87 μm, a value highly comparable to 1.81 μm found for the lateral spacing between the two protrusion apices. The connection is investigated further in Ch. 4.

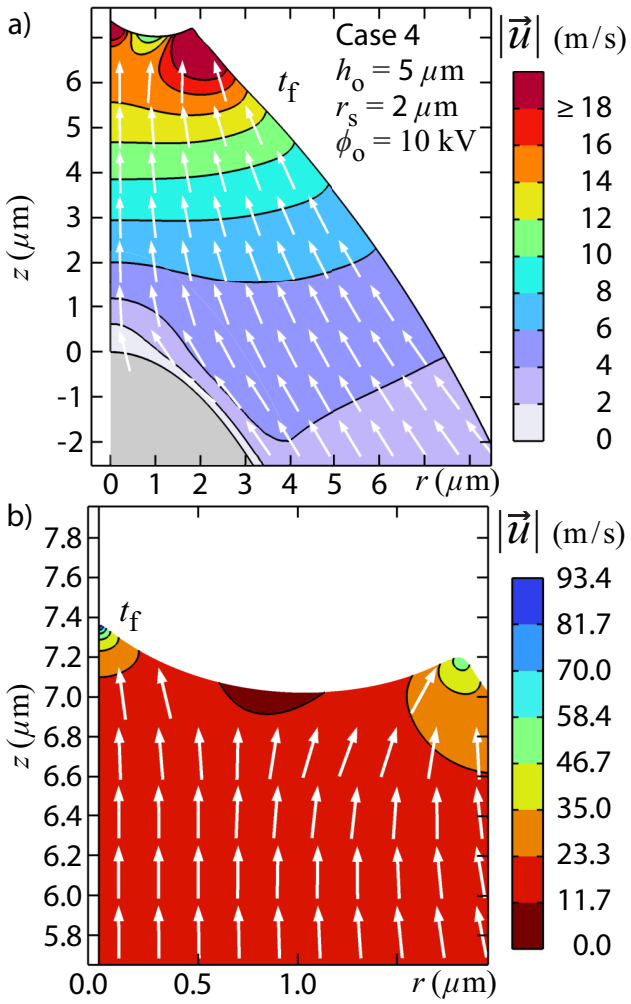

Figure 3.14: Instability mode example velocity at $t = t_f$ with $|\vec{u}|$ contours (black lines) linearly sampled for the (a) bulk and (b) tip view. All $\vec{u}$ arrow (white) lengths are normalized.

3.4.5.2 Instability $\vec{u}$ and p at $t = t_f$

The velocity $\vec{u}$ and pressure p distributions are shown in Fig. 3.14 and 3.15 for the instability example at $t = t_f$. Despite the presence of multiple protrusions, the flow fields around the two protrusions shown for the example share all characteristics found for the axial (Sec. 3.4.3.2) and coronal (Sec. 3.4.4.2) mode counterparts depending on the protrusion location. The different rates of protrusion development lead to values that greatly vary across the different apices.

3.4.6 Spatiotemporal $h(r,t)$ evolution of thin instability and dual mode examples

Shown in Fig. 3.16(a) is the $h(r,t)$ evolution of the instability mode example with now a thinly wetted liquid possessing $[h_o/(r_s + h_o)]^2 \ll 1$. The behaviors are the same as those

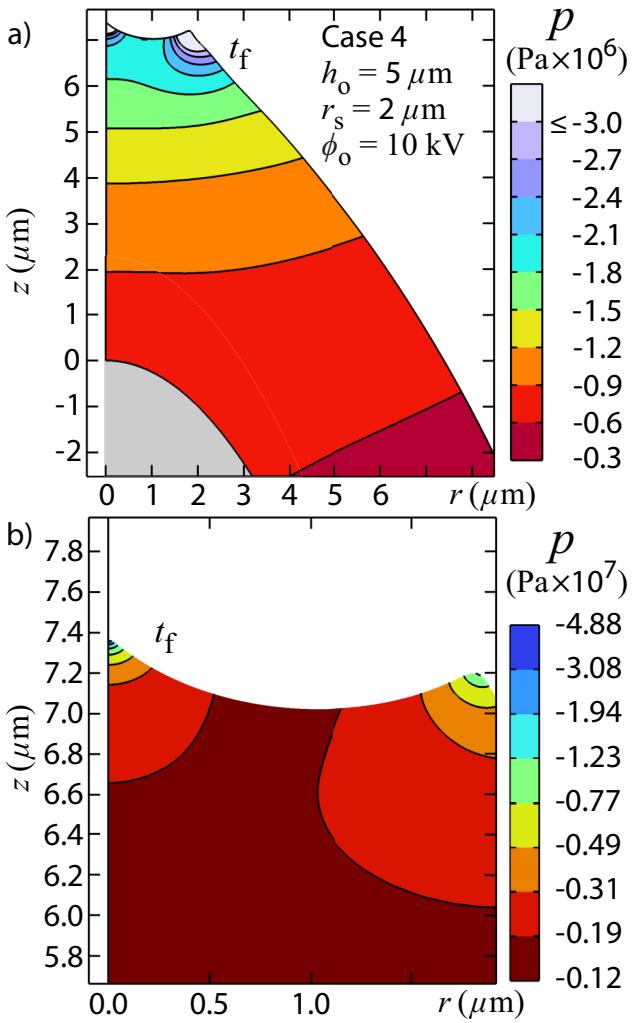

Figure 3.15: Instability mode example pressure at $t = t_f$ with p contours (black lines) linearly sampled for the (a) intermediate view and logarithmically for the (b) tip view.

described in Sec. 3.4.5 except that the bulk undergoes very little displacement such that the protrusions develop by draining just the initially available local liquid supply. The lateral apex-to-apex spacing between the two protrusions closest to $r = 0$ is found to be 0.54 μm, which is again highly comparable to maximally unstable wavelength 0.59 μm predicted for the equivalent flat liquid EHD surface instability [132] with same h_o and E_o.

Shown in Fig. 3.16(b) is an example of a "dual" mode where the two protrusion developing EHD modes are simultaneously generated. For this example, the instability develops with an additional coronal protrusion to its right. It also develops the most prominent protrusion apex, which is the coronal one, most off-axially at $r_f = 4.73\ \mu$m and $r_f/(r_s + h_o) = 0.93$ over all simulated systems. Only the instability and coronal dual mode kind has been

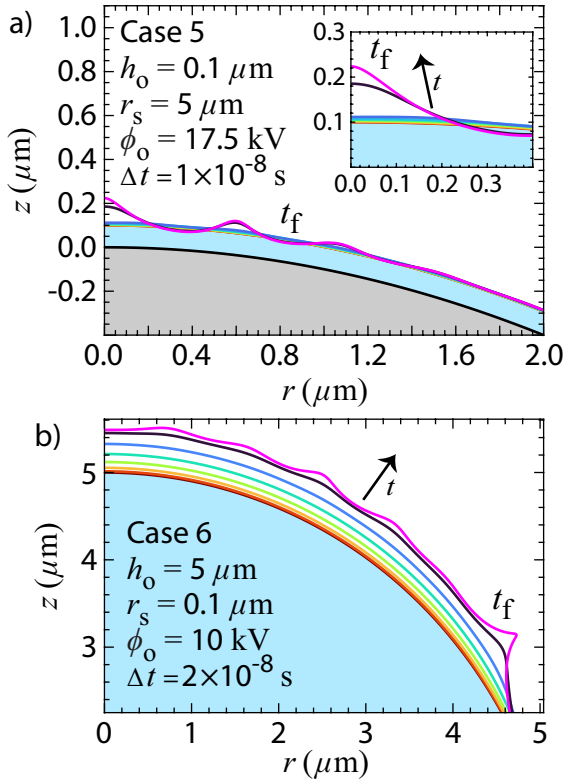

Figure 3.16: Spatiotemporal (a) instability mode example with $[h_o/(r_s + h_o)]^2 \ll 1$ and (b) dual mode example evolution with final $h(r, t_f)$ (pink line), initial liquid bulk (blue) and microemitter (grey). (a) Eight and (b) seven uniformly sampled $h(r, t)$ at Δt (colored lines) are shown in addition to $h(r, t_f)$. Inset in (a) shows $h(r, t)$ evolution around r_f.

observed in the conducted simulations. Those that seemed to have developed the axial and coronal protrusions were found to possess the apex-to-apex spacings comparable to the equivalent flat liquid EHD surface instability [132] with same h_o and E_o. Despite the dual development, all protrusions were still found to develop within $r \leq r_s + h_o$.

3.4.7 Termination time electric field lines

The strongly confined mode development to within $r \leq r_s + h_o$ documented for all modes in Sec. 3.4 suggests that the $\vec{E}(t_f)$ field lines emanating from the modes should retain desirable collimation possessed by initial field lines. Fig. 3.17 shows the field lines at $t = t_o$ and t_f for the dual mode case shown back in Fig. 3.16(b) possessing the largest r_f and $r_f/(r_s + h_o)$ out of all simulations. Indeed, the field lines quickly converge by just couple of tens of microns away from the surface as shown in Fig. 3.17(b). Fig. 3.17(a) confirms that they become indistinguishable such that the important t_f field lines retain desirable collimation. Though ion emission is not modeled in the simulations, the exhibited $\vec{E}(t_f)$ collimation strongly suggests that ions to be emitted from all systems documented in the

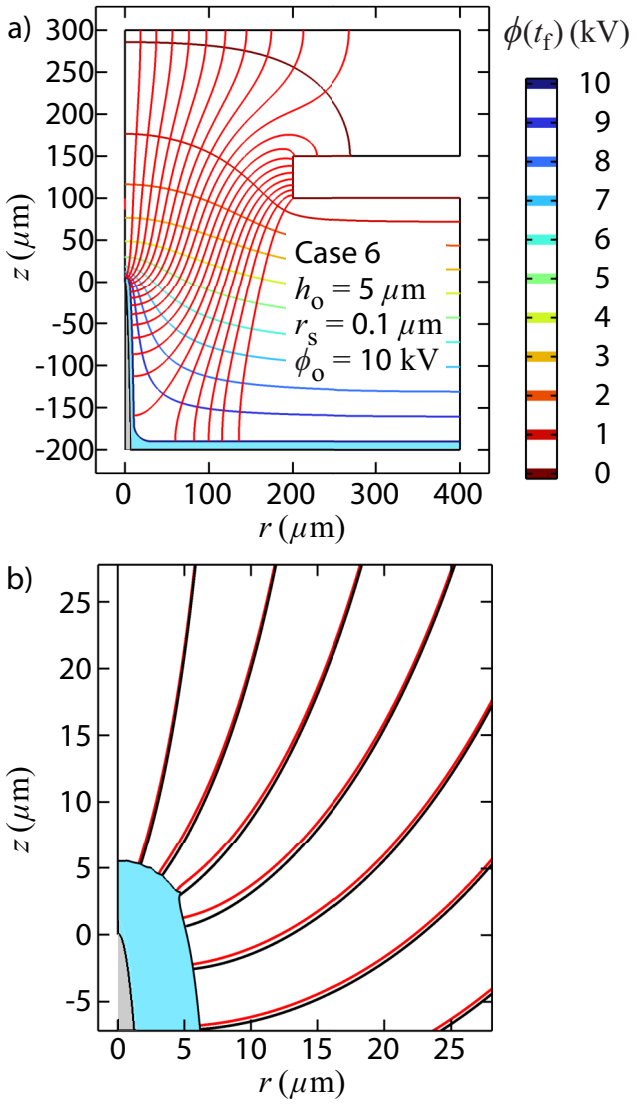

Figure 3.17: Vacuum $\phi(t_f)$ contour (colored lines) and $\vec{E}$ field lines at initial time $t = t_o$ (black lines) and final time $t = t_f$ (red lines) in the (a) full domain and (b) near liquid tip for the "Case 6" dual mode example (Fig. 3.16(b)). Field lines have been uniformly sampled from the extractor plane at $z = 100\ \mu$m at 10 μm lateral increments.

study will not lead to underspray [17, 77] known to cause catastrophic device failure.

3.5 Temporal evolution of protrusion apex quantities

This section presents results on the temporal evolution of key quantities extracted at the draining liquid apex $h(0,t)$ for the drainage mode and growing most prominent protrusion apex $h(r^{apex},t)$ for the axial, coronal and instability modes. The behavior for each mode is characterized using selected examples for which (h_o, r_s) are varied at a fixed value of ϕ_o. Tables present the (h_o, r_s, ϕ_o) combinations sampled for each mode as well as power law exponents extracted from ordinary least squares fitting for each listed quantity in the indicated time interval.

3.5.1 Drainage mode apex evolution

This section describes the results of the drainage mode apex evolution, where all quantities shown have been evaluated at the draining liquid apex $h(0,t)$. Table 3.4 presents the sampled (h_o, r_s, ϕ_o) combinations along with evaluated apex quantities and extracted power law exponents.

Table 3.4: Drainage mode apex quantity power law exponents. Listed quantities are the tracked quantity, h_o, r_s, aspect ratio squared $[h_o/(r_s + h_o)]^2$, ϕ_o, power law exponent (i.e. quantities $\sim t^\alpha$ where α is the exponent) with least squares fitting uncertainties and fitting t interval.

Quantity	h_o (μm)	r_s (μm)	$\left(\frac{h_o}{r_s+h_o}\right)^2$	ϕ_o (kV)	Power law exponent	Fitting t interval (s)
$h_o - h(0,t)$	0.5	5.0	8.26×10^{-3}	2.5	1.96 ± 6.24×10^{-3}	$[10^{-12}, 10^{-7}]$
	1.0	2.0	1.11×10^{-1}	2.5	1.96 ± 4.33×10^{-3}	$[10^{-12}, 10^{-7}]$
	5.0	2.0	5.10×10^{-1}	2.5	2.00 ± 1.22×10^{-2}	$[10^{-12}, 10^{-7}]$
$h(0,t)$	0.5	5.0	8.26×10^{-3}	2.5	-0.53 ± 1.20×10^{-3}	$[10^{-5}, 10^{-4}]$
	1.0	2.0	1.11×10^{-1}	2.5	-0.41 ± 1.62×10^{-4}	$[10^{-5}, 10^{-4}]$
	5.0	2.0	5.10×10^{-1}	2.5	-0.44 ± 2.02×10^{-4}	$[10^{-5}, 10^{-4}]$
$\lvert\vec{u}\rvert(0,t)$	0.5	5.0	8.26×10^{-3}	2.5	0.99 ± 5.06×10^{-3}	$[10^{-12}, 10^{-7}]$
	1.0	2.0	1.11×10^{-1}	2.5	1.01 ± 1.41×10^{-3}	$[10^{-12}, 10^{-7}]$
	5.0	2.0	5.10×10^{-1}	2.5	1.04 ± 8.17×10^{-3}	$[10^{-12}, 10^{-7}]$
$\lvert\vec{u}\rvert(0,t)$	0.5	5.0	8.26×10^{-3}	2.5	-1.70 ± 3.62×10^{-3}	$[10^{-5}, 10^{-4}]$
	1.0	2.0	1.11×10^{-1}	2.5	-1.42 ± 3.22×10^{-3}	$[10^{-5}, 10^{-4}]$
	5.0	2.0	5.10×10^{-1}	2.5	-1.46 ± 2.65×10^{-3}	$[10^{-5}, 10^{-4}]$

Shown in Fig. 3.18 is the temporal evolution of the apex (a) displacement $h_o - h(0,t)$, (b) height $h(0,t)$ and velocity magnitude $|\vec{u}|(0,t)$ for the sampled systems. Fig. 3.18(a) shows that the sampled early stage $h_o - h(0,t)$ evolution possess a power law dependence of $\sim t^2$, which corresponds to the $|\vec{u}|(0,t) = |\partial h(0,t)/\partial t|$ dependence of $\sim t$ in the same time

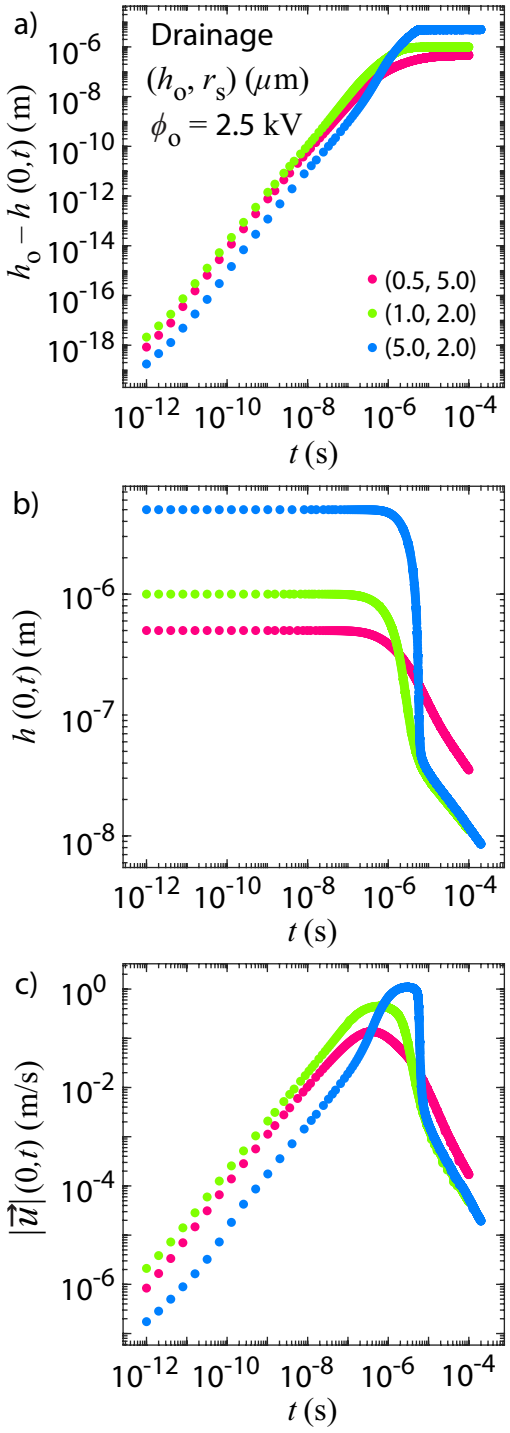

Figure 3.18: Temporal evolution of drainage mode apex (a) $h_o - h(0,t)$, (b) $h(0,t)$ and (c) $|\vec{u}|(0,t)$ for selected (h_o, r_s) combinations with $\phi_o = 2.5$ kV.

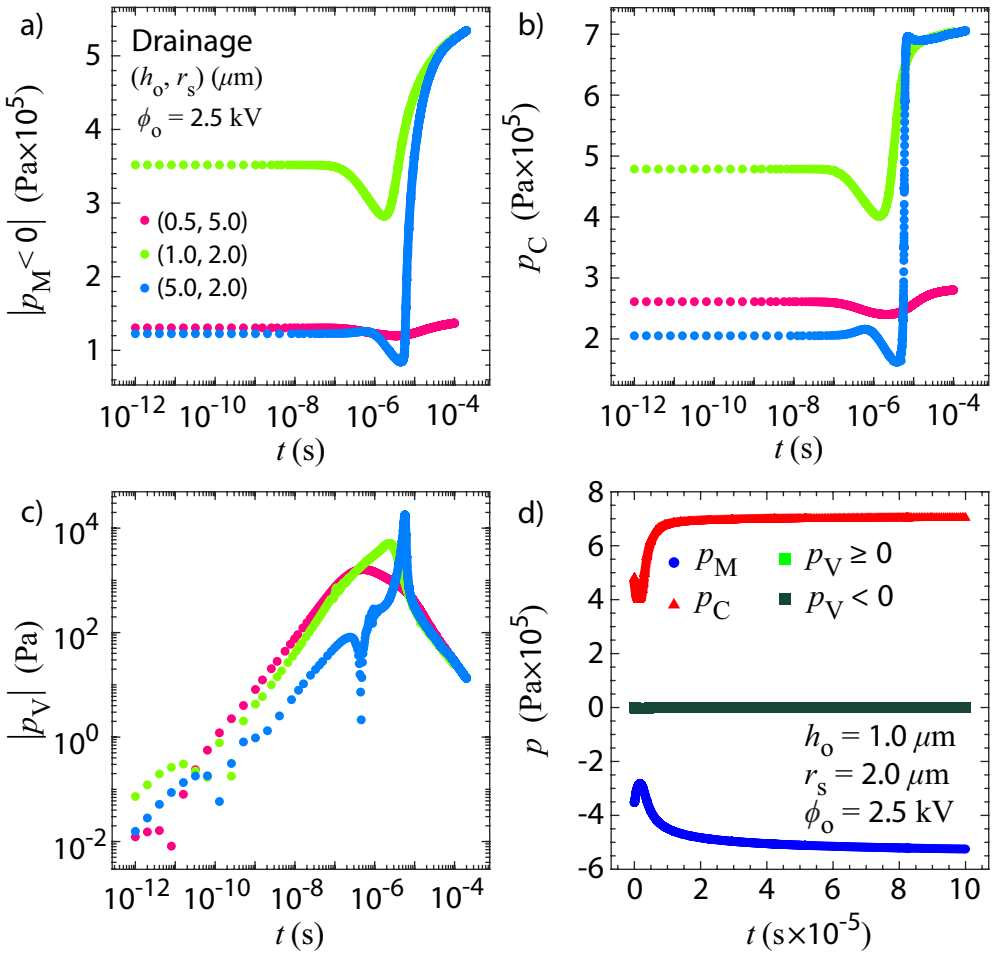

Figure 3.19: Temporal evolution of drainage mode apex pressure magnitudes (a) $|p_M|$, (b) p_C, (c) $|p_V|$ for selected (h_o, r_s) combinations with $\phi_o = 2.5$ kV. (d) Temporal evolution of the apex pressures p_M, p_C and p_V for a selected (h_o, r_s, ϕ_o) combination.

frame shown in Fig. 3.18(c). The power law exponents as listed in Table 3.4 indeed possess small fitting uncertainties and are robust as indicated by the lengthy fitting t interval. These dependencies arise due to the fact that the magnitudes of the apex Maxwell pressure p_M and capillary pressure p_C as shown in Fig. 3.19(a)-(b) are practically constant over the same interval, which sets a time independent and constant acceleration at the apex. Though the viscous pressure p_V evolves during the time frame as shown in Fig. 3.19(c), its magnitude is orders of magnitude smaller than the other two contributions. Fig. 3.18(b) shows that the apex height $h(0,t)$ seems to exhibit additional power law dependencies during the late stages of drainage simulated. This is observed after most of the apex bulk has drained from the microemitter apex. The exponents for $h(0,t)$ are again consistent with those found for $|\vec{u}|(0,t) = \partial h/\partial t$ over the same interval as shown in Table 3.4. No power laws could be found for $|p_M|$, p_C, $|p_V|$ or the total apex pressure p during the same time interval, however.

Fig. 3.19(d) lastly presents the apex pressure evolution for the selected drainage case. As already shown in Fig. 3.19(a)-(b), the apex p_M and p_C magnitudes slightly decrease away from the early stage evolution before increasing. The increase occurs as drainage reduces liquid thickness such that the liquid apex curvature radius $r_s + h_o$ decreases, which in turn increases the mean curvature $\mathcal{K}_h$ and the derived electric field $E \sim \phi_o/(r_s + h_o)$. However, during the simulated time interval, p_C is always stronger than p_M to encode the drainage. The viscous pressure p_V is also found to be negatively signed during the simulated interval for the shown example, which means it aids the always negative p_M to act against the dominant p_C and the resultant drainage.

3.5.2 Axial mode apex evolution

This section describes the results of the axial mode protrusion apex evolution, where all quantities shown have been evaluated at the developing axial protrusion apex $h(0,t)$. Table 3.5 presents the sampled (h_o, r_s, ϕ_o) combinations along with evaluated apex quantities and extracted power law exponents.

Table 3.5: Axial mode apex quantity power law exponents. Listed quantities are the tracked quantity, h_o, r_s, aspect ratio squared $[h_o/(r_s+h_o)]^2$, ϕ_o, power law exponent (i.e. quantities $\sim t^\alpha$ where α is the exponent) with least squares fitting uncertainties and fitting t interval.

Quantity	h_o (μm)	r_s (μm)	$\left(\frac{h_o}{r_s+h_o}\right)^2$	ϕ_o (kV)	Power law exponent	Fitting t interval (s)
$h(0,t)-h_o$	0.1	1.0	8.26×10^{-3}	2.5	$1.91 \pm 1.15\times10^{-2}$	$[10^{-12}, 10^{-8}]$
	0.2	1.0	2.78×10^{-2}	2.5	$1.93 \pm 8.06\times10^{-3}$	$[10^{-12}, 10^{-8}]$
	0.5	1.0	1.11×10^{-1}	2.5	$1.95 \pm 8.20\times10^{-3}$	$[10^{-12}, 10^{-8}]$
	1.0	0.1	8.26×10^{-1}	2.5	$1.95 \pm 6.48\times10^{-3}$	$[10^{-12}, 10^{-8}]$
	2.0	0.1	9.07×10^{-1}	2.5	$1.95 \pm 7.52\times10^{-3}$	$[10^{-12}, 10^{-8}]$
	5.0	0.1	9.61×10^{-1}	2.5	$1.97 \pm 8.91\times10^{-3}$	$[10^{-12}, 10^{-8}]$
$\lvert\vec{u}\rvert(0,t)$	0.1	1.0	8.26×10^{-3}	2.5	$0.93 \pm 5.55\times10^{-3}$	$[10^{-12}, 10^{-8}]$
	0.2	1.0	2.78×10^{-2}	2.5	$0.97 \pm 3.09\times10^{-3}$	$[10^{-12}, 10^{-8}]$
	0.5	1.0	1.11×10^{-1}	2.5	$0.99 \pm 1.50\times10^{-3}$	$[10^{-12}, 10^{-8}]$
	1.0	0.1	8.26×10^{-1}	2.5	$1.00 \pm 1.96\times10^{-4}$	$[10^{-12}, 10^{-8}]$
	2.0	0.1	9.07×10^{-1}	2.5	$1.00 \pm 5.48\times10^{-4}$	$[10^{-12}, 10^{-8}]$
	5.0	0.1	9.61×10^{-1}	2.5	$1.00 \pm 3.16\times10^{-4}$	$[10^{-12}, 10^{-8}]$
p_V^{apex}	0.1	1.0	8.26×10^{-3}	2.5	$0.97 \pm 8.34\times10^{-3}$	$[10^{-10}, 10^{-8}]$
	0.2	1.0	2.78×10^{-2}	2.5	$0.99 \pm 4.99\times10^{-3}$	$[10^{-10}, 10^{-8}]$
	0.5	1.0	1.11×10^{-1}	2.5	$0.95 \pm 5.70\times10^{-3}$	$[10^{-10}, 10^{-8}]$
	1.0	0.1	8.26×10^{-1}	2.5	$0.98 \pm 2.41\times10^{-3}$	$[10^{-10}, 10^{-8}]$
	2.0	0.1	9.07×10^{-1}	2.5	$0.96 \pm 7.65\times10^{-3}$	$[10^{-10}, 10^{-8}]$
	5.0	0.1	9.61×10^{-1}	2.5	$0.99 \pm 1.94\times10^{-3}$	$[10^{-10}, 10^{-8}]$

Shown in Fig. 3.20 is the temporal evolution of the apex (a) displacement $h(0,t) - h_o$,

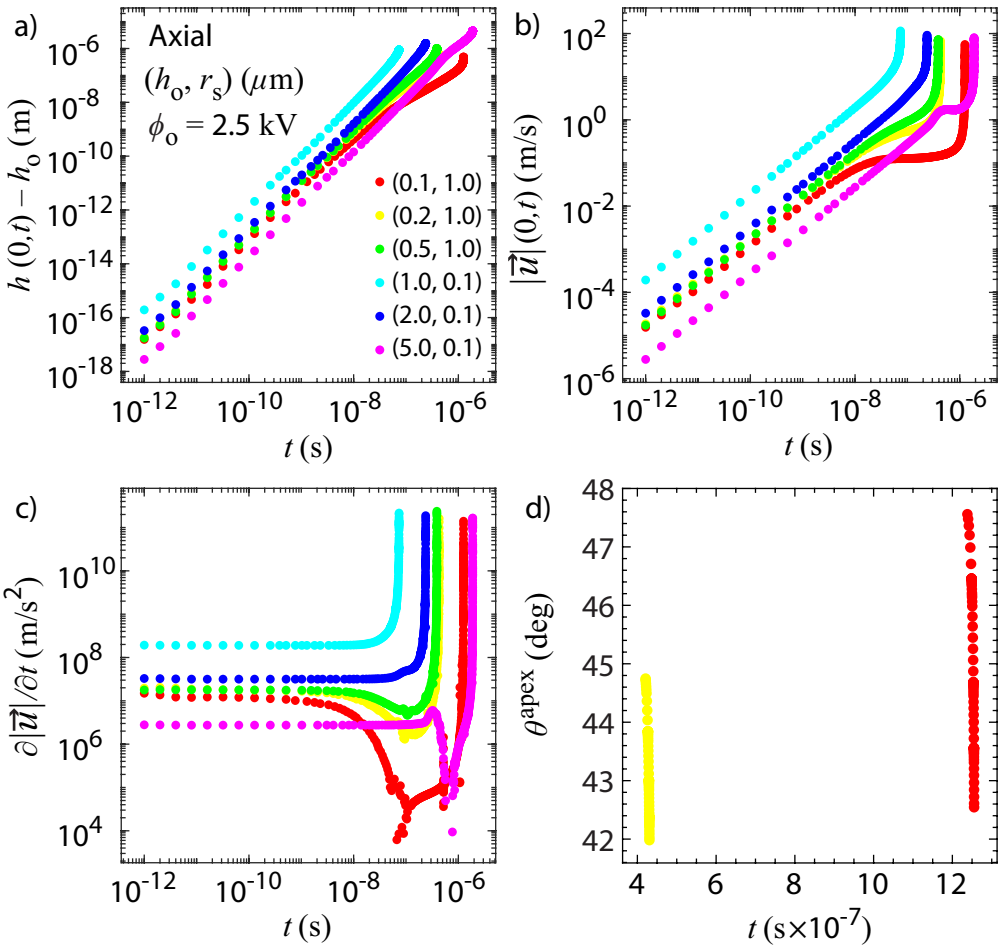

Figure 3.20: Temporal evolution of axial mode apex (a) $h(0,t)-h_o$, (b) $|\vec{u}|(0,t)$, (c) $\partial|\vec{u}|/\partial t$ and (d) θ^{apex} for selected (h_o, r_s) combinations with ϕ_o = 2.5 kV.

(b) velocity magnitude $|\vec{u}|(0,t)$, (c) acceleration $\partial|\vec{u}|/\partial t$ and (d) half angle θ^{apex} for the sampled systems. Fig. 3.20(a) and Table 3.5 show that the sampled early stage $h(0,t) - h_o$ evolution again exhibits a robust power law dependence of $\sim t^2$, which corresponds to the $|\vec{u}|(0,t) =\sim t$ and $\partial|\vec{u}|/\partial t \sim 1$ dependencies in the same time frame shown in Fig. 3.20(b)-(c). These dependencies again arise due to the practically constant apex Maxwell pressure p_M and capillary pressure p_C magnitudes in time as shown in Fig. 3.21(a)-(b). The viscous pressure magnitude $|p_V|$ as shown in Fig. 3.21(c) also increases at a power law dependence $\sim t$ during the early stage growth, which is explained by the fact that at $h(0,t)$, $p_V(0,t) \sim \partial w/\partial z$ such that $p_V \sim |\vec{u}|(0,t) \sim t$. The pressure is also found to be positive for most of the evolution to act against p_M driving the protrusion development, but is able to switch signs during the late stage development as indicated in Fig. 3.21(d) for a selected case.

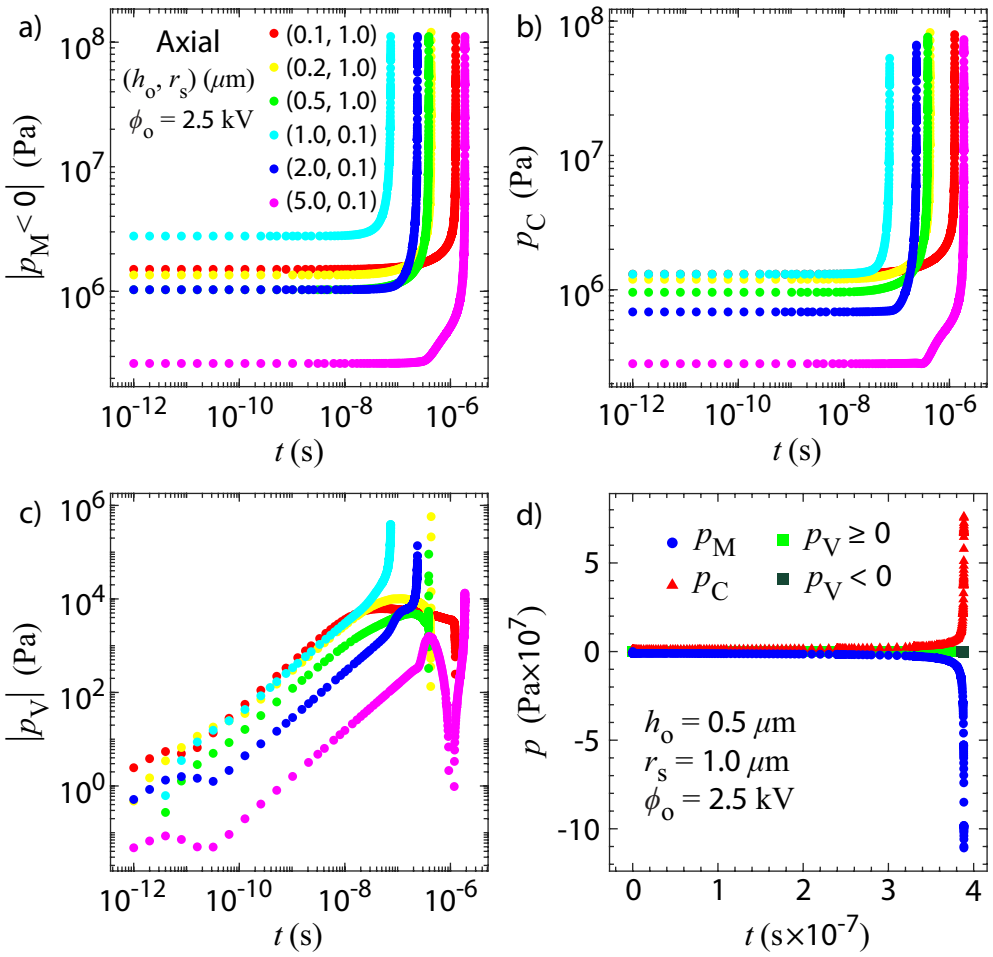

Figure 3.21: Temporal evolution of axial mode apex pressure magnitudes (a) $|p_M|$, (b) p_C, (c) $|p_V|$ for selected (h_o, r_s) combinations with $\phi_o = 2.5$ kV. (d) Temporal evolution of the apex pressures p_M, p_C and p_V for a selected (h_o, r_s, ϕ_o) combination.

The late stage growth exhibited by $|\vec{u}|(0,t)$, $\partial|\vec{u}|/\partial t$, $|p_M|$ and p_C evolutions is shown to be rapidly accelerating with enhancements at rates far greater than power law growths observed for the early stage growth. This is also indicated by the rapidly decreasing apex angle θ^{apex} evolution in Fig. 3.20(d) for the sampled systems that yielded extraction of θ^{apex}. The apex pressure evolution shown in Fig. 3.21(d) for a select case also confirms the rapidly accelerating p_M and p_C enhancement at the late time growth. This behavior is highly suggestive of self-similar dynamics originally predicted by Zubarev [165] to govern the late stage apex development and is further investigated in Ch. 5. The behavior for the evolution in between the early and late stage regimes is found to be variable as the apices for some systems are found to exhibit a decreasing acceleration. This was found to occur due to a reduction that could arise in the difference in the magnitudes between the always negative

p_M and positive p_C over the same time interval, which encodes a reduced acceleration. Such reduction was also found to be able to occur regardless of whether the initially wetted liquid is thin or thick as it occurs for the smallest and largest ratios of $[h_o/(r_s + h_o)]^2$ sampled in the plots.

3.5.3 Coronal mode apex evolution

This section describes the results of the coronal mode protrusion apex evolution, where all quantities shown have been evaluated at the developing coronal protrusion apex $h(r^{apex}, t)$. Table 3.6 presents the sampled (h_o, r_s, ϕ_o) combinations along with evaluated apex quantities and extracted power law exponents. Notably, the coronal mode in the conducted simulations was only found to occur for $h_o/r_s > 1$ or $[h_o/(r_s + h_o)]^2 > 0.25$.

Table 3.6: Coronal mode apex quantity power law exponents. Listed quantities are the tracked quantity, h_o, r_s, aspect ratio squared $[h_o/(r_s + h_o)]^2$, ϕ_o, power law exponent (i.e. quantities $\sim t^\alpha$ where α is the exponent) with least squares fitting uncertainties and fitting t interval.

Quantity	h_o (μm)	r_s (μm)	$\left(\frac{h_o}{r_s + h_o}\right)^2$	ϕ_o (kV)	Power law exponent	Fitting t interval (s)
$h(r^{apex}, t) - h(r^{apex}, 0)$	5.0	2.0	5.10×10^{-1}	7.5	$1.96 \pm 9.98{\times}10^{-3}$	$[10^{-12}, 10^{-7}]$
	5.0	0.5	8.26×10^{-1}	7.5	$1.96 \pm 9.09{\times}10^{-3}$	$[10^{-12}, 10^{-7}]$
	5.0	0.1	9.61×10^{-1}	7.5	$1.96 \pm 8.58{\times}10^{-3}$	$[10^{-12}, 10^{-7}]$
$\lvert\vec{u}\rvert^{apex}$	5.0	2.0	5.10×10^{-1}	7.5	$1.00 \pm 2.20{\times}10^{-4}$	$[10^{-12}, 10^{-7}]$
	5.0	0.5	8.26×10^{-1}	7.5	$1.00 \pm 1.42{\times}10^{-4}$	$[10^{-12}, 10^{-7}]$
	5.0	0.1	9.61×10^{-1}	7.5	$1.00 \pm 8.80{\times}10^{-5}$	$[10^{-12}, 10^{-7}]$
$\lvert p_V^{apex}\rvert$	5.0	2.0	5.10×10^{-1}	7.5	$0.98 \pm 5.91{\times}10^{-4}$	$[10^{-10}, 10^{-7}]$
	5.0	0.5	8.26×10^{-1}	7.5	$0.94 \pm 4.51{\times}10^{-3}$	$[10^{-10}, 10^{-7}]$
	5.0	0.1	9.61×10^{-1}	7.5	$0.98 \pm 1.62{\times}10^{-3}$	$[10^{-10}, 10^{-7}]$

Shown in Fig. 3.22 is the temporal evolution of the apex (a) displacement $h(r^{apex}, t) - h(r^{apex}, 0)$, (b) velocity magnitude $|\vec{u}|^{apex}$ and (c) $\partial|\vec{u}|^{apex}/\partial t$ for the sampled systems. The black marker indicates the time at which the coronal protrusion apex can start to be identified in $p_M(r, t)$ as a non-axial global minimum. It can be seen that the coronal protrusion indeed only visibly develops in the late stage development, which illustrates the highly dynamic nature of the EHD mode generation. Thus, the tracked quantities prior to the marked times have been evaluated at $h(0, t)$, which again exhibits robust power law dependencies (Table 3.6) consistent with those found in the sampled axial mode systems ($h(r^{apex}, t) - h(r^{apex}, 0) \sim t^2$, $|\vec{u}|^{apex} \sim t$ and $|p_V^{apex}| \sim t$). The pressure evolution as shown in Fig. 3.23 also exhibits consistent behavior as those found in the axial mode counterparts, with the extremely rapid pressure enhancement observed after the development of the

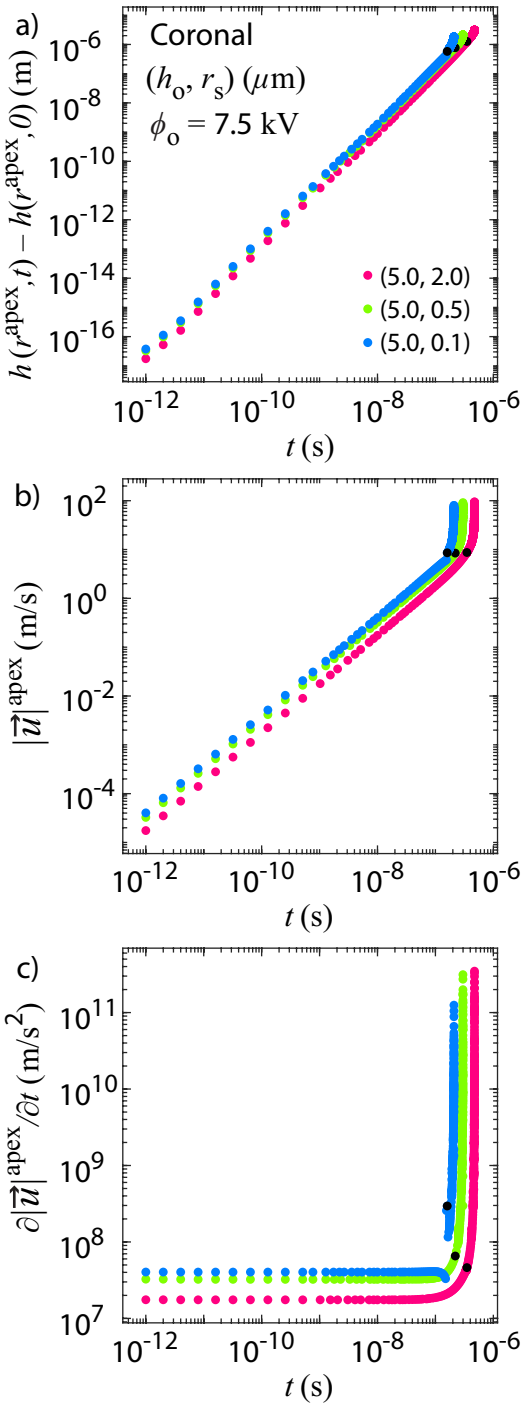

Figure 3.22: Temporal evolution of coronal mode protrusion apex (a) $h(r^{apex}, t) - h(r^{apex}, 0)$, (b) $|\vec{u}|(r^{apex}, t)$ and (c) $\partial|\vec{u}|/\partial t$ for selected (h_o, r_s) combinations with ϕ_o = 7.5 kV. Black markers signal t at which the coronal apices can start to be tracked.

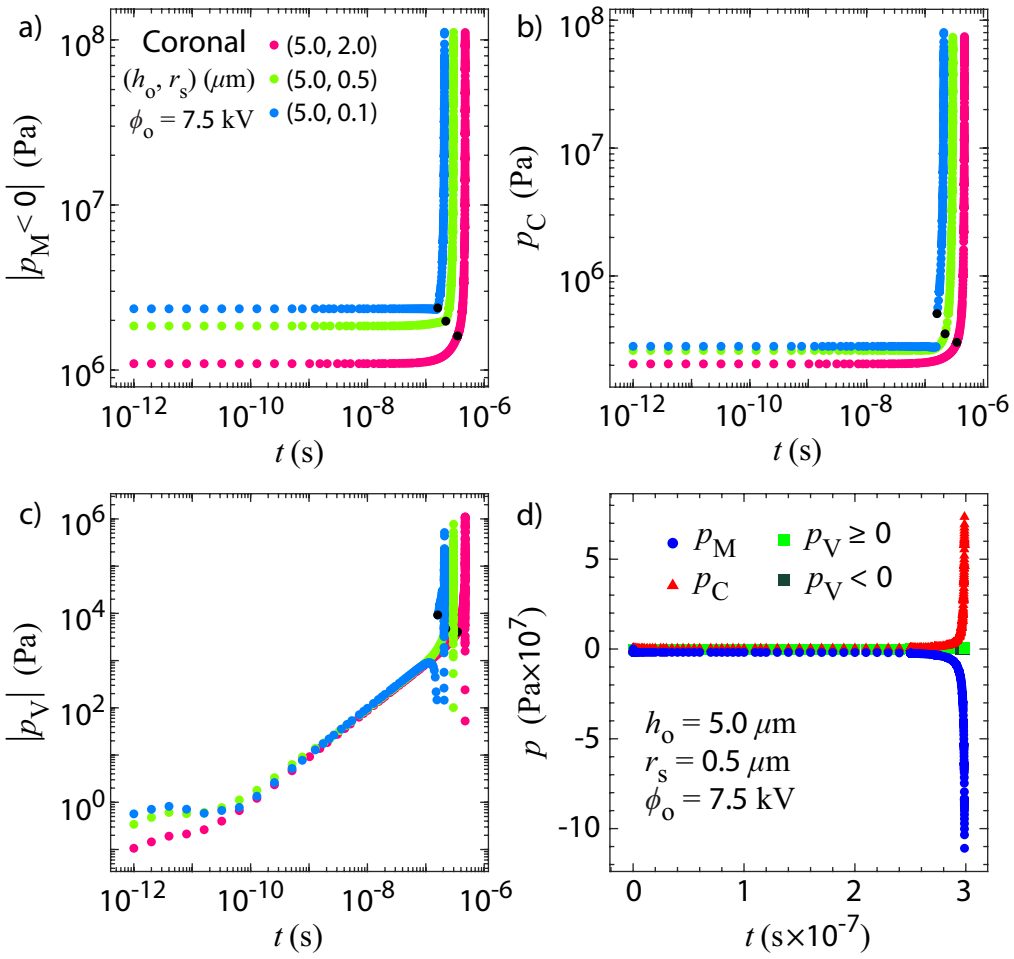

Figure 3.23: Temporal evolution of coronal mode apex pressure magnitudes (a) $|p_M|$, (b) p_C, (c) $|p_V|$ for selected (h_o, r_s) combinations with ϕ_o = 7.5 kV. Black markers signal t at which the coronal apices can start to be tracked. (d) Temporal evolution of the apex pressures p_M, p_C and p_V for a selected (h_o, r_s, ϕ_o) combination.

coronal protrusion. This is again suggestive of self-similar growth [165] even for the non-axial and asymmetric coronal protrusion apex and is further investigated in Ch. 5.

3.5.4 EHD instability mode apex evolution

This section describes the results of the EHD instability mode protrusion apex evolution, where all quantities shown have been evaluated at the developing most prominent protrusion apex $h(r^{apex}, t)$. The evolving protrusion apex r^{apex} is defined as the r coordinate on $h(r, t)$ possessing the global minimum of p_M. Table 3.7 presents the sampled (h_o, r_s, ϕ_o) combinations along with evaluated apex quantities and extracted power law exponents.

Shown in Fig. 3.24 is the temporal evolution of the apex (a) displacement $h(r^{apex}, t)$ –

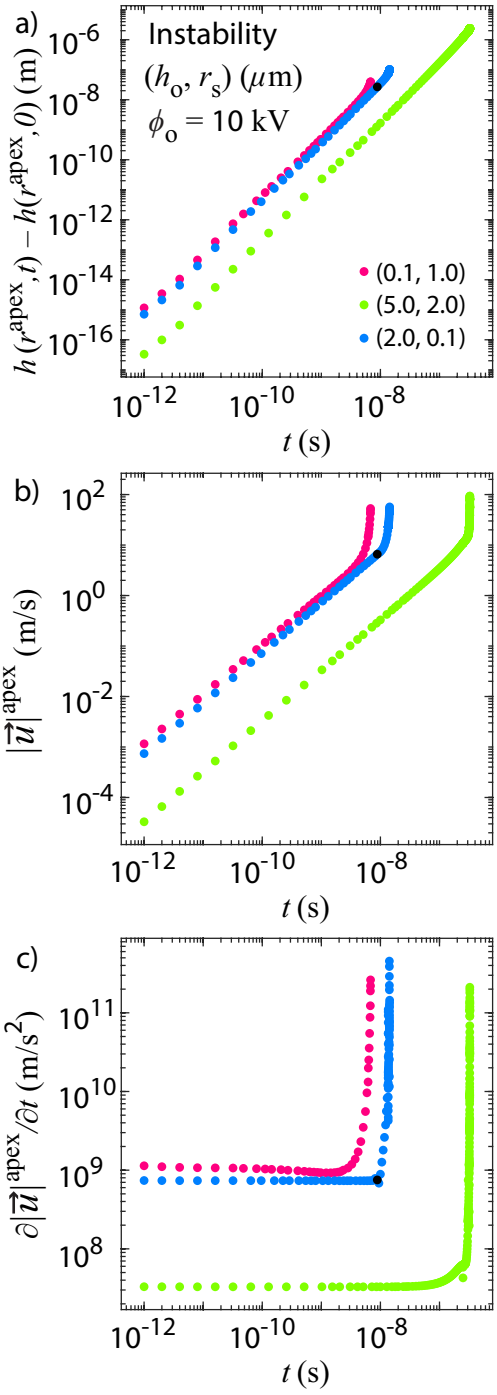

Figure 3.24: Temporal evolution of instability mode most prominent apex (a) $h(r^{apex}, t) - h(r^{apex}, 0)$, (b) $|\vec{u}|(r^{apex}, t)$ and (c) $\partial|\vec{u}|/\partial t$ for selected (h_o, r_s) combinations with $\phi_o = 10$ kV. Black marker signals t at which the most prominent apex can start to be tracked for the non-axial $r_f > 0$ case.

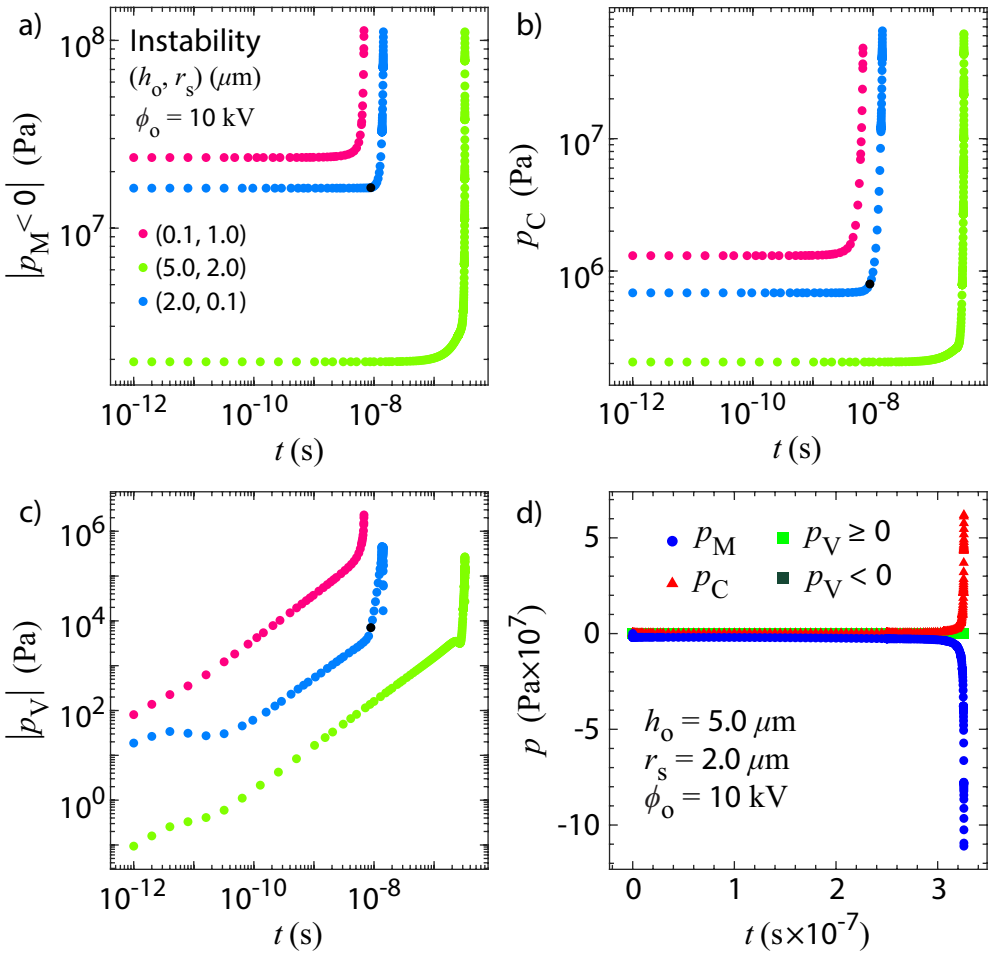

Figure 3.25: Temporal evolution of instability mode most prominent apex pressure magnitudes (a) $|p_M|$, (b) p_C, (c) $|p_V|$ for selected (h_o, r_s) combinations with $\phi_o = 10$ kV. Black marker signals t at which the most prominent apex can start to be tracked for the non-axial $r_f > 0$ case. (d) Temporal evolution of the apex pressures p_M, p_C and p_V for a selected (h_o, r_s, ϕ_o) combination.

$h(r^{apex}, 0)$, (b) velocity magnitude $|\vec{u}|^{apex}$ and (c) $\partial|\vec{u}|^{apex}/\partial t$ for the sampled systems. Fig. 3.25 presents the evolution of the apex (a) $|p_M|$, (b) p_C and (c) $|p_V|$ for the sampled systems and (d) evolution of the three pressures for a select example. The quantities all exhibit behaviors similar to those found in the axial and coronal modes with consistent power law exponents (Table 3.7) of $h(r^{apex}, t) - h(r^{apex}, 0) \sim t^2$, $|\vec{u}|^{apex} \sim t$ and $|p_V^{apex}| \sim t$. The consistency in the early stage power law growth and late stage extreme enhancement is found regardless of the axial/non-axialness of the most prominent protrusion apex and the presence of additional protrusions. The self similarity of the late stage evolution for the EHD instability most prominent protrusion is further investigated in Ch. 5.

Table 3.7: Instability mode apex quantity power law exponents. Listed quantities are the tracked quantity, h_o, r_s, aspect ratio squared $[h_o/(r_s + h_o)]^2$, ϕ_o, power law exponent (i.e. quantities $\sim t^\alpha$ where α is the exponent) with least squares fitting uncertainties and fitting t interval.

Quantity	h_o (μm)	r_s (μm)	$\left(\frac{h_o}{r_s+h_o}\right)^2$	ϕ_o (kV)	Power law exponent	Fitting t interval (s)
$h(r^{apex},t) - h(r^{apex},0)$	0.1	1.0	8.26×10^{-3}	10	$1.91 \pm 9.44\times10^{-3}$	$[10^{-12}, 10^{-9}]$
	5.0	2.0	5.10×10^{-1}	10	$1.97 \pm 1.77\times10^{-2}$	$[10^{-12}, 10^{-9}]$
	2.0	0.1	9.07×10^{-1}	10	$1.93 \pm 1.10\times10^{-2}$	$[10^{-12}, 10^{-9}]$
$\lvert\vec{u}\rvert^{apex}$	0.1	1.0	8.26×10^{-3}	10	$0.98 \pm 1.01\times10^{-3}$	$[10^{-12}, 10^{-9}]$
	5.0	2.0	5.10×10^{-1}	10	$1.00 \pm 4.30\times10^{-5}$	$[10^{-12}, 10^{-9}]$
	2.0	0.1	9.07×10^{-1}	10	$1.00 \pm 9.09\times10^{-5}$	$[10^{-12}, 10^{-9}]$
$\lvert p_V^{apex}\rvert$	0.1	1.0	8.26×10^{-3}	10	$1.00 \pm 5.94\times10^{-4}$	$[10^{-10}, 10^{-9}]$
	5.0	2.0	5.10×10^{-1}	10	$0.98 \pm 3.99\times10^{-3}$	$[10^{-10}, 10^{-9}]$
	2.0	0.1	9.07×10^{-1}	10	$0.94 \pm 1.02\times10^{-2}$	$[10^{-10}, 10^{-9}]$

3.6 Mode diagram

The multiplicity of EHD modes has been obtained just by varying h_o, r_s and ϕ_o despite the lack of local trigger sites on the initially smooth and uniformly wetted liquid surface and its $\mathcal{K}_h$, which suggests a strong influence of key initial conditions on the mode generation. To probe the influence, the dimensional governing equations and boundary conditions (Sec. 2.1) were nondimensionalized (Sec. 2.3) using choices of characteristic scales based on key initial conditions. The nondimensionalization yielded two dimensionless numbers in the Reynolds number $\mathsf{Re} = \rho w_c z_c/\mu = \sqrt{\rho\varepsilon_o/2}[\phi_o h_o/\mu(r_s + h_o)]$, which measures the ratio between the Maxwell generated inertia and viscous effects, and electric Weber number $\mathsf{We} = p_c r_c^2/\gamma z_c = \varepsilon_o\phi_o^2/2\gamma h_o$, which measures the ratio between the destabilizing Maxwell effects and the stabilizing capillary effects. They have been used to construct the mode diagram shown in Fig. 3.26. The values of Re and We accessed are $4 \leq \mathsf{Re} \leq 1250$ and $5 \leq \mathsf{We} \leq 24700$, indicating the sweeping nature of conducted simulations.

3.6.1 Shape of the accessed mode space

It can be seen that the accessed mode space in Fig. 3.26 takes a rotated rectangular shape. The dominant dependencies taken by the key nondimensional numbers are $\mathsf{Re} \sim \phi_o h_o/(r_s + h_o)$ and $\mathsf{We} \sim \phi_o^2/h_o$. The rotated orientation is resultant from the difference in ϕ_o dependency as We depends quadratically on ϕ_o whereas Re only depends linearly. Modulating just ϕ_o thereby results in a linear path with slope of 2 in the double logarithmic scale view shown in Fig. 3.26. In contrast, modulating just r_s results in a horizontal path along Re axis as We is independent of r_s. Changing just h_o leads to a largely vertical

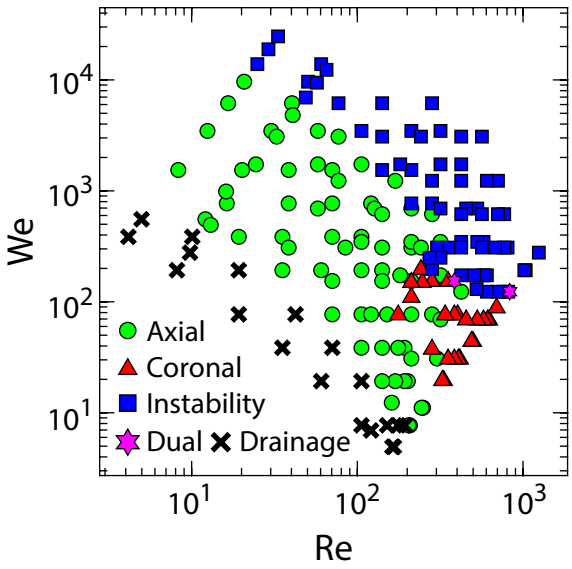

Figure 3.26: Mode diagram constructed from $\mathrm{Re} = \rho w_c z_c/\mu = \sqrt{\frac{\rho\varepsilon_o}{2}}\frac{\phi_o h_o}{\mu(r_s+h_o)}$ and $\mathrm{We} = p_c r_c^2/\gamma z_c = \frac{\varepsilon_o \phi_o^2}{2\gamma h_o}$.

path as $\mathrm{We} \sim 1/h_o$ possesses a much greater response than $\mathrm{Re} \sim h_o/(r_s+h_o)$, especially for $h_o \gg r_s$. Therefore, the systems at larger Re possess larger aspect ratio squared $[h_o/(r_s+h_o)]^2$ than to those at smaller Re. This ratio appears in the nondimensionalized Navier-Stokes equation Eq. 2.56 to quantify the so called "thin" (i.e. $[h_o/(r_s+h_o)]^2 \ll 1$) and "thick" (i.e. $[h_o/(r_s+h_o)]^2 \sim 1$) liquid regimes.

3.6.2 Mode clusters in Re and We

The mode diagram indeed presents strong clustering of the cataloged EHD modes in the constructed Re and We parameter space. The drainage mode is found to be generated for relatively low Re and We space for the set of systems simulated, correctly reflecting the observations on the less inertial flow generated from the weaker applied Maxwell effects relative to the stabilizing capillary effects. The Maxwell effects characterized by $p_M \sim E_c^2$ possessing the characteristic initial liquid apex scale $p_M^o \sim \phi_o^2/(r_s+h_o)^2$ can be reduced by decreasing ϕ_o, which reduces both Re and We, or by increasing $r_s + h_o$. Increasing r_s leads to a reduction in Re, whereas increasing h_o primarily leads to a reduction in We. Although increasing $r_s + h_o$ reduces the stabilizing $p_C^o \sim 1/(r_s+h_o)$, it also reduces the destabilizing $p_M^o \sim 1/(r_s+h_o)^2$ by an additional power, leading to a strong stabilization against protrusion formation. Interestingly, evaluating the actual initial apex pressures $p_C^o = 2\gamma/(r_s+h_o)$ and $p_M = -\varepsilon_o E_o^2/2$ yielded a criterion of $p_C^o > p_M^o$ for drainage system cataloged as intuit from

simple statics considerations.

The instability exhibits a similarly motivated clustering as it is found for the relatively high Re and We space, correctly reflecting the observations on the strongly inertial flow generated from the stronger destabilizing Maxwell effects compared to the stabilizing capillary effects. The Maxwell pressure possessing the characteristic initial liquid apex scale $p_M^o \sim \phi_o^2/(r_s + h_o)^2$ can be enhanced by increasing ϕ_o, which increases both Re and We, or by decreasing $r_s + h_o$. Decreasing r_s leads to an increase in Re, whereas decreasing h_o primarily leads to an increase in We. Although decreasing $r_s + h_o$ increases the stabilizing $p_C^o \sim 1/(r_s + h_o)$, it also enhances the destabilizing $p_M^o \sim 1/(r_s + h_o)^2$ by an additional power, leading to a strong destabilization of the liquid surface. It is interesting to note that the instability mode for the highest Re probed seems to be simply generated above a fixed We ~ 100, unlike the sloped character observed for lower Re.

The axial and coronal modes are generated in the parameter space between the drainage and instability regimes in which the Maxwell effects are strong enough to promote inertia and surface destabilization leading to just a singular liquid protrusion growth. The few dual mode cases reside on the boundary between the instability and single protrusion modes, signaling the dual mode as a transitory state as expected. Though the axial mode is generated for almost all of the parameter space probed, the coronal mode is only found for systems in which relatively stronger inertia is generated for the same strength of surface destabilization. This is especially apparent when Re is probed at fixed We less than approximately 100, as increasing just Re largely leads to drainage then axial and then coronal mode generation. This path is indeed induced when just r_s is made smaller as Re $\sim h_o/(r_s + h_o)$, which leads to larger values of the aspect ratio squared $[h_o/(r_s + h_o)]^2$ probing the relative thickness of the wetted liquid with respect to its apex curvature radius. In fact, the coronal mode for the conducted simulations was only found for systems with $h_o/r_s > 1$ or $[h_o/(r_s + h_o)]^2 > 0.25$ firmly in the thick liquid regime.

This observation indicates that wetting a relatively thicker liquid encodes greater vertical mobility of the liquid bulk to be supplied towards non-axial locations optimal for the coronal mode. Relatively thinner liquids instead encode an initially strongly lateral bulk flow that favorably accumulates supply at $r = 0$ optimal for the axial mode development. These behaviors can be ascertained from the extra $r_c^2/z_c^2 = (r_s + h_o)^2/h_o^2$ dependence of the nondimensionalized r component of the Navier-Stokes equation in Eq. 2.56. The aspect ratio squared need not be counted as a separate parameter, however, as the ratio $h_o/(r_s + h_o)$ and thereby the effects of the relative liquid thickness is included in Re.

3.7 Discussion

This section offers discussion on the importance of the long overlooked parameter h_o, rules of thumb for axial mode generation, additional signatures of mode confinement and consequences of algorithmic and geometric details chosen for the simulations.

3.7.1 Importance of initial liquid thickness

The microemitter apex curvature radius r_s has long been known as the characteristic length scale that strongly governs the LMIS ion emission characteristics, dating back to the current-voltage curves and emission voltage as a function of r_s documented by Wagner and Hall [152] for a liquid gold ion source. Our results indicate that the long overlooked initial liquid thickness h_o is another length scale strongly correlated to the ensuing EHD mode development as variations in h_o have now been shown to be able to drastically alter the generated mode even if r_s and ϕ_o are fixed. Without knowledge of h_o, neither $\mathsf{Re} \sim h_o/(r_s + h_o)$ nor $\mathsf{We} \sim 1/h_o$ could be estimated, which make it impossible to develop the mode diagram to correlate the mode outcome to key system parameters. The development of experimental techniques that can measure the opaque liquid metal layers wetted to highly curved substrates will be crucial for improved experimental reproducibility and extraction for further insight on the resultant mode development.

3.7.2 Rules of thumb for axial mode generation

The results now also provide three rules of thumb to generate the axial mode for such geometries. They are to operate with 1) low ϕ_o, 2) large initial liquid apex radius $r_s + h_o$ and 3) thinly wetted liquid $[h_o/(r_s+h_o)]^2 \ll 1$, which all lead to generation of moderate Re and We as previously discussed. The first two rules are consistent with the operating conditions implemented for real LMIS systems [108] as ϕ_o is typically incrementally increased from zero until the turn-on value is reached and the typically employed values of r_s are of $O(1\ \mu\mathrm{m})$. Though it is claimed that the liquid is supplied to the apex through thin film flow [108], it is unclear whether the third rule is actually met in practice for similar geometries due to reasons discussed in Sec. 3.7.1. An additional complication arises from grooves [10, 119] often etched into the microemitter surface in which liquid can flow via capillary action. Though they are known to improve the stability of continuous ion emission [10, 137, 152], too much supply delivered may lead to a thickly wetted liquid $[h_o/(r_s + h_o)]^2 \sim 1$ found to be favorable for coronal mode development. This again highlights a need for experimental techniques that can accurately measure h_o.

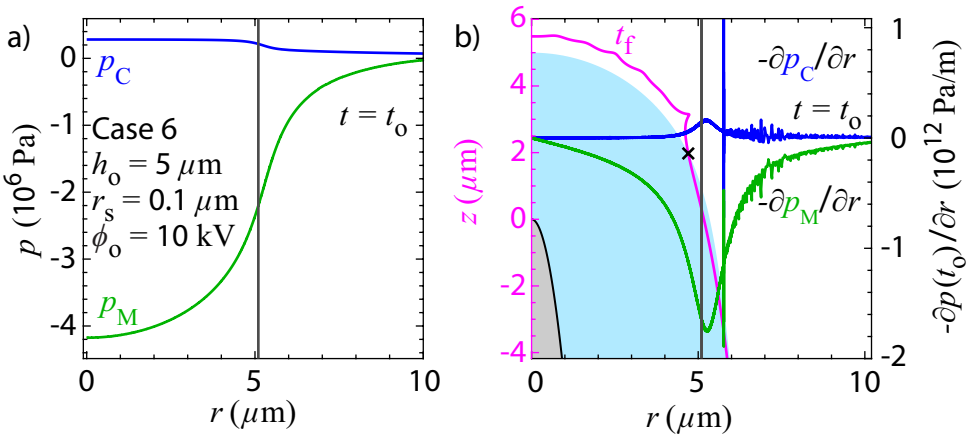

Figure 3.27: Initial $h(r,t_o)$ (a) p_C (blue) and p_M (green) and (b) $\partial p_C/\partial r$ (blue) and $\partial p_M/\partial r$ (green) with $r = r_s + h_o$ (black) overlaid on $h(r,t_f)$ (pink), initial liquid bulk (blue) and microemitter (gray) for "Case 6" dual mode example (Fig. 3.16(b)).

3.7.3 Additional initial signatures of mode confinement

All protrusion developing EHD mode generation have been found to be confined within $r \leq r_s + h_o$. The initial $h(r,t_o)$ was shown to possess $\mathcal{K}_h$ and E enhanced within $r \leq r_s + h_o$ to set up favorable initial conditions for mode confinement. As the flow is generated by $-\nabla p$, not p, the initial $-\partial p_C/\partial r = 2\gamma\partial\mathcal{K}_h/\partial r$ and $-\partial p_M/\partial r = [\varepsilon_o\partial(E^2)/\partial r]/2 = \varepsilon_o E\partial E/\partial r$ were also examined to search for signatures that can be correlated with the mode confinement. Fig. 3.27 shows the two pressures and gradients sampled for "Case 6" with the largest r_f and $r_f/(r_s + h_o)$. The deviations found for the initial time gradients, such as the extraneous spike at around $r \approx 6\ \mu$m, were found to be derived from mesh induced errors. Importantly, the locations of the deviations are past the mode generating bulk region such that these numerical deviations do not influence the ensuing dynamics. The Maxwell contribution $-\partial p_M/\partial r$ for such protrusion developing modes prevails to generate an initial net flow towards $r = 0$. While initial p_C and p_M are indeed the strongest at $r = 0$, the inflection points that encode the strongest initial forcing on the surface are located at around the same r and about $r = r_s + h_o$ as indicated by the extrema shown in Fig. 3.27(b). Though the location of the extrema and net initial $\partial p/\partial r$ minimum do not correspond to the final r_f location due to the strongly dynamic nature of the flow, they nevertheless indicate that the initial flow indeed strongly conditions the ensuing mode development to be confined within $r \leq r_s + h_o$.

3.7.4 Consequences of algorithmic and geometric details

This section examines the key algorithmic and geometric choices taken for the presented simulations and discusses the resulting consequences with respect to predictions and real systems.

3.7.4.1 Termination criterion

The simulations were terminated from the criterion set by $E^{apex} \geq 5$ GV/m, which still allowed the study to catalog the EHD mode development. However, it was deemed difficult to advance the simulations further due to the $O(10\,\text{GV/m})$ physical constraint [108] on the onset of ion emission and numerical errors incurred from the rapidly deforming tip elements due to large $|\vec{u}|_f$ and worsening tip resolution as R_f starts to be comparable to the minimum mesh size employed. These restrictions most likely preclude access to the protrusion tip spatiotemporal scales below which Zubarev [166] has recently predicted the onset of viscous dominated protrusion tip self-similar growth. Nevertheless, preliminary analysis indicates that the protrusion tip development accessed by the simulations indeed exhibits self-similarity as expected and is being further investigated for a future study.

3.7.4.2 Gravity and axisymmetry

Gravity was also neglected in the simulations. Had it been included, the Bond number extracted from the mode diagram scaling analysis would have been $\mathsf{Bo} = \rho g h_o / p_c = 2\rho g h_o (r_s + h_o)^2 / \varepsilon_o \phi_o^2$. Evaluating the number for the worst case combination of $h_o = 5$ μm, $r_s = 5$ μm and $\phi_o = 1.5$ kV for the simulated parameters yields the maximum $\mathsf{Bo} = 3\times10^{-6}$, which shows that gravity is indeed negligible for the modeled system over all h_o, r_s and ϕ_o simulated. This indicates that the results are also expected to be applicable for similarly constructed LMIS systems to be operated on ground.

The axisymmetric geometry implies that the coronal and instability modes would manifest as a single and multiple rings around the azimuth. However, it is anticipated that the rings will break up into discrete protrusions in experiments and full 3D simulations modeling the azimuthal degree of freedom due to the strong protrusion surface curvatures.

3.7.4.3 Microemitter shape, roughness and overall configuration

The modeled geometry was set to possess a smooth, parabolic microemitter surface coated with an initially smooth, uniformly thick liquid metal layer and placed in a domain where all parameters other than h_o, r_s and ϕ_o were fixed. In practice, microemitter shapes and

roughness and overall configurations can vary and not be well approximated by the choices taken in the simulations.

LMIS emitters are made from either electrochemically etched tungsten wires [68, 152] or micromachined silicon masks using deep reactive ion etching process [119]. The details of the etching processes can result in widely varying shapes, such as cones [68, 137] and hyperbolas [158], and surface roughness from sub-nanoscale features [158] to microscale grooves [10, 119]. These differences will encode variations in the generated $\mathcal{K}_h$ and vacuum $\vec{E}$ fields and thereby the resultant flow. The wetted liquid may also conform to the individual microemitter roughness if too thin, which will result in local trigger sites encoding non-axial mode development fundamentally different from that simulated here. The dimensions of fixed system parameters could also widely vary to generate $\vec{E}$ fields that further differ from those generated in the current geometry.

Despite these possibilities, the available *in-situ* images [35, 38, 39, 113] of liquid metal wetted microemitter tips prior to protrusion formation show smooth profiles that strongly conform to the overall tip geometry, not to the individual roughness. The tips of tungsten emitters with microscale apex radii typically found for real systems have also been shown to take strongly parabolic [10, 158] shapes resultant from the etching procedure. Even if the general profiles are non-parabolic, they still possess negative, nonuniform curvature maximally negative at the apex such that the general qualities of E enhancement and stabilizing capillary drainage leading to mode confinement for the parabolic microemitter are expected to hold. The initial $\vec{E}$ field lines generated from the initial liquid tip $r \leq r_s + h_o$ have also been shown in Sec. 3.3 to remain strongly collimated even as the fixed system dimensions were varied over values comparable to those taken here. The initial liquid apex E_o is also known to strongly scale as the applied potential divided by the initial liquid apex radius regardless of the detailed shape as long as the surface profile is thin and apex radius is small compared to the liquid apex to extractor gap spacing [84], which are often met in practice. Though the modeled geometry represents just one particular configuration possible for LMIS systems, these considerations suggest that the results may be applicable to a more general class of similarly dimensioned systems possessing curved, smoothly coated emitters.

3.8 Conclusion

The computational simulations described in this work present the spatiotemporal evolution of liquid metal gallium externally wetted to a curved microemitter and placed under an apertured extractor in a geometry with dimensions realistic to microarray LMIS/electrospray

space micropropulsion devices. The rapidly accelerating free surface is tracked by the arbitrary Lagrangian Eulerian finite element method. The stability and convergence of the simulations have been confirmed through mesh and relative tolerance convergence studies. The results reveal development of five different EHD modes categorized as drainage, axial, coronal, instability and dual characterized by the location and number of generated protrusions and modes. This multiplicity is obtained even though the initial liquid surface was always made to smoothly and uniformly coat the curved microemitter surface. Despite the multiplicity, all modes have been found to desirably develop within the liquid tip region $r \leq r_s + h_o$ due to the curvature derived initial pressure and pressure gradient enhancement. The localized mode development leads to desirably collimated final time electric field lines emanating from the protrusions irrespective of the mode. Though it is known that the late time protrusion development undergoes self-similar growth [165] governed by the local conditions, correlations between the final EHD mode development and the key initial liquid apex conditions r_s, ϕ_o and the often overlooked h_o have been extracted from a mode diagram constructed from the Reynolds Re and electric Weber We numbers and additionally supported by the aspect ratio squared $[h_o/(r_s+h_o)]^2$ information. Development of experimental techniques that can accurately measure h_o is anticipated to yield better reproducibility and ultimately lead to greater control over the mode generated for LMIS systems.

3.9 Appendix A: Convergence tests

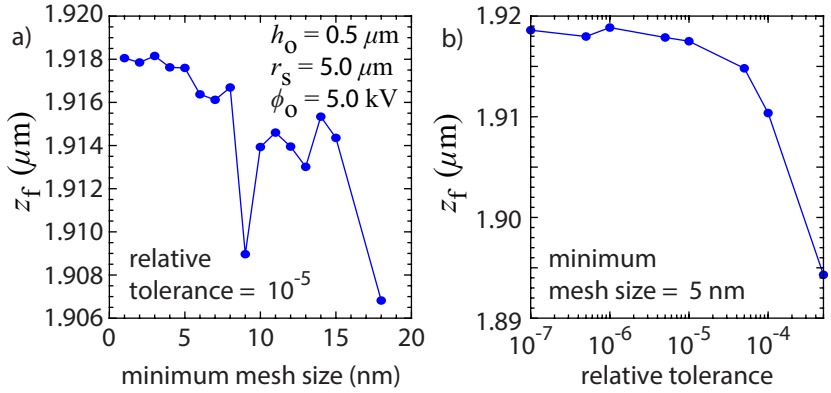

Figure 3.28: Convergence tests of protrusion apex z_f for a LMIS axial mode example with $h_o = 0.5$ μm, $r_s = 5.0$ μm and $\phi_o = 5.0$ kV as (a) minimum mesh size and (b) relative tolerance are changed.

The convergence tests on the protrusion apex z_f are shown in Fig. 3.28 for a selected LMIS axial mode example and on z_f and r_f for a LMIS coronal mode example in Fig. 3.29. The axial mode example z_f achieve good convergence with variations of $O(1$ nm)

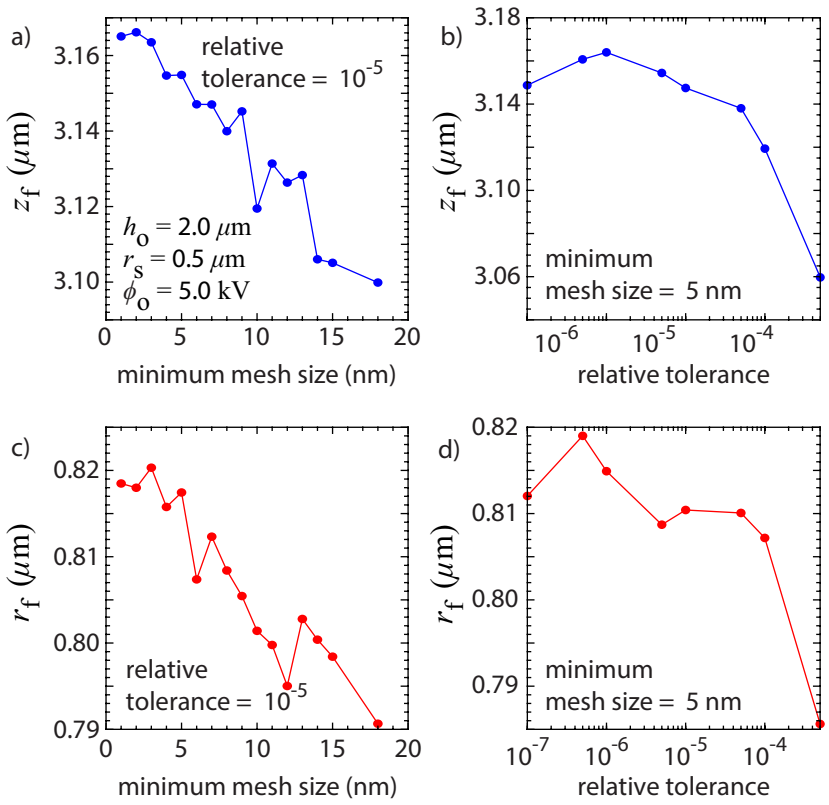

Figure 3.29: Convergence tests of protrusion apex (a)-(b) z_f and (c)-(d) r_f for a LMIS coronal mode example with $h_o = 2.0$ μm, $r_s = 0.5$ μm and $\phi_o = 5.0$ kV as minimum mesh size and relative tolerance are changed.

at the values of the minimum mesh size (5 nm) and relative tolerance (10^{-5}) applied to the simulations. The coronal mode example does posses slightly larger variations of $O(10\text{ nm})$ due to the complications that arise out of the non-axial location of the moving protrusion apex. Still, it can be seen that the apex coordinates r_f and z_f demonstrate good convergence at the values of the two parameters employed in the simulations. A stronger convergence is indeed observed for r_f, which is the much more significant coordinate that determines the axial/non-axialness of the protrusion tip separating the axial/coronal EHD mode. The protrusion apex Maxwell p_M and capillary p_C pressures are also shown in Ch. 5 to undergo self-similar growth marked by power law exponents β_M for p_M and β_C for p_C. The convergence of the two exponents for the same selected examples are additionally shown in Sec. 5.8.

3.10 Appendix B: Tables

The tables in the Appendix contain information about the computational geometry used in this study (Table 3.8), dependence on the initial liquid apex electric field E_o on fixed system

parameters (Table 3.9) and measured quantities extracted from the simulations (Tables 3.10-3.17).

Study	Study Type	Liquid	Emitter	$L_{emitter}$ (μm)	r_s (μm)	$2R_o$ (μm)	R_{ap} (μm)	d_{gap} (μm)	d_{ext} (μm)	ϕ_o (kV)	d_{top} (μm)	ϕ_{top} (V)
Li *et al.* [90]	Exp.	EMI-Im	Porous	150 to 180	5 to 25	450	150	50 to 170	150	-2.75 to 2.75	24000	-20
Dandavino *et al.* [28]	Exp.	EMI-BF_4	Capillary	100		737, 963	74	50	50	0.8		
Lenguito *et al.* [86]	Exp.	EAN	Capillary	60		1000	190		76	1.00 to 7.50		
Guerra-Garcia *et al.* [55]	Exp.	EMI-BF_4	Porous	170	15	450	150	0		-0.95 to 0.95	200	0
Marrese-Reading *et al.* [97, 98]	Exp.	Indium	Solid	300	1 to 3	500	200	54		1.20 to 3.60		
Natisin *et al.* [106]	Exp.	EMI-BF_4	Porous	300	10 to 20	546	254	0	76	-1.84 to 1.84		-40
Asher *et al.* [6]	Sim.	EMI-BF_4	Porous	300	14	1000	254	49	76	$\pm$1.5		
Petro *et al.* [111]	Sim.	EMI-BF_4	Capillary	150	10	600	150	100	30	1.34, 1.82, 2.13	500	
Current Study*	Sim.	Gallium	Solid	200	0.1 to 5.0	800	200	100	50	2.5, 5.0, 7.5, 10	150	-100

Table 3.8: Comparison of key domain dimensions to those documented in selected literature of microarray electrospray/liquid metal space micropropulsion systems. Each study is categorized as either experimental ("Exp.") or computational ("Sim."). Note* that for the current study, additional simulations using $\phi_o = 1.5$ to 20.0 kV were conducted for select cases in order to populate the mode diagram presented in Fig. 3.26(a). The main ϕ_o probed are the values provided in the table. The electrospray liquids are EMI-IM (1-ethyl-3-methylimidazolium bistrifluoromethylsulfonylimide), EMI-BF_4 (1-ethyl-3-methylimidazolium tetrafluoroborate) and EAN (ethylammonium nitrate). $L_{emitter}$ is the microemitter height; $2R_o$ is the microemitter array pitch; R_{ap} is the extractor aperture radius; d_{gap} is the microemitter apex to extractor underside plane gap spacing; d_{ext} is the extractor thickness; d_{top} is the extractor topside plane to ceiling gap spacing; ϕ_{top} is the ceiling potential.

Sampled for Case 2: $r_s = 2$ μm, $h_o = 5$ μm, $\phi_o = 5$ kV

ϕ_{top} (V)	E_o $\left(\frac{\text{GV}}{\text{m}}\right)$	d_{top} (μm)	E_o $\left(\frac{\text{GV}}{\text{m}}\right)$	d_{ext} (μm)	E_o $\left(\frac{\text{GV}}{\text{m}}\right)$	d_{gap} (μm)	E_o $\left(\frac{\text{GV}}{\text{m}}\right)$	R_{ap} (μm)	E_o $\left(\frac{\text{GV}}{\text{m}}\right)$	$L_{emitter}$ (μm)	E_o $\left(\frac{\text{GV}}{\text{m}}\right)$	R_{fillet} (μm)	E_o $\left(\frac{\text{GV}}{\text{m}}\right)$	d_{res} (μm)	E_o $\left(\frac{\text{GV}}{\text{m}}\right)$	R_o (μm)	E_o $\left(\frac{\text{GV}}{\text{m}}\right)$
-2	0.331	5	0.354	2	0.331	5	0.400	5	0.399	20	0.116	0.5	0.332	0.2	0.335	201	0.305
-5	0.331	10	0.351	5	0.331	10	0.396	10	0.399	50	0.196	1.0	0.332	0.5	0.335	210	0.313
-10	0.331	20	0.347	10	0.332	20	0.390	20	0.399	80	0.245	2.0	0.332	1.0	0.335	220	0.318
-20	0.331	50	0.340	20	0.332	50	0.368	50	0.395	100	0.268	5.0	0.332	2.0	0.335	250	0.326
-50	0.331	100	0.334	30	0.332	80	0.346	100	0.378	150	0.308	10.0	0.332	5.0	0.334	300	0.330
-100	0.332	150	0.332	50	0.332	100	0.332	200	0.332	200	0.332	20.0	0.332	10.0	0.332	400	0.332
-200	0.333	200	0.331	70	0.332	200	0.265	250	0.311	300	0.358	30.0	0.332	20.0	0.328	500	0.332
-400	0.335	300	0.330	100	0.331	300	0.216	300	0.293	400	0.371	40.0	0.332	30.0	0.323	1000	0.332
-600	0.338	500	0.329	150	0.331	400	0.180	350	0.278	500	0.377	60.0	0.332	40.0	0.319	2000	0.332
-800	0.340	1000	0.329	200	0.331	500	0.155	390	0.264	1000	0.385	80.0	0.331	50.0	0.314	5000	0.332
-1000	0.342	10000	0.329	500	0.331	1000	0.089	399	0.260	10000	0.386	100.0	0.331	100.0	0.278	10000	0.332

Table 3.9: Dependence of initial liquid apex electric field magnitude E_o on fixed system parameters sampled for "Case 2" in Table 3.3. Each parameter listed is changed one at a time from the values taken in the study that are highlighted in blue. The corresponding E_o values as each parameter is changed are listed in each corresponding column. The varied parameters are the ceiling potential ϕ_{top}, extractor topside plane to ceiling gap spacing d_{top}, extractor thickness d_{ext}, microemitter apex to extractor underside plane gap spacing d_{gap}, aperture radius R_{ap}, microemitter height $L_{emitter}$, fillet radius R_{fillet}, liquid reservoir thickness d_{res}, and lateral domain size (i.e. half of microemitter array pitch) R_o.

Table 3.10: Mode outcomes and measured quantities for systems with $h_o = 0.1$ μm. Listed quantities are h_o, r_s, aspect ratio squared $[h_o/(r_s+h_o)]^2$, ϕ_o, initial liquid apex electric field E_o, mode outcome ("Dr" for drainage, "A" for axial, "C" for coronal, "I" for instability and "Du" for dual), Reynolds number $\mathsf{Re} = \sqrt{\rho\varepsilon_o/2}[\phi_o h_o/\mu(r_s+h_o)]$, electric Weber number $\mathsf{We} = \varepsilon_o\phi_o^2/2\gamma h_o$, termination time t_f, most prominent protrusion apex coordinates r_f and z_f, ratio $r_{rel} = r_f/(r_s+h_o)$, apex curvature radius R_{apex}, apex speed $|\vec{u}|_f$, apex pressure p_f and axial θ_f (local minimum in θ at $t = t_f$ closest to $r = 0$) extracted at r_θ. The dash "-" in θ_f and r_θ entries indicate the axial systems which did not yield measurement of θ_f.

h_o (μm)	r_s	$\left(\frac{h_o}{r_s+h_o}\right)^2$	ϕ_o (kV)	E_o $\left(\frac{\text{GV}}{\text{m}}\right)$	Mode	Re	We	t_f (s)	r_f (μm)	r_{rel}	z_f (μm)	R_{apex} (nm)	u_f $\left(\frac{\text{m}}{\text{s}}\right)$	p_f (MPa)	θ_f (°)	r_θ (μm)
0.1	0.1	2.50×10^{-1}	2.5	2.69	A	106	385	2.00×10^{-9}	0.00	0.00	0.15	41.8	85.3	-76.0	-	-
0.1	0.1	2.50×10^{-1}	5.0	5.36	I	212	1540									
0.1	0.1	2.50×10^{-1}	7.5	8.04	I	318	3470									
0.1	0.1	2.50×10^{-1}	10.0	10.7	-	424	6170									
0.1	0.2	1.11×10^{-1}	2.5	1.80	A	71	385	4.99×10^{-9}	0.00	0.00	0.18	27.0	79.8	-57.1	-	-
0.1	0.2	1.11×10^{-1}	5.0	3.59	I	141	1540	1.49×10^{-9}	0.03	0.09	0.13	66.8	63.8	-90.2		
0.1	0.2	1.11×10^{-1}	7.5	5.37	I	212	3470									
0.1	0.2	1.11×10^{-1}	10.0	7.16	I	282	6170									
0.1	0.5	2.78×10^{-2}	2.5	0.97	A	35	385	3.66×10^{-8}	0.00	0.00	0.29	19.6	63.2	-37.8	46.8	0.07
0.1	0.5	2.78×10^{-2}	5.0	1.93	A	71	1540	6.50×10^{-9}	0.00	0.00	0.18	35.6	82.5	-69.1	63.7	0.05
0.1	0.5	2.78×10^{-2}	7.5	2.89	I	106	3470	3.25×10^{-9}	0.00	0.00	0.14	62.5	68.9	-85.3		
0.1	0.5	2.78×10^{-2}	10.0	3.84	I	141	6170	1.59×10^{-9}	0.07	0.12	0.11	53.0	32.8	-84.4		
0.1	1.0	8.26×10^{-3}	2.5	0.58	A	19	385	1.26×10^{-6}	0.00	0.00	0.58	18.1	55.8	-32.2	42.5	0.09
0.1	1.0	8.26×10^{-3}	5.0	1.16	A	39	1540	2.64×10^{-8}	0.00	0.00	0.24	24.2	74.7	-51.1	55.6	0.05
0.1	1.0	8.26×10^{-3}	7.5	1.74	A	58	3470	1.26×10^{-8}	0.00	0.00	0.19	36.2	82.5	-70.0	64.4	0.05
0.1	1.0	8.26×10^{-3}	10.0	2.32	I	77	6170	6.81×10^{-9}	0.00	0.00	0.14	29.7	53.0	-62.1		
0.1	2.0	2.27×10^{-3}	2.5	0.35	Dr	10	385									
0.1	2.0	2.27×10^{-3}	5.0	0.69	A	20	1540	2.01×10^{-7}	0.00	0.00	0.38	18.1	65.7	-41.3	48.9	0.05
0.1	2.0	2.27×10^{-3}	7.5	1.04	A	30	3470	5.84×10^{-8}	0.00	0.00	0.26	21.9	76.0	-54.7	55.3	0.04
0.1	2.0	2.27×10^{-3}	10.0	1.39	A	40	6170	3.25×10^{-8}	0.00	0.00	0.20	26.3	73.8	-60.2	60.7	0.04
0.1	5.0	3.84×10^{-4}	2.5	0.18	Dr	4	385									
0.1	5.0	3.84×10^{-4}	5.0	0.36	A	8	1540	1.43×10^{-5}	0.00	0.00	1.02	17.6	63.8	-35.6	44.5	0.09
0.1	5.0	3.84×10^{-4}	7.5	0.53	A	12	3470	1.32×10^{-6}	0.00	0.00	0.51	19.4	64.2	-37.0	48.0	0.06
0.1	5.0	3.84×10^{-4}	10.0	0.71	A	17	6170	4.48×10^{-7}	0.00	0.00	0.35	19.3	67.0	-44.1	51.2	0.05

Table 3.11: Mode outcomes and measured quantities for systems with $h_o = 0.2$ μm. Listed quantities are h_o, r_s, aspect ratio squared $[h_o/(r_s+h_o)]^2$, ϕ_o, initial liquid apex electric field E_o, mode outcome ("Dr" for drainage, "A" for axial, "C" for coronal, "I" for instability and "Du" for dual), Reynolds number $\mathsf{Re} = \sqrt{\rho\varepsilon_o/2}[\phi_o h_o/\mu(r_s+h_o)]$, electric Weber number $\mathsf{We} = \varepsilon_o\phi_o^2/2\gamma h_o$, termination time t_f, most prominent protrusion apex coordinates r_f and z_f, ratio $r_{rel} = r_f/(r_s+h_o)$, apex curvature radius R_{apex}, apex speed $|\vec{u}|_f$, apex pressure p_f and axial θ_f (local minimum in θ at $t = t_f$ closest to $r = 0$) extracted at r_θ. The dash "-" in θ_f and r_θ entries indicate the axial systems which did not yield measurement of θ_f.

h_o (μm)	r_s	$\left(\frac{h_o}{r_s+h_o}\right)^2$	ϕ_o (kV)	E_o $\left(\frac{\text{GV}}{\text{m}}\right)$	Mode	Re	We	t_f (s)	r_f (μm)	r_{rel}	z_f (μm)	R_{apex} (nm)	u_f $\left(\frac{\text{m}}{\text{s}}\right)$	p_f (MPa)	θ_f (°)	r_θ (μm)
0.2	0.1	4.44×10^{-1}	2.5	2.04	A	141	193	4.89×10^{-9}	0.00	0.00	0.31	35.1	104	-74.6	-	-
0.2	0.1	4.44×10^{-1}	5.0	4.07	I	282	771	1.21×10^{-9}	0.04	0.13	0.22	49.7	52.7	-92.1		
0.2	0.1	4.44×10^{-1}	7.5	6.10	I	424	1730									
0.2	0.1	4.44×10^{-1}	10.0	8.13	I	565	3080									
0.2	0.2	2.50×10^{-1}	2.5	1.49	A	106	193	8.79×10^{-9}	0.00	0.00	0.34	25.1	93.4	-61.9	-	-
0.2	0.2	2.50×10^{-1}	5.0	2.98	I	212	771	2.79×10^{-9}	0.05	0.12	0.26	38.9	80.6	-82.7		
0.2	0.2	2.50×10^{-1}	7.5	4.46	I	318	1730	0.83×10^{-9}	0.00	0.00	0.21	128	35.3	-102		
0.2	0.2	2.50×10^{-1}	10.0	5.94	I	424	3080									
0.2	0.5	8.16×10^{-2}	2.5	0.88	A	61	193	3.87×10^{-8}	0.00	0.00	0.48	20.8	75.1	-41.9	46.1	
0.2	0.5	8.16×10^{-2}	5.0	1.75	A	121	771	8.60×10^{-9}	0.00	0.00	0.33	38.0	96.2	-72.6	-	-
0.2	0.5	8.16×10^{-2}	7.5	2.62	I	182	1730	4.53×10^{-9}	0.06	0.09	0.27	38.0	71.2	-72.2		
0.2	0.5	8.16×10^{-2}	10.0	3.50	I	242	3080	2.36×10^{-9}	0.10	0.14	0.22	44.4	46.3	-78.9		
0.2	1.0	2.78×10^{-2}	2.5	0.55	A	35	193	4.31×10^{-7}	0.00	0.00	0.81	17.5	67.0	-37.3	42.0	0.16
0.2	1.0	2.78×10^{-2}	5.0	1.10	A	71	771	2.61×10^{-8}	0.00	0.00	0.41	25.2	91.9	-60.3	56.1	0.06
0.2	1.0	2.78×10^{-2}	7.5	1.65	A	106	1730	1.33×10^{-8}	0.00	0.00	0.33	35.1	89.1	-69.3	65.6	0.04
0.2	1.0	2.78×10^{-2}	10.0	2.20	I	141	3080	6.82×10^{-9}	0.00	0.00	0.26	31.1	69.3	-71.8		
0.2	2.0	8.26×10^{-3}	2.5	0.34	Dr	19	193									
0.2	2.0	8.26×10^{-3}	5.0	0.68	A	39	771	1.12×10^{-7}	0.00	0.00	0.59	21.2	78.9	-45.9	50.2	0.07
0.2	2.0	8.26×10^{-3}	7.5	1.01	A	58	1730	4.71×10^{-8}	0.00	0.00	0.44	26.5	86.9	-56.4	57.7	0.05
0.2	2.0	8.26×10^{-3}	10.0	1.35	A	77	3080	3.04×10^{-8}	0.00	0.00	0.39	35.9	95.5	-69.8	63.2	0.06
0.2	5.0	1.48×10^{-3}	2.5	0.18	Dr	8	193									
0.2	5.0	1.48×10^{-3}	5.0	0.35	A	16	771	2.77×10^{-6}	0.00	0.00	1.24	18.6	70.2	-38.7	45.1	0.09
0.2	5.0	1.48×10^{-3}	7.5	0.53	A	24	1730	4.18×10^{-7}	0.00	0.00	0.72	21.0	75.6	-42.9	49.6	0.07
0.2	5.0	1.48×10^{-3}	10.0	0.71	A	33	3080	2.05×10^{-7}	0.00	0.00	0.57	20.7	89.8	-58.5	53.2	0.05

Table 3.12: Mode outcomes and measured quantities for systems with $h_o = 0.5$ μm. Listed quantities are h_o, r_s, aspect ratio squared $[h_o/(r_s+h_o)]^2$, ϕ_o, initial liquid apex electric field E_o, mode outcome ("Dr" for drainage, "A" for axial, "C" for coronal, "I" for instability and "Du" for dual), Reynolds number $\mathsf{Re} = \sqrt{\rho\varepsilon_o/2}[\phi_o h_o/\mu(r_s+h_o)]$, electric Weber number $\mathsf{We} = \varepsilon_o\phi_o^2/2\gamma h_o$, termination time t_f, most prominent protrusion apex coordinates r_f and z_f, ratio $r_{rel} = r_f/(r_s+h_o)$, apex curvature radius R_{apex}, apex speed $|\vec{u}|_f$, apex pressure p_f and axial θ_f (local minimum in θ at $t = t_f$ closest to $r = 0$) extracted at r_θ. The dash "-" in θ_f and r_θ entries indicate the axial systems which did not yield measurement of θ_f.

h_o (μm)	r_s	$\left(\frac{h_o}{r_s+h_o}\right)^2$	ϕ_o (kV)	E_o $\left(\frac{\text{GV}}{\text{m}}\right)$	Mode	Re	We	t_f (s)	r_f (μm)	r_{rel}	z_f (μm)	R_{apex} (nm)	u_f $\left(\frac{\text{m}}{\text{s}}\right)$	p_f (MPa)	θ_f (°)	r_θ (μm)
0.5	0.1	6.94×10^{-1}	2.5	1.25	C	176	77	2.33×10^{-8}	0.10	0.16	0.94	23.4	109	-50.8		
0.5	0.1	6.94×10^{-1}	5.0	2.48	I	353	308	6.49×10^{-9}	0.15	0.25	0.60	28.0	74.2	-59.5		
0.5	0.1	6.94×10^{-1}	7.5	3.72	I	529	694	1.85×10^{-9}	0.04	0.07	0.52	44.3	40.5	-79.2		
0.5	0.1	6.94×10^{-1}	10.0	4.96	I	706	1230	0.50×10^{-9}	0.03	0.05	0.50	437	10.4	-107		
0.5	0.2	5.10×10^{-1}	2.5	1.02	A	151	77	2.72×10^{-8}	0.00	0.00	0.84	24.3	94.3	-51.8	-	-
0.5	0.2	5.10×10^{-1}	5.0	2.04	I	303	308	9.13×10^{-9}	0.00	0.00	0.66	32.6	87.5	-65.9		
0.5	0.2	5.10×10^{-1}	7.5	3.05	I	454	694	3.28×10^{-9}	0.08	0.11	0.54	33.9	55.7	-67.7		
0.5	0.2	5.10×10^{-1}	10.0	4.07	I	605	1230	1.32×10^{-9}	0.10	0.14	0.51	56.1	31.9	-86.0		
0.5	0.5	2.50×10^{-1}	2.5	0.70	A	106	77	7.24×10^{-8}	0.00	0.00	1.02	20.4	81.1	-40.7	-	-
0.5	0.5	2.50×10^{-1}	5.0	1.40	A	212	308	1.81×10^{-8}	0.00	0.00	0.77	36.5	108	-70.3	-	-
0.5	0.5	2.50×10^{-1}	7.5	2.09	I	318	694	9.58×10^{-9}	0.06	0.06	0.65	28.0	80.2	-59.4		
0.5	0.5	2.50×10^{-1}	10.0	2.79	I	424	1230	4.89×10^{-9}	0.24	0.24	0.53	35.2	64.8	-69.3		
0.5	1.0	1.11×10^{-1}	2.5	0.48	A	71	77	3.89×10^{-7}	0.00	0.00	1.49	18.9	72.2	-35.3	-	-
0.5	1.0	1.11×10^{-1}	5.0	0.96	A	141	308	3.82×10^{-8}	0.00	0.00	0.87	27.4	98.7	-57.7	56.6	0.07
0.5	1.0	1.11×10^{-1}	7.5	1.44	A	212	694	2.09×10^{-8}	0.00	0.00	0.77	40.1	106	-74.3	65.0	0.06
0.5	1.0	1.11×10^{-1}	10.0	1.92	I	282	1230	1.24×10^{-8}	0.11	0.08	0.64	24.3	68.7	-51.8		
0.5	2.0	4.00×10^{-2}	2.5	0.31	Dr	42	77									
0.5	2.0	4.00×10^{-2}	5.0	0.63	A	85	308	1.11×10^{-7}	0.00	0.00	1.11	23.2	90.1	-49.0	51.6	0.08
0.5	2.0	4.00×10^{-2}	7.5	0.94	A	127	694	5.38×10^{-8}	0.00	0.00	0.90	30.3	101	-63.3	58.9	0.06
0.5	2.0	4.00×10^{-2}	10.0	1.25	A	169	1230	3.20×10^{-8}	0.00	0.00	0.73	27.3	83.3	-57.8	61.3	0.03
0.5	5.0	8.26×10^{-3}	2.5	0.17	Dr	19	77									
0.5	5.0	8.26×10^{-3}	5.0	0.34	A	39	308	8.33×10^{-7}	0.00	0.00	1.92	20.9	81.0	-42.1	46.6	0.15
0.5	5.0	8.26×10^{-3}	7.5	0.51	A	58	694	2.69×10^{-7}	0.00	0.00	1.30	23.3	90.2	-49.1	51.9	0.08
0.5	5.0	8.26×10^{-3}	10.0	0.68	A	77	1230	1.60×10^{-7}	0.00	0.00	1.08	26.2	95.8	-55.5	56.1	0.06

Table 3.13: Mode outcomes and measured quantities for systems with $h_o = 1.0$ μm. Listed quantities are h_o, r_s, aspect ratio squared $[h_o/(r_s+h_o)]^2$, ϕ_o, initial liquid apex electric field E_o, mode outcome ("Dr" for drainage, "A" for axial, "C" for coronal, "I" for instability and "Du" for dual), Reynolds number $\mathsf{Re} = \sqrt{\rho\varepsilon_o/2}[\phi_o h_o/\mu(r_s+h_o)]$, electric Weber number $\mathsf{We} = \varepsilon_o\phi_o^2/2\gamma h_o$, termination time t_f, most prominent protrusion apex coordinates r_f and z_f, ratio $r_{rel} = r_f/(r_s+h_o)$, apex curvature radius R_{apex}, apex speed $|\vec{u}|_f$, apex pressure p_f and axial θ_f (local minimum in θ at $t = t_f$ closest to $r = 0$) extracted at r_θ. The dash "-" in θ_f and r_θ entries indicate the axial systems which did not yield measurement of θ_f.

h_o (μm)	r_s	$\left(\frac{h_o}{r_s+h_o}\right)^2$	ϕ_o (kV)	E_o $\left(\frac{\text{GV}}{\text{m}}\right)$	Mode	Re	We	t_f (s)	r_f (μm)	r_{rel}	z_f (μm)	R_{apex} (nm)	u_f $\left(\frac{\text{m}}{\text{s}}\right)$	p_f (MPa)	θ_f (°)	r_θ (μm)
1.0	0.1	8.26×10^{-1}	2.5	0.79	A	193	39	7.37×10^{-8}	0.00	0.00	1.89	27.2	115	-57.9	-	-
1.0	0.1	8.26×10^{-1}	5.0	1.58	Du	385	154	2.38×10^{-8}	0.73	0.67	1.09	23.1	87.6	-48.5		
1.0	0.1	8.26×10^{-1}	7.5	2.36	I	578	347	7.26×10^{-9}	0.00	0.00	1.07	31.2	65.0	-64.0		
1.0	0.1	8.26×10^{-1}	10.0	3.15	I	770	617	3.27×10^{-9}	0.21	0.19	1.01	33.9	44.9	-69.0		
1.0	0.2	6.94×10^{-1}	2.5	0.70	A	176	39	8.05×10^{-8}	0.00	0.00	1.72	22.2	91.7	-46.2	-	-
1.0	0.2	6.94×10^{-1}	5.0	1.39	C	353	154	3.10×10^{-8}	0.57	0.48	1.32	23.1	95.0	-48.9		
1.0	0.2	6.94×10^{-1}	7.5	2.08	I	529	347	9.88×10^{-9}	0.00	0.00	1.11	31.3	73.9	-64.0		
1.0	0.2	6.94×10^{-1}	10.0	2.77	I	706	617	4.51×10^{-9}	0.16	0.13	1.03	28.6	49.5	-60.3		
1.0	0.5	4.44×10^{-1}	2.5	0.54	A	141	39	1.65×10^{-7}	0.00	0.00	1.94	20.5	81.8	-40.9	-	-
1.0	0.5	4.44×10^{-1}	5.0	1.07	C	282	154	4.66×10^{-8}	0.15	0.10	1.67	25.5	109	-54.4		
1.0	0.5	4.44×10^{-1}	7.5	1.60	I	424	347	2.26×10^{-8}	0.09	0.06	1.31	24.3	85.3	-51.8		
1.0	0.5	4.44×10^{-1}	10.0	2.13	I	565	617	1.06×10^{-8}	0.12	0.08	1.11	22.1	58.0	-46.3		
1.0	1.0	2.50×10^{-1}	2.5	0.40	A	106	39	7.13×10^{-7}	0.00	0.00	2.55	19.7	74.9	-37.7	-	-
1.0	1.0	2.50×10^{-1}	5.0	0.80	A	212	154	6.79×10^{-8}	0.00	0.00	1.63	27.4	103	-58.1	56.1	0.07
1.0	1.0	2.50×10^{-1}	7.5	1.20	A	318	347	3.90×10^{-8}	0.00	0.00	1.49	36.4	112	-70.2	64.5	0.05
1.0	1.0	2.50×10^{-1}	10.0	1.60	I	424	617	2.25×10^{-8}	0.00	0.00	1.25	31.5	88.7	-64.2		
1.0	2.0	1.11×10^{-1}	2.5	0.28	Dr	71	39									
1.0	2.0	1.11×10^{-1}	5.0	0.56	A	141	154	1.50×10^{-7}	0.00	0.00	1.89	24.0	94.8	-51.5	52.0	0.09
1.0	2.0	1.11×10^{-1}	7.5	0.84	A	212	347	7.62×10^{-8}	0.00	0.00	1.63	29.5	106	-61.3	59.0	0.06
1.0	2.0	1.11×10^{-1}	10.0	1.12	A	282	617	4.46×10^{-8}	0.00	0.00	1.35	29.2	93.0	-61.2	60.4	0.04
1.0	5.0	2.78×10^{-2}	2.5	0.16	Dr	35	39									
1.0	5.0	2.78×10^{-2}	5.0	0.33	A	71	154	7.32×10^{-7}	0.00	0.00	2.87	21.2	86.3	-43.5	47.6	0.14
1.0	5.0	2.78×10^{-2}	7.5	0.49	A	106	347	2.79×10^{-7}	0.00	0.00	2.11	24.5	96.7	-52.0	53.0	0.07
1.0	5.0	2.78×10^{-2}	10.0	0.65	A	141	617	1.72×10^{-7}	0.00	0.00	1.81	27.1	100	-57.8	56.5	0.06

Table 3.14: Mode outcomes and measured quantities for systems with $h_o = 2.0$ μm. Listed quantities are h_o, r_s, aspect ratio squared $[h_o/(r_s+h_o)]^2$, ϕ_o, initial liquid apex electric field E_o, mode outcome ("Dr" for drainage, "A" for axial, "C" for coronal, "I" for instability and "Du" for dual), Reynolds number $\mathsf{Re} = \sqrt{\rho\varepsilon_o/2}[\phi_o h_o/\mu(r_s+h_o)]$, electric Weber number $\mathsf{We} = \varepsilon_o\phi_o^2/2\gamma h_o$, termination time t_f, most prominent protrusion apex coordinates r_f and z_f, ratio $r_{rel} = r_f/(r_s+h_o)$, apex curvature radius R_{apex}, apex speed $|\vec{u}|_f$, apex pressure p_f and axial θ_f (local minimum in θ at $t = t_f$ closest to $r = 0$) extracted at r_θ. The dash "-" in θ_f and r_θ entries indicate the axial systems which did not yield measurement of θ_f.

h_o (μm)	r_s	$\left(\frac{h_o}{r_s+h_o}\right)^2$	ϕ_o (kV)	E_o $\left(\frac{\text{GV}}{\text{m}}\right)$	Mode	Re	We	t_f (s)	r_f (μm)	r_{rel}	z_f (μm)	R_{apex} (nm)	u_f $\left(\frac{\text{m}}{\text{s}}\right)$	p_f (MPa)	θ_f (°)	r_θ (μm)
2.0	0.1	9.07×10^{-1}	2.5	0.48	A	202	19	2.37×10^{-7}	0.00	0.00	3.54	21.7	91.2	-45.0	-	-
2.0	0.1	9.07×10^{-1}	5.0	0.96	C	403	77	8.02×10^{-8}	1.61	0.77	2.16	18.8	85.4	-34.7		
2.0	0.1	9.07×10^{-1}	7.5	1.44	I	605	173	3.37×10^{-8}	0.60	0.29	2.20	20.0	65.7	-38.5		
2.0	0.1	9.07×10^{-1}	10.0	1.92	I	807	308	1.43×10^{-8}	0.32	0.15	2.08	22.0	56.9	-45.7		
2.0	0.2	8.26×10^{-1}	2.5	0.45	A	193	19	2.77×10^{-7}	0.00	0.00	3.53	20.8	86.1	-41.9	-	-
2.0	0.2	8.26×10^{-1}	5.0	0.89	C	385	77	9.65×10^{-8}	1.36	0.62	2.54	19.5	85.1	-36.8		
2.0	0.2	8.26×10^{-1}	7.5	1.33	I	578	173	4.34×10^{-8}	0.23	0.10	2.38	18.4	65.0	-33.5		
2.0	0.2	8.26×10^{-1}	10.0	1.78	I	770	308	1.58×10^{-8}	0.00	0.00	2.11	24.4	60.0	-51.9		
2.0	0.5	6.40×10^{-1}	2.5	0.38	A	169	19	5.27×10^{-7}	0.00	0.00	3.89	19.9	79.8	-39.0	-	-
2.0	0.5	6.40×10^{-1}	5.0	0.75	C	339	77	1.31×10^{-7}	0.81	0.33	3.15	17.9	87.2	-30.8		
2.0	0.5	6.40×10^{-1}	7.5	1.13	I	508	173	7.10×10^{-8}	1.14	0.46	2.51	22.8	91.1	-47.6		
2.0	0.5	6.40×10^{-1}	10.0	1.50	I	678	308	2.83×10^{-8}	0.25	0.10	2.23	21.4	69.9	-43.9		
2.0	1.0	4.44×10^{-1}	2.5	0.31	A	141	19	5.86×10^{-6}	0.00	0.00	4.05	19.5	74.4	-37.4	-	-
2.0	1.0	4.44×10^{-1}	5.0	0.62	A	282	77	1.57×10^{-7}	0.00	0.00	3.24	26.2	106	-55.7	55.0	0.08
2.0	1.0	4.44×10^{-1}	7.5	0.92	I	424	173	9.99×10^{-8}	0.65	0.22	3.03	22.5	99.5	-48.2		
2.0	1.0	4.44×10^{-1}	10.0	1.23	I	565	308	5.24×10^{-8}	0.42	0.14	2.47	20.6	80.6	-40.5		
2.0	2.0	2.50×10^{-1}	2.5	0.24	Dr	106	19									
2.0	2.0	2.50×10^{-1}	5.0	0.47	A	212	77	2.59×10^{-7}	0.00	0.00	3.45	23.0	96.2	-48.6	51.6	0.09
2.0	2.0	2.50×10^{-1}	7.5	0.71	A	318	173	1.36×10^{-7}	0.00	0.00	3.04	27.3	105	-57.7	57.7	0.06
2.0	2.0	2.50×10^{-1}	10.0	0.94	I	424	308	8.30×10^{-8}	0.38	0.10	2.63	19.5	80.6	-37.4		
2.0	5.0	8.16×10^{-2}	2.5	0.15	Dr	61	19									
2.0	5.0	8.16×10^{-2}	5.0	0.30	A	121	77	8.62×10^{-7}	0.00	0.00	4.57	22.0	90.4	-45.6	48.2	0.14
2.0	5.0	8.16×10^{-2}	7.5	0.45	A	182	173	3.59×10^{-7}	0.00	0.00	3.61	25.5	101	-54.7	53.4	0.07
2.0	5.0	8.16×10^{-2}	10.0	0.60	A	242	308	2.31×10^{-7}	0.00	0.00	3.25	27.7	105	-58.8	57.0	0.06

Table 3.15: Mode outcomes and measured quantities for systems with $h_o = 5.0$ μm. Listed quantities are h_o, r_s, aspect ratio squared $[h_o/(r_s+h_o)]^2$, ϕ_o, initial liquid apex electric field E_o, mode outcome ("Dr" for drainage, "A" for axial, "C" for coronal, "I" for instability and "Du" for dual), Reynolds number $\mathsf{Re} = \sqrt{\rho\varepsilon_o/2}[\phi_o h_o/\mu(r_s+h_o)]$, electric Weber number $\mathsf{We} = \varepsilon_o\phi_o^2/2\gamma h_o$, termination time t_f, most prominent protrusion apex coordinates r_f and z_f, ratio $r_{rel} = r_f/(r_s+h_o)$, apex curvature radius R_{apex}, apex speed $|\vec{u}|_f$, apex pressure p_f and axial θ_f (local minimum in θ at $t = t_f$ closest to $r = 0$) extracted at r_θ. The dash "-" in θ_f and r_θ entries indicate the axial systems which did not yield measurement of θ_f.

h_o (μm)	r_s	$\left(\frac{h_o}{r_s+h_o}\right)^2$	ϕ_o (kV)	E_o $\left(\frac{\text{GV}}{\text{m}}\right)$	Mode	Re	We	t_f (s)	r_f (μm)	r_{rel}	z_f (μm)	R_{apex} (nm)	u_f $\left(\frac{\text{m}}{\text{s}}\right)$	p_f (MPa)	θ_f (°)	r_θ (μm)
5.0	0.1	9.61×10^{-1}	2.5	0.24	A	208	8	1.88×10^{-6}	0.00	0.00	9.49	19.7	80.1	-38.3	-	-
5.0	0.1	9.61×10^{-1}	5.0	0.49	C	415	31	4.64×10^{-7}	4.12	0.81	6.35	17.1	81.4	-26.0		
5.0	0.1	9.61×10^{-1}	7.5	0.73	C	623	69	2.09×10^{-7}	4.61	0.90	4.00	17.9	80.1	-30.5		
5.0	0.1	9.61×10^{-1}	10.0	0.97	Du	830	123	1.28×10^{-7}	4.73	0.93	3.14	19.2	81.7	-37.4		
5.0	0.2	9.25×10^{-1}	2.5	0.24	A	204	8	2.89×10^{-6}	0.00	0.00	9.75	19.4	78.4	-37.2		
5.0	0.2	9.25×10^{-1}	5.0	0.47	C	407	31	5.10×10^{-7}	3.65	0.70	7.01	16.6	79.9	-24.1		
5.0	0.2	9.25×10^{-1}	7.5	0.70	C	611	69	2.38×10^{-7}	4.27	0.82	4.64	17.6	73.9	-29.3		
5.0	0.2	9.25×10^{-1}	10.0	0.94	I	814	123	1.39×10^{-7}	0.68	0.13	5.77	17.7	70.3	-30.2		
5.0	0.5	8.26×10^{-1}	2.5	0.22	Dr	193	8									
5.0	0.5	8.26×10^{-1}	5.0	0.43	C	385	31	5.99×10^{-7}	2.66	0.48	8.03	17.0	71.7	-24.6		
5.0	0.5	8.26×10^{-1}	7.5	0.65	C	578	69	2.99×10^{-7}	3.59	0.65	5.81	19.5	91.4	-38.2		
5.0	0.5	8.26×10^{-1}	10.0	0.86	I	770	123	1.65×10^{-7}	0.00	0.00	5.97	24.1	88.6	-51.2		
5.0	1.0	6.94×10^{-1}	2.5	0.19	Dr	176	8									
5.0	1.0	6.94×10^{-1}	5.0	0.39	C	353	31	6.97×10^{-7}	0.95	0.16	9.31	17.3	80.8	-27.1		
5.0	1.0	6.94×10^{-1}	7.5	0.58	C	529	69	3.69×10^{-7}	2.73	0.46	6.86	17.3	83.5	-27.9		
5.0	1.0	6.94×10^{-1}	10.0	0.78	I	706	123	2.22×10^{-7}	0.87	0.15	6.45	18.7	76.3	-33.6		
5.0	2.0	5.10×10^{-1}	2.5	0.17	Dr	151	8									
5.0	2.0	5.10×10^{-1}	5.0	0.33	A	303	31	7.57×10^{-7}	0.00	0.00	8.25	23.1	97.3	-48.5	50.6	0.10
5.0	2.0	5.10×10^{-1}	7.5	0.50	C	454	69	4.73×10^{-7}	1.42	0.20	7.97	19.3	94.7	-38.2		
5.0	2.0	5.10×10^{-1}	10.0	0.66	I	605	123	3.26×10^{-7}	0.00	0.00	7.36	23.2	93.4	-48.8		
5.0	5.0	2.50×10^{-1}	2.5	0.12	Dr	106	8									
5.0	5.0	2.50×10^{-1}	5.0	0.24	A	212	31	1.55×10^{-6}	0.00	0.00	9.44	21.0	91.3	-42.7	48.3	0.13
5.0	5.0	2.50×10^{-1}	7.5	0.37	A	318	69	7.06×10^{-7}	0.00	0.00	8.02	24.8	103	-53.1	53.2	0.07
5.0	5.0	2.50×10^{-1}	10.0	0.49	A	424	123	4.59×10^{-7}	0.00	0.00	7.31	26.4	105	-56.2	55.7	0.06

Table 3.16: Mode outcomes and measured quantities for additional simulations of $h_o = 0.1$, 0.2 and 0.5 μm conducted to further populate the mode diagram in Fig. 3.26(a). Listed quantities are h_o, r_s, aspect ratio squared $[h_o/(r_s+h_o)]^2$, ϕ_o, initial liquid apex electric field E_o, mode outcome ("Dr" for drainage, "A" for axial, "C" for coronal, "I" for instability and "Du" for dual), Reynolds number $\mathsf{Re} = \sqrt{\rho\varepsilon_o/2}[\phi_o h_o/\mu(r_s+h_o)]$, electric Weber number $\mathsf{We} = \varepsilon_o\phi_o^2/2\gamma h_o$, termination time t_f, most prominent protrusion apex coordinates r_f and z_f, ratio $r_{rel} = r_f/(r_s+h_o)$, apex curvature radius R_{apex}, apex speed $|\vec{u}|_f$, apex pressure p_f and axial θ_f (local minimum in θ at $t = t_f$ closest to $r = 0$) extracted at r_θ. The dash "-" in θ_f and r_θ entries indicate the axial systems which did not yield measurement of θ_f.

h_o (μm)	r_s	$\left(\frac{h_o}{r_s+h_o}\right)^2$	ϕ_o (kV)	E_o $\left(\frac{\text{GV}}{\text{m}}\right)$	Mode	Re	We	t_f (s)	r_f (μm)	r_{rel}	z_f (μm)	R_{apex} (nm)	u_f $\left(\frac{\text{m}}{\text{s}}\right)$	p_f (MPa)	θ_f (°)	r_θ (μm)
0.1	2.0	2.27×10^{-3}	3.0	0.42	A	12	555	1.65×10^{-5}	0.00	0.00	0.99	17.3	61.7	-34.7	42.4	0.11
0.1	2.0	2.27×10^{-3}	4.0	0.56	A	16	987	6.69×10^{-7}	0.00	0.00	0.52	18.2	62.0	-36.7	45.7	0.06
0.1	2.0	2.27×10^{-3}	12.5	1.73	I	50	9630	1.87×10^{-8}	0.15	0.07	0.16	20.5	49.4	-41.3		
0.1	2.0	2.27×10^{-3}	15.0	2.08	I	61	13900	1.02×10^{-8}	0.00	0.00	0.13	23.9	42.3	-50.6		
0.1	5.0	3.84×10^{-4}	3.0	0.21	Dr	5	555									
0.1	5.0	3.84×10^{-4}	12.5	0.89	A	21	9630	2.32×10^{-7}	0.00	0.00	0.27	22.4	67.4	-46.6	54.6	0.04
0.1	5.0	3.84×10^{-4}	15.0	1.07	I	25	13900	1.19×10^{-7}	0.00	0.00	0.20	21.0	56.6	-42.5		
0.1	5.0	3.84×10^{-4}	17.5	1.25	I	29	18900	7.07×10^{-8}	0.00	0.00	0.22	40.1	100	-75.2		
0.1	5.0	3.84×10^{-4}	20.0	1.42	I	33	24700	4.10×10^{-8}	0.24	0.05	0.17	19.4	51.3	-36.7		
0.2	5.0	1.48×10^{-3}	3.0	0.21	Dr	10	277									
0.2	5.0	1.48×10^{-3}	4.0	0.28	A	13	493	2.57×10^{-5}	0.00	0.00	1.98	18.5	68.9	-34.8	43.1	0.18
0.2	5.0	1.48×10^{-3}	12.5	0.88	A	41	4820	1.32×10^{-7}	0.00	0.00	0.47	25.1	82.0	-53.1	56.6	0.05
0.2	5.0	1.48×10^{-3}	15.0	1.06	I	49	6940	9.75×10^{-8}	0.27	0.05	0.41	20.1	64.0	-39.1		
0.2	5.0	1.48×10^{-3}	17.5	1.23	I	57	9440	5.25×10^{-8}	0.00	0.00	0.31	24.9	69.7	-52.9		
0.2	5.0	1.48×10^{-3}	20.0	1.41	I	65	12300	3.86×10^{-8}	0.02	0.00	0.33	48.9	110	-83.0		
0.5	0.1	6.94×10^{-1}	3.0	1.49	C	212	111	1.73×10^{-8}	0.22	0.37	0.78	22.0	94.5	-46.2		
0.5	0.1	6.94×10^{-1}	3.5	1.74	C	247	151	1.35×10^{-8}	0.26	0.43	0.71	25.3	97.2	-54.4		
0.5	0.1	6.94×10^{-1}	4.0	1.99	I	282	197	1.09×10^{-8}	0.29	0.49	0.64	25.6	90.9	-54.5		
0.5	0.1	6.94×10^{-1}	4.5	2.24	I	318	250	8.44×10^{-9}	0.13	0.22	0.65	26.0	79.2	-55.4		
0.5	0.2	5.10×10^{-1}	3.5	1.43	C	212	151	1.82×10^{-8}	0.08	0.12	0.86	29.5	114	-62.0		
0.5	0.2	5.10×10^{-1}	4.0	1.63	C	242	197	1.50×10^{-8}	0.15	0.21	0.79	27.7	104	-59.0		
0.5	0.2	5.10×10^{-1}	4.5	1.83	I	272	250	1.22×10^{-8}	0.00	0.00	0.74	26.6	86.9	-56.8		

Table 3.17: Mode outcomes and measured quantities for additional simulations $h_o = 2.0$ and 5.0 μm conducted to further populate the mode diagram in Fig. 3.26(a). Listed quantities are h_o, r_s, aspect ratio squared $[h_o/(r_s + h_o)]^2$, ϕ_o, initial liquid apex electric field E_o, mode outcome ("Dr" for drainage, "A" for axial, "C" for coronal, "I" for instability and "Du" for dual), Reynolds number $\mathsf{Re} = \sqrt{\rho\varepsilon_o/2}[\phi_o h_o/\mu(r_s + h_o)]$, electric Weber number $\mathsf{We} = \varepsilon_o\phi_o^2/2\gamma h_o$, termination time t_f, most prominent protrusion apex coordinates r_f and z_f, ratio $r_{rel} = r_f/(r_s + h_o)$, apex curvature radius R_{apex}, apex speed $|\vec{u}|_f$ and apex pressure p_f. No θ_f could be extracted for the axial systems presented here.

h_o (μm)	r_s	$\left(\frac{h_o}{r_s+h_o}\right)^2$	ϕ_o (kV)	E_o $\left(\frac{\text{GV}}{\text{m}}\right)$	Mode	Re	We	t_f (s)	r_f (μm)	r_{rel}	z_f (μm)	R_{apex} (nm)	u_f $\left(\frac{\text{m}}{\text{s}}\right)$	p_f (MPa)
2.0	0.1	9.07×10^{-1}	1.5	0.29	Dr	121	7							
2.0	0.1	9.07×10^{-1}	2.0	0.39	A	161	12	5.25×10^{-7}	0.00	0.00	3.82	19.0	75.9	-35.7
2.0	0.1	9.07×10^{-1}	3.5	0.67	C	282	38	1.61×10^{-7}	1.30	0.62	3.13	16.2	69.5	-21.7
2.0	0.1	9.07×10^{-1}	6.5	1.25	I	524	130	4.99×10^{-8}	0.00	0.00	2.41	22.8	74.9	-47.6
5.0	0.1	9.61×10^{-1}	2.0	0.20	Dr	166	5							
5.0	0.1	9.61×10^{-1}	3.0	0.29	A	249	11	9.67×10^{-7}	0.00	0.00	8.88	20.8	88.6	-41.7
5.0	0.1	9.61×10^{-1}	4.0	0.39	C	332	20	7.77×10^{-7}	3.44	0.67	8.73	17.2	67.6	-25.7
5.0	0.1	9.61×10^{-1}	6.0	0.58	C	498	44	3.18×10^{-7}	4.42	0.87	5.05	17.4	82.6	-28.7
5.0	0.1	9.61×10^{-1}	12.5	1.21	I	1040	193	5.62×10^{-8}	0.00	0.00	5.23	22.5	66.6	-46.8
5.0	0.1	9.61×10^{-1}	15.0	1.46	I	1250	277	3.15×10^{-8}	0.00	0.00	5.13	25.2	67.5	-53.5
5.0	0.2	9.25×10^{-1}	2.0	0.19	Dr	163	5							
5.0	0.2	9.25×10^{-1}	3.0	0.28	A	244	11	1.04×10^{-6}	0.00	0.00	8.82	20.9	89.3	-42.1
5.0	0.2	9.25×10^{-1}	4.0	0.38	C	326	20	8.43×10^{-7}	2.69	0.52	9.63	17.8	79.6	-30.4
5.0	0.2	9.25×10^{-1}	6.0	0.56	C	489	44	3.56×10^{-7}	4.01	0.77	5.70	17.2	78.7	-27.7
5.0	0.2	9.25×10^{-1}	8.5	0.80	C	692	89	1.94×10^{-7}	4.39	0.84	4.23	19.3	89.8	-37.9
5.0	0.2	9.25×10^{-1}	12.5	1.17	I	1020	193	7.63×10^{-8}	0.97	0.19	5.33	19.6	72.0	-37.8

Chapter 4

ELECTROHYDRODYNAMIC SURFACE INSTABILITY GROWTH OF RELEVANCE TO LIQUID METAL ION SOURCES

4.1 Introduction

Krohn's discovery of ion emission from an electrified liquid metal droplet [78] in the early 1960s has spurred strong interest in developing systems that emit such highly energetic ion beams. They are emitted from apices of protrusions that grow from a liquid metal film subject to an imbalance of destabilizing Maxwell (electric) and stabilizing capillary forces. These small scale systems known as liquid metal ion sources (LMIS) [22] now form the basis for high resolution focused ion beam systems [108] used for instrumentation ranging from microscopy to nanofabrication. There is also a growing interest in developing miniaturized LMIS microarray devices to actuate space micropropulsion [103].

There exists a wealth of literature on treating such protrusion growth process as a surface electrohydrodynamic (EHD) instability. It dates back to analyses conducted by Tonks [145] and Frenkel [47] for a perfectly conducting, inviscid, flat, infinitely thick and infinitely spanning liquid under a normal electric field that culminated in a critical field strength needed for sustained periodic distortion of the liquid surface. A subsequent linear stability analysis conducted by de Surgy *et al.* [131, 132] appealed to the full Navier-Stokes equation to derive a dispersion relation for the growth rate of surface instabilities valid for all wavelength disturbances for an arbitrarily thick and viscous liquid and an arbitrarily thick vacuum. The liquid thickness and viscosity were found to strongly influence the dynamics such as the selection of the dominant wavenumber with the largest growth rate. Static [53, 54] and dynamical [133] stability analyses of a perfectly conducting, inviscid, flat but now finitely spanning liquid have also uncovered modifications to the critical field strength induced solely from the geometry.

Recent finite element simulations that track the spatiotemporal EHD mode development in a LMIS geometry realistic to space micropropulsive devices unveiled an "instability" mode that culminated in the development of multiple protrusions in a wave-like pattern (see Ch. 3). In particular, the protrusion apex-to-apex spacings extracted for select cases were found to be highly comparable to the dominant instability wavelengths calculated from the dispersion relation found by de Surgy *et al.* [132] with appropriate substitutions for key physical variables. The resemblance was found despite the presence of an apertured extractor

and a highly curved microemitter substrate, both of which introduce strong nonlinearities to the ensuing EHD process. Though the nonlinear static and dynamical stability of viscous films flowing over inclined planes [73, 148] and small substrate topography [146, 147] have been previously analyzed for long-wave asymptotics, that for the liquid metal surface in more realistic geometries such as that previously simulated (see Ch. 3) still remains unknown due to the challenges of analytically solving the highly coupled and nonlinear equations in such geometries. It is also difficult to experimentally access the nano-microscale spatiotemporal scales involved during protrusion development prior to ion emission. The advent of advanced computational techniques allowing simulations of instability development in such geometries provides the only path forward to probe the dynamical details.

This study presents results from computational simulations that model the liquid metal surface EHD instability growth as the basic flat liquid, flat apertureless extractor system is first imbued with an extractor aperture and then a curved microemitter. The arbitrary Lagrangian Eulerian finite element method [32] is used to track the spatiotemporal evolution of the rapidly accelerating liquid free surface. Sec. 4.3 outlines the key simulation details and delineates the data analysis methodology taken to extract simulation results to be compared against the analytical predictions. The results show that the extractor aperture strongly stabilizes the surface inside the aperture by generating a nonuniform initial surface electric field depressed inside the aperture. The field distribution ultimately excites drainage of the liquid inside the aperture that suppresses instability development. The microemitter curvature is also found to strongly stabilize the surface to ultimately confine the instability development within the liquid tip region given by the initial liquid apex curvature radius. The stabilization is generated by the curvature encoded initial tip electric field enhancement inducing bulk flow into the tip region and capillary drainage acting against the destabilizing Maxwell effects to flatten and stabilize the curved liquid surface. The instability development in the flat liquid, apertureless extractor system, flat liquid, apertured extractor system and curved microemitter, apertured extractor system (i.e. LMIS geometry) whose initial surfaces are roughened by small random noise is characterized in Sec. 4.4 using the spatiotemporal evolution of the surface and power spectrum of selected cases. Despite the strongly stabilizing mechanisms generated by the aperture and microemitter curvature, however, a strong correlation is obtained between the dominant instability wavenumbers extracted from the LMIS instability mode systems and the de Surgy *et al.* predicted dominant wavenumbers. Discussion on the LMIS liquid reservoir, consequences of gravity to instability development and geometry restricted observance of the instability mode are offered in Sec. 4.5 before the key findings are summarized in Sec. 4.6.

4.2 Linear stability of the flat liquid, flat apertureless extractor system

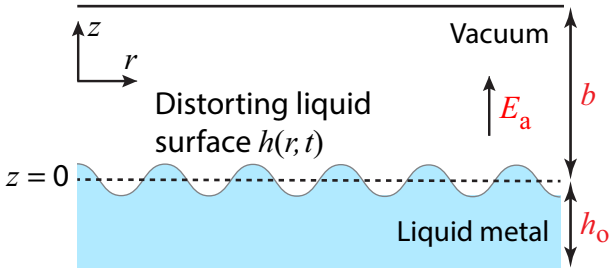

Figure 4.1: Schematic of the flat liquid, flat apertureless extractor system in axisymmetric coordinates (r, z). Liquid thickness is h_o, vacuum thickness is b and applied electric field is E_a. The liquid surface undergoing distortion is $z = h(r,t) = \sum_k J_0(kr)\exp(st)$, where k is the wavenumber and s is the growth rate.

The linear stability analysis of the arbitrarily thick and viscous flat liquid metal layer under a normal electric field was originally conducted by de Surgy *et al.* [131, 132] in Cartesian (x, z) coordinates with gravity. The analysis has been repeated in Ch. 2 for the same system (sketched in Fig. 4.1) in axisymmetric (r, z) coordinates without gravity. The analysis results in the dimensional dispersion relation (Eq. 2.157) between the instability growth rate s and wavenumber k. Key simulation results to be described in the subsequent sections are compared against predictions derived from Eq. 2.157.

4.3 Computational methods

This section first describes the computational geometries used for simulations conducted in this chapter. The details of governing equations and boundary conditions may be found in Sec. 2.1, whereas those for the computational algorithm may be found in the previous study on the spatiotemporal evolution of EHD modes in a realistic LMIS geometry (see Ch. 3). The data analysis used to extract key results is then outlined. Definitions of physical variables, material constants used for liquid metal gallium (Ga) at the melting point [69] and vacuum permittivity and key initial variables are the same as those introduced back in Table 3.1.

4.3.1 Key simulation details

The key details of the simulations conducted for the Fig. 4.2(a) flat liquid, flat apertureless extractor, flat apertured extractor, Fig. 4.2(b) flat liquid, flat apertured extractor and Fig. 4.2(c) LMIS geometry with a curved microemitter are presented in this section.

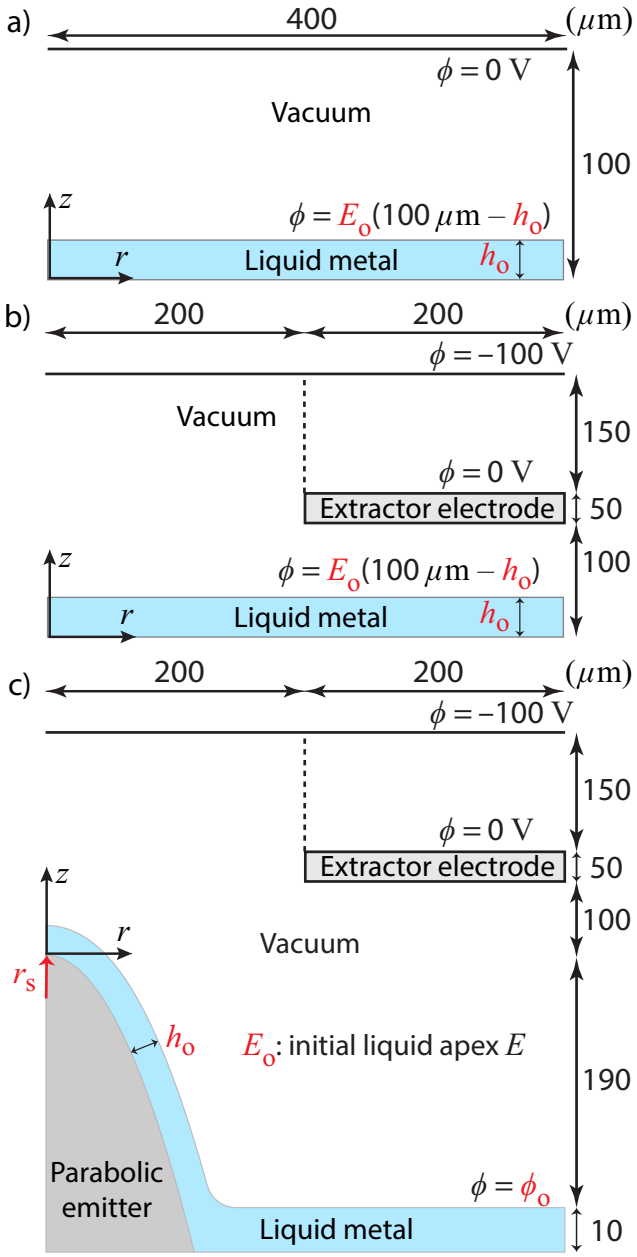

Figure 4.2: Sketch of computational geometries for the (a) flat liquid, flat apertureless extractor, (b) flat liquid, flat apertured extractor and (c) LMIS geometry with a curved microemitter, flat apertured extractor. The details of the LMIS geometry are the same as that shown back in Fig. 3.1(a).

4.3.1.1 Flat liquid, flat apertureless extractor system

Shown in Fig. 4.2(a) is the axisymmetric flat liquid, flat apertureless extractor geometry. The geometry consists of an initially flat liquid metal gallium layer of thickness h_o that is placed under a flat apertureless extractor distanced by vertical gap distance 100 μm $- h_o$ from the liquid surface $z = h(r,t)$. The liquid surface is subject to a positive electric potential of $\phi = E_o(100\ \mu\text{m} - h_o)$, where E_o is the initial liquid apex electric field found for the LMIS system being compared against. This is such that the initial E generated for the flat liquid under the extractor is equal to E_o to isolate the effect of the extractor aperture and the microemitter curvature on instability development. The instability development in this system is characterized in Sec. 4.4 using a select example listed in Table 4.2.

The dimensional governing equations and boundary conditions of the EHD distortion in the geometry have been presented in Sec. 2.1. Due to the finite domain size, additional boundary condition $\partial\phi/\partial r = 0$ on $r = 0$ and rightmost domain wall is applied to set the electric flux equal to zero. The no slip and no penetration conditions (Eq. 2.20) are also additionally imposed on the rightmost domain wall.

The initial liquid surface is described as

$$h(r, t = 0) = h_o + \text{uniform random noise} \tag{4.1}$$

where the unperturbed flat liquid surface is additionally imbued with a small degree of surface roughness. This is modeled by uniform random noise with seed values between $[-h_o, h_o]/10^4$ sampled at every mesh element node placed along the surface. It was noted during convergence studies that reducing the noise amplitude by two orders of magnitude and below the chosen value led to numerics induced errors in the simulated instability development when key results were compared against the analytical predictions. The surface mesh is set to possess uniform element side length around a tenth of the predicted dominant instability wavelength λ_m.

4.3.1.2 Flat liquid, flat apertured extractor system

Shown in Fig. 4.2(b) is the axisymmetric flat liquid, flat apertured extractor geometry. The instability development in this system is characterized in Sec. 4.4 using a select example listed in Table 4.2. The fixed system parameters, governing equations and boundary conditions and computational algorithm are the same as those used for the flat liquid, flat apertureless extractor geometry except that the entire apertured extractor surface is set as the potential ground, with an additional small potential of $\phi = -100$ V applied to the domain ceiling. The liquid surface and ceiling potential are simultaneously smoothly ramped up

from zero to their full values during the first $t_o = 10^{-12}$ s to prevent small initial time step sizes.

4.3.1.3 LMIS system

Shown in Fig. 4.2(c) is the axisymmetric (r, z) computational domain of a realistic LMIS geometry in a vacuum without gravity and has been previously described (see Ch. 3). The details of the governing equations and boundary conditions, and the computational algorithm are also the same as those previously described there. The geometry primarily consists of a smooth, parabolic microemitter with apex curvature radius r_s externally wetted with a liquid metal layer. The initial liquid surface is described as

$$h(r, t = 0) = \text{smooth offset surface} + \text{uniform random noise} \tag{4.2}$$

where the liquid layer smoothly offset to the microemitter surface by a constant initial thickness h_o (see Sec. 3.2.1 for detailed description) is additionally imbued with uniform random noise with seed values between $[-h_o, h_o]/10^4$ sampled at every mesh element node placed along the surface. The results to be discussed are only those from the combinations that lead to the "instability" EHD mode resulting in multiple, regularly spaced protrusions along the liquid surface. Only h_o, r_s and ϕ_o have been varied across simulations. The full list of the combinations simulated in this study is provided in Tables 4.4-4.5.

4.3.2 Data analysis details

This section provides the details of the data analysis applied to extract key analytic and simulation results used to characterize the instability development in the different simulation geometries.

4.3.2.1 Extraction of flat liquid, flat apertureless geometry analytical predictions

The transcendental form of the flat liquid, flat apertureless geometry dispersion relation Eq. 2.157 does not yield a closed analytic relation between s and k as found in the asymptotic limits. However, if the values for the material constants ρ, γ and μ, liquid and vacuum thickness h_o and b and the applied electric field E_c are known for a system, then Eq. 2.157 may be numerically solved to yield a numerical growth rate curve $s(k)$ over a sampled k interval that could be used for comparison. For this study, $s(k)$ was numerically constructed over the unstable wavenumbers k using MATLAB's [2] implementation of the Levenberg-Marquardt [87, 96] method optimal for solving such nonlinear equations. The range of unstable wavenumbers goes from $k = 0$ to the marginally stable wavenumber $k = k_{marg}$

Table 4.1: Definitions of the spectral analysis variables and referenced quantities introduced for this chapter.

Spectral variables	Symbol
Wavenumber	k
Wavelength	$\lambda = 2\pi/k$
Instability growth rate	$s(k)$
Hankel transform	$F(k)$
Power spectrum	$PS(k)$
Referenced quantities	**Symbol**
Protrusion apex vertical displacement	$\delta h = h(r^{apex}, t) - h_o$
Instability protrusion apex averaged δh	$\overline{\delta h}$
Marginally stable k	k_{marg}
Most unstable k from Eq. 2.157	k_m
Most unstable λ from Eq. 2.157	$\lambda_m = 2\pi/k_m$
LMIS extracted k_m at t_f	k_{sim}
LMIS extracted λ_m at t_f	$\lambda_{sim} = 2\pi/k_{sim}$

corresponding to the non-trivial zero of Eq. 2.157. This wavenumber was also numerically determined using the Levenberg-Marquardt method.

The dispersion relations in the viscous regime permit real $s(k) < 0$ that encode dampening of the perturbation, whereas those in the inviscid regime do not and instead only permit a purely imaginary growth rate encoding oscillation outside the unstable regime. The dispersion curves calculated for all combinations of h_o and E_o generated for the LMIS instability systems were found to closely approximate those of the inviscid limit (see Appendix 4.9) such that real solutions numerically calculated for $s(k)$ for $k > k_{marg}$ were found to be zero. The Re cataloged for the instability systems indeed show that the systems are much closer to the inviscid limit than the viscous limit. Thus, the calculated $s(k)$ from $k = 0$ to $k = k_{marg}$ actually represents the entire band of real $s(k)$ encoded by the initial conditions of the systems of interest.

The maximum growth rate s_m and its wavenumber k_m corresponding to the dominant instability mode were extracted using the MATLAB's implementation of the golden section search algorithm [72] to iteratively minimize the inverse of the growth rate calculated from Eq. 2.157 over the interval between $0 < k < k_{marg}$.

4.3.2.2 Spectral Analysis

Spectral analysis of the axisymmetric simulations was conducted by computing the discrete Hankel transform [43] of the spatiotemporally evolving surface $h(r,t)$. The MATLAB code utilized for numerical calculation of the discrete Hankel transform is that described and provided by Chouinard and Baddour [20]. The underlying mathematical theory and operational rules [7] showed that the proposed discrete Hankel transform can be used to approximate the continuous forward and inverse Hankel transform in the same manner that the discrete Fourier transform is well known to be able to approximate the continuous Fourier transform. The discrete Hankel transform $F(k,t)$ for the surface $h(r,t)$ sampled at time t is defined as

$$F\left(k_m = \frac{j_m}{L}, t\right) = \frac{L^2}{j_n} \sum_{a=1}^{n-1} \frac{2J_\nu(j_a j_m / j_n)}{J_{\nu+1}^2(j_a)} \left[h\left(r_a = \frac{j_a}{j_n} L, t\right) - h_o\right] \tag{4.3}$$

where L is the radial span of the transformed $h(r,t)$, n is the number of sampled points on $h(r,t)$, J_ν is the Bessel function of the first kind of order ν and j_a is the ath zero of J_ν. The utilized algorithm samples the data at $r = r_a = j_a L / j_n$ and returns the transform evaluated at wavenumbers $k = k_m = j_m / L$ that scale as the zeros of J_ν. Linear interpolation of $h(r,t)$ was used to sample the data at the requested locations. Order $\nu = 0$ was selected due to the two dimensional axisymmetric nature of the computational domain [92], where it is known that the Hankel transform of order zero is in fact equal to the two dimensional Fourier transform of an axisymmetric function.

The power spectrum calculated from $F(k,t)$ is then

$$PS(k,t) = \frac{|F(k,t)|^2}{n} \tag{4.4}$$

for which the maxima will correspond to the dominant modes that develop from the liquid surface. The simulation growth rate at each time $s(k,t)$ can then be extracted from $PS(k,t)$ evolution by

$$s(k,t) = \frac{1}{2} \frac{\partial \ln [PS(k,t)]}{\partial t} \tag{4.5}$$

as $F(k,t) \sim \exp(st)$ such that $PS(k,t) \sim \exp(2st)$. The simulation $s(k,t)$ at each time step t taken is calculated using the numerical gradient function implemented in MATLAB. The calculated growth rates can then be compared against $s(k)$ as predicted by Eq. 2.157. As Eq. 4.5 assumes linear growth, the time interval during which the extracted $s(k,t)$ agrees with the Eq. 2.157 predicted $s(k)$ will be constitute the linear growth regime. The extracted $s(k,t)$ at times in which the growth is not linear will possess significant deviations. The

extracted $s(k,t)$ were found to be stable with respect to the choice of window function applied to the surface data.

For the flat liquid simulations, L was set to be the computational domain width of 400 μm and n was set to equal the number of mesh node points placed on $h(r,t)$. The Bessel function zeros are not equally spaced, which means the sampled r coordinates and k wavenumbers are also not equally spaced. However, as the spacings between the zeros are known to quickly approach π, the minimum and maximum wavenumbers sampled can be estimated by the following. The minimum k sampled (and also the wavenumber space resolution) can be approximated by π/L or 7.85×10^3 1/m, which is a couple of orders of magnitude less than the smallest k_m predicted for the simulated systems. The maximum k sampled can be approximated by $n\pi/L$. For the flat liquid simulations shown in Sec. 4.4, $n = 6000$ as the mesh element size (of cubic Lagrange order) was set to be 0.2 μm, which is about a tenth of the predicted λ_m. This results in the maximum k sampled of 4.71×10^7 1/m, which is much larger than the predicted k_m. Thus, the wavenumbers sampled possess adequate resolution and are sampled well past the wavenumber band of interest for the conducted simulations.

For the LMIS simulations, the transforms were computed for the $h(r,t)$ data that were additionally subject to the Hanning (Hann) window [15] in order to reduce spectral leakage and enhance the spectral content associated with the instability formation. The windowed Hankel transform $N(k,t)$ for $h(r,t)$ is defined as

$$N\left(k_m = \frac{j_m}{L}, t\right) = \frac{L^2}{j_n} \sum_{a=1}^{n-1} \frac{2J_\nu(j_a j_m/j_n)}{J_{\nu+1}^2(j_a)} \left[h\left(r_a = \frac{j_a}{j_n}L, t\right) - h(r = L, t)\right] W(r_a) \tag{4.6}$$

where the surface data is offset according to $h(r_a,t) - h(L,t)$ in order to be consistent with the assumption [43] that the to be transformed signal equals zero for all $r > L$. The axisymmetric Hanning window [66, 157] is described by

$$W(r_a) = \cos^2\left(\frac{\pi r_a}{2L}\right) = 0.5\left[1 + \cos\left(\frac{\pi r_a}{L}\right)\right] \tag{4.7}$$

The radial span L of the sampled signal was set to be r at which the initial liquid surface $h(r,0) \leq -150$ μm. The cutoff criterion was implemented to exclude the fillet region, which attaches to the wetted liquid surface at around $z = -170$ μm. The span L was found to range from $L = 5.68$ μm found for the $r_s = 0.1$ and $h_o = 0.2$ μm system possessing the smallest $r_s + h_o$ to $L = 29.6$ μm for the $r_s = 2$ μm and $h_o = 5$ μm possessing the largest $r_s + h_o$. The number of sampled points n was set to be $L/5$ nm, where 5 nm corresponds to the minimum mesh element size applied to the LMIS geometry. The described scheme was found to be more than adequate to access and resolve the wavenumber space of interest for each LMIS simulation.

The simulated dominant instability wavenumber k_{sim} was identified by searching for a local maximum in $PS(k, t_f)$ near the predicted k_m for the flat liquid, flat apertureless extractor geometry. The extracted k_{sim} $h(r, t)$ are compared against the Eq. 2.157 predicted k_m in Sec. 4.4.4 and in Tables 4.4-4.5. The growth rate $s(k, t)$ curves were extracted for the LMIS simulations using Eq. 4.5, though no existing analytic predictions exist to compare against.

4.4 Results

Table 4.2: Label, key initial variables, termination time and sampling time for examples shown in Sec. 4.4. The aperture radius is 200 μm. The electric field E_c reported for the flat liquid systems is equal to $\phi_o/(100\ \mu m - h_o)$, whereas that for the LMIS system is the initial liquid apex E_o. For the flat liquid, apertureless extractor system, Eq. 2.157 predicts $k_m = 3.37 \times 10^6$ 1/m ($\lambda_m = 1.86$ μm), $s_m = 4.68 \times 10^7$ 1/s and $k_{marg} = 5.41 \times 10^6$ 1/m. Measurements of key quantities for all LMIS instability simulations conducted (53 in total) are provided in Tables 4.4 - 4.5.

Label	h_o (μm)	r_s (μm)	ϕ_o (kV)	E_c $\left(\frac{\text{GV}}{\text{m}}\right)$	t_f (μs)	Δt (μs)
Flat liquid, apertureless extractor	5.0	-	62.9	0.662	0.141	0.016
Flat liquid, apertured extractor	5.0	-	62.9	0.662	0.144	0.016
LMIS geometry	5.0	2.0	10.0	0.662	0.186	0.020

This section presents results characterizing the surface EHD instability growth in the three systems: flat liquid layer under a flat apertureless extractor, flat liquid layer under a flat apertured extractor and curved liquid layer under a flat apertured extractor. The examples used to characterize the growth are listed in Table 4.2. Measurements of key physical quantities defined in Table 4.1 for all LMIS instability systems simulated in the previous study (see Ch. 3) are provided in Tables 4.4-4.5. In particular, the λ_m predicted for the flat liquid, apertureless extractor example to be shown is the lowest of all predicted values for h_o and E_o combinations possessed by the LMIS instability systems. The chosen systems thereby possess the smallest number of protrusions that could be fitted inside the finite domain size, presenting the greatest challenge for the simulations to accurately track the instability development from the liquid surface.

It should be emphasized that the results for examples shown in this section and systems cataloged in Tables 4.4-4.5 have been extracted from just singular realizations of the random noise applied to the initial liquid surface.

4.4.1 Instability development in the flat liquid, apertureless extractor geometry

This section presents the simulation results of the surface EHD instability generation for the selected flat liquid layer, flat apertureless extractor system as listed in Table 4.2.

4.4.1.1 Spatiotemporal surface evolution

Shown in Fig. 4.3 is the spatiotemporal $h(r,t)$ evolution in the flat liquid, flat apertureless extractor geometry. Fig. 4.3(a) shows that the entire surface destabilizes as each vertical spike in the plotted $h(r,t)$ represents a protrusion that has developed from the base liquid surface. The initial electric field $E(t_o)$ possesses small noise induced deviations about the value E_o for the perfectly flat liquid surface. The vertical displacements of protrusion apices become increasingly larger as time progresses and culminates in significant variations in the individual protrusion heights found at the termination time t_f. Fig. 4.3(b) shows the protrusion development along a small segment sampled in r. Though the protrusions possess significantly varying heights, the wavelength selected during linear growth is found to be largely retained throughout the simulated growth. Fig. 4.3(c) presents an inset with a reduced z axis to show the early t liquid surface evolution. The wavelength selection is correctly found to be unbiased by the initially noisy liquid surface as the noise only acts to expedite the observance of the simulated instability by imbuing small perturbations in the initial surface curvature and the resultant electric field $E(t_o)$.

4.4.1.2 Temporal evolution of the instability protrusion apex displacement

Shown in Fig. 4.4 is the temporal evolution of the surface displacement $\overline{\delta h}(t)$ averaged at the instability protrusion apex $r^{apex}(t = t_f)$ coordinates for the flat liquid, apertureless extractor example. Fig. 4.4(a) shows that $\overline{\delta h}(t)$ exhibits an accelerating growth marked by increasing deviations in the individual δh as observed back in Fig. 4.3(a). The linear t, log $\overline{\delta h}$ evolution shown in Fig. 4.4(b) demonstrates that the system exhibits linear growth for a significant time interval. The slope of the fitted line between the 4th ($t = 0.048$ μs) and 9th ($t = 0.128$ μs) sampled time in Fig. 4.6(a) is found to be $(4.52 \pm 0.004) \times 10^7$ 1/s, which is in good agreement to the Eq. 2.157 predicted $s_m = 4.68 \times 10^7$ 1/s for the current system. The early time growth exhibits transient effects resultant from the initial random noise applied to the liquid surface and the aperiodicity imposed by the mismatch between the domain size and the encoded λ_m. Such effects manifest in the large propagated errors for $\ln(\overline{\delta h})$ observed for the early time growth. The late time growth is found to be accelerating away from the linear regime as the protrusion apices have started to undergo nonlinear growth, where it is known that such growth proceeds in a self-similar manner

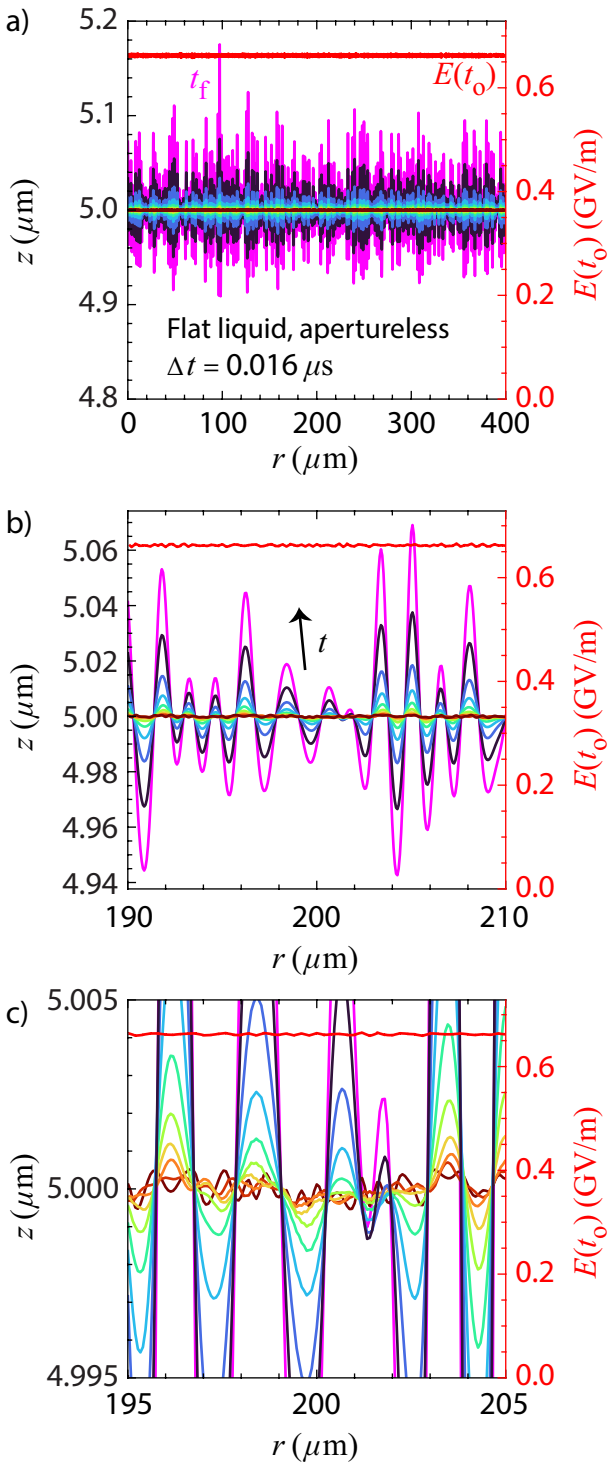

Figure 4.3: Spatiotemporal evolution of flat liquid, apertureless extractor example $h(r,t)$ (colored lines) uniformly sampled in t with Δt over the (a) full domain length, (b) view between r = 190 and 210 μm and (c) inset with reduced z axis. The final $h(r,t_f)$ (pink line) and initial electric field $E(t_o)$ (red line) are also overlaid in all panels. The extractor surface is at z = 100 μm.

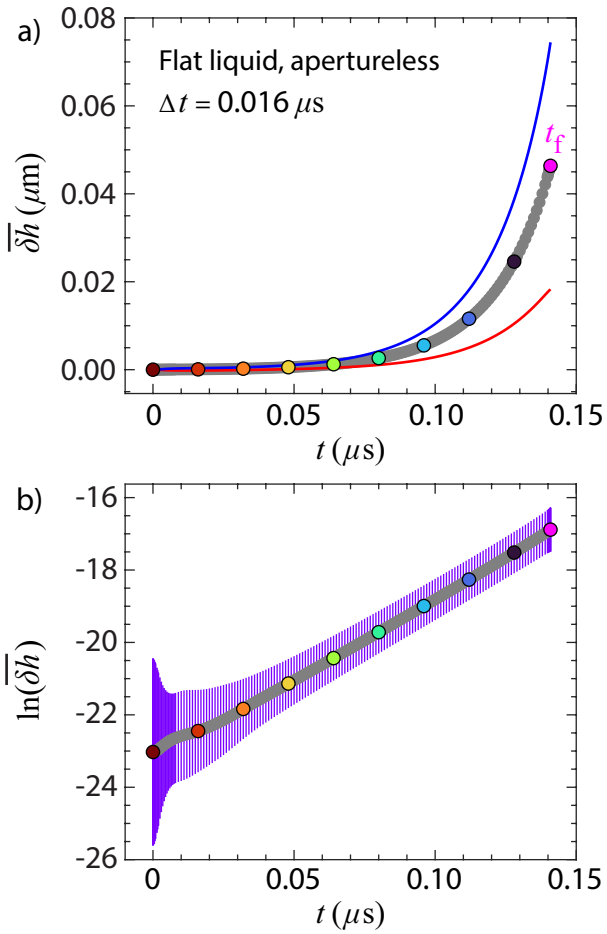

Figure 4.4: Temporal evolution of the instability protrusion apex averaged $\overline{\delta h}(t)$ (grey markers) for the flat liquid, aperture less extractor example in (a) linear-linear and (b) linear-log scales with colored markers sampled at Δt. Blue and red lines in (a) denote values one standard error above and below $\overline{\delta h}$, respectively. Purple lines in (b) are errorbars denoting the propagated standard error for $\ln(\overline{\delta h})$.

[165] leading to a runaway process and finite time blowup of the protrusion apex Maxwell p_M and capillary p_C pressures. The deviation from the linear regime is still only slight even at $t = t_f$ as the simulation is terminated when just a single protrusion apex $E^{apex} \geq 5$ GV/m.

4.4.1.3 Instability power spectrum and growth rate

Shown in Fig. 4.5(a) is the temporal evolution of the Hankel transform power spectrum $PS(k,t)$ extracted from the $h(r,t)$ evolution for the flat liquid, aperture less extractor system. The power spectrum magnitudes have been suppressed from the extra scaling factor L^2/j_n in the discrete Hankel transform Eq. 4.3. This scaling factor also leads to the power spectrum

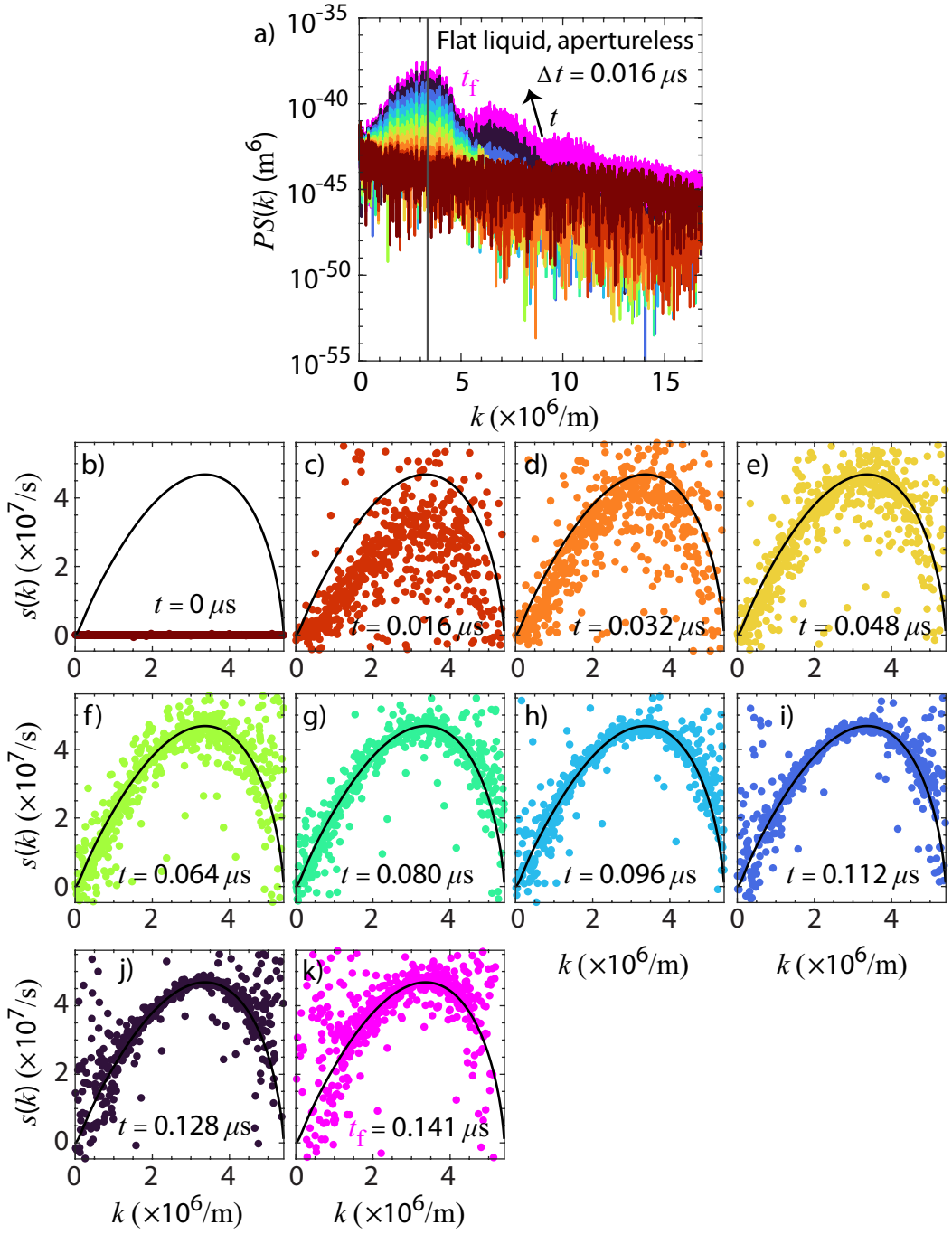

Figure 4.5: Temporal evolution of (a) $h(r,t)$ Hankel transform power spectrum $PS(k,t)$ (colored lines) with k_m (vertical black line) and (b)-(k) extracted growth rate $s(k,t)$ snapshots between $k = 0$ and $k = k_{marg}$ compared against predicted s (curved black line) at sampled t instances for the flat liquid, apertureless extractor example.

units of m^6 that evidently explains the corresponding magnitudes that seem extremely small: taking the sixth root of the power spectrum magnitudes gives sensible values in the nm to μm range as previously found for the $h(r,t) - h_o$ displacements. There is a clear global PS maximum developing at the predicted k_m indicated by the vertical black line from early t, confirming the dominant mode selection as predicted by the de Surgy *et al.* [131, 132] linear stability analysis. The higher harmonics of k_m are also found to develop at late t as the growth transitions into the nonlinear regime.

The growth rate $s(k,t)$ snapshots over $k = [0, k_{marg}]$ at sampled t instances are shown in Fig. 4.5(b)-(k). Fig. 4.5(b)-(e) show that the extracted s quickly converges to the Eq. 2.157 predicted s as the instability develops from the initially noisy surface. It was noted that $s(k, t = 0)$ possesses fluctuations about $s = 0$ that are not visible at the scales provided. Fig. 4.5(f)-(i) confirm the linear growth observed from $\overline{\delta h}$ evolution as the extracted s maintain good agreement with the predicted s. Fig. 4.5(j)-(k) demonstrate the transition from linear to nonlinear growth as the growth rates become increasingly larger than the predicted values for k away from k_m. However, the growth rate agreement for k around k_m is still sustained even at t_f, which confirms the retention of the linear growth encoded dominant instability wavelength observed from the $h(r,t)$ evolution.

4.4.2 Instability development in the flat liquid, apertured extractor geometry

This section presents the simulation results of the surface EHD instability generation in the flat liquid layer, flat apertured extractor geometry.

4.4.2.1 Spatiotemporal surface evolution

Shown in Fig. 4.6 is the spatiotemporal $h(r,t)$ evolution in the flat liquid, flat apertured extractor system. Fig. 4.6(a) first shows that the adding an aperture generates a nonuniform initial E on $h(r,t_o)$ as the presence of an aperture strongly suppresses $E(t_o)$ outside the extractor. This effect has been confirmed to be an aperture generated effect as the domain ceiling height and potential were found to have negligible effect on the generated E. Even under the extractor, $E(t_o)$ does not quite converge to the apertureless value E_o until probed considerably within the extractor length at around $r = 300$ μm. The non-uniform distribution is indeed found to strongly suppress instability development within the aperture. The suppression is induced despite how $E(t_o)$ found inside the aperture is strong enough to generate the dominant $\lambda_m \ll R_{ap}$ for the original apertureless geometry. For reference, the field value $E(t_o) = 0.360$ GV/m found at $r = 0$ would have excited a dominant instability wavelength of $\lambda_m = 6.14$ μm had there been no aperture. This wavelength is still more than

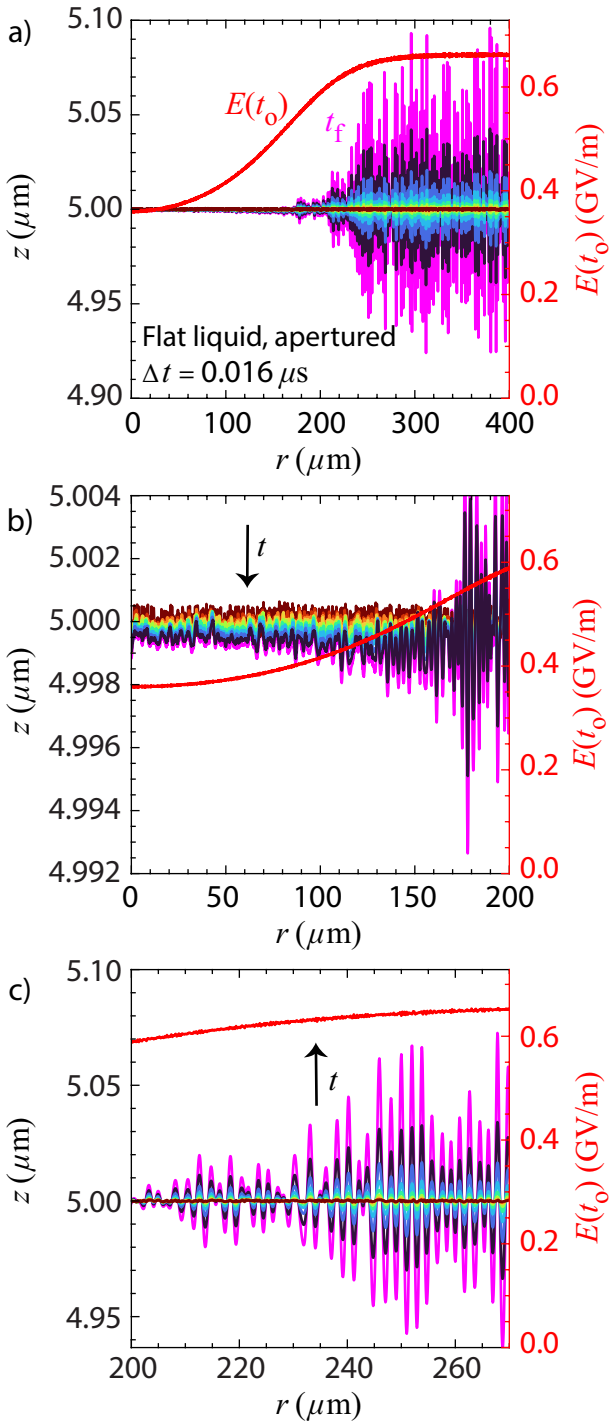

Figure 4.6: Spatiotemporal evolution of flat liquid, apertured extractor example $h(r,t)$ (colored lines) uniformly sampled in t with Δt over the (a) full domain length, (b) within the aperture radius $r \leq 200$ μm and (c) inset under the extractor between $r = 200$ and 270 μm. The final $h(r,t_f)$ (pink line) and initial electric field $E(t_o)$ (red line) are also overlaid in all panels. The extractor surface is at $z = 100$ μm.

an order of magnitude smaller than the aperture radius. The suppression was found not to be generated from viscous effects as the viscous pressure p_V at the surface and shear viscous stress contributions in the bulk inside the aperture were found to be orders of magnitude smaller than the initial p_M even at $t = t_f$ due to the small Ga viscosity of 1.94×10^{-3} Pa s.

Tracking the surface evolution just under the aperture as presented in Fig. 4.6(b) reveals that the liquid under the aperture actually undergoes drainage. This is generated by the nonuniform initial E that generates an initial Maxwell pressure gradient $-\partial p_M/\partial r = \varepsilon_o E \partial E/\partial r$ that drives bulk flow along the positive r direction. Even though the drainage is slight, it is still able to strongly suppress instability development inside the aperture as liquid supply is persistently being redirected towards the surface under the extractor. Shown instead in Fig. 4.6(c) is the inset presenting the surface evolution under the extractor between $r = 200$ and 270 μm. The protrusions increase in height when probed farther into the region under the extractor as the effect of the aperture becomes increasingly minimized. The drainage induced by the aperture does generate an evolving base state from which the surface instability develops. However, since the drainage in Fig. 4.6(b) was found to be minuscule compare to the protrusion heights, the underlying base state profile is seen to be essentially flat in the views provided. It was found (Sec. 4.7) that lowering E_o induced greater drainage from slower instability growth such that the underlying base state under the extractor was clearly found to assume a lobe like shape from the surface of which the instability was found to still develop.

4.4.2.2 Temporal evolution of the instability protrusion apex displacement

Shown in Fig. 4.7 is the temporal evolution of the surface displacement $\overline{\delta h}(t)$ averaged at the instability protrusion apex r coordinates documented at $t = t_f$ in the flat liquid, apertured extractor system. Only the δh for protrusion apices located under the extractor $r \geq 200$ μm have been taken into consideration. Fig. 4.7(a) still shows that $\overline{\delta h}(t)$ exhibits an accelerating growth marked by increasing deviations in the individual δh as observed back in Fig. 4.6(a). The value at $t = t_f$ is slightly smaller compared to the apertureless system as the protrusions close to the aperture possess smaller heights due to the nonuniform $E(t_o)$ generated. Fig. 4.7(b) also still shows that the system undergoes linear growth for a significant time interval between the 4th ($t = 0.048$ μs) and 9th ($t = 0.128$ μs) sampled time in Fig. 4.6(a). This is observed despite an evolving base state from the bulk flow generated by the aperture because the drainage was found to be much smaller than the surface displacements induced by the instability development. The slope of the fitted line is found to be $(4.31 \pm 0.004) \times 10^7$ 1/s, which is also in good agreement with the Eq. 2.157

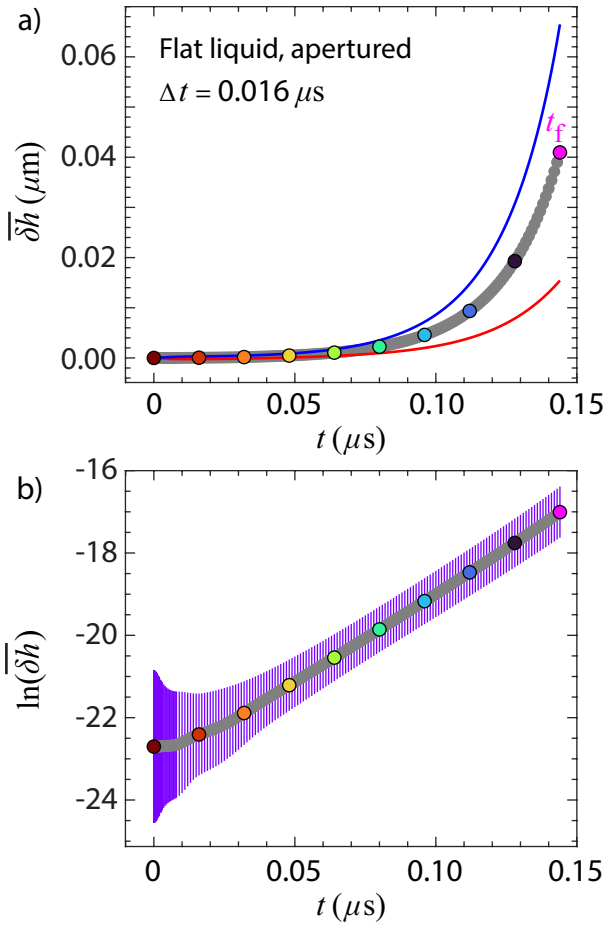

Figure 4.7: Temporal evolution of the instability protrusion apex averaged $\overline{\delta h}(t)$ (grey markers) for the flat liquid, apertured extractor example in (a) linear-linear and (b) linear-log scales. Blue and red lines in (a) denote values one standard error above and below $\overline{\delta h}$, respectively. Purple lines in (b) are errorbars denoting the propagated standard error for $\ln(\overline{\delta h})$.

predicted $s_m = 4.68 \times 10^7$ 1/s for the apertureless system. The very early and late t growth still retain their characteristic behavior induced by transient effects and nonlinear growth, respectively.

4.4.2.3 Instability power spectrum and growth rate

Shown in Fig. 4.8(a) is the temporal evolution of the Hankel transform power spectrum $PS(k,t)$ extracted from the $h(r,t)$ evolution for the flat liquid, apertured extractor system. Again, the power spectrum magnitudes have been suppressed from the extra scaling factor L^2/j_n in the discrete Hankel transform Eq. 4.3. This leads to the power spectrum units of m^6 that suppresses the magnitudes: taking the sixth root gives sensible values in the nm

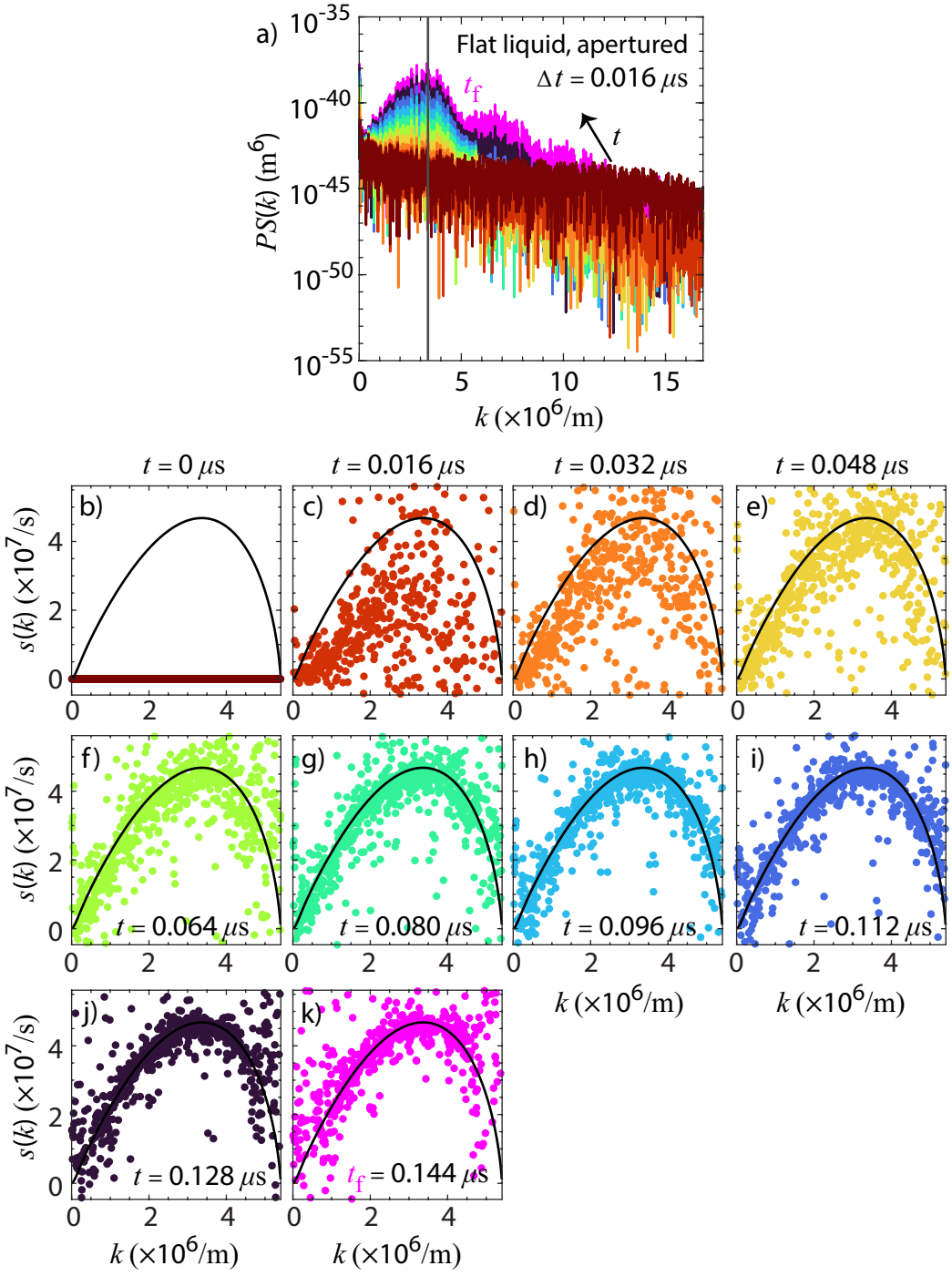

Figure 4.8: Temporal evolution of (a) $h(r,t)$ Hankel transform power spectrum $PS(k,t)$ (colored lines) with k_m (vertical black line) and (b)-(k) extracted growth rate $s(k,t)$ snapshots between $k = 0$ and $k = k_{marg}$ compared against predicted s (curved black line) at the sampled t for the flat liquid, apertured extractor example.

to μm range as previously found for the $h(r,t) - h_o$ displacements. The power spectrum evolution is consistent with that observed for the apertureless counterpart. The early time spectra exhibit the dominant instability mode selection at $k = k_m$ as predicted from the linear stability analysis of the apertureless system. The higher order harmonics are also observed at $t = t_f$. The behavior is observed despite the presence of an aperture as the instability growth induced by strong E_o occurs much faster than the aperture generated bulk drainage. The bulk drainage effects manifest as an additional $PS(k,t)$ maximum located at $k = 0$.

The growth rate $s(k,t)$ snapshots over $k = [0, k_{marg}]$ at sampled t instances are shown in Fig. 4.8(b)-(k). Fig. 4.8(b)-(e) show that the extracted s approaches the Eq. 2.157 predicted s as the instability develops from the initially noisy surface. It was again noted that $s(k, t = 0)$ possesses fluctuations about $s = 0$ that are not visible at the scales provided. Fig. 4.8(f)-(i) show the linear growth observed from $\overline{\delta h}$ evolution as the extracted s exhibit good agreement with the predicted s. The larger spread in the extracted s can be attributed to the absence of instability protrusions within the apertured region that spans the first 200 μm in the r direction. Fig. 4.8(j)-(k) again demonstrate the transition from linear to nonlinear growth, though the growth rates near $k = k_m$ still possess good agreement such that the linear growth encoded dominant instability wavelength is maintained even in the nonlinear regime simulated.

4.4.3 Instability development in the LMIS geometry

This section presents the simulation results of the surface EHD instability generation in the LMIS geometry possessing a liquid metal layer externally wetted to a curved microemitter and placed under an apertured extractor.

4.4.3.1 Spatiotemporal surface evolution

Shown in Fig. 4.9(a)-(b) is the spatiotemporal $h(r,t)$ evolution of the EHD instability mode generated in the LMIS geometry with a curved microemitter and apertured extractor. The initial $E(t_o)$ possesses much larger deviations than those found for the flat liquid counterparts. This is due to the curvature of the initial liquid profile and smaller initial surface mesh element lengths, which in turns induces stronger deviations in the local surface curvature that strongly influences the local electric field value. Nevertheless, the subsequent liquid surface evolution is clearly shown to not be adversely correlated with noise induced deviations initial conditions. It is notable that the underlying field distribution in the inset Fig. 4.9(b) in which the instability protrusions reside closely approximates the

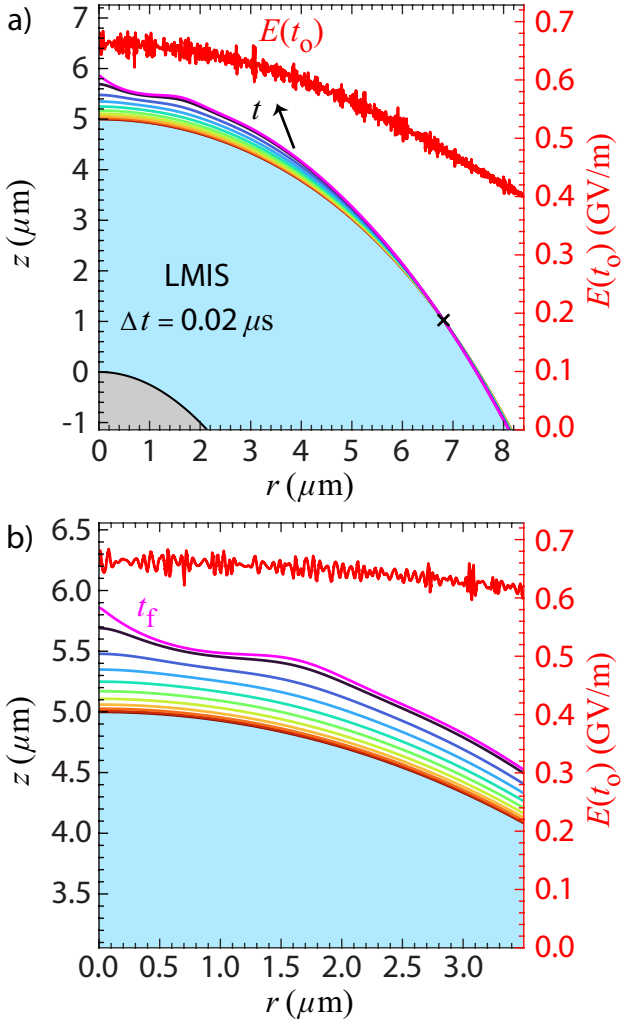

Figure 4.9: Spatiotemporal evolution of $h(r,t)$ in the (a) wide and (b) inset view uniformly sampled in t with Δt (colored lines) and additionally at $t = t_f$ (pink) for the LMIS example. The initial liquid bulk (blue) and microemitter (grey) have also been colored in (a). The extractor surface is at $z = 100\ \mu$m. The black cross marks where $h(r,t_f) = h(r,0)$.

uniform distribution found for the flat liquid, flat apertureless extractor system despite the microemitter curvature and extractor aperture.

As discussed in the previous study (see Ch. 3) on EHD mode development in the current geometry, the instability protrusions are only found within a small region near the microemitter apex given by $r \leq r_s + h_o$. This is due to the local initial E enhancement generated by the microemitter curvature that favorably conditions protrusion development. The enhancement and subsequent instability development is found despite the presence of the extractor aperture, which was found to reduce the field and suppress instability for the liquid inside for the flat liquid counterpart. This clearly demonstrates the strong prevalence of the microemitter curvature over the aperture in determining the ensuing dynamics. The microemitter encodes a negative, nonuniform curvature gradient that additionally generates a stabilizing capillary forcing that persistently acts to try to drain the wetted liquid by flattening the negatively curved liquid free surface. This capillary drainage additionally stabilizes the entire wetted surface against instability development. The nonuniform initial surface E distribution finally encodes a bulk flow that drains supply past the point marked by the cross in Fig. 4.9(a) and directs it into liquid bulk within $r \leq r_s + h_o$ that underpins the instability development. The protrusions were found to be visible from the evolving base state much later in the growth relative to their flat liquid counterparts as better observed in the inset view Fig. 4.9(b). This flow also suppresses instability development for the surface away from $r \leq r_s + h_o$, much like the draining flow found in the flat liquid, apertured extractor system.

4.4.3.2 Most prominent protrusion apex vertical displacement temporal evolution

Shown in Fig. 4.10 is the temporal evolution of the most prominent instability protrusion $\delta h^{apex}(t)$ found for the LMIS geometry. For this example, it happen that $r^{apex} = 0$ such that $\delta h^{apex}(t)$ can be simply tracked by evaluating $z^{apex}(t) - h_o$ throughout the entire simulated growth. The linear t, log δh^{apex} scale shown in Fig. 4.10(b) indeed reveals that the protrusion development can no longer be described by a linear growth of $\exp(st)$ found for the flat liquid counterparts. This is expected as the protrusions instead develop from an evolving base state that grows from the bulk flow induced by the curvature enhanced E. In fact, tracking the evolution in the double logarithmic scale shown in Fig. 4.10(c) indicates that δh^{apex} undergoes a power law growth for much of the evolution leading to late time growth. The fitted power law exponent between the second ($t = 0.02$ μs or $\log(t) = -17.7$) and ninth ($t = 0.16$ μs or $\log(t) = -15.6$) sampled times is 2.05 with standard error 3.31×10^{-3}, consistent with the exponents found in Sec. 3.5. As the surface was found to

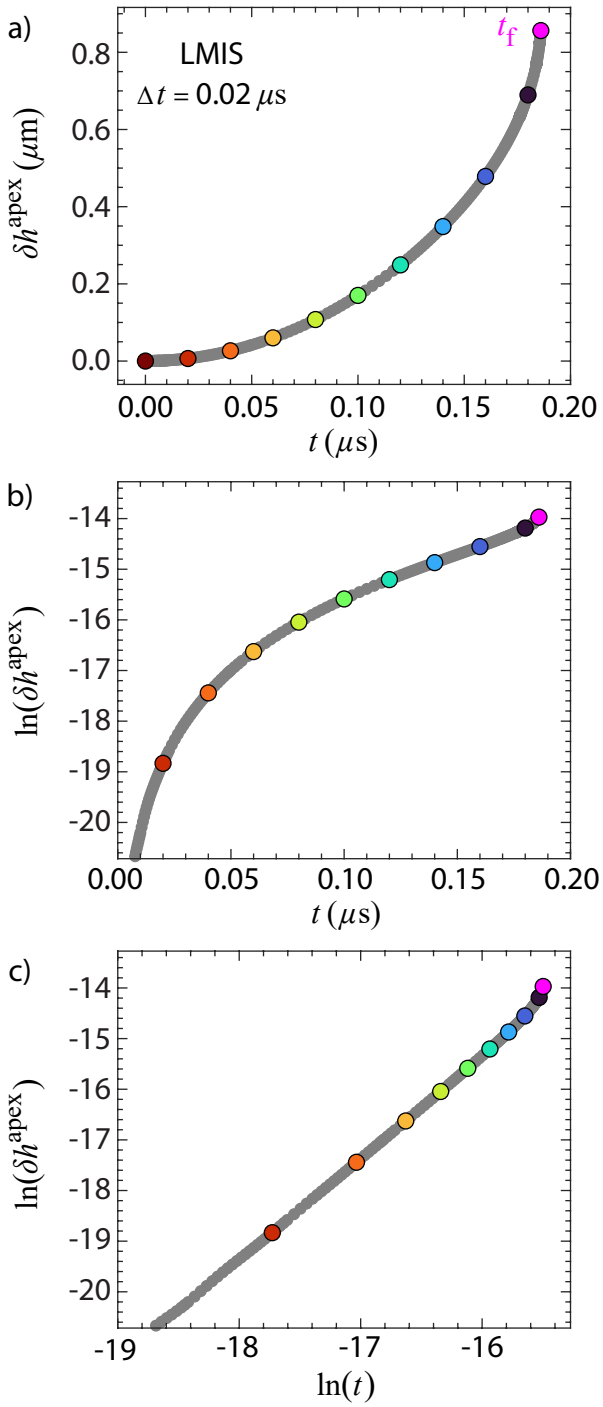

Figure 4.10: Temporal evolution of most prominent protrusion apex $\delta h^{apex}(t)$ in (a) linear-linear, (b) linear-log and (c) log-log scales for the LMIS example.

exhibit no protrusion development for much of the fitting interval, the power law growth can be then attributed to the evolving bulk rather than the instability. The late time growth deviates from the power law growth as the protrusion apex develops from the evolving bulk. Preliminary analysis indicates that the growth is self-similar, which is further investigated in Ch. 5.

4.4.3.3 Instability power spectrum and growth rate

Shown in Fig. 4.11(a) is the temporal evolution of the Hankel transform power spectrum $PS(k,t)$ extracted from the $h(r,t)$ evolution for the LMIS system. Again, the power spectrum magnitudes have been suppressed from the extra scaling factor L^2/j_n in the discrete Hankel transform Eq. 4.3. This scaling factor also leads to the power spectrum units of m^6 that evidently explains the corresponding magnitudes that seem extremely small: taking the sixth root of the power spectrum magnitudes gives sensible values in the nm to μm range as previously found for the $h(r,t) - h_o$ displacements. The power spectrum at all t possesses a global maximum at $k = 0$. The initial $t = 0$ spectrum over the shown k also possesses a strongly jagged profile reflecting the noisy initial liquid surface. Many of the jagged variations actually become amplified as time progresses. This is due to the fact that although the surface perturbations are orders of magnitude smaller than h_o, the derived variations in the electric field were shown in Sec. 4.4.3.1 to not be equally minuscule compared to the underlying field distribution. Such variations are generated from the strong local curvatures encoded by the small element side lengths used to mesh the perturbed initial surface. As the electric field tends to amplify the individual roughness encoded by the random noise, the power spectrum signatures associated with the noise also become amplified during the growth. The instability development also only results in a handful of protrusions, which further reduces its spectral content.

Despite these difficulties, the power spectrum at $t = t_f$ exhibits a clear local maximum away from $k = 0$ as accentuated in the inset that provides a magnified view in the linear k, linear $PS(k,t)$ scale. Unlike the maxima in the flat liquid systems, this maximum is only a local maximum as it is orders of magnitude smaller than that at $k = 0$. The content at k lower than that of the local maximum may be associated with the underlying system geometry possessing the characteristic length scales h_o ($k = 2\pi/h_o = 0.126 \times 10^7$ 1/m), r_s ($k = 2\pi/r_s = 0.314 \times 10^7$ 1/m) and $h_o + r_s$ ($k = 2\pi/(h_o + r_s) = 0.090 \times 10^7$ 1/m). As the instability protrusions are small relative to the liquid thickness and do not extend past $r = r_s + h_o$, the spectral content associated with the instability is indeed weaker than that encoded by the underlying geometry. It is also interesting to note that this local maximum is

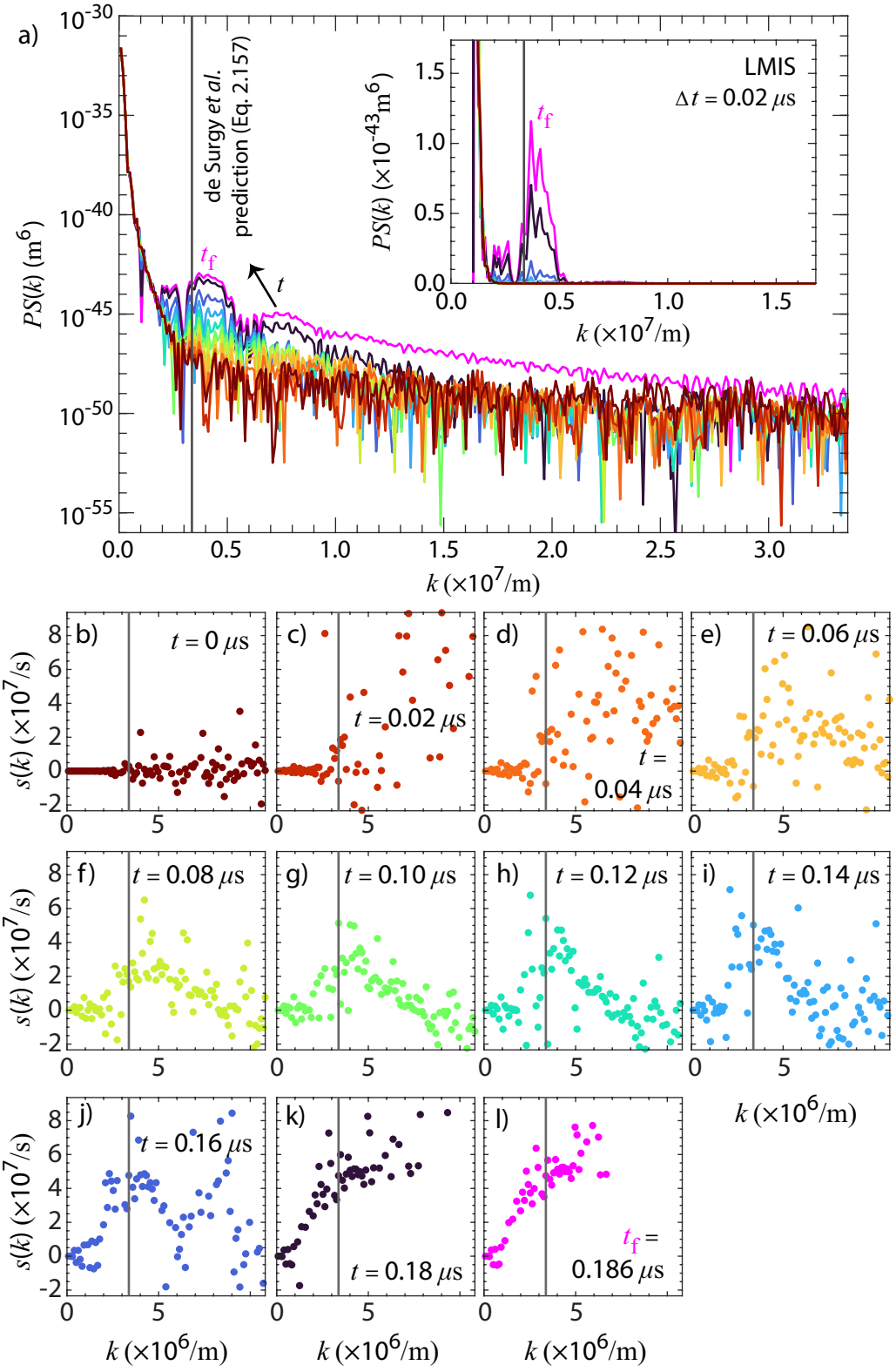

Figure 4.11: Temporal evolution of (a) $h(r,t)$ Hankel transform power spectrum $PS(k,t)$ (colored lines) and (b)-(l) extracted growth rate $s(k,t)$ snapshots at the sampled t for the LMIS example. Eq. 2.157 predicted k_m (vertical black line) is also given for comparison for each panel. The inset in (a) shows $PS(k,t)$ in a double linear scale.

found to be located closely to k_m predicted by Eq. 2.157 for the flat liquid, flat apertureless extractor system just from having substituted h_o and $E_c = E_o$ measured at the initial liquid apex. The spectrum also exhibits the second harmonic of the local maximum as seen in the main linear k, log $PS(k,t)$ scale. This maximum has been thereby cataloged as the LMIS system dominant instability wavenumber k_{sim}.

The growth rate $s(k,t)$ snapshots at sampled t instances are shown in Fig. 4.11(b)-(l). Only the simulation extracted $s(k,t)$ have been plotted as there exists no prior analytical prediction applicable for such LMIS geometry. Fig. 4.11(b)-(d) shows the early stage growth that possesses no particular structure as it dominated by the amplification of the random noise. However, $s(k,t)$ in Fig. 4.11(e)-(i) exhibits a visible maximum around k_m predicted by Eq. 2.157 for the flat liquid, flat apertureless extractor system. The instability signature arises in k space despite $h(r,t)$ at the same sampled times not yet having visibly developed instability protrusions. Fig. 4.11(j)-(l) show the rapid emergence of higher harmonic signatures as the growth rates away from k_m become far greater than the vertical view provided. The low k growth rates also come to possess a mirrored profile about $s(k) = 0$.

4.4.3.4 Example of LMIS instability with a non-axial most prominent protrusion

The LMIS instability example discussed in this section possesses the most prominent protrusion that develops axially at $r = 0$. However, such a protrusion in the wave-like chain can also develop non-axially as sampled in Fig. 4.12 for $h_o = 2$ μm, $r_s = 1$ μm and $\phi_o = 10$ kV. Tables 4.4-4.5 indeed show that the most prominent protrusion apex coordinate r_f catalogued for the conducted LMIS instability simulations can take widely varying values with no discernible correlations for the axial/non-axialness to the key initial variables h_o, r_s and ϕ_o. It also needs not be the protrusion that is closest to $r = 0$: that for the example sampled in Fig. 4.12(a) is actually the second closest protrusion that is located at $r_f = 0.70$ μm.

Spectral analysis of $h(r,t)$ evolution for such systems is conducted in the exact same manner as conducted for the axial apex counterparts. Fig. 4.12(b) presents the power spectrum temporal evolution, which exhibit the same qualitative behavior as that sampled for the axial apex counterparts. There still exists a global maximum at $k = 0$ indicating bulk flow with early time $PS(k,t)$ distribution that reflect the random noise applied to the initial surface. There arise now two local maxima with highly comparable magnitudes near k_m predicted by Eq. 2.157, where the maximum with the larger magnitude has been cataloged as k_{sim}. Higher harmonics of the two local maxima are also readily visible in the shown spectrum

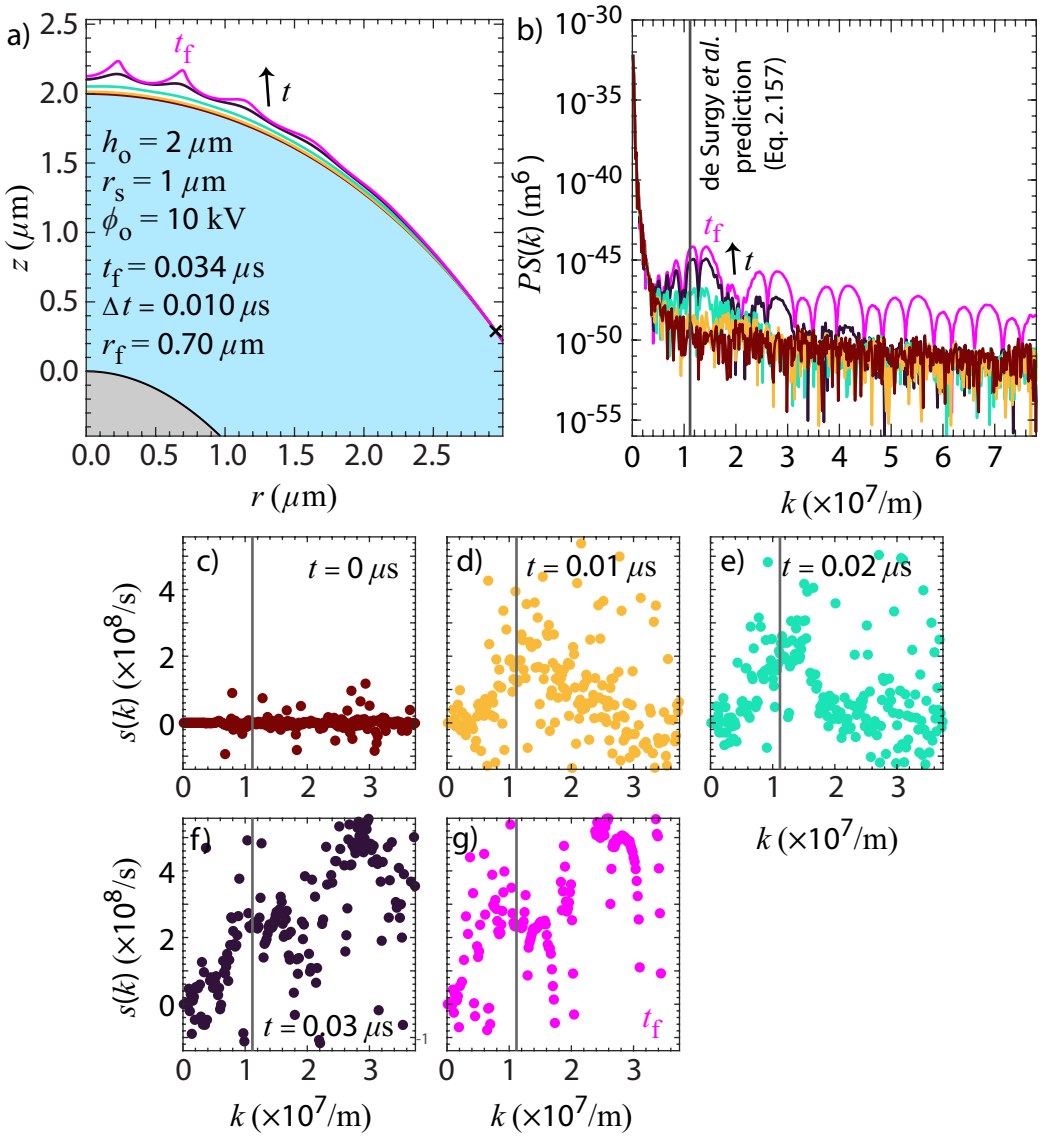

Figure 4.12: Spatiotemporal evolution of (a) $h(r,t)$ and (b) $PS(k,t)$ uniformly sampled in t with Δt (colored lines) and additionally at $t = t_f$ (pink) for a LMIS instability example with $r_f > 0$. The initial liquid bulk (blue) and microemitter (grey) have also been colored in (a). The black cross in (a) marks where $h(r,t_f) = h(r,0)$. The extractor surface is at $z = 100\ \mu$m. The inset in (b) shows $PS(k,t)$ in a double linear scale. Eq. 2.157 predicted k_m (vertical black line) is also given for comparison for (b)-(g).

evolution.

The growth rate $s(k,t)$ snapshots at sampled t instances are shown in Fig. 4.12(c)-(g) show similar qualitative behavior as that sampled for the axial most prominent protrusion apex example. Fig. 4.11(d)-(e) exhibits a discernible maximum around k_m predicted by Eq. 2.157 for the flat liquid, flat apertureless extractor system, albeit with a greater spread due to the presence of the doubled $PS(k,t)$ maxima. Again, this signature arises despite the lack of visible protrusions in the sampled $h(r,t)$. Fig. 4.11(f)-(g) indeed show the emergence of higher harmonic signatures as the growth rates away from k_m become much greater than that of the original instability signature.

4.4.4 Comparison of dominant wavenumber extracted from LMIS instability to de Surgy *et al.* prediction for flat liquid instability

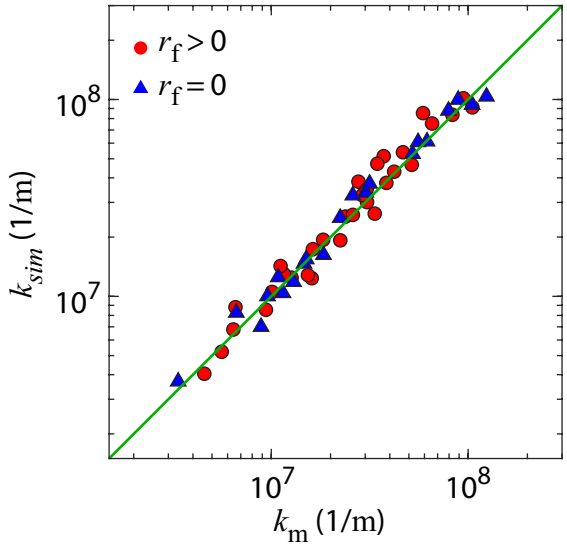

Figure 4.13: Comparison of LMIS instability extracted k_{sim} to Eq. 2.157 predicted k_m for flat liquid instability. The markers have been coded by the most prominent protrusion apex $r_f = 0$ (blue triangle) or $r_f > 0$ (red circle). Green line denotes $k_m = k_{sim}$.

The dominant wavenumbers k_{sim} extracted from the LMIS instability mode systems simulated for this study are compared against the k_m predicted from the linear stability analysis of the "equivalent" flat liquid, flat apertureless extractor geometry. The predicted k_m have been calculated from Eq. 2.157 just by substituting h_o for the liquid thickness, $b = 100\ \mu\text{m} - h_o$ for the vacuum thickness and $E_a = E_o$ extracted from the initial liquid apex at $r = 0$. The wavenumbers k_{sim} have been extracted regardless of whether the most prominent protrusion apex forms axially $r_f = 0$ as shown in Fig. 4.9 or non-axially $r_f > 0$ as sampled in Fig. 4.12.

Fig. 4.13 shows that the extracted k_{sim} are in excellent agreement with k_m irrespective of the axial/non-axialness of the most prominent protrusion apex location. A power law fit between k_m and k_{sim} yields an exponent of 1.01 ± 0.02, which is almost perfectly linear and supports the visual agreement found in Fig. 4.13. This agreement arises despite the nonlinear instability suppression mechanisms and the evolving base state induced by the curved microemitter and apertured extractor, which were not modeled in the de Surgy *et al.* linear stability analysis. It is also found despite the characteristic liquid thickness h_o and electric field E_o values having been taken from the initial state of the system despite the observed evolution of the mode generating liquid bulk.

The initial electric field distribution shown in Fig. 4.9(a) indicates that it is primarily determined by the microemitter curvature and not the extractor aperture, which was also shown back in Ch. 3. The surface profile is also $O(100\ \mu\text{m})$ away from the aperture plane and the instability develops on the liquid apex region contained within the aperture, which all indicate that the aperture exerts little influence on the instability development in the LMIS geometry. As for the microemitter curvature, the initial electric field distribution in the instability developing region has been found to closely approximate an uniform distribution as found in the flat liquid, flat apertureless extractor geometry.

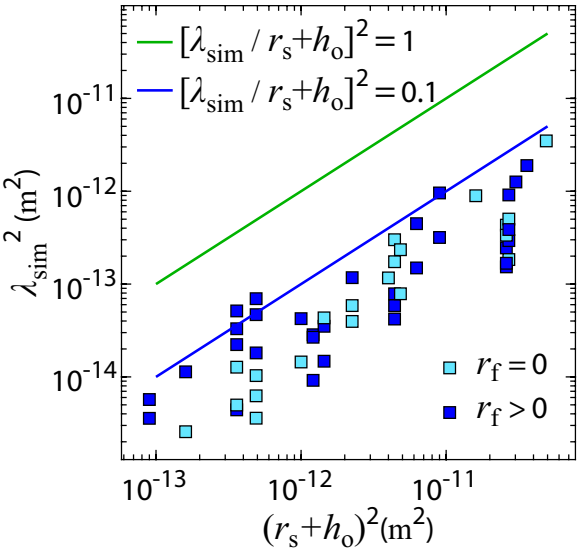

Figure 4.14: Comparison between $(r_s + h_o)^2$ and extracted λ_{sim}^2 for LMIS instability systems possessing $r_f = 0$ (light blue squares) and $r_f > 0$ (dark blue squares). The denoted lines represent $[\lambda_{sim}/r_s + h_o]^2 = 1$ (blue) and $[\lambda_{sim}/r_s + h_o]^2 = 0.1$ (green).

The correlation prompts a comparison between $r_s + h_o$ and extracted λ_{sim}. The comparison of the length scales squared shown in Fig. 4.14 demonstrates that the cataloged instability systems possess λ_{sim}^2 that is at most around a tenth of and generally significantly less than the

local domain width squared $(r_s + h_o)^2$ available for mode generation (the ratios $[\lambda_{sim}/(r_s + h_o)]^2$ can be found in Tables 4.4 - 4.5). As the aspect ratio squared $[h_o/(r_s + h_o)]^2$ arising out of the nondimensionalized Navier-Stokes equation (Eq. 2.56) determines whether the liquid layer can be taken to be thin or thick, the squares of the two characteristic length scales have been compared in the same spirit to determine whether the liquid surface curvature can be taken to be relatively flat compared to the instability wavelength. Indeed, the comparison shows that this holds for the simulated LMIS instability systems and thereby explains the strong linear correlation between k_m and k_{sim}.

4.5 Discussion

This section offers discussion on the LMIS liquid reservoir, consequences of a gravityless system and LMIS geometry limited instability mode generation.

4.5.1 LMIS liquid reservoir

The LMIS geometry additionally possesses a flat liquid reservoir of thickness 10 μm wetted to the domain floor with a vertical gap distance of 290 μm. The reservoir mimics the liquid in the flat liquid, flat apertureless extractor system such that if a strong electric field is applied, the surface will be destabilized and give rise to protrusions that could eventually give rise to undesirable ion emission to the extractor underside. However, no instability development were found at the reservoir for the LMIS simulations. This is primarily due to the reservoir λ_m predicted by Eq. 2.157 with liquid thickness 10 μm and electric field $\phi_o/290$ μm being comparable or larger than the chosen extractor span of 200 μm as shown in Table 4.3. The same is true for the marginally stable wavelength λ_{marg} such that no unstable wavelengths can be fitted within the chosen extractor span for the majority of ϕ_o applied. There is also the fillet that stitches the reservoir to the liquid wetted to the microemitter that generates drainage from its positive surface curvature that further stabilizes the reservoir surface against instability development. The reservoir was also found to hardly deform during the simulated t_f as the instability develops over timescales orders of magnitude smaller than the characteristic instability growth timescale $2\pi/s_m$ predicted for the reservoir.

4.5.2 Consequences of a gravityless system

The original stability analysis conducted by de Surgy *et al.* [131, 132] included gravity as another force acting on the liquid. The original dispersion relation with gravity [132] is

$$\begin{gathered} 4qk^3\left[q - k\coth(kh_o)\coth(qh_o)\right] - \\ (q^2+k^2)^2\left[q\coth(kh_o)\coth(qh_o) - k\right] + \\ \frac{4qk^2(q^2+k^2)}{\sinh(kh_o)\sinh(qh_o)} = \\ \frac{\rho}{\mu^2}\left[\gamma k^3 - \varepsilon_o E_a^2 k^2\coth(kb) + \rho g k\right]\left[q\coth(qh_o) - k\coth(kh_o)\right] \end{gathered} \tag{4.8}$$

which only differs from Eq. 2.157 by the extra $\rho g k$ term on the RHS of the equality. The effect of gravity on the stability of the liquid surface can be first probed through considering the condition for marginal stability in which $s = 0$ for nonzero k. For systems under gravity, the condition is known to be

$$\gamma k^3 - \varepsilon_o E_a^2 k^2\coth(kb) + \rho g k = 0 \tag{4.9}$$

which is independent of the liquid viscosity and thickness. Though there is the $\coth(kb)$ factor resultant from the liquid surface to extractor plane gap distance b, it will suffice to examine the outcomes in the two asymptotic limits of the thick (i.e. $kb \gg 1 \rightarrow \coth(kb) = 1$) and thin (i.e. $kb \ll 1 \rightarrow \coth(kb) = 1/kb$) vacuum. The thick vacuum limit is most applicable for the simulated geometries as $b = 100$ μm is at least an order of magnitude larger than the largest predicted λ_m cataloged in Tables 4.4-4.5. For the thick vacuum limit, the nontrivial solutions for k are

$$k = \frac{\varepsilon_o E_a^2 \pm \sqrt{\varepsilon_o^2 E_a^4 - 4\gamma\rho g}}{2\gamma} \tag{4.10}$$

Since k was taken to be a real number in the analysis, the term under the square root must also be positive, leading to a condition on the applied electric field strength must exceed the value given by

$$E_{crit} > \sqrt{\frac{2}{\varepsilon_o}\sqrt{\gamma\rho g}} \tag{4.11}$$

which is indeed the critical field strength required to destabilize the liquid metal surface as found by Tonks [145] and Frenkel [47]. A similar criterion arises for the thin vacuum limit as Eq. 4.9 reduces to

$$\gamma k^2 - \varepsilon_o \frac{E_a^2}{b} + \rho g = 0 \tag{4.12}$$

where the solution for k is

$$k = \sqrt{\frac{\varepsilon_o E_a^2/b - \rho g}{\gamma}} \tag{4.13}$$

such that for a real k, the applied field must exceed

$$E_{crit} > \sqrt{\frac{\rho g b}{\varepsilon_0}} \tag{4.14}$$

where now the field depends on the vacuum thickness b instead of the surface tension γ. For both vacuum limits, the applied electric field must exceed a critical value to destabilize the surface in the presence of gravity. However, in the absence of gravity $g = 0$, the critical electric field for instability vanishes for both thin and thick vacuum, meaning that the surface is always unstable under any applied E_a.

As the simulations were conducted without gravity, it is best to consider whether adding gravity would have significantly affected the extracted results. The first consideration can be made by simply calculating E_{crit} applicable for the simulated flat liquid, flat apertureless extractor geometry. As $b = 100\ \mu\text{m} - h_o$ is many orders of magnitude larger than the dominant λ_m, E_{crit} for the thick vacuum limit is appropriate and yields 6.84×10^6 V/m. This value is more than an order of magnitude less than the smallest E_o generated in the LMIS simulations cataloged in the previous study (see Ch. 3), much less those found to generate the instability mode as cataloged in Tables 4.4-4.5. Another consideration that can be taken is to calculate the Bond number Bo. The definition of Bo for the LMIS geometry consistent with the scaling analysis used previously is $\text{Bo} = \rho g h_o / p_c$ where $p_c = -\varepsilon_o E_c^2/2 = -\varepsilon_o \phi_o^2/[2(r_s + h_o)^2]$ as E_c taken at the initial liquid apex is known to dominantly scale as $\phi_o/(r_s + h_o)$. This gives $\text{Bo} = 2\rho g h_o (r_s + h_o)^2/\varepsilon_o \phi_o^2$. Evaluating the number for the worst case combination of $h_o = 5\ \mu$m, $r_s = 5\ \mu$m and $\phi_o = 4.0$ kV from the simulated instability system parameters yields the maximum $\text{Bo} = 4.22 \times 10^{-7}$, which indeed shows that gravity is negligible for the modeled system over the h_o, r_s and ϕ_o simulated. For the flat liquid systems, p_c can be defined as just $p_c = -\varepsilon_o E_a^2/2$ where E_a is the electric field applied to the liquid surface. The worst case scenario of $E_a = 0.662$ GV/m and $h_o = 5\ \mu$m still only gives the maximum $\text{Bo} = 1.54 \times 10^{-7}$ such that the gravity is negligible for the modeled systems.

4.5.3 LMIS geometry limited instability mode generation

The comparison between λ_{sim}^2 and $(r_s + h_o)^2$ shown in Sec. 4.4.4 shows $[\lambda_{sim}/(r_s + h_o)]^2 \ll 1$ to explain the strong linear correlation between k_m and k_{sim}. This fact about the two characteristic lateral length scales can also be interpreted as the microemitter curvature providing an additional stabilizing effect derived from geometric considerations as it sets an effective domain size only within which the protrusions are able to form. This can be restated into the observation that the field strength needed to excite the instability mode for the LMIS

geometry depends on the available domain width provided by $r_s + h_o$, which is consistent with the observations found from previous analysis [53, 54, 133] and experiments [54, 132] for flat liquid systems that have been laterally bounded in cylindrical and rectangular baths. Indeed, the experiments have noted that for flat liquid bath sizes made comparable or smaller than the predicted instability wavelength, the surface gave rise to growths of single protrusions instead of the instability. This is consistent with the previously cataloged observance of the single protrusion axial and coronal (i.e. non-axial protrusion) EHD modes (see Ch. 3) and even the drainage EHD mode (i.e. drainage of wetted liquid with no protrusion development) in the same LMIS geometry. The λ_m encoded for such modes were indeed found to be larger than those for the instability systems for the same $(r_s + h_o)$ and above the threshold line $[\lambda_m/(r_s + h_o)]^2 = 0.1$.

4.6 Conclusion

The computational simulations described in this work probe the effect of an extractor aperture and curved microemitter on the liquid metal surface EHD instability development from the base flat liquid layer, flat apertureless extractor geometry. Adding an aperture to the flat liquid, flat apertureless extractor geometry strongly suppresses instability formation inside the aperture by encoding a nonuniform electric field distribution weakening inside the aperture that ultimately generates stabilizing liquid drainage. This suppression occurs despite the electric field strengths still being strong enough to encode dominant instability wavelengths that are much smaller than the aperture radius. Adding a curved microemitter to the flat liquid, apertured extractor system instead strongly confines instability development to within just the liquid tip region $r \leq r_s + h_o$. The negative, nonuniform microemitter curvature encodes stabilizing capillary drainage acting to flatten the curved liquid surface and also generates a locally enhanced initial electric field distribution that drains liquid past $r \leq r_s + h_o$. Despite the instability suppression mechanisms generated by the addition of extractor aperture and microemitter curvature, the instability wavenumbers extracted from the LMIS instability mode systems possess excellent agreement with those predicted from the flat liquid layer, flat apertureless extractor geometry linear stability analysis [131, 132] when the initial liquid apex electric field value is substituted as the characteristic field value. This arises due to the smallness of the extracted instability wavelength squared compared to $(r_s + h_o)^2$, which places the instability generating liquid surface to be well approximated as a flat surface. The strong linear correlation equips researchers with a simple estimate of the characteristic instability wavelength encoded for similar LMIS geometries under similar initial conditions. This may potentially equip researchers with the ability to control the generated instability wavelength for applications where such formations are desirable.

4.7 Appendix A: Instability development in the flat liquid, flat apertured extractor with a weakly applied field

The example shown for the instability development in the flat liquid, flat apertureless extractor possessed such strong electric fields so that the drainage of liquid inside the aperture was minimal. The minimal drainage was observed despite the fact that E_a chosen was the lowest value of the LMIS initial liquid apex E_o that generated the instability for the systems simulated. The draining motion and the effect of the extractor aperture have been probed further by conducting another simulation in which h_o is the same as the example shown in Sec. 4.4.2 but E_a has been reduced to half the original value. This results in the updated values of $\lambda_m = 7.14$ μm and $\beta_m = 6.16 \times 10^6$ 1/s, which encodes a much slower instability growth compared to the original example.

The slow down in the instability development is indeed able to reveal the liquid drainage in more detail as shown in Fig. 4.15(a). The drainage is shown to be able to continuously suppress instability development inside the aperture. The drained liquid is directed under the extractor, where the instability protrusions close to the aperture are found to develop out of the growing liquid bulk.

The temporal evolution of the $h(r,t)$ power spectrum is shown in Fig. 4.15(b). Though the dominant instability mode as predicted from the apertureless geometry is still found to be selected, there is now a clear additional peak at $k = 0$ that represents the spectral content of the underlying liquid bulk motion. The growth rate $s(k,t)$ snapshots shown in Fig. 4.15(c)-(l) further support the observation. The extracted curves in Fig. 4.15(f)-(l) possess good agreement with the prediction except for low k. There, the growth rates are larger than those predicted in the absence of the aperture due to the persistent presence of the draining bulk motion throughout the evolution.

4.8 Appendix B: Instability confinement from initial pressure gradient

It was noted in the previous study (see Ch. 3) that all protrusion developing EHD mode generation in the LMIS geometry was confined within $r \leq r_s + h_o$. Examination of the initial pressure gradient $-\partial p/\partial r$ for the capillary p_C and Maxwell p_M revealed a global maximum for $-\partial p_C/\partial r = 2\gamma\partial\mathcal{K}_h/\partial r$ and a global minimum for $-\partial p_M/\partial r = [\varepsilon_o\partial(E^2)/\partial r]/2 = \varepsilon_o E\partial E/\partial r$ at around the same r and within $r \leq r_s + h_o$.

A similar behavior for the initial $-\partial p_M/\partial r$ is confirmed for the flat liquid, apertured extractor example as shown in Fig. 4.16(a). There is no initial capillary pressure gradient as the initial surface is perfectly flat. The gradient shown in the panel is that averaged every 10 mesh elements as the fluctuations generated by the random noise injected to the initial liquid

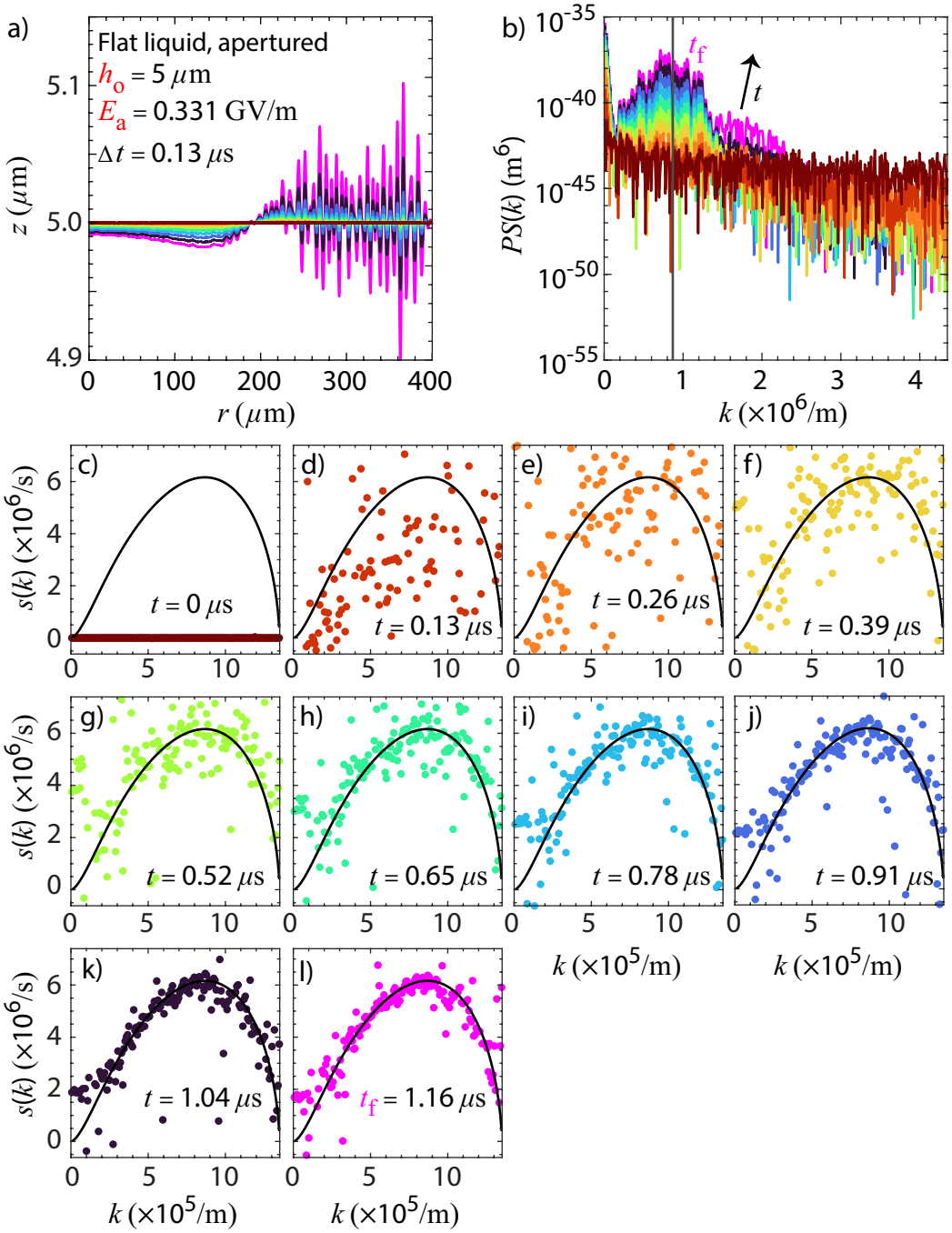

Figure 4.15: Instability development in the flat liquid, flat apertured extractor geometry with $h_o = 5\ \mu$m and $E_a = 0.331$ GV/m. The extractor surface is at $z = 100\ \mu$m. (a) Spatiotemporal evolution of $h(r,t)$ (colored lines) uniformly sampled in t with Δt and additionally $h(r,t_f)$ (pink line). (b) Temporal evolution of $h(r,t)$ power spectrum $PS(k,t)$ (colored lines) with k_m (vertical black line). (c)-(l) Extracted growth rate $s(k,t)$ snapshots between $k = 0$ and $k = k_{marg}$ compared against predicted s (curved black line) at sampled t instances.

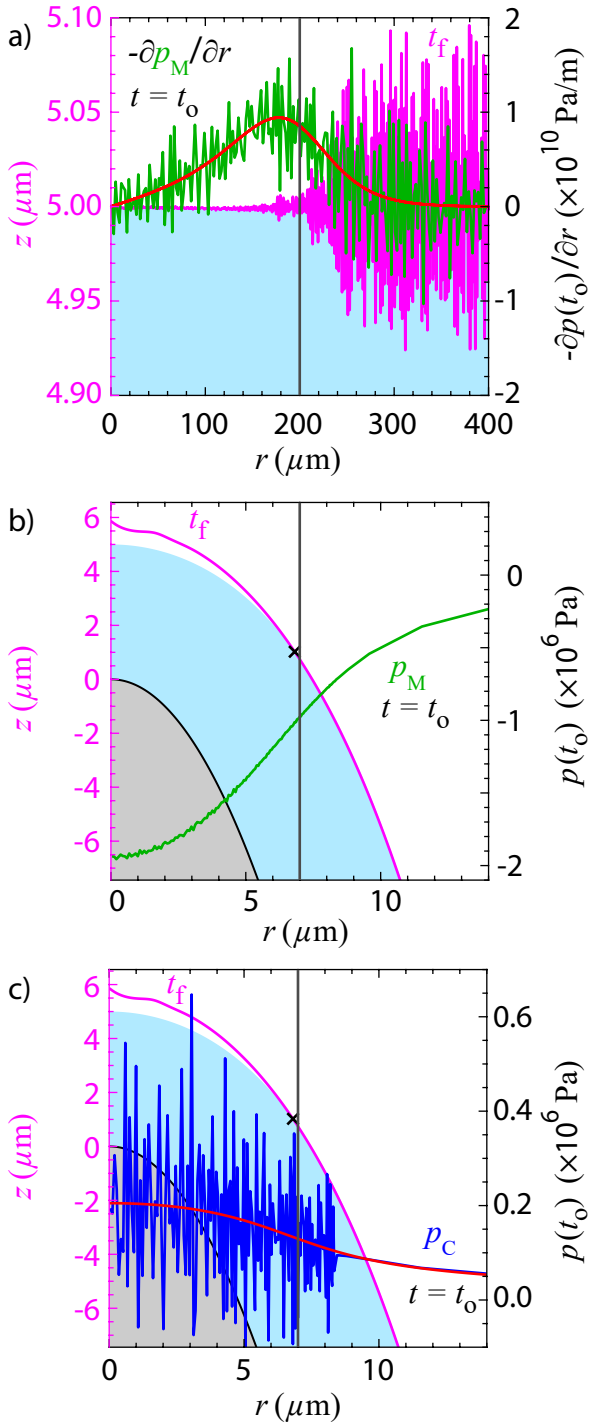

Figure 4.16: Instability confinement from initial pressure gradient in the flat liquid, flat apertured extractor and LMIS geometry. (a) Initial $-\partial p_M/\partial r$ and $h(r, t_f)$ (pink) for the flat liquid, flat apertured extractor system. Green curve is $-\partial p_M/\partial r$ averaged every 10 mesh elements. Red curve is that calculated for the noiseless liquid surface. Vertical line marks the aperture radius. (b) Initial p_M (green) and (c) p_C (blue) averaged every 10 mesh elements with and $h(r, t_f)$ (pink) for the LMIS system. The red curve in (c) is the analytic p_C for the noiseless liquid surface. Initial liquid bulk (blue) and microemitter (grey) shown wherever applicable. The black cross marks where $h(r, t_f) = h(r, 0)$. Vertical line marks $r = r_s + h_o$.

surface was found to conceal the underlying gradient profile. Despite the noise induced fluctuations, the averaged behavior is found to track that calculated for the noiseless initial liquid surface. The gradient is now oppositely signed compared to the LMIS counterpart to correctly encode an initial flow that immediately starts to drain the liquid under the aperture and direct it under the extractor. The global maximum is located at around $r = 178$ μm for the example, which is near but not exactly at the aperture radius $r = 200$ μm. This location is found to confine instability development to its right in the direction of the drainage flow.

The random noise applied to the liquid surface mesh for the LMIS geometry also induced similar issues with visualizing the underlying gradient profile for the Maxwell p_M and now also the capillary pressure p_C generated by the microemitter curvature. The surface curvature and the smaller mesh element sizes induced fluctuations much more significant than those found in the flat liquid counterparts. For this reason, the two pressures averaged over every 10 elements are plotted instead for the LMIS geometry example along with $h(r, t_f)$ in Fig. 4.16(b) for p_M and Fig. 4.16(b) for p_C. The deviations in the averaged p_C are still much greater than those for p_M as it directly reflects the noise induced modifications to the local surface curvature. However, the underlying distribution is still found to track the predicted profile for the noiseless surface. The two pressures on average indeed possess the largest magnitudes at $r = 0$. It can be reasoned that the inflection points for the two pressures are located near $r = r_s + h_o$. The sign of $-\partial p/\partial r$ is then positive for p_C and negative for p_M, indicating the opposing directions of the flow encoded by the two pressures. The Maxwell contributions prevails over the capillary contribution for the instability systems examined in this study such that the net initial flow supplies liquid towards $r = 0$. This thereby strongly conditions the ensuing instability development to be confined within $r \leq r_s + h_o$.

4.9 Appendix C: Comparison between full dispersion curve and asymptotic limits for simulated systems

Shown in Fig. 4.17 is the comparison between the dispersion curve calculated from Eq. 2.157 and those calculated from Eq. 2.158-2.161 in the asymptotic thin/thick and inviscid/viscous liquid limits for the example listed in Table 4.2. It can be seen that for the chosen example, the thick inviscid liquid $s(k)$ best approximates the actual $s(k)$ calculated directly from Eq. 2.157 as λ_m is smaller than h_o and Re is substantially larger than 1. All other limits overestimate $s(k)$ by at least an order of magnitude. Tables 4.4-4.5 show that the parameters leading to the LMIS instability mode generally place the system better approximated by the inviscid limit than the viscous limit as $\mathsf{Re} \gg 1$. Comparisons between h_o and λ_m show that the ratio h_o/λ_m can span from the thin to thick limit depending on the system conditions.

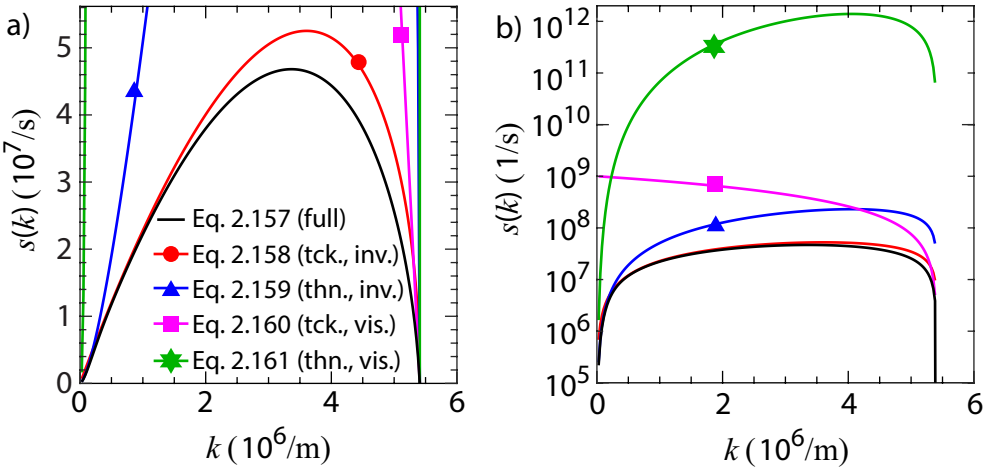

Figure 4.17: Comparison of $s(k)$ calculated from Eq. 2.157 (black) to those from Eq. 2.158-2.161 in the thin/thick and inviscid/viscous liquid limits for the flat liquid, flat apertureless extractor example listed in Table 4.2. They are plotted in (a) linear k, linear s and (b) linear k, log s scales from $k \in [0, k_{marg}]$. Markers are only meant as a guide.

4.10 Appendix D: Comparison between analytic dispersion curves with and without gravity

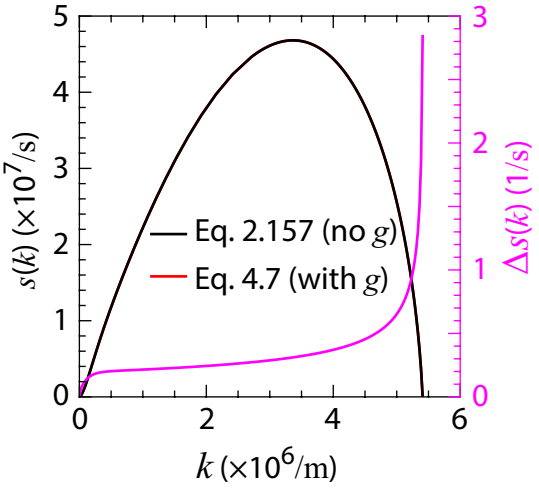

Figure 4.18: Comparison of flat liquid, apertureless extractor example $s(k)$ as predicted with (red; Eq. 4.8) and without gravity (black; Eq. 2.157). The difference Δs between Eq. 2.157 and Eq. 4.8 is plotted in pink.

The growth rates s with and without gravity have been calculated for the flat liquid, flat apertureless extractor example in Fig. 4.18. The comparison shows that gravity would have hardly affected the dynamics for the systems probed in this study as the difference Δs is found to be many orders of magnitude smaller than the found s over the examined k. This

provides another argument justifying the gravityless systems used to study the instability development for parameter regimes relevant to LMIS systems.

4.11 Appendix E: Tables

The tables in the Appendix present measurements of the quantities defined in Table 4.1 extracted from the LMIS instability EHD mode simulations (Tables 4.4-4.5).

Table 4.3: Measured quantities defined in Table 4.1 for the liquid reservoir in the LMIS geometry. The reservoir thickness is 10 μm and is vertically displaced from the extractor plane by 290 μm as indicated in Fig. 4.2(c). Listed quantities are ϕ_o, initial reservoir electric field $E = \phi_o/(290\ \mu\text{m})$, maximally unstable k_m, $\lambda_m = 2\pi/k_m$ and s_m from Eq. 2.157, and marginally stable k_{marg} and $\lambda_{marg} = 2\pi/k_{marg}$.

ϕ_o (kV)	Reservoir E (V/m)	k_m (1/m)	λ_m (μm)	s_m (1/s)	k_{marg} (1/m)	λ_{marg} (μm)
1.5	5.17×10^{6}	7.66×10^{2}	8200	4.12×10^{-2}	1.08×10^{3}	5800
2.0	6.90×10^{6}	1.04×10^{3}	6070	1.34×10^{-1}	1.46×10^{3}	4290
2.5	8.62×10^{6}	1.32×10^{3}	4780	3.38×10^{-1}	1.86×10^{3}	3380
3.0	1.03×10^{7}	1.61×10^{3}	3900	7.30×10^{-1}	2.28×10^{3}	2760
3.5	1.21×10^{7}	1.93×10^{3}	3260	1.42×10^{0}	2.73×10^{3}	2300
4.0	1.38×10^{7}	2.27×10^{3}	2760	2.59×10^{0}	3.21×10^{3}	1960
4.5	1.55×10^{7}	2.65×10^{3}	2370	4.46×10^{0}	3.74×10^{3}	1680
5.0	1.72×10^{7}	3.07×10^{3}	2050	7.41×10^{0}	4.32×10^{3}	1460
6.0	2.07×10^{7}	4.06×10^{3}	1550	1.91×10^{1}	5.68×10^{3}	1110
6.5	2.24×10^{7}	4.66×10^{3}	1350	3.00×10^{1}	6.49×10^{3}	968
7.5	2.59×10^{7}	6.10×10^{3}	1030	7.28×10^{1}	8.38×10^{3}	750
8.5	2.93×10^{7}	7.84×10^{3}	802	1.72×10^{2}	1.06×10^{4}	591
10.0	3.45×10^{7}	1.09×10^{4}	576	5.58×10^{2}	1.47×10^{4}	428
12.5	4.31×10^{7}	1.71×10^{4}	368	2.60×10^{3}	2.29×10^{4}	274
15.0	5.17×10^{7}	2.45×10^{4}	256	7.51×10^{3}	3.30×10^{4}	190
17.5	6.03×10^{7}	3.33×10^{4}	189	1.63×10^{4}	4.49×10^{4}	140
20.0	6.90×10^{7}	4.33×10^{4}	145	3.00×10^{4}	5.87×10^{4}	107

Table 4.4: Measured quantities defined in Table 4.1 for the LMIS instability simulations with h_o = 0.1, 0.2 and 0.5 μm. Listed quantities are h_o, r_s, ϕ_o, initial liquid apex electric field E_o, Reynolds number $\mathsf{Re} = \sqrt{\rho\varepsilon_o/2}[\phi_o h_o/\mu(r_s+h_o)]$, electric Weber number $\mathsf{We} = \varepsilon_o\phi_o^2/2\gamma h_o$, termination time t_f, maximally unstable k_m and $\lambda_m = 2\pi/k_m$ from Eq. 2.157, extracted k_{sim} and $\lambda_{sim} = 2\pi/k_{sim}$ from LMIS Hankel transform power spectrum evolution and the ratio $[\lambda_{sim}/(r_s + h_o)]^2$.

h_o (μm)	r_s (μm)	ϕ_o (kV)	E_o $\left(\frac{\text{GV}}{\text{m}}\right)$	Re	We	t_f (s)	r_f (μm)	k_m $\left(\frac{10^7}{\text{m}}\right)$	k_{sim}	λ_m (μm)	λ_{sim}	$\left(\frac{\lambda_{sim}}{r_s+h_o}\right)^2$
0.1	0.2	5.0	3.59	141	1540	1.49×10^{-9}	0.022	8.32	8.36	0.076	0.075	0.063
0.1	0.5	7.5	2.89	106	3470	2.65×10^{-9}	0.000	5.57	6.07	0.113	0.103	0.030
0.1	0.5	10.0	3.84	141	6170	1.12×10^{-9}	0.077	9.46	10.1	0.066	0.062	0.011
0.1	1.0	10.0	2.32	77	6170	6.31×10^{-9}	0.072	3.72	5.15	0.169	0.122	0.012
0.1	2.0	12.5	1.73	50	9630	1.67×10^{-8}	0.122	2.24	1.93	0.280	0.326	0.024
0.1	2.0	15.0	2.08	61	13900	7.54×10^{-9}	0.137	3.07	3.01	0.205	0.209	0.010
0.1	5.0	15.0	1.07	25	13900	9.22×10^{-8}	0.000	0.957	1.00	0.657	0.628	0.015
0.1	5.0	17.5	1.25	29	18900	3.73×10^{-8}	0.288	1.27	1.24	0.495	0.505	0.010
0.1	5.0	20.0	1.42	33	24700	2.39×10^{-8}	0.288	1.61	1.24	0.391	0.508	0.010
0.2	0.1	5.0	4.07	282	771	8.42×10^{-10}	0.016	10.5	9.12	0.060	0.069	0.053
0.2	0.2	5.0	2.98	212	771	2.41×10^{-9}	0.042	5.90	8.53	0.106	0.074	0.034
0.2	0.2	7.5	4.46	318	1730	4.61×10^{-10}	0.000	12.4	10.3	0.051	0.061	0.023
0.2	0.5	7.5	2.62	182	1730	3.39×10^{-9}	0.076	4.67	5.39	0.135	0.116	0.028
0.2	0.5	10.0	3.50	242	3080	1.26×10^{-9}	0.000	7.95	8.78	0.079	0.072	0.010
0.2	1.0	10.0	2.20	141	3080	7.14×10^{-9}	0.087	3.35	2.63	0.187	0.239	0.040
0.2	5.0	15.0	1.06	49	6940	6.30×10^{-8}	0.000	0.887	0.700	0.708	0.898	0.030
0.2	5.0	17.5	1.23	57	9440	4.76×10^{-8}	0.365	1.16	1.30	0.542	0.484	0.009
0.2	5.0	20.0	1.41	65	12300	2.71×10^{-8}	0.000	1.47	1.47	0.429	0.428	0.007
0.5	0.1	4.0	1.99	282	197	9.39×10^{-9}	0.194	2.77	3.82	0.227	0.164	0.075
0.5	0.1	4.5	2.24	318	250	6.66×10^{-9}	0.097	3.46	4.72	0.182	0.133	0.049
0.5	0.1	5.0	2.48	353	308	4.44×10^{-9}	0.084	4.21	4.30	0.149	0.146	0.059
0.5	0.1	7.5	3.72	529	694	1.01×10^{-9}	0.000	8.90	9.97	0.071	0.063	0.011
0.5	0.2	4.5	1.83	272	250	1.11×10^{-8}	0.065	2.38	2.54	0.264	0.247	0.125
0.5	0.2	5.0	2.04	303	308	7.92×10^{-9}	0.108	2.90	3.27	0.216	0.192	0.076
0.5	0.2	7.5	3.05	454	694	2.02×10^{-9}	0.000	6.18	6.12	0.102	0.103	0.021
0.5	0.2	10.0	4.07	605	1233	6.10×10^{-10}	0.000	10.5	9.40	0.060	0.067	0.009
0.5	0.5	7.5	2.09	318	694	6.92×10^{-9}	0.131	3.05	3.49	0.206	0.180	0.032
0.5	0.5	10.0	2.79	424	1233	2.99×10^{-9}	0.000	5.22	5.29	0.120	0.119	0.014
0.5	1.0	10.0	1.92	282	1233	8.57×10^{-9}	0.000	2.59	3.26	0.242	0.193	0.017

Table 4.5: Measured quantities defined in Table 4.1 for the LMIS instability simulations with h_o = 1.0, 2.0 and 5.0 μm. Listed quantities are h_o, r_s, ϕ_o, initial liquid apex electric field E_o, Reynolds number $\mathsf{Re} = \sqrt{\rho\varepsilon_o/2}[\phi_o h_o/\mu(r_s+h_o)]$, electric Weber number $\mathsf{We} = \varepsilon_o\phi_o^2/2\gamma h_o$, termination time t_f, maximally unstable k_m and $\lambda_m = 2\pi/k_m$ from Eq. 2.157, extracted k_{sim} and $\lambda_{sim} = 2\pi/k_{sim}$ from LMIS Hankel transform power spectrum evolution and the ratio $[\lambda_{sim}/(r_s + h_o)]^2$.

h_o (μm)	r_s	ϕ_o (kV)	E_o $\left(\frac{\text{GV}}{\text{m}}\right)$	Re	We	t_f (s)	r_f (μm)	k_m $\left(\frac{10^7}{\text{m}}\right)$	k_{sim}	λ_m (μm)	λ_{sim}	$\left(\frac{\lambda_{sim}}{r_s+h_o}\right)^2$
1.0	0.1	7.5	2.36	578	347	4.29×10^{-9}	0.121	3.84	3.77	0.164	0.167	0.023
1.0	0.1	10.0	3.15	770	617	1.55×10^{-9}	0.136	6.56	7.55	0.096	0.083	0.006
1.0	0.2	7.5	2.08	529	347	5.84×10^{-9}	0.000	3.02	3.37	0.208	0.187	0.024
1.0	0.2	10.0	2.77	706	617	2.50×10^{-9}	0.166	5.17	4.66	0.121	0.135	0.013
1.0	0.5	7.5	1.60	424	347	1.46×10^{-8}	0.215	1.83	1.94	0.342	0.324	0.047
1.0	0.5	10.0	2.13	565	617	5.50×10^{-9}	0.000	3.16	3.74	0.199	0.168	0.013
1.0	1.0	10.0	1.60	424	617	1.35×10^{-8}	0.000	1.84	1.62	0.341	0.387	0.037
2.0	0.1	6.5	1.25	524	130	3.31×10^{-8}	0.000	1.15	1.04	0.548	0.605	0.083
2.0	0.1	7.5	1.44	605	173	1.70×10^{-8}	0.000	1.51	1.54	0.417	0.407	0.038
2.0	0.1	10.0	1.92	807	308	7.73×10^{-9}	0.146	2.60	2.59	0.242	0.242	0.013
2.0	0.2	7.5	1.33	578	173	2.26×10^{-8}	0.000	1.30	1.18	0.484	0.531	0.058
2.0	0.2	10.0	1.78	770	308	9.93×10^{-9}	0.000	2.24	2.50	0.280	0.251	0.013
2.0	0.5	7.5	1.13	508	173	4.66×10^{-8}	0.000	0.939	0.854	0.669	0.736	0.087
2.0	0.5	10.0	1.50	678	308	1.81×10^{-8}	0.247	1.63	1.74	0.386	0.362	0.021
2.0	1.0	7.5	0.924	424	173	8.07×10^{-8}	0.669	0.642	0.678	0.979	0.926	0.095
2.0	1.0	10.0	1.23	565	308	3.37×10^{-8}	0.697	1.11	1.43	0.564	0.441	0.022
2.0	2.0	10.0	0.941	424	308	6.27×10^{-8}	0.000	0.664	0.826	0.946	0.761	0.036
5.0	0.1	12.5	1.21	1040	193	2.39×10^{-8}	0.000	1.08	1.25	0.580	0.502	0.010
5.0	0.1	15.0	1.46	1250	277	1.52×10^{-8}	0.575	1.54	1.28	0.409	0.490	0.009
5.0	0.2	10.0	0.936	814	123	7.88×10^{-8}	0.641	0.658	0.880	0.955	0.714	0.019
5.0	0.2	12.5	1.17	1020	193	3.29×10^{-8}	0.003	1.01	1.05	0.622	0.597	0.013
5.0	0.5	10.0	0.861	770	123	9.15×10^{-8}	1.52	0.560	0.523	1.12	1.20	0.048
5.0	1.0	10.0	0.775	706	123	1.28×10^{-7}	0.918	0.457	0.404	1.38	1.55	0.067
5.0	2.0	10.0	0.662	605	123	1.86×10^{-7}	0.000	0.337	0.369	1.87	1.70	0.059

Chapter 5

SELF-SIMILAR GROWTH OF ELECTROHYDRODYNAMIC MODES OF RELEVANCE TO LIQUID METAL ION SOURCES

5.1 Introduction

Krohn's discovery of ion emission from an electrified liquid metal droplet [78] in the early 1960s has spurred strong interest in developing systems that emit such highly energetic ion beams. They are emitted from apices of protrusions that grow from a liquid metal film subject to an imbalance of destabilizing Maxwell (electric) and stabilizing capillary forces. These small scale systems known as liquid metal ion sources (LMIS) [22] now form the basis for high resolution focused ion beam systems [108] used for instrumentation ranging from microscopy to nanofabrication. There is also a growing interest in developing miniaturized LMIS microarray devices to actuate space micropropulsion [103].

There exist many previous studies that viewed such liquid protrusion growth as an electrohydrodynamic (EHD) instability. The body of literature extends back to Tonks [145], who analyzed the destabilizing Maxwell and stabilizing capillary and gravitational pressure imbalance of a small hemispherical protrusion on top of a flat, perfectly conducting liquid under a normal electric field. The dynamical model yielded a critical field strength required for sustained distortion of the liquid surface, which was subsequently confirmed by Frenkel [47] through a EHD stability analysis of the flat, inviscid liquid surface. Yet in the same analysis, Tonks also realized that for applied fields stronger than the critical value, the protrusion apex pressure cannot maintain an equilibrium as the Maxwell pressure increases as the square of the apex radius whereas the capillary and gravitational pressure scale inversely with the radius and linearly with the apex height, respectively. This accelerating pressure imbalance which generates a runaway protrusion growth led him to the realization that this growth should proceed in a self-similar fashion characterized by self enhancement of the apex field and curvature.

Zubarev [165] later analyzed this late time dynamical behavior of the perfectly conducting, ideal liquid protrusion tip to uncover further details of the self-similar growth. He made the natural and correct assumption on how the protrusion tip field will appreciably and rapidly exceed the externally applied field if local conditions prevail. This permitted the substitution of the decay condition specifying a vanishing field for the usual condition specifying a uniform field at infinite distance from the surface such that the tip liquid

motion could be analyzed without regard for any particular geometry. The governing EHD equations now invariant about dilations permitted a set of self-similar transformations amenable to asymptotic analysis. The asymptotic solutions in the laboratory frame indeed exhibit self-similar growth characterized by finite time divergence of the apex Maxwell and capillary pressures to infinity, indeed indicating self enhancement of the apex field and curvature. Zhou and Troian [164] later focused on the influence of inertial effects and included time reversal symmetry to reveal a multiplicity of self-similar solutions. Zubarev [166] has recently extended the analysis for the originally inviscid liquid to include a finite liquid viscosity, which was found to result in modifications to the self-similar power law exponents.

The self similarity has since been observed through numerical simulations of the axially symmetric protrusion development from a flat layer conducted by Suvorov [134, 136] and Albertson and Troian [5] and from a droplet conducted by Betelu *et al.* [14], Fontelos *et al.* [44], Burton and Taborek [18] and Garzon *et al.* [49]. Previous simulations conducted in this thesis (see Ch. 3) have been able to track the spatiotemporal evolution of the electrified liquid metal layer prior to ion emission in a LMIS geometry realistic to space micropropulsion devices, where preliminary analysis indeed indicated that the protrusions in the modeled geometry indeed undergo rapid spatiotemporal acceleration with accelerated tip sharpening and field self enhancement indicative of self-similar growth. These simulations finally make it possible to probe whether self-similar growth is indeed exhibited by the protrusions that develop in geometries of relevance to real LMIS systems.

This study presents results from computational simulations that track self-similar growth of EHD modes that develop in the geometry modeling a realistic LMIS system possessing a highly curved microemitter substrate and extractor aperture. The arbitrary Lagrangian Eulerian finite element method [32] is used to track the spatiotemporal evolution of the rapidly accelerating liquid free surface prior to ion emission. Sec. 5.2 shows the extended review given by Zhou and Troian [164] on the original Zubarev analysis of self-similar growth of a perfectly conducting, inviscid protrusion tip [165]. Sec. 5.3 outlines the key simulation details, delineates the methodology taken to extract protrusion apex Maxwell and capillary pressure self-similar exponents and presents notes on the checks of the employed computational algorithm shown to recover the asymptotic exponents in the inviscid [165] and the recently analyzed viscous [166] limits. The results show that the protrusions in the modeled LMIS geometry indeed undergo self-similar growth during the late stage development. The self similarity is also shown to be preserved regardless of the axial/non-axialness of the protrusion tip and additional presence of neighboring protrusions found in

the EHD coronal and instability modes. The self-similar exponents for the axial protrusions are found to collapse in the Reynolds number and electric Weber number parameter space. The exponents are also shown to possess a dichotomy related to the axial/non-axialness of the protrusion tip, where the non-axial exponents are found to be significantly larger than the axial counterparts. The self-similar growth of the different EHD modes is characterized in Sec. 5.4 using the spatiotemporal evolution of the liquid surface and protrusion apex pressures of select examples and distributions of self-similar exponents in the constructed parameter spaces. Discussion on the comparison of self-similar exponents across the different systems, limitations of the conducted simulations and notes on the protrusion half angle measurements are offered in Sec. 5.5 before the key findings are summarized in Sec. 5.6.

5.2 Overview of Zubarev self-similar analysis

Zubarev's original self-similar analysis [165] for the late time dynamical behavior of an axisymmetric protrusion developing from a perfectly conducting, incompressible, inviscid, irrotational liquid in vacuum was reviewed and expanded in extensive detail by Zhou and Troian [164] in their work that unveiled a multiplicity of inertial self-similar solutions. This section follows their review for completeness and to motivate the data analysis employed to extract self-similar exponents from the conducted simulations. The fitting methodology is described in detail in Sec. 5.3.2.

The axisymmetric (r, z) coordinate system is set such that the origin coincides with the protrusion blowup point. For a perfectly conducting liquid with no net charge, all mobile charges reside on the liquid surface $z = h(r, t)$ and rearrange instantaneously compared to fluid motion time scales so as to maintain the liquid at constant electric potential $\phi(r, z, t)$. The electric field $\vec{E}(r, z, t)$ inside the liquid bulk is thereby zero whereas that on the surface can only sustain a normal component. The field in the vacuum domain $z \geq h(r, t)$ is obtained from the gradient of the electric potential and satisfies

$$\vec{E} = -\nabla\phi \quad \text{in } z \geq h \tag{5.1}$$

$$\nabla \cdot \vec{E} = 0 \quad \text{in } z \geq h \tag{5.2}$$

$$\nabla^2\phi = \phi_{rr} + \frac{\phi_r}{r} + \phi_{zz} = 0 \quad \text{in } z \geq h \tag{5.3}$$

The velocity field $\vec{u}$ for the liquid domain $z \leq h(r, t)$ subject to incompressible ($\nabla \cdot \vec{u} = 0$) and irrotational ($\nabla \times \vec{u} = 0$) flow is obtained from the gradient of the velocity potential

$\psi(r,z,t)$ and satisfy

$$\vec{u} = -\nabla\psi \quad \text{in } z \le h \tag{5.4}$$

$$\nabla \cdot \vec{u} = 0 \quad \text{in } z \le h \tag{5.5}$$

$$\nabla^2\psi = \psi_{rr} + \frac{\psi_r}{r} + \psi_{zz} = 0 \quad \text{in } z \le h \tag{5.6}$$

Conservation of mass and momentum is enforced through the unsteady, inviscid, irrotational Bernoulli's equation applied to $h(r,t)$ given by

$$\begin{aligned}\left[\rho\psi_t + \underbrace{\frac{\rho}{2}\left(\psi_r^2 + \psi_z^2\right)}_{\text{Kinetic pressure}}\right]_{z=h} \\ = \underbrace{\frac{\varepsilon_o}{2}\left(\phi_r^2 + \phi_z^2\right)_{z=h}}_{\text{Maxwell pressure}} + \underbrace{\frac{\gamma}{(1+h_r^2)^{1/2}}\left(\frac{h_{rr}}{1+h_r^2} + \frac{h_r}{r}\right)}_{\text{Capillary pressure}}\end{aligned} \tag{5.7}$$

where it is assumed that gravitational forces are negligible compared to other forces in the problem. The underbraced terms describe contributions to the surface pressure driving the velocity potential. The Maxwell pressure pulls the liquid into the vacuum whereas the capillary pressure opposes the Maxwell pressure. The kinetic pressure signifies the kinetic energy per unit volume acting on $h(r,t)$ derived from the laboratory frame advective acceleration term in the Euler equation.

Zubarev nondimensionalized the system of equations using the following scalings (nondimensional variables in uppercase)

$$(R,Z,H) = \frac{\varepsilon_o}{\gamma}E_c^2 \times (r,z,h) \tag{5.8a}$$

$$T = \frac{\varepsilon_o^{3/2}}{\rho^{1/2}\gamma}E_c^3 \times t \tag{5.8b}$$

$$\Phi = \frac{\varepsilon_o}{\gamma}E_c \times \phi \quad \text{in } Z \ge H \tag{5.8c}$$

$$\Psi = \frac{\rho^{1/2}\varepsilon_o^{1/2}}{\gamma}E_c \times \psi \quad \text{in } Z \le H \tag{5.8d}$$

where E_c is an asymptotic electric field strength such that $\phi(z \to \infty) = -E_c z$.

The dimensionless equations are

$$\begin{aligned}\left[\Psi_T + \frac{1}{2}\left(\Psi_R^2 + \Psi_Z^2\right)\right]_{Z=H} = \frac{1}{2}\left(\Phi_R^2 + \Phi_Z^2\right)_{Z=H} \\ + \frac{1}{(1+H_R^2)^{1/2}}\left(\frac{H_{RR}}{1+H_R^2} + \frac{H_R}{R}\right)\end{aligned} \tag{5.9}$$

$$\nabla^2\Psi = 0 \quad \text{in } Z \leq H \tag{5.10}$$

$$\nabla^2\Phi = 0 \quad \text{in } Z \geq H \tag{5.11}$$

with the following dimensionless boundary conditions

$$\text{Equipotential } \Phi = 0 \quad \text{at } Z = H \tag{5.12a}$$

$$\text{Decay } \lim_{R^2+Z^2\to\infty} \left(\Phi_R^2 + \Phi_Z^2\right) = 0 \quad \text{for } Z > H \tag{5.12b}$$

$$\text{Decay } \lim_{R^2+Z^2\to\infty} \left(\Psi_R^2 + \Psi_Z^2\right) = 0 \quad \text{for } Z < H \tag{5.12c}$$

$$\text{Symmetry } \Phi_R(R = 0) = 0 \quad \text{for } Z \geq H \tag{5.12d}$$

$$\text{Symmetry } \Psi_R(R = 0) = 0 \quad \text{for } Z \leq H \tag{5.12e}$$

$$\text{Symmetry } H_R(R = 0) = 0 \tag{5.12f}$$

$$\text{Kinematic } H_T - \Psi_Z + \Psi_R H_R = 0 \quad \text{at } Z = H \tag{5.12g}$$

where the kinematic condition is the last condition is the usual kinematic boundary condition for free surface flows that require the material points on the moving surface move with the local surface flow velocity. Zubarev invoked the decay conditions specifying vanishing electric and velocity field strengths far from the protrusion tip. The underlying assumption is that the electric field at the strongly curved protrusion apex becomes strongly amplified from accelerated field self enhancement, which also accordingly increases the flow speed. The far field values therefore become negligible compared to the local protrusion tip values and make the decay conditions applicable.

Noting that the equations and boundary conditions are dilation invariant under the transformations $(\Psi, \Phi) \to \alpha \times (\Psi, \Phi)$, $(R, Z, T) \to \alpha^2 \times (R, Z, T)$ and $T \to \alpha^3 T$, Zubarev uncovered similarity solutions to the system of equations of the form (dimensionless self-similar variables in uppercase and decorated by a tilde)

$$(\tilde{R}, \tilde{Z}, \tilde{H}) = \frac{(R, Z, H)}{(T_C - T)^{2/3}} \tag{5.13a}$$

$$\tilde{\Phi} = \frac{\Phi}{(T_C - T)^{1/3}} \text{ for } \tilde{Z} \geq \tilde{H} \tag{5.13b}$$

$$\tilde{\Psi} = \frac{\Psi}{(T_C - T)^{1/3}} \text{ for } \tilde{Z} \leq \tilde{H} \tag{5.13c}$$

$$\text{where } T_C - T > 0$$

where T_C is the asymptotic time at which the Maxwell and capillary pressure at the protrusion apex diverge to infinity due to field self enhancement. It is noteworthy that the solutions imply that the protrusion apex curvature will shrink rapidly as $T_C - T \to 0$ and

thereby indicate accelerated tip sharpening. The dimensionless governing equations in the self-similar frame then become

$$\begin{aligned}&\left[\frac{2\tilde{\Psi}_{\tilde{R}}\tilde{R}+2\tilde{\Psi}_{\tilde{Z}}\tilde{H}-\tilde{\Psi}}{3}+\frac{\tilde{\Psi}_{\tilde{R}}^2+\tilde{\Psi}_{\tilde{Z}}^2}{2}\right]_{\tilde{Z}=\tilde{H}}\\&=\frac{1}{2}\left(\tilde{\Phi}_{\tilde{R}}^2+\tilde{\Phi}_{\tilde{Z}}^2\right)_{\tilde{Z}=\tilde{H}}+\frac{1}{(1+\tilde{H}_{\tilde{R}}^2)^{1/2}}\left(\frac{\tilde{H}_{\tilde{R}\tilde{R}}}{1+\tilde{H}_{\tilde{R}}^2}+\frac{\tilde{H}_{\tilde{R}}}{\tilde{R}}\right)\end{aligned}\tag{5.14}$$

$$\nabla^2\tilde{\Psi}=0\quad\text{in }\tilde{Z}\le\tilde{H}\tag{5.15}$$

$$\nabla^2\tilde{\Phi}=0\quad\text{in }\tilde{Z}\ge\tilde{H}\tag{5.16}$$

and the boundary conditions

$$\text{Equipotential }\tilde{\Phi}=0\quad\text{at }\tilde{Z}=\tilde{H}\tag{5.17a}$$

$$\text{Decay }\lim_{\tilde{R}^2+\tilde{Z}^2\to\infty}\left(\tilde{\Phi}_{\tilde{R}}^2+\tilde{\Phi}_{\tilde{Z}}^2\right)=0\quad\text{for }\tilde{Z}>\tilde{H}\tag{5.17b}$$

$$\text{Decay }\lim_{\tilde{R}^2+\tilde{Z}^2\to\infty}\left(\tilde{\Psi}_{\tilde{R}}^2+\tilde{\Psi}_{\tilde{Z}}^2\right)=0\quad\text{for }\tilde{Z}<\tilde{H}\tag{5.17c}$$

$$\text{Symmetry }\tilde{\Phi}_{\tilde{R}}(\tilde{R}=0)=0\quad\text{for }\tilde{Z}\ge\tilde{H}\tag{5.17d}$$

$$\text{Symmetry }\tilde{\Psi}_{\tilde{R}}(\tilde{R}=0)=0\quad\text{for }\tilde{Z}\le\tilde{H}\tag{5.17e}$$

$$\text{Symmetry }\tilde{H}_{\tilde{R}}(\tilde{R}=0)=0\tag{5.17f}$$

$$\text{Kinematic }\underbrace{2(\tilde{R}\tilde{H}_{\tilde{R}}-\tilde{H})=3(\tilde{\Psi}_{\tilde{Z}}-\tilde{H}_{\tilde{R}}\tilde{\Psi}_{\tilde{R}})}_{\text{at }\tilde{Z}=\tilde{H}}\tag{5.17g}$$

The set of asymptotic self-similar solutions for $\tilde{\Phi}$, $\tilde{\Psi}$ and $\tilde{H}$ were found to be

$$\tilde{\Phi}(\tilde{R},\tilde{Z})=\sum_{n=0}^{\infty}a_n\frac{\partial^{3n}}{\partial\tilde{Z}^{3n}}\left[(\tilde{R}^2+\tilde{Z}^2)^{1/4}P_{1/2}(\cos\theta)\right]\tag{5.18}$$

$$\tilde{\Psi}(\tilde{R},\tilde{Z})=\sum_{n=0}^{\infty}b_n\frac{\partial^{3n}}{\partial\tilde{Z}^{3n}}(\tilde{R}^2+\tilde{Z}^2)^{-1/2}\tag{5.19}$$

$$\tilde{H}(\tilde{R},\tilde{Z})=\sum_{n=0}^{\infty}c_n\tilde{R}^{1-3n}\tag{5.20}$$

where $P_{1/2}(\cos\theta)$ is the Legendre polynomial of the first kind of order 1/2 and $\theta=\tan^{-1}(\tilde{R}/\tilde{Z})$ denotes the polar angle in spherical coordinates.

In the limit $\mathsf{R} = \sqrt{\tilde{R}^2 + \tilde{Z}^2} \to \infty$, the leading order behavior of the physical fields is

$$\tilde{\Phi}(\mathsf{R}) = a_o \mathsf{R}^{1/2} P_{1/2}(\cos\theta) + O\left(\frac{1}{\mathsf{R}^5}\right) \tag{5.21}$$

$$\tilde{\Psi}(\mathsf{R}) = \frac{b_o}{\mathsf{R}} + O\left(\frac{1}{\mathsf{R}^{7/2}}\right) \tag{5.22}$$

$$\tilde{H}(\mathsf{R}) = \mathsf{R}\cot\theta_o + O\left(\frac{1}{\mathsf{R}^5}\right) \tag{5.23}$$

where

$$a_o = [2(-c_o - b_o)]^{1/2} \left[\frac{dP_{1/2}(\cos\theta)}{d\theta}\right]_{\theta_o}^{-1} > 0 \tag{5.24}$$

$$b_o = \text{free parameter} \quad 0 < b_o < \cos\theta_o \tag{5.25}$$

$$c_o = \cot\theta_o < 0 \tag{5.26}$$

and θ_o is the angle that satisfies a null equipotential condition on the liquid surface $P_{1/2}(\cos\theta) = 0$ or $\theta_o \approx 131°$. The solutions therefore describe a liquid surface that lies above a conical envelope with an interior half angle $\theta_T = 360° - 2\theta_o = 49.3°$, which is the classic Taylor angle [141]. The liquid shape in the laboratory frame describes a dynamic protrusion with a radially symmetric radial sink flow towards the protrusion apex. It can be seen that the apex Maxwell p_M and capillary p_C pressures scale according to $\sim (t_c - t)^{-2/3}$ (t_c is the dimensional mathematical blowup time) and thereby undergo self-similar growth leading to finite time blow up.

Zhou and Troian [164] later detailed a more general solution from an approach outlined in a subsequent work [136] of Zubarev in which the surface kinetic pressure contributes to the same order as the Maxwell and capillary pressures. Time-reversal symmetry was also additionally included in the analysis to unveil a rich multiplicity of inertial flow configurations with liquid surface shapes possessing both radial and angular dependence. Zubarev has also recently extended the analysis [166] to viscous liquids and found the self similarity to be still preserved, in which the pressure providing the main competitive balance to p_M shifts from p_C to p_V. A notable difference between the inviscid and viscous self-similar growth was found for the Maxwell pressure, which was shown to scale as $\sim (t_c - t)^{-1}$ instead of $\sim (t_c - t)^{-2/3}$ for the inviscid limit.

5.3 Computational methods

This section first summarizes the computational geometries used for simulations conducted in this chapter. The details of governing equations and boundary conditions may be found in Sec. 2.1, whereas those for the computational algorithm may be found in the previous study

on the spatiotemporal evolution of EHD modes in a realistic LMIS geometry (see Ch. 3). The self-similar fitting methodology and notes on checks of the employed computational algorithm are then presented. Definitions of physical variables, material constants used for liquid metal gallium (Ga) at the melting point [69] and vacuum permittivity and key initial variables are the same as those introduced back in Table 3.1.

5.3.1 Key simulation details

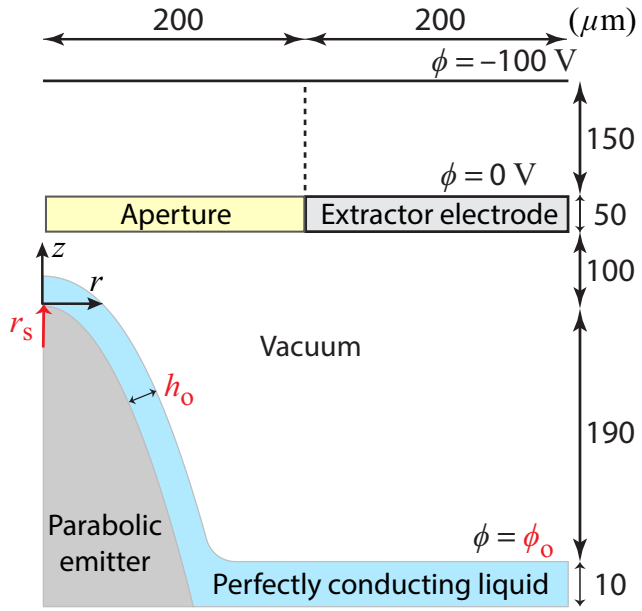

Figure 5.1: Sketch of computational geometry. The details of the geometry are the same as that shown back in Fig. 3.1(a). The extractor electrode is extended to cover the aperture region for "System 1" described in Sec. 5.3.1.1.

The key details of the simulations conducted for the Fig. 5.1 LMIS geometry with and without the extractor aperture are presented in this section.

5.3.1.1 System 1: LMIS geometry without extractor aperture

Shown in Fig. 5.1 is the axisymmetric (r, z) computational domain of a realistic LMIS geometry in a vacuum without gravity and has been previously described (see Ch. 3). The geometry primarily consists of a smooth, parabolic microemitter with apex curvature radius r_s externally wetted with a liquid metal layer. The initial liquid surface is described as a smooth surface offset by a constant initial thickness h_o to the microemitter surface (see Sec. 3.2.1 for detailed description).

$$h(r, t = 0) = \text{smooth offset surface} \tag{5.27}$$

For "system 1," the flat extractor extends through the region labeled as the "aperture" and provides the electric potential ground $\phi = 0$. The domain is then vertically constrained by the extractor electrode and thus the dimensions and boundary conditions expressed above the extractor do not apply. Only h_o, r_s and ϕ_o have been varied across simulations. The combinations that have been simulated all lead to the "axial" EHD mode resulting in the development of a single, axially symmetric protrusion. The full list of combinations is provided in Table 5.4. The key parameters for the example used to characterize the self-similar growth of the system are provided in Table 5.2.

5.3.1.2 Systems 2, 3 and 4: Axial, coronal and instability EHD modes in LMIS geometry

If the region labeled as the "aperture" in Fig. 5.1 is opened to yield an extractor aperture, the geometry then describes the previously described (see Ch. 3) computational domain of a realistic LMIS geometry. Simulations whose data are to be analyzed in this chapter have already been conducted in Ch. 3, where the initial liquid surface was modeled to be perfectly smooth.

The labels for the system types to be analyzed are as follow. "System 2" refers to the cases that result in the "axial" EHD mode described by a single, axially symmetric protrusion. The full list of h_o, r_s and ϕ_o combinations analyzed for the system type is provided in Table 5.5. "System 3" refers to the cases that result in the "coronal" EHD mode described by a single but non-axial protrusion. The full list of h_o, r_s and ϕ_o combinations analyzed for the system type is provided in Table 5.7. "System 4" refers to the cases that result in the "instability" EHD mode described by multiple protrusions in a wave-like pattern. For these cases, the analysis is centered around the most prominent protrusion whose apex achieves the termination criterion $E^{apex} \geq 5$ GV/m. The full list of h_o, r_s and ϕ_o combinations analyzed for the system type is provided in Table 5.8 for those with an axial most prominent protrusion (System 4.1) and Table 5.9 for those with a non-axial most prominent protrusion (System 4.2). The key parameters for the examples used to characterize the self-similar growth of the systems are provided in Table 5.2.

5.3.2 Self-similar exponent fitting methodology

The Zubarev analysis [165] indicates that self-similar growth of the axial protrusion apex may be best examined by analyzing the apex Maxwell p_M and capillary p_C pressure temporal evolution in the rescaled time $t_c - t$, where t_c is the mathematical asymptotic time at which the two pressures diverge to infinity. As the self-similar growth found by Zubarev

Table 5.1: Definitions of the self-similar analysis variables and referenced quantities introduced for this chapter.

Self-similar variables	Symbol
Fitted blowup time	t_*
p_M self-similar exponent	β_M
p_C self-similar exponent	β_C
Referenced quantities	**Symbol**
Δt for self-similar regime	Δt_{SS}
Number of self-similar fit decades	n

describes the late time dynamical behavior of the liquid metal protrusion apex just prior to ion emission, if the apex $\log_{10}|p|$ can be fitted with a straight line with slope β in an extended interval in $\log_{10}(t_c - t)$ extending backwards from $t_c - t_f$, then it can be said to be undergoing self-similar power law growth in the form $p \sim (t_c - t)^{-\beta}$.

The quantities to be optimized and fitted for each analyzed system are the fitted blowup time t_* yielding the best self-similar fit and self-similar exponents β_M for the most prominent protrusion apex p_M and β_C for the most prominent protrusion apex p_C. These are found through an iterative optimization procedure described below. The viscous exponent β_V was unable to be measured due to changes in its sign (as also found in simulations conducted by Albertson and Troian [5]) and remeshing induced fluctuations often observed within the self-similar fitting regime.

For systems 1 and 2 whose protrusion apices are always located at $r = 0$, the procedure first searches for t_* that yields the minimum residual of the ordinary least squares (OLS) linear fit conducted for the apex p_M evolution in the $\log_{10}(t_* - t)$ vs $\log_{10}|p|$ coordinates. For each trial asymptotic time t_{trial}, an OLS p_M fit is conducted over an extended period in $t_{trial} - t$ extending backwards from $t_{trial} - t_f$. The optimal t_c is found by utilizing the MATLAB [2] minimizer routine "fmindbnd," which uses the golden section search algorithm [72] to iteratively minimize a function within a specified search interval in its argument. The search interval is set as $t_f < t_{trial} < t_f + 10^{-8}$ s and the minimized function is the OLS p_M residual. The procedure has been found to be highly stable and convergent with respect to the available optimization parameters for the axial protrusions. Once t_* and β_M have been determined, β_C is then found by simply conducting an OLS p_C fit over the same period in $t_* - t$ in the $\log_{10}(t_* - t)$ vs $\log_{10}|p|$ coordinates.

As for systems 3 and 4 resulting in non-axial most prominent protrusion development, the same self-similar power law growths of the form $(t_* - t)^{-\beta}$ were sought even though the assumptions of a single, axially symmetric protrusion apex made in Zubarev's [165] analysis no longer become satisfied. Slight modifications to the fitting methodology described for systems 1 and 2 have been implemented. The main modification is that the linear regression fits in the double logarithmic scale have been conducted using MATLAB's implementation of robust least squares (RLS) in which the to be fitted data is iteratively reweighted [64]. This was implemented over OLS as the apex pressure data was found to become susceptible to inadequate mesh resolution of the non-axial protrusion apices at late times from a mesh convergence study of a selected system. The deviations in the data were specifically found to be triggered after remeshing events in the late time protrusion development. Notably, this phenomenon was entirely absent for systems 1 and 2, even though these simulations were also subject to remeshing events at similar stages in the protrusion development. What leads to the perceived difference is that for axial protrusions, the protrusion apex r^{apex} is always exactly defined at $r = 0$, whereas that for non-axial protrusions is evolving and thus only as well defined as allowed by the available mesh resolution. Remeshing events for such protrusions place new mesh nodes at slightly different locations on the protrusion tip surface, which can generate significant deviations in the apex pressure data as the apex curvature radius becomes comparable to the chosen mesh element side lengths. RLS was found to be able to minimize the influence of such data on the self-similar fits by assigning minimal to zero weights. The rest of the described fitting procedure remains the same.

The fits during the optimization and exponent extraction process are taken over the last 1.5 decades for system 2 simulations. For all other systems, the number of decades was reduced to 1.0 for simulations that did not clearly yield 1.5 decades of fittable data.

The fitting error of the extracted exponents for the axial protrusions found for systems 1, 2 and 4.1 are always of $O(10^{-3})$ or less. Those for the non-axial protrusions found for systems 3 and 4.2 are still of $O(10^{-3})$ or less but are generally larger than the axial protrusion counterparts. The fitting error for β_C is also found to be systematically larger than β_M, with a significant difference found for the non-axial protrusions. This will be shown to be due to the later realization of self-similar growth found for p_C than p_M.

Despite the small fitting errors, the exponents will be reported to $O(10^{-2})$ accuracy as the mesh and relative tolerance convergence tests of select axial cases yielded exponents that were stable but still possessing fluctuations of $O(10^{-2})$. Therefore, readers should always have the mesh and relative tolerance errors in mind when evaluating the exponents, even though the fitting errors may seem very small.

5.3.3 Checks on computational algorithm

The computational algorithm utilized for this study has been previously shown (see Ch. 4) to be able to capture the linear growth of surface EHD surface instabilities for the flat liquid metal layer with arbitrary thickness and viscosity under a normal electric field with arbitrary vacuum thickness that has been well analyzed in the literature [131, 132]. This demonstrates the validity of the employed algorithm to be able to accurately simulate the physics and various couplings inherent in the problem down to the first order surface perturbations.

Separate checks on the ability of the algorithm to capture the self-similar growth were conducted. The checks were motivated by the simulation of an axial protrusion development from a flat liquid metal layer subject to a normal applied electric field conducted by Suvorov [134], who utilized the state of the art computational techniques available at the time to numerically confirm the predicted self-similar growth for the first time. For this study, a simulation of the Suvorov geometry was indeed found to yield 1.5 decades of self-similar growth in $t_* - t$ using the fitting methodology described in Sec. 5.3.2. The results of the simulation are shown in Sec. 5.7. The extracted exponents were found to be $\beta_M \approx 0.75 \pm 2.6 \times 10^{-4}$ and $\beta_C \approx 0.74 \pm 1.5 \times 10^{-3}$. Albertson and Troian [5] previously conducted a simulation of the same geometry in a dimensionless system and extracted $\beta_M \approx 0.78 \pm 4 \times 10^{-4}$ and $\beta_C \approx 0.72 \pm 8 \times 10^{-4}$. The two sets of extracted values are found to be consistent.

In addition, the liquid viscosity in the Suvorov geometry was modulated in order to check whether the extracted exponents exhibit converging behavior to those predicted by Zubarev in the inviscid [165] ($\beta_M = \beta_C = 2/3$) and viscous [166] regimes ($\beta_M = \beta_V = 1$). This allows direct modulation of the strengths of the viscous effects needed to probe the behavior. The results for the simulation conducted with viscosity reduced tenfold and enhanced thousandfold are shown in Sec. 5.7. As the geometry does not possess a curved microemitter, $r_s = 0$ such that the definition of the $\mathsf{Re} = \sqrt{\rho\varepsilon_o/2}(\phi_o/\mu)[h_o/(r_s + h_o)]$ taken in this work is simply reduced to $\mathsf{Re} = \sqrt{\rho\varepsilon_o/2}(\phi_o/\mu)$, which respectively results in $\mathsf{Re} \approx 1850$ and $\mathsf{Re} \approx 0.185$ for the two cases. For $\mathsf{Re} \approx 1850$ simulation, $\beta_M \approx 0.69 \pm 9.8 \times 10^{-4}$ and $\beta_C \approx 0.71 \pm 3.3 \times 10^{-3}$ that tend towards the predicted inviscid values. The closest Re simulated by Albertson and Troian [5] is $\mathsf{Re} = 2000$, which yielded $\beta_M \approx 0.70 \pm 0 \times 10^{-4}$ and $\beta_C \approx 0.70 \times 3 \times 10^{-4}$ that are again consistent. For $\mathsf{Re} \approx 0.185$ simulation, $\beta_M \approx 0.99 \pm 1.2 \times 10^{-4}$, $\beta_C \approx 0.76 \pm 6.4 \times 10^{-4}$ and also $\beta_V \approx 1.04 \pm 1.6 \times 10^{-3}$ that tend towards the predicted β_M and β_V in the recent analysis made by Zubarev [166]. The closest Re simulated by Albertson and Troian [5] is $\mathsf{Re} = 0.2$, which yielded $\beta_M \approx 0.99 \pm 1 \times 10^{-4}$, $\beta_C \approx 0.78 \pm 1.3 \times 10^{-3}$ and $\beta_V \approx 1.01 \pm 4 \times 10^{-4}$

that are again consistent. The exponent values extracted from the current set of simulations are consistent with those previously extracted by Albertson and Troian [5] with differences that do not exhibit a clear trend. They also tend to the inviscid [165] and viscous [166] limit values predicted by Zubarev. The larger fitting errors observed for the current study's simulations are due to the physically motivated simulation termination criterion set by $E_f = 5$ GV/m that reduces the number of fittable decades to 1.0 - 1.5. This is smaller than the 2.5 decades accessed by Albertson and Troian [5] simulations that were instead terminated when the apex curvature radius attained a small dimensionless value. These checks nevertheless confirm the ability of the fitting methodology to extract β_M and β_C from the simulated protrusion development.

5.4 Results

Table 5.2: Labels and key parameters for examples shown in Sec. 5.4 for each system. System 1 is the apertureless geometry axial mode, system 2 is the LMIS axial mode, system 3 is the LMIS coronal mode and system 4 is the LMIS instability mode divided into the axial (system 4.1: $r_f = 0$) and non-axial (system 4.2: $r_f > 0$) most prominent protrusion. Measurements of key quantities for all simulated systems (112 in total) are provided in Tables 5.4-5.9.

System Type	h_o (μm)	r_s (μm)	ϕ_o (kV)	E_c $\left(\frac{\text{GV}}{\text{m}}\right)$	t_f (μs)	Re	We
System 1: apertureless LMIS axial	1.0	5.0	5.0	0.39	0.44	71	154
System 2: LMIS axial	1.0	5.0	5.0	0.33	0.73	71	154
System 3: LMIS coronal	2.0	0.5	5.0	0.75	0.13	339	77
System 4.1: LMIS instability ($r_f = 0$)	5.0	0.5	10.0	0.86	0.17	770	123
System 4.2: LMIS instability ($r_f > 0$)	5.0	0.2	10.0	0.94	0.14	814	123

This section presents results characterizing the self-similar growth of axial protrusions in the four systems described in Sec. 5.3.1. The examples used to characterize the growth for each system are listed in Table 5.2. Measurements of key quantities defined in Table 5.1 for the conducted simulations are provided in Tables 5.4-5.9.

5.4.1 Self-similar growth in system 1: apertureless LMIS axial mode

This section presents the simulation results of the self-similar growth of axial protrusions for system 1 of the LMIS geometry without the extractor aperture. The parameter values for the example system are listed in Table 5.2.

5.4.1.1 Example system 1 evolution

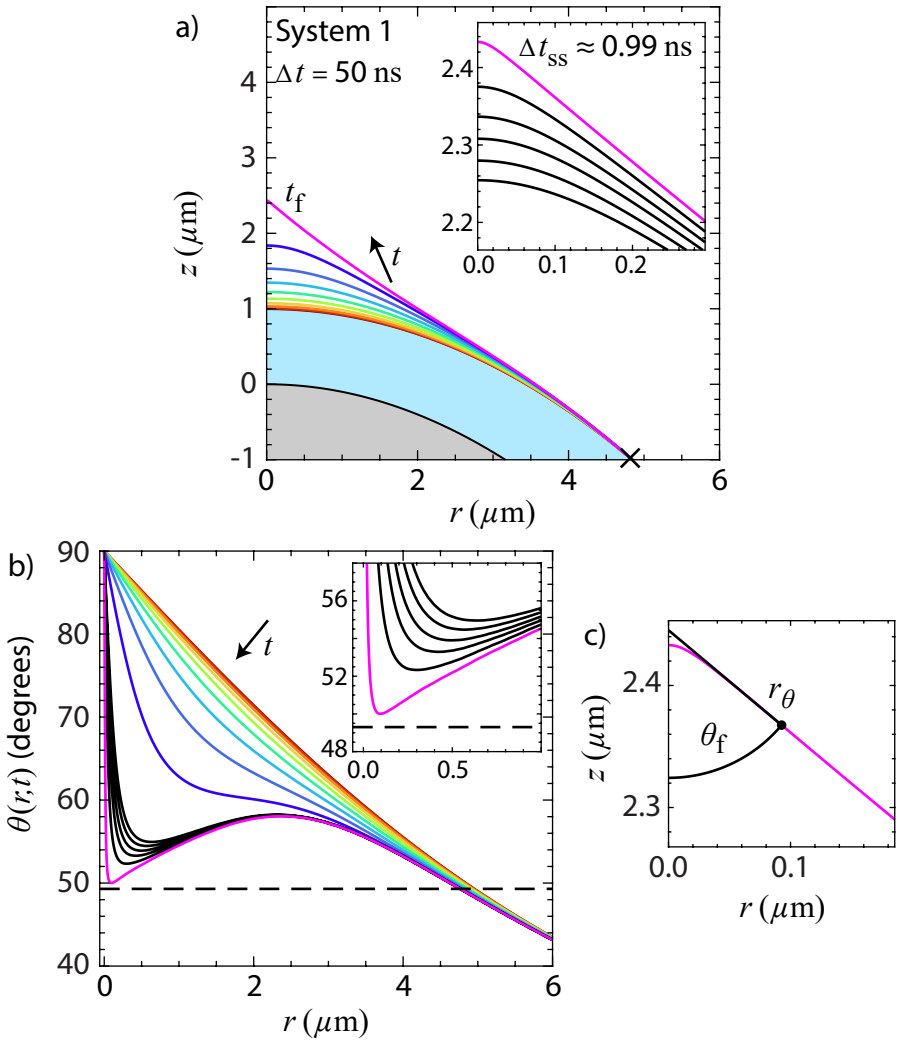

Figure 5.2: Spatiotemporal evolution of the system 1 example. The evolution is similar as that shown back in Sec. 3.4.3 and has been shown for a parameter set relevant to this chapter. (a) Surface $h(r,t)$ evolution that is first uniformly sampled in t at Δt (colored lines) and then uniformly sampled at Δt_{ss} (black lines) during the self-similar regime for the inset of the sharpening apex. The final $h(r,t_f)$ (pink line), initial liquid bulk (blue) and microemitter (grey) are also shown. Black cross marks where $h(r,t_f) \leq h(r,0)$. (b) Half angle $\theta(r,t)$ evolution with the Taylor cone [141] angle 49.3° (dashed line) denoted. Inset shows that near the sharpening apex. (c) Definition of θ_f and r_θ.

Shown in Fig. 5.2(a) is the spatiotemporal $h(r,t)$ evolution of the axial protrusion developing out of the system 1 example. The axial mode development is naturally induced by the microemitter curvature generated local apex $\vec{E}$ enhancement shown previously (see Ch. 3) that induces preferential liquid deformation leading to such mode formation. The addition of microemitter curvature was also shown to generate a positive, nonuniform p_C strongest

at the initial liquid apex that acts against the negative p_M pulling the liquid into the vacuum. The surface indeed exhibits rapid spatiotemporal $h(r,t)$ acceleration that culminates in the accelerated protrusion apex sharpening during self-similar growth as shown in the inset. The mode development is indeed shown to be highly confined to occur well within the initial liquid apex region specified by $r \leq r_s + h_o$.

Fig. 5.2(b) presents the local surface half angle $\theta(r,t)$ evolution in $r \leq r_s + h_o$. The quantity $\theta(r,t) = -\tan^{-1}[(\partial h/\partial r)^{-1}]$ measures the angle between $r = 0$ and the surface tangent evaluated at the $h(r,t)$ mesh nodes. The half angle $\theta(r,t)$ decreases in t and ultimately culminates in a local minimum close to $r = 0$ as shown at $t = t_f$. The value and r coordinate at t_f have been designated as θ_f and r_θ, whose definitions are also visually shown in Fig. 5.2(c). The accelerating nature of the tip sharpening is again shown by the rapid reduction of the minimum θ value and its r coordinate sampled during the self-similar growth. Though the sampled θ_f is close to the "Taylor cone" [141] value of 49.3°, those found for other axial systems were found to widely vary below and above as cataloged in Tables 5.4, confirming the dynamic development [5, 135, 136, 164] of such protrusions.

The axial protrusion apex pressure temporal evolution shown in Fig. 5.3 shows that the Maxwell p_M and capillary p_C pressures indeed undergo blowup during the late stage development contained within the indicated self-similar fit interval. The time step variations in the shown data represent the adaptive nature of the time stepping algorithm employed, which is shown to be able to appropriately reduce the time step sizes during the blowup regime of interest. The negative Maxwell pressure is always dominant and primarily balanced by the positive capillary pressure, which is of the same order but always smaller throughout the evolution. They are found to be at least an order of magnitude stronger than p_V during the entire evolution. The viscous pressure is found to be able to switch signs during the self-similar fit interval, which shows its ability to either resist ($p_V > 0$) or aid ($p_V < 0$) the protrusion developing flow. It also exhibits remeshing induced fluctuations that prevent self-similar exponent extraction. Despite the presence of microemitter curvature, p_M and p_C are indeed found to undergo self-similar growth that extends backwards from $t = t_f$. The Maxwell pressure looks to exhibit self-similar growth much earlier in $t_* - t$ past the conducted fitting interval, whereas p_C is seen to curve upwards to provide the main competitive balance.

5.4.1.2 Distribution of system 1 self-similar exponents

The distribution of system 1 self-similar exponents β_M and β_C and their difference $\Delta\beta = \beta_M - \beta_C$ in the Reynolds number $\mathsf{Re} = \sqrt{\rho\varepsilon_o/2}(\phi_o h_o)/\mu(r_s + h_o)$ and electric Weber

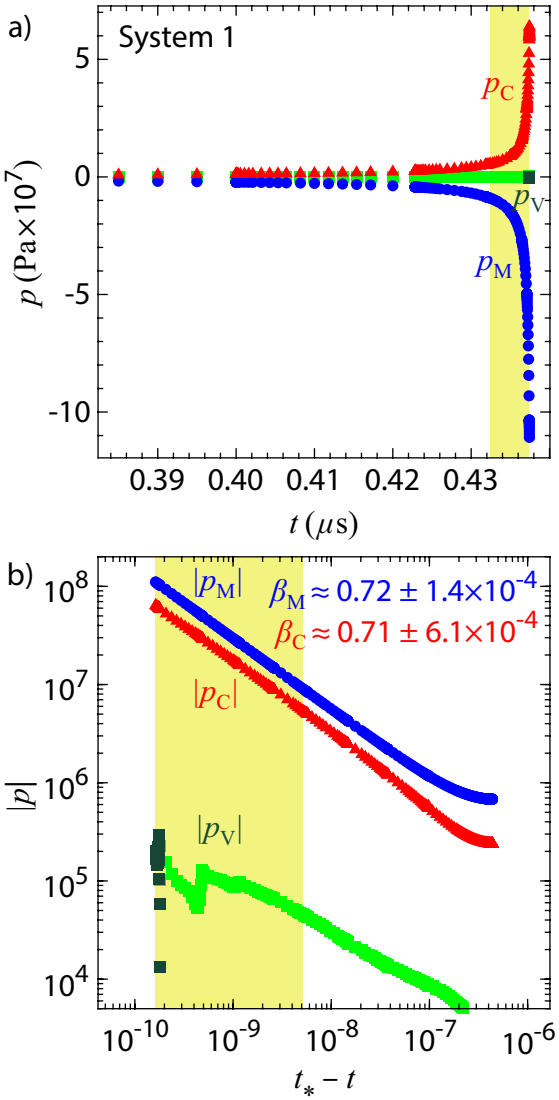

Figure 5.3: Protrusion apex Maxwell p_M (blue circle), capillary p_C (red triangle) and viscous p_V (dark $p_V < 0$ and light $p_V \geq 0$ green square) pressure temporal evolution for the system 1 example in (a) linear p, linear t scale and (b) log $|p|$, log rescaled time $t_* - t$ scale. Self-similar exponents β_M and β_C and their fitting errors have been extracted over the last 1.5 decades in $t_* - t$ (yellow interval).

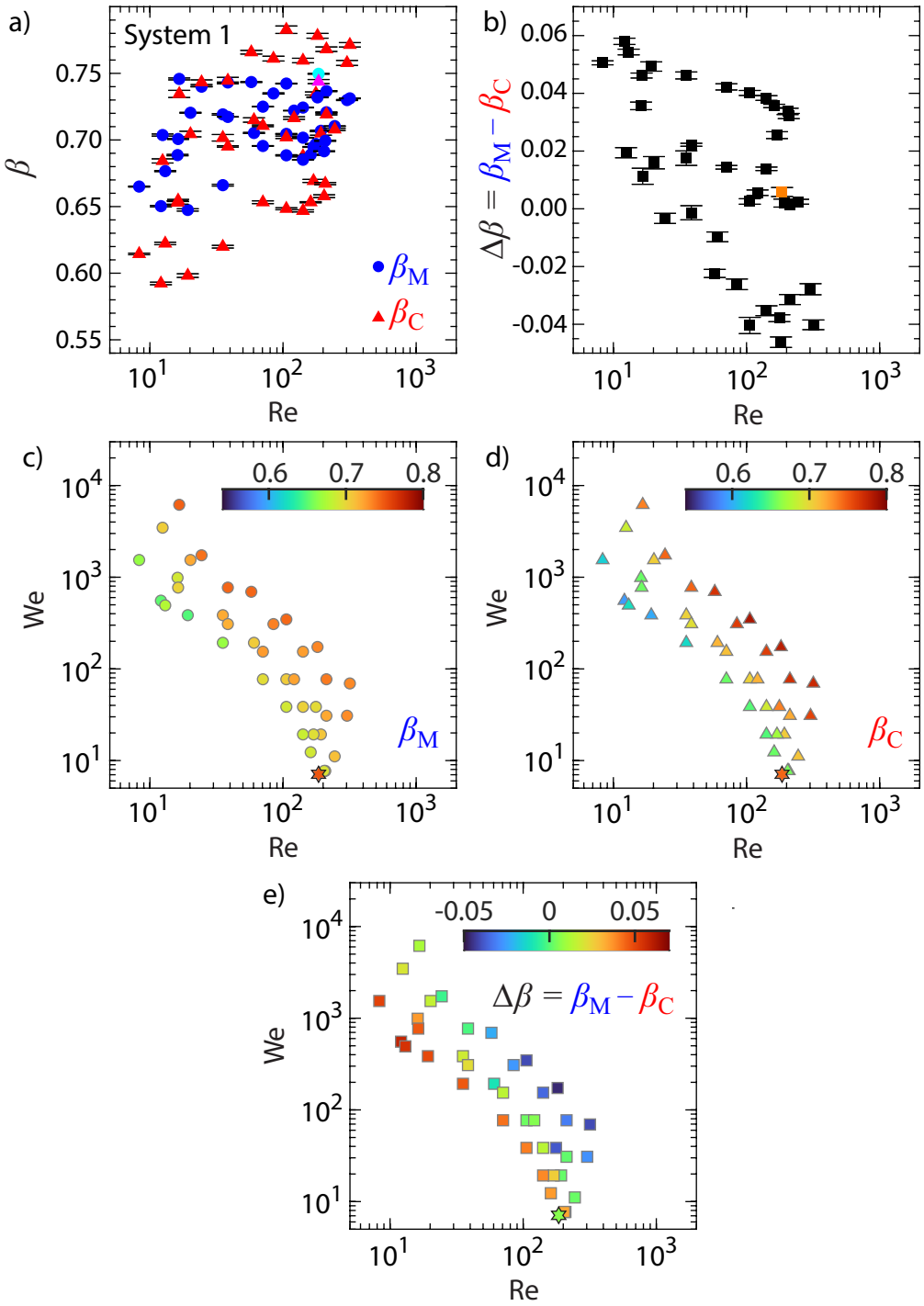

Figure 5.4: Self-similar exponents β_M (circle) and β_C (triangle) and also $\Delta\beta = \beta_M - \beta_C$ (square) extracted from system 1 simulations plotted (a)-(b) against Re and (c)-(e) in the Re and We parameter space. The values for all system 1 simulations can be found in Table 5.4. The error bars in (a)-(b) indicate the fitting errors. The marker colors in (c)-(e) indicate the β and $\Delta\beta$ value corresponding to the respective colorbars. The results from a separate simulation of the Suvorov [134] geometry are marked by (a) β_M cyan circle and β_C magenta triangle, (b) $\Delta\beta$ orange square and (c)-(e) hexagons.

number $\mathsf{We} = \varepsilon_o \phi_o^2 / 2\gamma h_o$ is shown in Fig. 5.4. The two parameters were extracted from nondimensionalization of governing equations conducted for the previous study on EHD mode development in the LMIS geometry (see Ch. 3). Table 5.4 provides the full list of exponents. The results from a separate simulation of the Suvorov geometry [134] described back in Sec. 5.3.3 have also been plotted in the panels. As the system does not possess a curved microemitter, $r_s = 0$ such that Re reduces to $\mathsf{Re} = \sqrt{\rho \varepsilon_o / 2}(\phi_o / \mu)$. The system possesses $\mathsf{Re} \approx 185$ and $\mathsf{We} \approx 7$, which have been extracted by noting $\rho = 6090$ kg/m^3, $\gamma = 0.720$ N/m, $\mu = 2.13 \times 10^{-3}$ Pa s, $h_o = 5$ μm and $\phi_o = 2.4$ kV used in his study.

Fig. 5.4(a) shows that β_M remains stable and capped at around $\beta \approx 0.75$ with respect to Re accessed by the axial mode in the LMIS geometry without an aperture. The capillary exponent β_C exhibits a similar behavior with similar values but displays wider spread, which results in equally wide variations in $\Delta\beta$ as shown in Fig. 5.4(b). The variations are found to arise even for simulations of similar Re, which demonstrates that Re does not provide a complete description of the self-similar behavior for the current geometry. The values of Re accessed by the system are $O(10 - 100)$, which does not quite place the ensuing dynamics in the inviscid regime. Most of the extracted β_M are between the values for the inviscid [165] ($\beta_M = 2/3$) and viscous [166] ($\beta_M = 1$) limits predicted by Zubarev, and closer to the inviscid value than the viscous value. In contrast, β_C values possess a significant spread that is not reflected in the inviscid and viscous limit predictions (both $\beta_C = 2/3$).

The exponents and the difference are instead found to coherently collapse when the electric Weber number We measuring the relative strengths of the destabilizing Maxwell effects to stabilizing capillary effects is taken into account. The corresponding distributions in the Re and We parameter space are shown in Fig. 5.4(c)-(e). The collapse is observed despite the fact that Re and We are based on initial condition variables h_o, r_s and ϕ_o, even though the self similarity arises during late stage development far removed from the initial state. For the same Re, systems with larger We are found to possess larger β_M and β_C until the values stabilize at around 0.75. The difference $\Delta\beta$ is found to be lowered as We increases. For the same We, systems with larger Re are found to possess larger β and lowered $\Delta\beta$ as well. The exponents extracted from a separate simulation of the Suvorov geometry [134] (described back in Sec. 5.3.3) are plotted as hexagons in the same panels. In that system, there is no microemitter curvature that generates the capillary drainage that additionally acts against protrusion development. This is accompanied by self-similar exponents that are indeed significantly larger than those in the nearby Re and We region. The smallest exponent values can be found on the boundary between the axial and drainage mode (see Ch. 3) that results in draining of the liquid without protrusion development. The exponent

values stabilize in the region most distanced from the drainage region. The difference $\Delta\beta$ also exhibits similar trends. It should be noted that the systems in which $\beta_C > \beta_M$ required a reduction in the number of decades in $t_* - t$ used for self-similar fitting due to the visibly curving p_C behavior in the log $|p|$, log rescaled time $t_* - t$ scale. The behavior was found to bias the extracted β_C to take larger values than those perceived. It may be that such behavior has not been fully excluded even with the fitting regime reduction.

5.4.2 Self-similar growth in system 2: LMIS axial mode

This section presents the simulation results of the self-similar growth of axial protrusions for system 2 of the LMIS axial mode. The parameter values for the example system are listed in Table 5.2.

5.4.2.1 Example system 2 evolution

Shown in Fig. 5.5 is the spatiotemporal $h(r,t)$ evolution of the axial protrusion developing out of the system 2 example. The qualitative characteristics of its development are no different than that exhibited by the system 1 counterpart shown in Sec. 5.4.1.1. The liquid deformation leading to the axial protrusion is confined within $r \leq r_s + h_o$ and the surface undergoes a rapid spatiotemporal evolution with accelerated tip sharpening exhibited during self-similar growth. Notably, termination times t_f cataloged for system 2 cases have been found to be significantly larger than those extracted from system 1 counterparts. This is due to the aperture generated reduction (see Ch. 3) in the initial electric field E, which leads to a weaker initial p_M leading to a slower growth. This is shown in Fig. 5.5(c), where the p_M reduction occurs all along the shown surface r. It still retains local enhancement generated by the microemitter curvature, which demonstrates the prevalence of microemitter curvature over extractor aperture on the generated electric fields. The values of E_o for the two geometries are listed in Table 5.6 for the axial systems probed in this study, where the reduction is found to be around 15 to 17 percent from the apertureless value. This slowdown is actually accompanied by a reduction in θ_f as shown in Fig. 5.5(b), where θ_f is now found to be lower than the Taylor cone value. This reduction is simply generated by the aperture generated E reduction that results in a longer t_f afforded by the protrusion to develop and sharpen. The reduction also results in larger r_θ measured for the smaller θ_f.

The axial protrusion apex pressure temporal evolution shown in Fig. 5.6 is again no different than that exhibited by the system 1 example. The Maxwell and capillary pressures are orders of magnitude larger than p_V during the entire evolution and undergo rapid enhancement during the self-similar fit interval indicated in the panels. Again, the viscous pressure

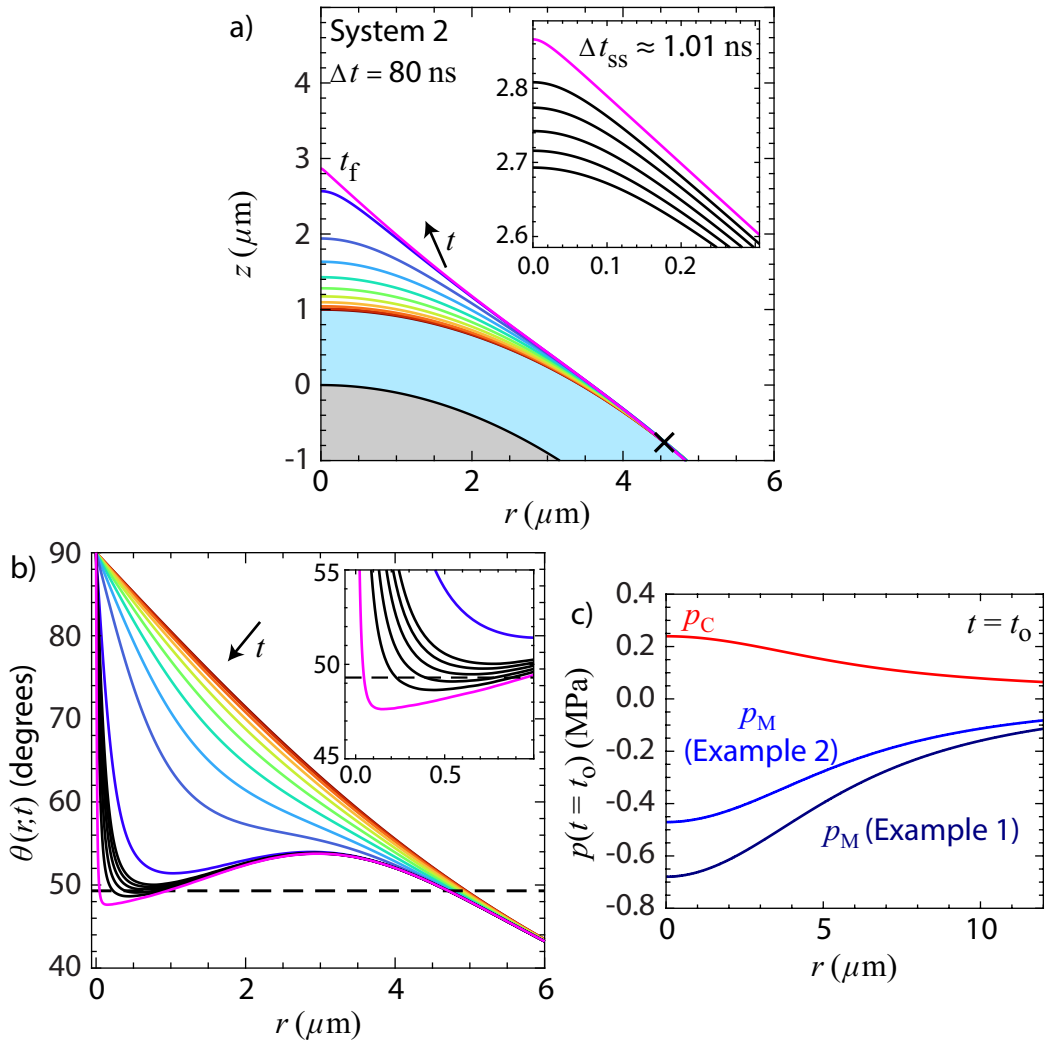

Figure 5.5: Spatiotemporal evolution of the system 2 example. The evolution is similar as that shown back in Sec. 3.4.3 and has been shown for a parameter set relevant to this chapter. (a) Surface $h(r,t)$ evolution that is first uniformly sampled in t at Δt (colored lines) and then uniformly sampled at Δt_{ss} (black lines) during the self-similar regime for the inset of the sharpening apex. The final $h(r,t_f)$ (pink line), initial liquid bulk (blue) and microemitter (grey) are also shown. Black cross marks where $h(r,t_f) \leq h(r,0)$. (b) Half angle $\theta(r,t)$ evolution with the Taylor cone [141] angle 49.3° (dashed line) denoted. Inset shows that near the sharpening apex. (c) Initial p_C and p_M for the current example and system 1 example shown in Fig. 5.2.

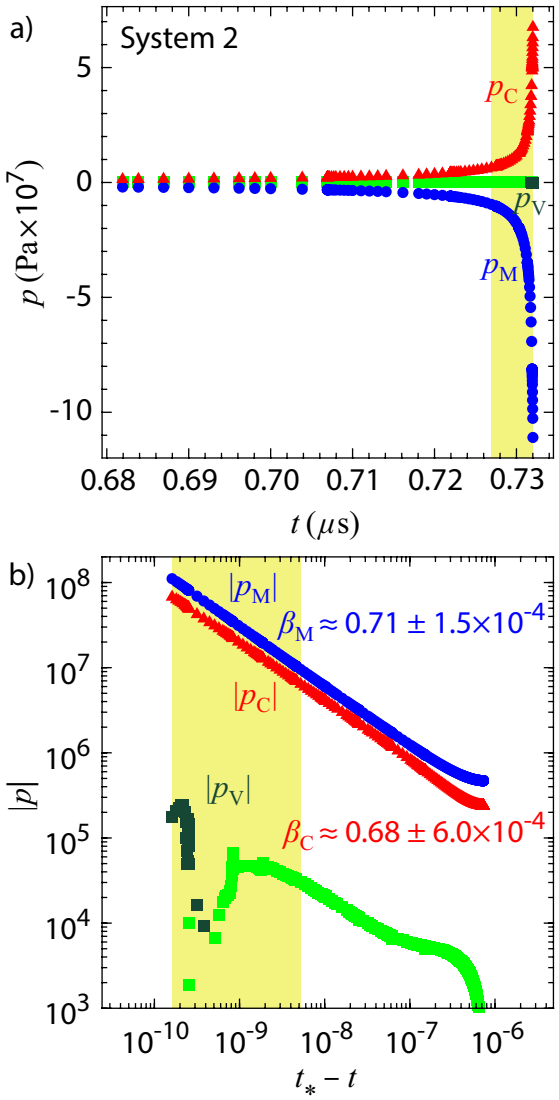

Figure 5.6: Protrusion apex Maxwell p_M (blue circle), capillary p_C (red triangle) and viscous p_V (dark $p_V < 0$ and light $p_V \geq 0$ green square) pressure temporal evolution for the system 2 example in (a) linear p, linear t scale and (b) log $|p|$, log rescaled time $t_* - t$ scale. Self-similar exponents β_M and β_C and their fitting errors have been extracted over the last 1.5 decades in $t_* - t$ (yellow interval).

can switch signs and possesses remeshing induced variations during the self-similar fit interval, which precludes fitting for β_V. Despite the added presence of an extractor aperture in addition to microemitter curvature, the apex p_M and p_C are again found to undergo self-similar growth that characterizes late time protrusion development.

5.4.2.2 Distribution of system 2 self-similar exponents

The distribution of system 2 self-similar exponents β_M and β_C and their difference $\Delta\beta = \beta_M - \beta_C$ in the Reynolds number Re and electric Weber number We is shown in Fig. 5.7. Table 5.5 provides the full list of exponents. The results from a separate simulation of the Suvorov geometry [134] possessing $\mathsf{Re} \approx 185$ and $\mathsf{We} \approx 7$ extracted back in Sec. 5.4.1.2 have also been separately plotted in the panels.

The overall trends are consistent with those found for the system 1 counterparts discussed in Sec. 5.4.1.2. Fig. 5.7(a) shows that β_M remains stable and again capped at around $\beta \approx 0.75$. Similar behavior is observed for β_C with larger variations in the values, which leads to variations in $\Delta\beta$ as shown in Fig. 5.4(b). Again, most of the extracted β_M are between the values for the inviscid ($\beta_M = 2/3$) and viscous ($\beta_M = 1$) limits predicted by Zubarev, with a significant spread in β_C that is not reflected in the predictions in the two limits (both $\beta_C = 2/3$). The exponents and the difference are found to coherently collapse when plotted in the Re and We parameter space as shown in Fig. 5.4(c)-(e). Systems increasingly distanced from the drainage mode region in the parameter space are found to possess larger β_M and β_C and lowered $\Delta\beta$ until the values stabilize. The addition of an extractor aperture can be seen to induce no significant effect on the qualitative behavior of the exponents and their differences. This is consistent with the fact that the extractor aperture is placed some 100 μm $- h_o$ away from the initial liquid apex, which is much farther than the protrusion apex coordinate z_f accessed by the simulated protrusions.

5.4.3 Self-similar growth in system 3: LMIS coronal mode

This section presents the simulation results of the self-similar growth of axial protrusions for system 3 of the LMIS coronal mode. The parameter values for the example system are listed in Table 5.2.

5.4.3.1 Example system 3 evolution

Shown in Fig. 5.8(a) is the spatiotemporal $h(r,t)$ evolution of the coronal mode developing out of the system 3 example. A single, non-axially located protrusion develops from the initially curved and smooth surface. The protrusion does not visibly protrude from the

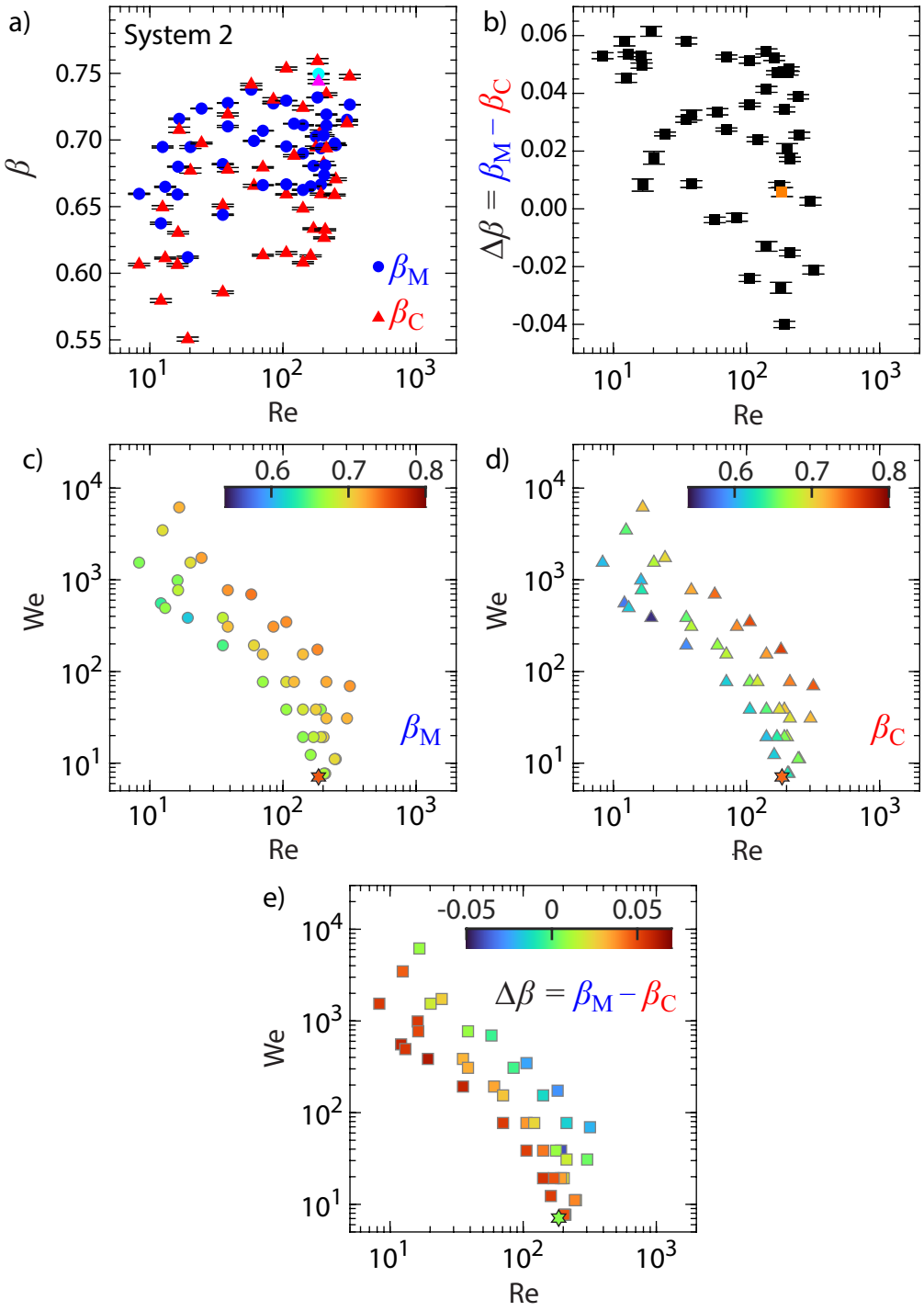

Figure 5.7: Self-similar exponents β_M (circle) and β_C (triangle) and also $\Delta\beta = \beta_M - \beta_C$ (square) extracted from system 2 simulations plotted (a)-(b) against Re and (c)-(e) in the Re and We parameter space. The values for all system 2 simulations analyzed can be found in Table 5.5. The error bars in (a)-(b) indicate the fitting errors. The marker colors in (c)-(e) indicate the β and $\Delta\beta$ value corresponding to the respective colorbars. The results from a separate simulation of the Suvorov [134] geometry are marked by (a) β_M cyan circle and β_C magenta triangle, (b) $\Delta\beta$ orange square and (c)-(e) hexagons.

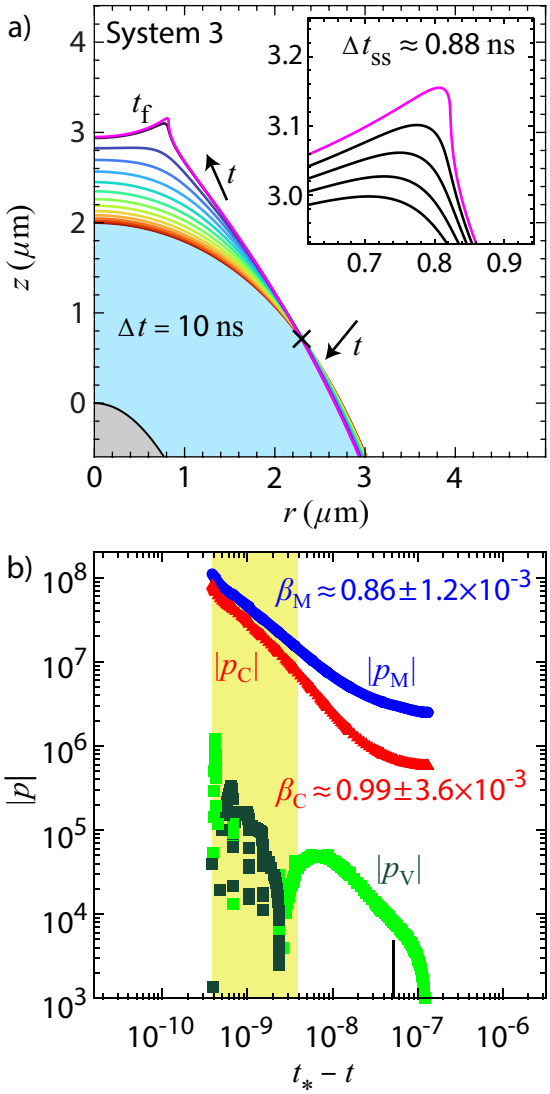

Figure 5.8: Spatiotemporal evolution of the system 3 example. (a) Surface $h(r,t)$ evolution that is first uniformly sampled in t at Δt (colored lines) and then uniformly sampled at Δt_{ss} (black lines) during the self-similar regime for the inset of the sharpening apex. The final $h(r,t_f)$ (pink line), initial liquid bulk (blue) and microemitter (grey) are also shown. Black cross marks where $h(r,t_f) \leq h(r,0)$. The evolution is similar as that shown back in Sec. 3.4.4 and has been shown for a parameter set relevant to this chapter. (b) Protrusion apex Maxwell p_M (blue circle), capillary p_C (red triangle) and viscous p_V (dark $p_V < 0$ and light $p_V \geq 0$ green square) pressure temporal evolution log $|p|$, log rescaled time $t_* - t$ scale. Self-similar exponents β_M and β_C and their fitting uncertainties have been extracted over the last 1.0 decades in $t_* - t$ (yellow interval). The black line indicates t at which coronal protrusion signature arises as a local maximum in p_C.

underlying liquid bulk until very late in the simulated evolution. It protrudes at an angle to the underlying bulk and is asymmetric about the evolving r^{apex}, which prevents extraction of half angle θ_f measurements. The inset indeed shows the accelerated tip sharpening still observed during the late time development.

The coronal protrusion apex pressure evolution is shown in Fig. 5.8(b) in the double logarithmic scale. The magnitudes of the three pressures again order themselves as $|p_M| > |p_C| \gg |p_V|$ like their axial counterparts. The viscous pressure again undergoes a sign change during the self-similar fitting interval that precludes β_V extraction. The Maxwell and capillary pressure data at the very late stages of simulated protrusion development indeed exhibit observable mesh induced deviations from straight lines. Despite the deviations, the RLS fitting procedure is still found to extract a strong self-similar fit for p_M with β_M fitting error comparable to those found for the axial protrusions. The capillary pressure p_C, however, is found to be visibly curving during a significant portion of the fitting interval. Reliably extracting β_C for coronal systems was found to be much more difficult than extracting β_M due to this behavior. Therefore, β_C values reported in Table 5.7 should not be taken too seriously. Nevertheless, the protrusion apex has been shown to undergo self-similar growth despite the non-axial development. The exponent values have also been found to be significantly larger than those extracted for the axial mode examples cataloged so far, signaling that the non-axial protrusion apex undergoes a faster self-similar growth.

5.4.3.2 Distribution of system 3 self-similar exponents

The distribution of system 3 self-similar exponents β_M and β_C and their difference $\Delta\beta = \beta_M - \beta_C$ in the Reynolds number Re and electric Weber number We is shown in Fig. 5.9. Table 5.7 provides the full list of exponents.

As previously shown (see Ch. 3), the coronal mode clusters around Re slightly higher than that accessed by the axial mode. The exponent values shown in Fig. 5.9(a) are indeed systematically larger than those extracted for systems 1 and 2. The capillary β_C values are found to be systematically larger than β_M but it should again be reminded that β_C values presented should not be taken too seriously due to the previously stated issues regarding the p_C evolution. This also applies to the differences $\Delta\beta$ values presented in Fig. 5.9(b). Both β_M and β_C cluster around $\beta \approx 1$. Although $\beta \approx 1$ is the predicted β_M value in the viscous limit [166], the Re values are not in the viscous regime and p_C, not p_V, is always found to provide the main competitive balance to p_M for system 3 simulations. No obvious collapse or trend could be extracted in the Re and We parameter space shown in Fig. 5.9(c)-(e). Nevertheless, the difference in axial/non-axialness and symmetry/asymmetry

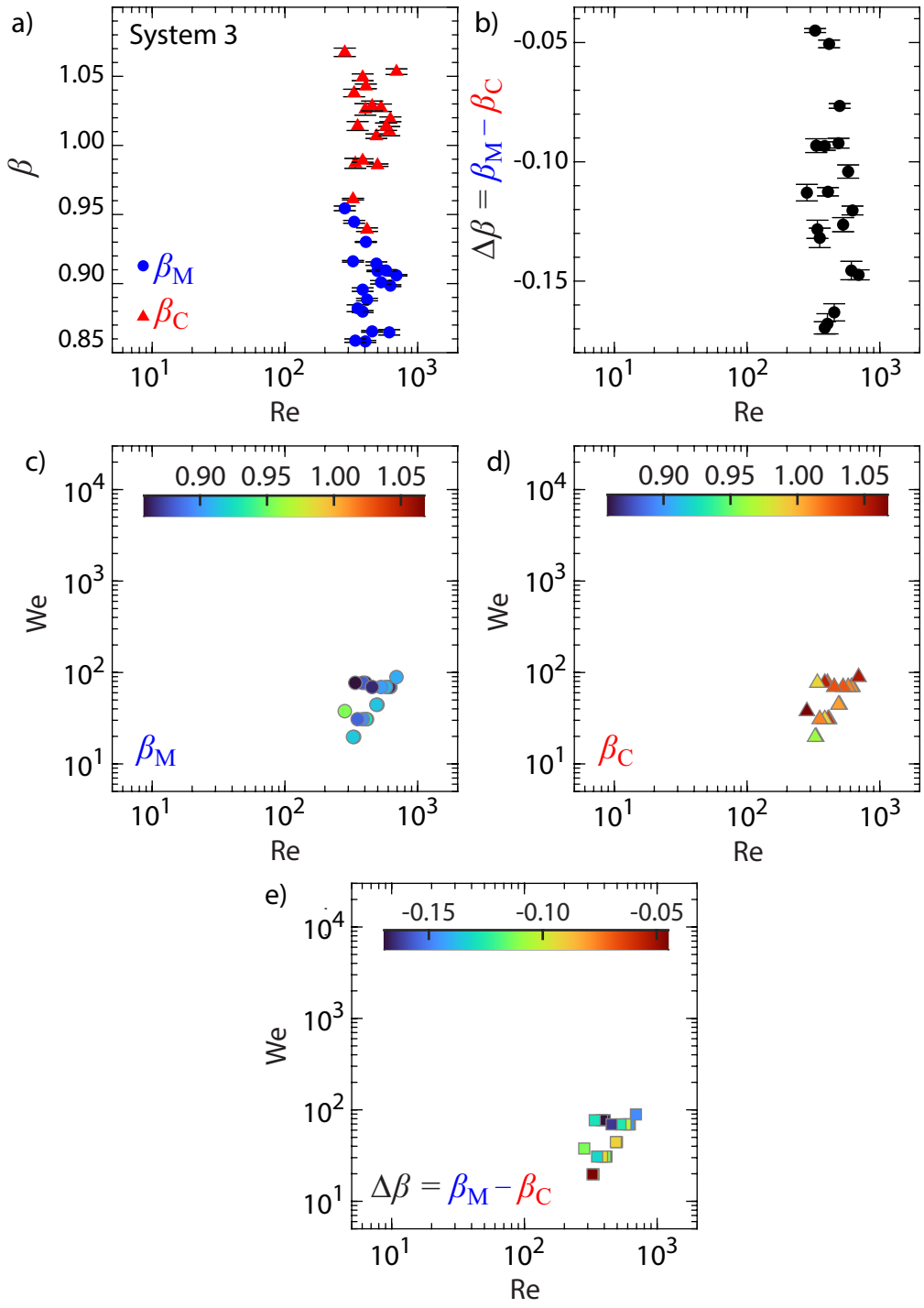

Figure 5.9: Self-similar exponents β_M (circle) and β_C (triangle) and also $\Delta\beta = \beta_M - \beta_C$ (square) extracted from system 3 simulations plotted (a)-(b) against Re and (c)-(e) in the Re and We parameter space. The values for all system 3 simulations analyzed can be found in Table 5.7. The error bars in (a)-(b) indicate the fitting errors. The marker colors in (c)-(e) indicate the β and $\Delta\beta$ value corresponding to the respective colorbars.

of the growing protrusion apex is shown to be accompanied by the dichotomy that arises between systems 1-2 and system 3 simulations. It is unknown how much influence each characteristic exerts on the self similarity, however, as the two effects are intimately tied to each other.

5.4.4 Self-similar growth in system 4: LMIS instability mode

This section presents the simulation results of the self-similar growth of axial protrusions for system 4 of the LMIS instability mode. The parameter values for the example systems are listed in Table 5.2.

5.4.4.1 Example system 4 evolution

The self-similar fits have also been conducted for system 4 case that culminates in the development of multiple protrusions in a wave-like pattern along the liquid surface. Fig. 5.10(a)-(b) show the spatiotemporal surface evolution for examples where the most prominent protrusion apex develops axially (Fig. 5.10(a)) and non-axially (Fig. 5.10(b)). Despite the seemingly simultaneous development of the protrusions, only a single protrusion is found to possess $E^{apex} \geq 5$ GV/m at t_f regardless of the number of protrusions. As a result, self-similar exponents were extracted just for the most prominent protrusion apex. The characteristics of protrusion development for the axial and non-axial most prominent protrusion apex are consistent with those found for system 2 and system 3, respectively.

Fig. 5.10(c) for the axially and Fig. 5.10(d) for the non-axially located most prominent protrusion apex indeed presents self-similar growth of p_M with β_M fitting errors comparable to those extracted for axial mode systems. The self-similar growth is observed despite the presence and simultaneous development of additional protrusions, which highlights the strongly locally characterized development as encoded by self-similar processes. The axially located apex β are also consistent with those extracted for the axial mode systems, whereas the non-axially located apex β are also much larger than the axially located counterparts and consistent with those extracted for the coronal mode systems. The capillary pressure p_C once again exhibits much later onset of self-similar growth for both examples as it is found to curve during the fitting intervals.

5.4.4.2 Distribution of system 4 self-similar exponents

The distribution of system 4 self-similar exponents β_M and β_C and their difference $\Delta\beta = \beta_M - \beta_C$ in the Reynolds number Re and electric Weber number We is shown in Fig. 5.11. Table 5.8 and 5.9 provide the full list of exponents for the axial and non-axial most

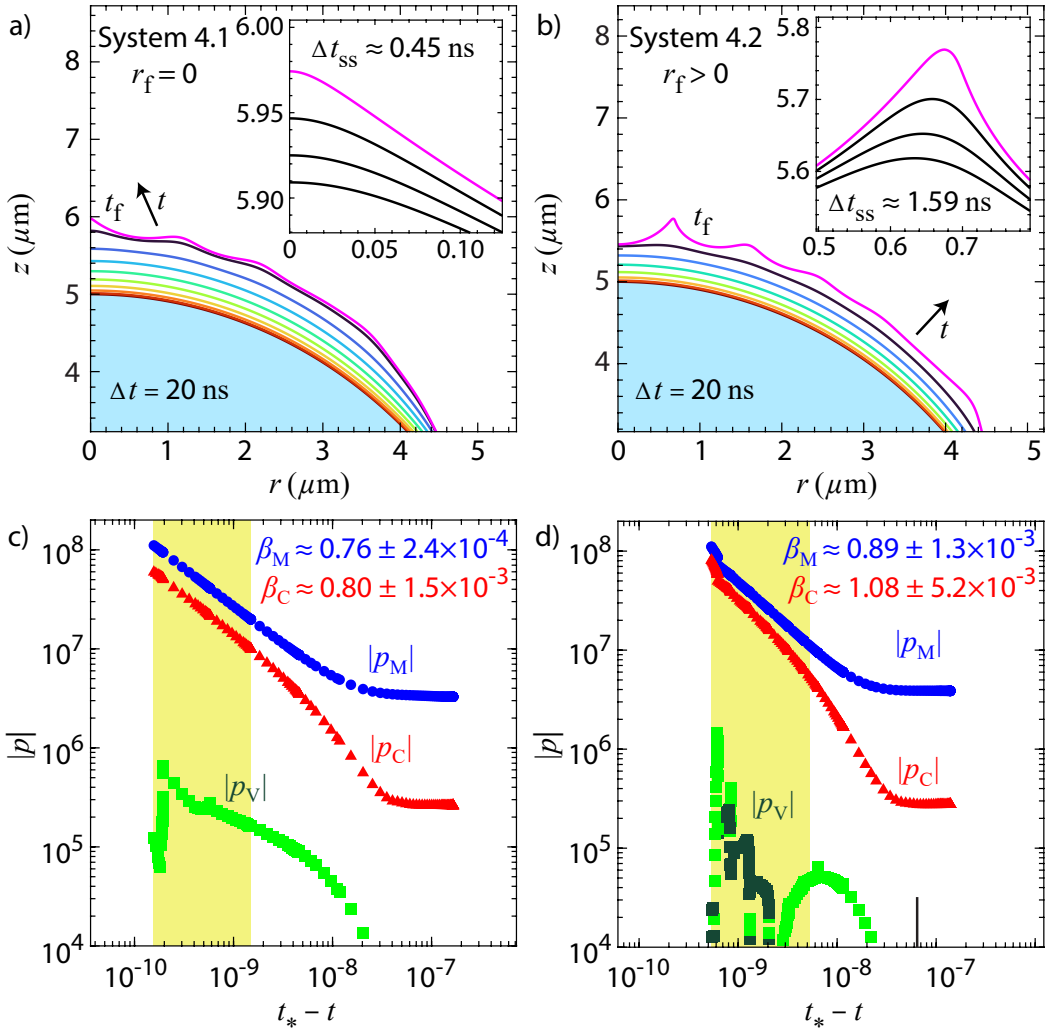

Figure 5.10: Spatiotemporal evolution of the system 4 examples. The most prominent protrusion is located at $r_f = 0$ for (a), (c) and $r_f > 0$ for (b), (d). Panels (a) and (b) show the $h(r,t)$ evolution that is first uniformly sampled in t at Δt (colored lines) and then uniformly sampled at Δt_{ss} (black lines) during the self-similar regime for the inset of the sharpening apex. The final $h(r,t_f)$ (pink line), initial liquid bulk (blue) and microemitter (grey) are also shown. The evolution is similar as that shown back in Sec. 3.4.5 and has been shown for parameter sets relevant to this chapter. Panels (c) and (d) show the protrusion apex Maxwell p_M (blue circle), capillary p_C (red triangle) and viscous p_V (dark $p_V < 0$ and light $p_V \geq 0$ green square) pressure temporal evolution log $|p|$, log rescaled time $t_* - t$ scale. Self-similar exponents β_M and β_C and their fitting uncertainties have been extracted over the last 1.0 decades in $t_* - t$ (yellow interval). The black line in (d) indicates t at which the most prominent protrusion signature arises as a local maximum in p_C.

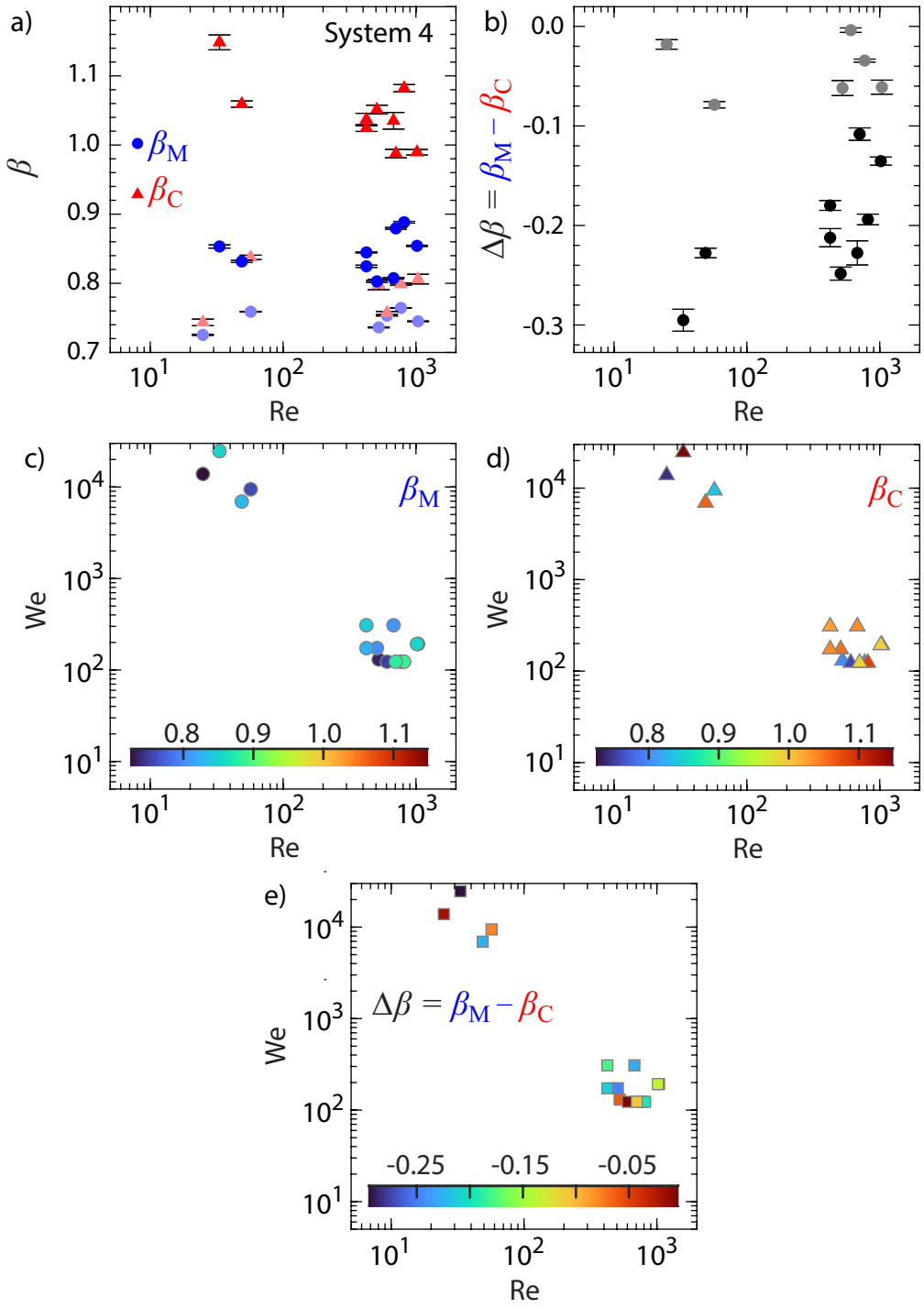

Figure 5.11: Self-similar exponents β_M (circle) and β_C (triangle) and also $\Delta\beta = \beta_M - \beta_C$ (square) extracted from system 4 simulations plotted (a)-(b) against Re and (c)-(e) in the Re and We parameter space.The values for all system 4 simulations analyzed can be found in Table 5.8 for $r_f = 0$ cases and Table 5.9 for $r_f > 0$ cases. The error bars in (a)-(b) indicate the fitting errors. The lighter markers indicate cases with $r_f = 0$, whereas the darker markers indicate cases with $r_f > 0$. The marker colors in (c)-(e) indicate the β and $\Delta\beta$ value corresponding to the respective colorbars.

prominent protrusion apex cases, respectively. The exponent values shown in Fig. 5.11(a) and differences shown in Fig. 5.11(b) are indeed found to separate depending on whether the most prominent protrusion is of the axial or coronal type, further confirming the resultant dichotomy of the self-similar protrusion apex growth. The separation is found to be intact despite the presence of additional protrusions that undergo simultaneous development from the liquid surface, correctly indicating that such presence induces no significant influence on the highly localized self-similar growth of individual protrusion apices. No obvious trends in the Re and We parameter space could be identified for β_M, β_C and $\Delta\beta$ in Fig. 5.11(c)-(e). It is noteworthy that the axial most prominent protrusion apex β_M remains capped at $\beta \approx 0.75$ despite the orders of magnitude increase in We compared to the system 1 and 2 axial counterparts. Similar behavior is found for β_C, albeit with larger deviation due to the previously stated issues with the p_C evolution in the fitting interval.

5.5 Discussion

This section offers discussion on the comparison of self-similar exponents between the systems, the limitations of the simulations conducted for this study and notes on the protrusion half angle measurements.

5.5.1 Comparison of self-similar exponents between the systems

The comparison between the exponents for systems 1 and 2 are found in Table 5.6. The differences were measured for pairs of systems that possess the same h_o, r_s and ϕ_o values. Both exponents undergo slight reductions as the extractor aperture is introduced, which reduces the E generated on the liquid surface and leads to weakened p_M inducing protrusion development and tip sharpening. The reduction is found to be the greatest for the systems possessing relatively small We for the Re values leading to axial mode development. The self-similar exponents extracted from system 2 (Table 5.5) and 3 (Table 5.7) have been found to be vastly different. Both exponents for system 3 are found to be around 1 and systematically greater than system 2 counterparts, whose values are found to be capped at around 0.75. The difference in exponents is accompanied by the differences in the protrusion apex location and protrusion profile symmetry found between the two systems, although how much influence each characteristic exerts on the exponents is unknown. Unlike system 2 exponents that exhibited collapse in the Re and We space, system 3 exponents did not exhibit a similar collapse. System 4 exponents (Table 5.8 and Table 5.9) do indicate that the presence and growth of neighboring protrusions do not significantly influence the self-similar growth. The extracted exponents also confirm the dichotomy found between system 2 and system 3 values depending on whether the most prominent protrusion apex

being analyzed is of the axial or coronal type. This further suggests that the underlying mechanism leading to the exhibited dichotomy is related to the axial/non-axialness and/or symmetry/asymmetry of the growing protrusion.

5.5.2 Limitations of the conducted simulations

Some choices made for the computational algorithm utilized for the conducted simulations lead to the following limitations on extracting the self-similar growth of the protrusions. While gravity was neglected in the simulations, the maximum Bond number $\mathsf{Bo} = \rho g h_o / p_c = 2\rho g h_o (r_s + h_o)^2 / \varepsilon_o \phi_o^2$ characterizing the influence of gravitational effects for the analyzed systems evaluates to $\mathsf{Bo} = 1.69 \times 10^{-6}$ for the worst possible combination of $h_o = 5$ μm, $r_s = 5$ μm and $\phi_o = 2.0$ kV. This shows that gravity is indeed negligible for the modeled system over all h_o, r_s and ϕ_o simulated.

The simulations were terminated from the criterion set by $E^{apex} \geq 5$ GV/m, which still allowed the previous study (see Ch. 3) to catalog the EHD mode development and the current study to extract values for β_M and β_C over meaningful intervals in the rescaled $t_* - t$. It was deemed difficult to advance the simulations further in time due to the $O(10$ GV/m$)$ physical constraint [108] for field evaporation of ions from liquid metals, which has not been modeled in the current simulations. In addition, the numerical errors incurred from the worsening protrusion tip mesh resolution were found to be significant past the termination criterion for the axial mode systems and even prior to the criterion as observed for the non-axial protrusion apices.

These restrictions preclude access to the protrusion tip spatiotemporal scales below which Zubarev [166] has recently predicted the onset of viscous dominated protrusion tip self-similar growth, which primarily results in the change of predicted β_M from 2/3 to 1. The characteristic length and time scales that specify the onset of such growth were estimated to be tens of nanometers and tens of picoseconds prior to the asymptotic blowup time t_c. Although the simulations are able to access protrusion apex radii of tens of nanometers as previously cataloged (see Ch. 3), the $t_* - t_f$ values accessed as determined by the self-similar fits are found to be still a couple of orders of magnitude larger than the predicted time scales. As such, no transition of the self-similar growth into the viscous dominated regime was observed in the simulated protrusion development prior to ion emission. Zubarev also estimated the critical electric field value for the onset of viscous dominated growth to be of $O(10$ GV/m$)$, which is the order of magnitude value for field evaporation of ions from liquid metals. As the simulations are terminated when $E^{apex} \geq 5$ GV/m, the absence of the transition into the viscous dominated self-similar growth is consistent with the estimated

field criterion.

The restrictions also preclude further correlation analysis of the non-axial protrusion apex β_M and β_C to variables such as the protrusion apex coordinate r_f. This is due to the fact that the variations in the extracted β across system 3 and system 4.2 simulations were found to be comparable to variations found during the coronal mode mesh convergence study, even with the RLS fitting procedure. This arises from the fact that the most critical data at the latest t that most strongly determines the goodness of t_* and β_M fits is that most susceptible to mesh induced numerical error. The spurious errors in the apex pressures were found to be significantly suppressed as the minimum mesh size employed was made significantly smaller than that used for the simulations (5 nm). However, such small mesh sizes become too small for the continuum approximation to retain its validity [118]. Future numerical modeling that attempts to conduct such correlation analysis may have to seek alternative methods that intrinsically allow sub nanoscale spatial resolution, sew together separate calculations made at different scales or utilize much higher order element discretizations to overcome the outlined difficulties. Nevertheless, the simulations have still been able to show how such protrusions still undergo self-similar growth and how they possess exponents vastly different from their axial counterparts, both of which have yet to been shown in the literature.

5.5.3 On the half angle measurements

The measurements θ_f of the local minimum in θ at $t = t_f$ closest to $r = 0$ presented for systems 1 and 2 in Tables 5.4 and 5.5, respectively, and their comparison in Table 5.6 present interesting observations. The first is that θ_f was found to systematically decrease as the extractor aperture was introduced, which was accompanied by a reduction in β and increase in r_θ. The values are also found to increase as β increases, which seems in direct contradiction to the findings by Fontelos *et al.* [44] and Zubarev [166] on the relationship between the limiting protrusion angle and the self-similar exponent. However, it should be reminded that all simulations conducted in this study were strictly terminated once $E^{apex} \geq 5$ GV/m. The evolution of $\theta(r,t)$ presented back in Fig. 5.2(b) and Fig. 5.5(b) also shows that the protrusion profile exhibits a rapidly accelerating apex sharpening during the late stage growth even at the termination time t_f such that changes to the termination criterion can lead to significant changes in the reported θ_f value. Thus, θ_f should not be understood to be the limiting or asymptotic protrusion half angle as discussed in the literature but rather a measurement extracted at just an instance in time $t = t_f$ derived from a physically motivated but still an arbitrary simulation termination criterion.

5.6 Conclusion

The computational simulations described in this work examine the self-similar growth of EHD modes that develop in the geometry modeling a realistic LMIS system. The accelerating protrusion development and tip sharpening are tracked by the arbitrary Lagrangian Eulerian finite element method. The self-similar exponents of the protrusion apex Maxwell and capillary pressures have been extracted from least squares fitting procedures yielding small fitting errors. The results show that the protrusions in the modeled LMIS geometry possessing a highly curved microemitter substrate and extractor aperture indeed undergo self-similar power law growth during the late stage development. The self-similar growth is also found to be preserved even for the EHD coronal mode resulting in a non-axial, asymmetric protrusion development and for the EHD instability mode resulting in simultaneous development of multiple protrusions in a wave-like pattern.

The self-similar exponents extracted from the EHD axial mode simulations are shown to collapse in the parameter space generated by the Reynolds number and also the electric Weber number. Further comparison of exponents between the axial, coronal and instability EHD modes reveals a dichotomy of exponent values induced by the change in mode as the protrusions that are non-axial possess exponents systematically larger than the axial counterparts. Future work that further examines the effects of asymmetry and non-axial locations of the developing protrusion apices may be able to identify the exact effect that each detail imposes on the observed dichotomy of exponents.

5.7 Appendix A: Simulations of the Suvorov geometry

This section presents the results from the separate simulations of the Suvorov [134] geometry conducted for checks on the computational algorithm and fitting methodology described back in Sec. 5.3.3. The material constants employed by Suvorov for liquid gallium are $\rho = 6090$ kg/m^3, $\gamma = 0.72$ N/m and $\mu = 2.13 \times 10^{-3}$ Pa s. The axisymmetric geometry replicating that employed by Suvorov consists of a flat liquid layer with thickness $h_o = 5$ μm that is augmented with a small Gaussian bump. The initial liquid shape is described as $h(r, t = 0) = \delta \exp(-r^2/\lambda^2)$ with $\lambda = 10\delta = 1$ μm. The Gaussian apex curvature radius is equal to $\lambda^2/2\delta = 5$ μm, which is of the same order of the microemitter apex radii utilized in this study and in real LMIS emitters. The liquid is placed under a flat, apertureless extractor with vertical gap distance 5 μm. The computational domain width is also set to be 5 μm. The applied electric potential to the surface is $\phi = 2.4$ kV such that the electric field generated for the flat liquid surface is $E = 0.48$ GV/m. The details of the computational algorithm employed are the same as those utilized in our simulations.

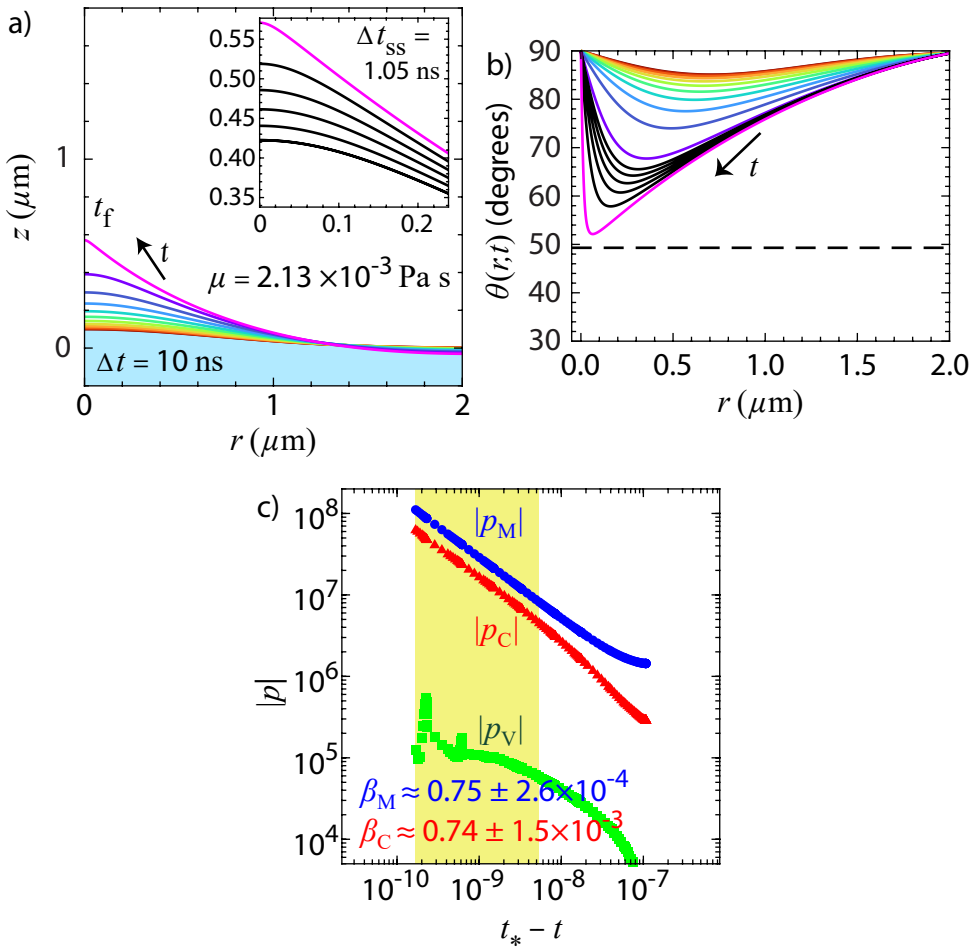

Figure 5.12: Spatiotemporal evolution of the Suvorov [134] system. (a) Surface $h(r,t)$ evolution that is first uniformly sampled in t at Δt (colored lines) and then uniformly sampled at Δt_{ss} (black lines) in the inset of the sharpening apex. The final $h(r,t_f)$ (pink line) and initial liquid bulk (blue) are also shown. (b) Half angle $\theta(r,t)$ evolution with the Taylor cone [141] angle 49.3° (dashed line) denoted. (c) Protrusion apex Maxwell p_M (blue circle), capillary p_C (red triangle) and viscous p_V (dark $p_V < 0$ and light $p_V \geq 0$ green square) pressure temporal evolution log $|p|$, log rescaled time $t_* - t$ scale. Self-similar exponents β_M and β_C and their fitting uncertainties have been extracted over the last 1.5 decades in $t_* - t$ (yellow interval).

Table 5.3: Key parameters and quantities for separate simulations conducted for the Suvorov [134] geometry. The initial conditions kept fixed in the simulations are $\rho = 6090$ kg/m^3, $\gamma = 0.720$ N/m, $h_o = 5$ μm and $\phi_o = 2.4$ kV. As the geometry does not possess a curved microemitter, $r_s = 0$ such that Re reduces to $\mathsf{Re} = \sqrt{\rho\varepsilon_o/2}(\phi_o/\mu)$. The quantities are μ, Re, t_f, self-similar exponents β and axial θ_f (local minimum in θ at $t = t_f$ closest to $r = 0$) extracted at $r = r_\theta$.

System	μ (Pa s)	Re	t_f (s)	θ_f (°)	r_θ (μm)
Fig. 5.12	2.13×10^{-3}	185	1.1×10^{-7}	52.1	0.064
Fig. 5.13	2.13×10^{-4}	1850	1.0×10^{-7}	54.0	0.060
Fig. 5.14	2.13×10^{0}	0.185	7.0×10^{-6}	41.8	0.206

System	β_M	β_C	β_V
Fig. 5.12	$0.75 \pm 2.6 \times 10^{-4}$	$0.74 \pm 1.5 \times 10^{-3}$	
Fig. 5.13	$0.69 \pm 9.8 \times 10^{-4}$	$0.71 \pm 3.3 \times 10^{-3}$	
Fig. 5.14	$0.99 \pm 1.2 \times 10^{-4}$	$0.76 \pm 6.4 \times 10^{-4}$	$1.04 \pm 1.6 \times 10^{-3}$

Shown in Fig. 5.12 is the spatiotemporal evolution of the liquid metal in the described Suvorov geometry. The Gaussian bump induces the growth of a single axial protrusion that undergoes rapid spatiotemporal acceleration. The surface $h(r,t)$ evolution shows the depletion of the bulk liquid that supports the protrusion development. The inset shown in Fig. 5.12(a) shows the accelerated protrusion apex sharpening occurring during the late stage development characterized by self-similar growth. Fig. 5.12(b) shows the local surface half angle $\theta(r,t)$ evolution that again shows the accelerated sharpening and tighter confinement of the protrusion apex development. These are marked by a reduction in the $\theta(r,t)$ minimum and its r coordinate that culminates in $\theta_f = 52.1°$ and $r_\theta = 0.064$ μm at $t = t_f$. Fig. 5.12(c) confirms the self-similar growth of the protrusion apex during late stage development with the exponents that approximate $\beta \approx 0.75$. The Maxwell exponent is in between the inviscid ($\beta_M = 2/3$) and viscous ($\beta_M = 1$, $\beta_C = 2/3$) limits due to the intermediate $\mathsf{Re} \approx 185$ value. Both exponents were shown in Sec. 5.3.3 to be consistent with those extracted from the dimensionless simulations of the same geometry conducted by Albertson and Troian [5].

Shown in Fig. 5.13 is the spatiotemporal evolution in the same Suvorov geometry but with the liquid viscosity set to $\mu = 2.13 \times 10^{-4}$ Pa s, which is ten times smaller than that originally employed in Fig. 5.12. This leads to a tenfold increase in $\mathsf{Re} \approx 1850$. The reduction in μ leads to a slightly shorter and duller protrusion apex at $t = t_f$ as seen in Fig. 5.13(a) and its

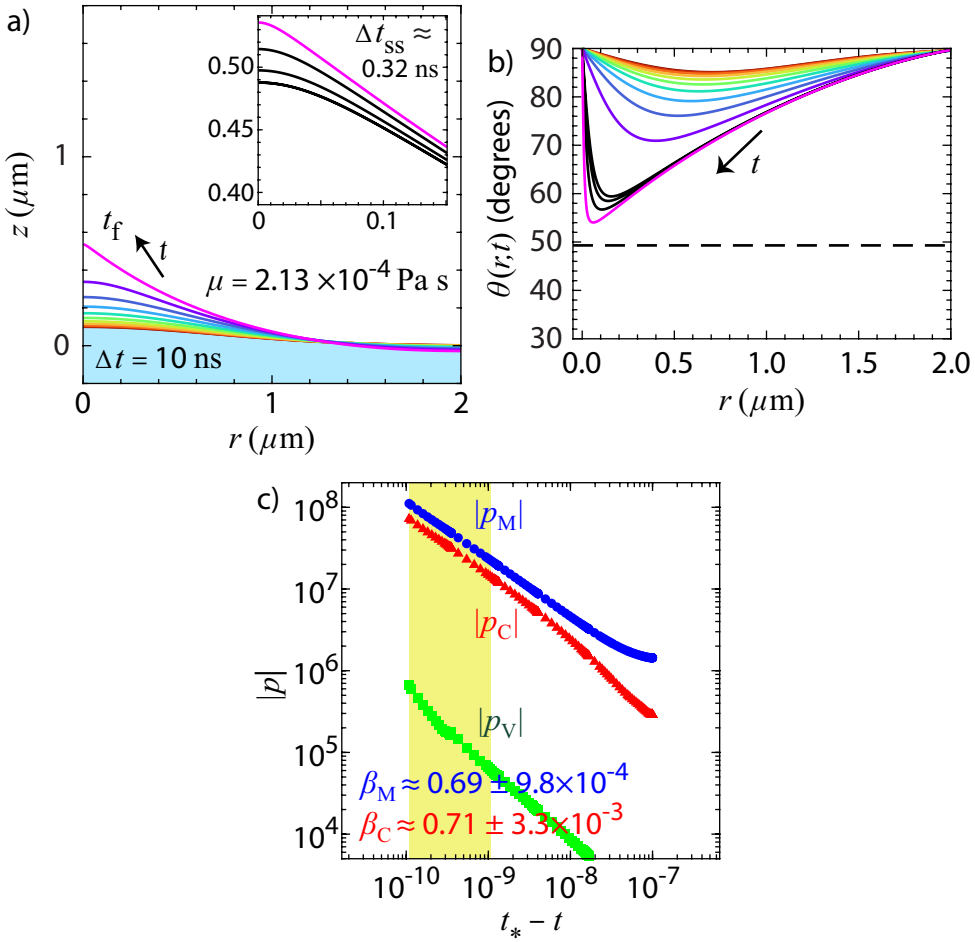

Figure 5.13: Spatiotemporal evolution of the Suvorov [134] system with μ reduced tenfold. (a) Surface $h(r,t)$ evolution that is first uniformly sampled in t at Δt (colored lines) and then uniformly sampled at Δt_{ss} (black lines) in the inset of the sharpening apex. The final $h(r,t_f)$ (pink line) and initial liquid bulk (blue) are also shown. (b) Half angle $\theta(r,t)$ evolution with the Taylor cone [141] angle 49.3° (dashed line) denoted. (c) Protrusion apex Maxwell p_M (blue circle), capillary p_C (red triangle) and viscous p_V (dark $p_V < 0$ and light $p_V \geq 0$ green square) pressure temporal evolution log $|p|$, log rescaled time $t_* - t$ scale. Self-similar exponents β_M and β_C and their fitting uncertainties have been extracted over the last 1.0 decades in $t_* - t$ (yellow interval).

inset. Fig. 5.13(b) more clearly shows the difference as the reduction in $\theta(r,t)$ is smaller leading to the extracted $\theta_f = 54.0°$ larger than that in the original system and $r_\theta = 0.060$ μm smaller than that in the original system. Fig. 5.13(c) demonstrates that the increase in Re correctly leads to a reduction in both β_M and β_C towards $\beta = 2/3$ as predicted by Zubarev [165]. Both exponents were also shown in Sec. 5.3.3 to be consistent with those extracted from Albertson and Troian [5] for Re = 2000 in the same dimensionless geometry.

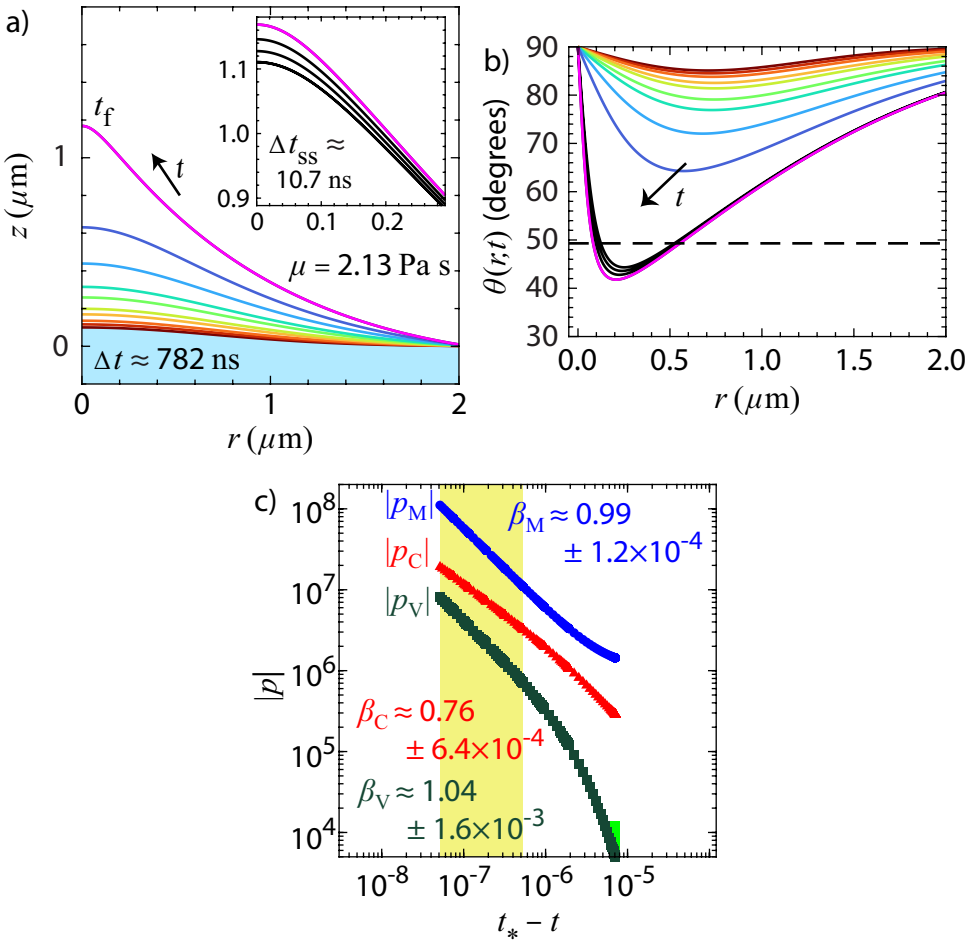

Figure 5.14: Spatiotemporal evolution of the Suvorov [134] system with μ enhanced thousandfold. (a) Surface $h(r,t)$ evolution that is first uniformly sampled in t at Δt (colored lines) and then uniformly sampled at Δt_{ss} (black lines) in the inset of the sharpening apex. The final $h(r,t_f)$ (pink line) and initial liquid bulk (blue) are also shown. (b) Half angle $\theta(r,t)$ evolution with the Taylor cone [141] angle 49.3° (dashed line) denoted. (c) Protrusion apex Maxwell p_M (blue circle), capillary p_C (red triangle) and viscous p_V (dark $p_V < 0$ and light $p_V \geq 0$ green square) pressure temporal evolution log $|p|$, log rescaled time $t_* - t$ scale. Self-similar exponents β_M and β_C and their fitting uncertainties have been extracted over the last 1.0 decades in $t_* - t$ (yellow interval).

Shown in Fig. 5.14 is the spatiotemporal evolution in the same Suvorov geometry but with

the liquid viscosity set to $\mu = 2.13$ Pa s, which is thousand times larger than that originally employed in Fig. 5.12. This leads to a reduction in $\mathsf{Re} \approx 0.185$. The enhancement in μ leads to much more elongated protrusion profile as seen in Fig. 5.14(a) and its inset. Fig. 5.14(b) more clearly shows the difference as the reduction in $\theta(r,t)$ is larger leading to the extracted $\theta_f = 41.8°$ smaller than that in the original system and the Taylor cone angle [141] and $r_\theta = 0.206$ μm larger than that in the original system. The decrease in Re leads to an increase in both β_M towards $\beta_M = 1$ as predicted by Zubarev [166]. The normal viscous pressure, which now takes magnitudes comparable to p_C that once provided the main competitive balance, now permits extraction of β_V, whose value closely approximates $\beta_V = 1$ predicted by Zubarev [166]. Interestingly, p_V is found to be negative almost entirely throughout the simulated evolution, which indicates that it actually aids the always negative p_M in driving the apex development. The capillary exponent β_C is shown to be not significantly affected. The three exponents were also shown in Sec. 5.3.3 to be consistent with those extracted from Albertson and Troian [5] for $\mathsf{Re} = 0.2$ in the same dimensionless geometry.

5.8 Appendix B: Convergence tests

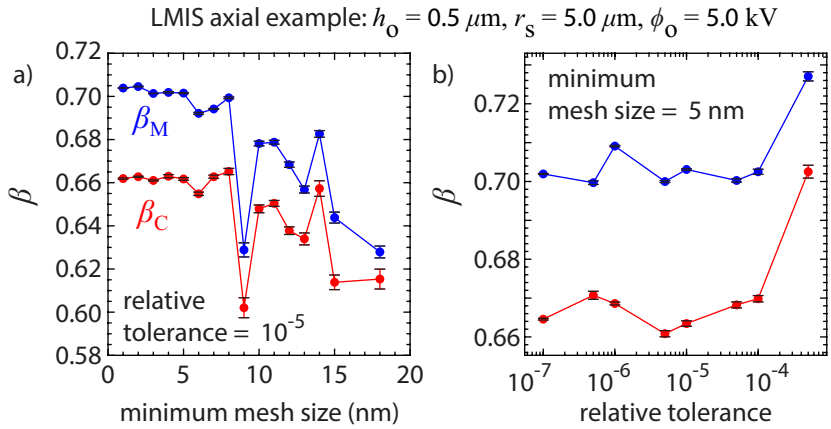

Figure 5.15: Convergence tests of Maxwell β_M and capillary β_C exponents for a LMIS axial mode example with $h_o = 0.5$ μm, $r_s = 5.0$ μm and $\phi_o = 5.0$ kV as (a) minimum mesh size and (b) relative tolerance are changed. For each simulation, exponents were extracted over OLS fits of the last 1.5 decades in $t_* - t$. Error bars represent the fitting errors.

Convergence of the most prominent protrusion apex coordinates r_f and z_f for the selected LMIS axial (system 2) and coronal mode (system 3) examples have already been shown in Sec. 3.9. This set of tests shown here additionally shows the convergence of self-similar exponents β_M and β_C for the same selected examples. The results are shown in Fig. 5.15 for the LMIS axial mode example and Fig. 5.16 for the LMIS coronal mode example. As stated

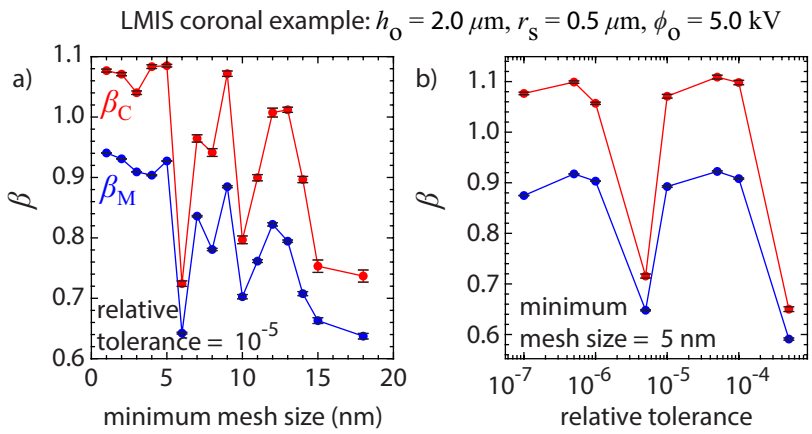

Figure 5.16: Convergence tests of Maxwell β_M and capillary β_C exponents for a LMIS coronal mode example with $h_o = 2.0$ μm, $r_s = 0.5$ μm and $\phi_o = 5.0$ kV as (a) minimum mesh size and (b) relative tolerance are changed. For each simulation, exponents were extracted over RLS fits of the last 1.0 decades in $t_* - t$. Error bars represent the fitting errors.

in the text, the fitting errors are much smaller than the mesh and relative tolerance induced variations in β values, which are of $O(10^{-2})$. It can also be seen that the coronal example possesses larger deviations in β due to the complications that arise out of the non-axial location of the moving protrusion apex. Still, it is shown that the two exponents achieve good convergence at the values of the minimum mesh size (5 nm) and relative tolerance (10^{-5}) applied to the simulations.

5.9 Appendix C: Tables

The tables in the Appendix present measurements of the quantities defined in Table 5.1 extracted from the simulations in the different systems.

Table 5.4 shows the system 1 (i.e. axial protrusion from LMIS geometry without extractor aperture) self-similar exponents.

Table 5.5 shows the system 2 (i.e. LMIS axial mode) self-similar exponents.

Table 5.6 shows the difference between self-similar exponents extracted from systems 1 and 2.

Table 5.7 shows the system 3 (i.e. LMIS coronal mode) self-similar exponents.

Table 5.8 and 5.9 show the system 4 (i.e. LMIS instability mode) self-similar exponents for cases with most prominent protrusion apex at $r_f = 0$ and $r_f > 0$, respectively.

Table 5.4: System 1 self-similar exponents and measured quantities. Quantities are h_o, r_s, ϕ_o, initial liquid apex E_o, Reynolds number $\mathsf{Re} = \sqrt{\rho\varepsilon_o/2}[\phi_o h_o/\mu(r_s + h_o)]$, electric Weber number $\mathsf{We} = \varepsilon_o\phi_o^2/2\gamma h_o$, protrusion apex z_f, β_M and β_C with fitting errors, t_f, $\tau(t_f) = t_* - t_f$, number of decades in $t_* - t$ used for self-similar fitting n and axial θ_f (local minimum in θ at $t = t_f$ closest to $r = 0$) extracted at $r = r_\theta$. The dash "-" in θ_f and r_θ entries indicate those which did not yield measurement of θ_f.

System 1: axial mode in LMIS geometry without extractor aperture

h_o (μm)	r_s	ϕ_o (kV)	E_o $\left(\frac{\text{GV}}{\text{m}}\right)$	Re	We	z_f (μm)	β_M^{S1}	β_C^{S1}	t_f (s)	$\tau(t_f)$ (ns)	n	θ_f (°)	r_θ (μm)
0.1	0.5	2.5	1.13	35	385	0.25	$0.72 \pm 5.6\times10^{-4}$	$0.70 \pm 2.5\times10^{-3}$	2.1×10^{-8}	0.16	1.0	50.4	0.06
0.1	1.0	2.5	0.68	19	385	0.42	$0.65 \pm 8.5\times10^{-4}$	$0.60 \pm 1.4\times10^{-3}$	2.2×10^{-7}	0.16	1.5	45.1	0.07
0.1	2.0	3.0	0.49	12	555	0.66	$0.65 \pm 5.1\times10^{-4}$	$0.59 \pm 9.6\times10^{-4}$	1.8×10^{-6}	0.17	1.5	44.4	0.08
0.1	2.0	4.0	0.66	16	987	0.41	$0.69 \pm 5.1\times10^{-4}$	$0.65 \pm 1.2\times10^{-3}$	2.6×10^{-7}	0.17	1.5	48.1	0.06
0.1	2.0	5.0	0.82	20	1540	0.32	$0.72 \pm 3.3\times10^{-4}$	$0.70 \pm 2.1\times10^{-3}$	1.1×10^{-7}	0.16	1.0	51.8	0.05
0.1	5.0	5.0	0.43	8	1540	0.72	$0.67 \pm 3.4\times10^{-4}$	$0.61 \pm 6.0\times10^{-4}$	4.0×10^{-6}	0.16	1.5	46.0	0.07
0.1	5.0	7.5	0.64	12	3470	0.40	$0.70 \pm 7.9\times10^{-4}$	$0.68 \pm 1.6\times10^{-3}$	6.4×10^{-7}	0.16	1.5	50.1	0.05
0.1	5.0	10.0	0.86	17	6170	0.27	$0.75 \pm 7.2\times10^{-4}$	$0.73 \pm 2.7\times10^{-3}$	2.4×10^{-7}	0.17	1.0	53.3	0.04
0.2	0.5	2.5	1.02	61	193	0.42	$0.71 \pm 4.0\times10^{-4}$	$0.71 \pm 1.6\times10^{-3}$	2.4×10^{-8}	0.15	1.5	50.0	0.10
0.2	1.0	2.5	0.65	35	193	0.64	$0.67 \pm 6.7\times10^{-4}$	$0.62 \pm 1.0\times10^{-3}$	1.2×10^{-7}	0.16	1.5	45.3	0.12
0.2	2.0	5.0	0.80	39	771	0.51	$0.74 \pm 2.8\times10^{-4}$	$0.74 \pm 2.4\times10^{-3}$	7.4×10^{-8}	0.16	1.0	53.1	0.06
0.2	5.0	4.0	0.34	13	493	1.34	$0.68 \pm 3.6\times10^{-4}$	$0.62 \pm 9.2\times10^{-4}$	3.8×10^{-6}	0.17	1.5	44.7	0.11
0.2	5.0	5.0	0.42	16	771	0.94	$0.70 \pm 3.3\times10^{-4}$	$0.65 \pm 7.9\times10^{-4}$	9.7×10^{-7}	0.17	1.5	46.9	0.08
0.2	5.0	7.5	0.64	24	1730	0.61	$0.74 \pm 1.5\times10^{-4}$	$0.74 \pm 1.7\times10^{-3}$	2.6×10^{-7}	0.16	1.5	52.0	0.06
0.5	0.5	2.5	0.82	106	77	0.93	$0.70 \pm 2.8\times10^{-4}$	$0.70 \pm 9.1\times10^{-4}$	4.6×10^{-8}	0.15	1.5	-	-
0.5	1.0	2.5	0.57	71	77	1.21	$0.70 \pm 2.7\times10^{-4}$	$0.65 \pm 1.0\times10^{-3}$	1.4×10^{-7}	0.17	1.5	44.4	0.47
0.5	2.0	5.0	0.74	85	308	1.00	$0.73 \pm 4.5\times10^{-4}$	$0.76 \pm 1.8\times10^{-3}$	7.9×10^{-8}	0.15	1.0	54.6	0.07
0.5	5.0	5.0	0.41	39	308	1.57	$0.72 \pm 9.5\times10^{-5}$	$0.70 \pm 5.0\times10^{-4}$	4.5×10^{-7}	0.16	1.5	49.0	0.10
0.5	5.0	7.5	0.62	58	694	1.15	$0.74 \pm 2.8\times10^{-4}$	$0.77 \pm 1.4\times10^{-3}$	1.9×10^{-7}	0.15	1.0	54.5	0.07
1.0	0.2	2.5	0.81	176	39	1.74	$0.70 \pm 3.4\times10^{-4}$	$0.73 \pm 1.2\times10^{-3}$	6.5×10^{-8}	0.14	1.0	-	-
1.0	0.5	2.5	0.63	141	39	1.77	$0.70 \pm 2.5\times10^{-4}$	$0.69 \pm 5.5\times10^{-4}$	1.0×10^{-7}	0.16	1.5	-	-
1.0	1.0	2.5	0.47	106	39	2.12	$0.69 \pm 4.4\times10^{-4}$	$0.65 \pm 7.4\times10^{-4}$	2.4×10^{-7}	0.17	1.5	-	-
1.0	2.0	5.0	0.67	141	154	1.76	$0.72 \pm 2.1\times10^{-4}$	$0.76 \pm 1.7\times10^{-3}$	1.1×10^{-7}	0.15	1.0	54.8	0.07
1.0	5.0	5.0	0.39	71	154	2.43	$0.73 \pm 2.3\times10^{-4}$	$0.71 \pm 1.0\times10^{-3}$	4.4×10^{-7}	0.16	1.5	50.0	0.10
1.0	5.0	7.5	0.59	106	347	1.93	$0.74 \pm 2.8\times10^{-4}$	$0.78 \pm 2.8\times10^{-3}$	2.0×10^{-7}	0.15	1.0	55.7	0.07
2.0	0.1	2.0	0.45	161	12	3.55	$0.69 \pm 4.0\times10^{-4}$	$0.65 \pm 4.2\times10^{-4}$	2.7×10^{-7}	0.16	1.5	-	-
2.0	0.2	2.5	0.52	193	19	3.50	$0.71 \pm 4.0\times10^{-4}$	$0.70 \pm 1.3\times10^{-3}$	2.1×10^{-7}	0.15	1.5	-	-
2.0	0.5	2.5	0.44	169	19	3.52	$0.69 \pm 3.2\times10^{-4}$	$0.67 \pm 1.1\times10^{-3}$	2.8×10^{-7}	0.16	1.5	-	-
2.0	1.0	2.5	0.37	141	19	3.97	$0.69 \pm 1.9\times10^{-4}$	$0.65 \pm 7.9\times10^{-4}$	5.3×10^{-7}	0.16	1.5	-	-
2.0	2.0	5.0	0.56	212	77	3.25	$0.74 \pm 3.6\times10^{-4}$	$0.77 \pm 1.7\times10^{-3}$	1.9×10^{-7}	0.15	1.0	54.5	0.07
2.0	5.0	5.0	0.36	121	77	4.01	$0.72 \pm 1.4\times10^{-4}$	$0.72 \pm 9.4\times10^{-4}$	5.4×10^{-7}	0.16	1.5	50.6	0.10
2.0	5.0	7.5	0.54	182	173	3.38	$0.73 \pm 2.8\times10^{-4}$	$0.78 \pm 1.8\times10^{-3}$	2.7×10^{-7}	0.15	1.0	56.1	0.06
5.0	0.1	2.5	0.29	208	8	8.86	$0.70 \pm 3.5\times10^{-4}$	$0.67 \pm 8.4\times10^{-4}$	9.8×10^{-7}	0.16	1.5	-	-
5.0	0.2	2.5	0.28	204	8	8.83	$0.69 \pm 2.8\times10^{-4}$	$0.66 \pm 1.1\times10^{-3}$	1.1×10^{-6}	0.16	1.5	-	-
5.0	0.2	3.0	0.33	244	11	9.19	$0.71 \pm 2.1\times10^{-4}$	$0.71 \pm 8.1\times10^{-4}$	8.3×10^{-7}	0.15	1.5	-	-
5.0	2.0	5.0	0.40	303	31	8.15	$0.73 \pm 3.8\times10^{-4}$	$0.76 \pm 1.9\times10^{-3}$	5.8×10^{-7}	0.15	1.0	54.1	0.08
5.0	5.0	5.0	0.30	212	31	8.55	$0.72 \pm 1.8\times10^{-4}$	$0.72 \pm 4.7\times10^{-4}$	9.9×10^{-7}	0.16	1.5	50.6	0.09
5.0	5.0	7.5	0.45	318	69	7.68	$0.73 \pm 2.6\times10^{-4}$	$0.77 \pm 1.7\times10^{-3}$	5.3×10^{-7}	0.15	1.0	55.9	0.07

Table 5.5: System 2 self-similar exponents and measured quantities. Quantities are h_o, r_s, ϕ_o, initial liquid apex E_o, Reynolds number $\mathsf{Re} = \sqrt{\rho\varepsilon_o/2}[\phi_o h_o/\mu(r_s + h_o)]$, electric Weber number $\mathsf{We} = \varepsilon_o\phi_o^2/2\gamma h_o$, protrusion apex z_f, β_M and β_C with fitting errors, t_f, $\tau(t_f) = t_* - t_f$ and axial θ_f extracted (local minimum in θ at $t = t_f$ closest to $r = 0$) at $r = r_\theta$. Last 1.5 decades in $t_* - t$ were used to extract β for each simulation. The dash "-" in θ_f and r_θ entries indicate those which did not yield measurement of θ_f.

System 2: LMIS axial mode											
h_o (μm)	r_s	ϕ_o (kV)	E_o $\left(\frac{\text{GV}}{\text{m}}\right)$	Re	We	z_f (μm)	β_M^{S2}	β_C^{S2}	t_f (s)	$\tau(t_f)$ (ns)	θ_f (°)	r_θ (μm)
0.1	0.5	2.5	0.97	35	385	0.29	$0.68 \pm 4.5\times10^{-4}$	$0.65 \pm 8.7\times10^{-4}$	3.7×10^{-8}	0.17	46.8	0.07
0.1	1.0	2.5	0.58	19	385	0.58	$0.61 \pm 7.8\times10^{-4}$	$0.55 \pm 1.5\times10^{-3}$	1.3×10^{-6}	0.16	42.5	0.09
0.1	2.0	3.0	0.42	12	555	0.99	$0.64 \pm 8.3\times10^{-4}$	$0.58 \pm 1.4\times10^{-3}$	1.7×10^{-5}	0.15	42.4	0.11
0.1	2.0	4.0	0.56	16	987	0.53	$0.66 \pm 5.0\times10^{-4}$	$0.61 \pm 9.7\times10^{-4}$	6.7×10^{-7}	0.16	45.7	0.06
0.1	2.0	5.0	0.69	20	1540	0.38	$0.69 \pm 1.1\times10^{-3}$	$0.68 \pm 1.9\times10^{-3}$	2.0×10^{-7}	0.14	48.9	0.05
0.1	5.0	5.0	0.36	8	1540	1.02	$0.66 \pm 4.5\times10^{-4}$	$0.61 \pm 9.3\times10^{-4}$	1.4×10^{-5}	0.15	44.5	0.09
0.1	5.0	7.5	0.54	12	3470	0.51	$0.69 \pm 7.0\times10^{-4}$	$0.65 \pm 1.3\times10^{-3}$	1.3×10^{-6}	0.17	48.0	0.06
0.1	5.0	10.0	0.71	17	6170	0.35	$0.72 \pm 6.1\times10^{-4}$	$0.71 \pm 2.0\times10^{-3}$	4.5×10^{-7}	0.14	51.2	0.05
0.2	0.5	2.5	0.88	61	193	0.48	$0.70 \pm 3.2\times10^{-4}$	$0.67 \pm 1.0\times10^{-3}$	3.9×10^{-8}	0.17	46.1	0.13
0.2	1.0	2.5	0.55	35	193	0.82	$0.64 \pm 4.9\times10^{-4}$	$0.59 \pm 9.4\times10^{-4}$	4.3×10^{-7}	0.15	42.0	0.16
0.2	2.0	5.0	0.68	39	771	0.59	$0.73 \pm 2.3\times10^{-4}$	$0.72 \pm 1.2\times10^{-3}$	1.1×10^{-7}	0.16	50.2	0.07
0.2	5.0	4.0	0.28	13	493	0.47	$0.66 \pm 4.5\times10^{-4}$	$0.61 \pm 6.4\times10^{-4}$	2.6×10^{-5}	0.17	43.1	0.18
0.2	5.0	5.0	0.35	16	771	1.24	$0.68 \pm 3.3\times10^{-4}$	$0.63 \pm 8.3\times10^{-4}$	2.8×10^{-6}	0.16	45.1	0.10
0.2	5.0	7.5	0.53	24	1730	0.72	$0.72 \pm 2.3\times10^{-4}$	$0.70 \pm 6.1\times10^{-4}$	4.2×10^{-7}	0.17	49.6	0.07
0.5	0.5	2.5	0.70	106	77	1.02	$0.70 \pm 3.6\times10^{-4}$	$0.66 \pm 4.6\times10^{-4}$	7.2×10^{-8}	0.17	-	-
0.5	1.0	2.5	0.48	71	77	1.49	$0.67 \pm 2.9\times10^{-4}$	$0.61 \pm 6.5\times10^{-4}$	3.9×10^{-7}	0.17	-	-
0.5	2.0	5.0	0.63	85	308	1.11	$0.73 \pm 2.3\times10^{-4}$	$0.73 \pm 1.3\times10^{-3}$	1.1×10^{-7}	0.16	51.6	0.08
0.5	5.0	5.0	0.34	39	308	1.92	$0.71 \pm 7.3\times10^{-4}$	$0.68 \pm 1.6\times10^{-3}$	8.3×10^{-7}	0.17	46.6	0.15
0.5	5.0	7.5	0.51	58	694	1.30	$0.74 \pm 1.9\times10^{-4}$	$0.74 \pm 9.4\times10^{-4}$	2.7×10^{-7}	0.16	51.9	0.08
1.0	0.1	2.5	0.79	193	39	1.89	$0.67 \pm 4.7\times10^{-4}$	$0.71 \pm 1.0\times10^{-3}$	7.4×10^{-8}	0.13	-	-
1.0	0.2	2.5	0.70	176	39	1.72	$0.70 \pm 4.1\times10^{-4}$	$0.69 \pm 8.7\times10^{-4}$	8.1×10^{-8}	0.16	-	-
1.0	0.5	2.5	0.54	141	39	1.94	$0.69 \pm 3.3\times10^{-4}$	$0.65 \pm 9.7\times10^{-4}$	1.7×10^{-7}	0.17	-	-
1.0	1.0	2.5	0.40	106	39	2.55	$0.67 \pm 4.3\times10^{-4}$	$0.62 \pm 9.4\times10^{-4}$	7.1×10^{-7}	0.17	-	-
1.0	2.0	5.0	0.56	141	154	1.89	$0.71 \pm 4.2\times10^{-4}$	$0.72 \pm 1.6\times10^{-3}$	1.5×10^{-7}	0.15	52.0	0.09
1.0	5.0	5.0	0.33	71	154	2.87	$0.71 \pm 1.5\times10^{-4}$	$0.68 \pm 5.2\times10^{-4}$	7.3×10^{-7}	0.16	47.6	0.14
1.0	5.0	7.5	0.49	106	347	2.11	$0.73 \pm 1.4\times10^{-4}$	$0.75 \pm 1.1\times10^{-3}$	2.8×10^{-7}	0.15	53.0	0.07
2.0	0.1	2.0	0.39	161	12	3.82	$0.67 \pm 3.4\times10^{-4}$	$0.61 \pm 7.1\times10^{-4}$	5.3×10^{-7}	0.17	-	-
2.0	0.1	2.5	0.48	202	19	3.54	$0.70 \pm 6.5\times10^{-4}$	$0.68 \pm 1.5\times10^{-3}$	2.4×10^{-7}	0.16	-	-
2.0	0.2	2.5	0.45	193	19	3.53	$0.69 \pm 4.0\times10^{-4}$	$0.66 \pm 7.5\times10^{-4}$	2.8×10^{-7}	0.16	-	-
2.0	0.5	2.5	0.38	169	19	3.89	$0.68 \pm 3.2\times10^{-4}$	$0.63 \pm 6.3\times10^{-4}$	5.3×10^{-7}	0.17	-	-
2.0	1.0	2.5	0.31	141	19	4.05	$0.66 \pm 4.2\times10^{-4}$	$0.61 \pm 7.6\times10^{-4}$	5.9×10^{-6}	0.17	-	-
2.0	2.0	5.0	0.47	212	77	3.45	$0.72 \pm 4.3\times10^{-4}$	$0.73 \pm 8.9\times10^{-4}$	2.6×10^{-7}	0.15	51.6	0.09
2.0	5.0	5.0	0.30	121	77	4.57	$0.71 \pm 1.8\times10^{-4}$	$0.69 \pm 7.8\times10^{-4}$	8.6×10^{-7}	0.16	48.2	0.14
2.0	5.0	7.5	0.45	182	173	3.61	$0.73 \pm 2.5\times10^{-4}$	$0.76 \pm 1.9\times10^{-3}$	3.6×10^{-7}	0.15	53.4	0.07
5.0	0.1	2.5	0.24	208	8	9.49	$0.68 \pm 3.1\times10^{-4}$	$0.63 \pm 7.0\times10^{-4}$	1.9×10^{-6}	0.17	-	-
5.0	0.1	3.0	0.29	249	11	8.88	$0.70 \pm 2.7\times10^{-4}$	$0.67 \pm 9.9\times10^{-4}$	9.7×10^{-7}	0.16	-	-
5.0	0.2	2.5	0.24	204	8	9.75	$0.67 \pm 3.2\times10^{-4}$	$0.63 \pm 6.6\times10^{-4}$	2.9×10^{-6}	0.17	-	-
5.0	0.2	3.0	0.28	244	11	8.82	$0.70 \pm 3.6\times10^{-4}$	$0.66 \pm 6.6\times10^{-4}$	1.0×10^{-6}	0.17	-	-
5.0	2.0	5.0	0.33	303	31	8.25	$0.72 \pm 2.4\times10^{-4}$	$0.71 \pm 1.3\times10^{-3}$	7.6×10^{-7}	0.15	50.6	0.10
5.0	5.0	5.0	0.24	212	31	9.44	$0.71 \pm 3.0\times10^{-4}$	$0.69 \pm 6.7\times10^{-4}$	1.6×10^{-6}	0.16	48.3	0.13
5.0	5.0	7.5	0.37	318	69	8.02	$0.73 \pm 1.9\times10^{-4}$	$0.75 \pm 1.4\times10^{-3}$	7.1×10^{-7}	0.15	53.2	0.07

Table 5.6: Measured quantity differences between system 1 (Table 5.4) and system 2 (Table 5.5). Quantities are h_o, r_s, ϕ_o, initial liquid apex E_o, Reynolds number $\mathsf{Re} = \sqrt{\rho\varepsilon_o/2}[\phi_o h_o/\mu(r_s+h_o)]$, electric Weber number $\mathsf{We} = \varepsilon_o\phi_o^2/2\gamma h_o$, self-similar exponents β_M and β_C and also $\Delta\beta = \beta^{S1} - \beta^{S2}$, axial θ_f extracted at $r = r_\theta$ and also $\Delta\theta_f = \theta_f^{S1} - \theta_f^{S2}$ and $\Delta r_\theta = r_\theta^{S1} - r_\theta^{S2}$. The dash "-" in θ_f and r_θ entries indicate those which did not yield measurement of θ_f.

h_o (μm)	r_s	ϕ_o (kV)	E_o^{S1} $\left(\frac{\text{GV}}{\text{m}}\right)$	E_o^{S2}	Re	We	β_M^{S1}	β_M^{S2}	β_C^{S1}	β_C^{S2}	θ_f^{S1} (°)	θ_f^{S2}	r_θ^{S1} (μm)	r_θ^{S2}	$\Delta\beta_M$	$\Delta\beta_C$	$\Delta\theta_f$ (°)	Δr_θ (μm)
0.1	0.5	2.5	1.13	0.97	35	385	0.72	0.68	0.70	0.65	50.4	46.8	0.06	0.07	0.04	0.05	3.6	-0.01
0.1	1.0	2.5	0.68	0.58	19	385	0.65	0.61	0.60	0.55	45.1	42.5	0.07	0.09	0.04	0.05	2.6	-0.03
0.1	2.0	3.0	0.49	0.42	12	555	0.65	0.64	0.59	0.58	44.4	42.4	0.08	0.11	0.01	0.01	2.0	-0.04
0.1	2.0	4.0	0.66	0.56	16	987	0.69	0.66	0.65	0.61	48.1	45.7	0.06	0.06	0.03	0.05	2.4	-0.01
0.1	2.0	5.0	0.82	0.69	20	1540	0.72	0.69	0.70	0.68	51.8	48.9	0.05	0.05	0.03	0.03	2.9	0.00
0.1	5.0	5.0	0.43	0.36	8	1540	0.67	0.66	0.61	0.61	46.0	44.5	0.07	0.09	0.01	0.01	1.4	-0.02
0.1	5.0	7.5	0.64	0.54	12	3470	0.70	0.69	0.68	0.65	50.1	48.0	0.05	0.06	0.01	0.03	2.1	-0.01
0.1	5.0	10.0	0.86	0.71	17	6170	0.75	0.72	0.73	0.71	53.3	51.2	0.04	0.05	0.03	0.03	2.1	0.00
0.2	0.5	2.5	1.02	0.88	61	193	0.71	0.70	0.71	0.67	50.0	46.1	0.10	0.13	0.01	0.05	3.9	-0.02
0.2	1.0	2.5	0.65	0.55	35	193	0.67	0.64	0.62	0.59	45.3	42.0	0.12	0.16	0.02	0.03	3.3	-0.04
0.2	2.0	5.0	0.80	0.68	39	771	0.74	0.73	0.74	0.72	53.1	50.2	0.06	0.07	0.02	0.03	3.0	-0.01
0.2	5.0	4.0	0.34	0.28	13	493	0.68	0.66	0.62	0.61	44.7	43.1	0.11	0.18	0.01	0.01	1.6	-0.07
0.2	5.0	5.0	0.42	0.35	16	771	0.70	0.68	0.65	0.63	46.9	45.1	0.08	0.10	0.02	0.02	1.8	-0.01
0.2	5.0	7.5	0.64	0.53	24	1730	0.74	0.72	0.74	0.70	52.0	49.6	0.06	0.07	0.02	0.05	2.5	-0.01
0.5	0.5	2.5	0.82	0.70	106	77	0.70	0.70	0.70	0.66	-	-	-	-	0.01	0.04		
0.5	1.0	2.5	0.57	0.48	71	77	0.70	0.67	0.66	0.61	44.4	-	0.47	-	0.03	0.04		
0.5	2.0	5.0	0.74	0.63	85	308	0.73	0.73	0.76	0.73	54.6	51.6	0.07	0.08	0.01	0.03	3.1	-0.02
0.5	5.0	5.0	0.41	0.34	39	308	0.72	0.71	0.70	0.68	49.0	46.6	0.10	0.15	0.01	0.02	2.3	-0.05
0.5	5.0	7.5	0.62	0.51	58	694	0.74	0.74	0.77	0.74	54.5	51.9	0.07	0.08	0.01	0.02	2.6	-0.01
1.0	0.2	2.5	0.81	0.70	176	39	0.70	0.70	0.74	0.69	-	-	-	-	0.00	0.05		
1.0	0.5	2.5	0.63	0.54	141	39	0.70	0.69	0.69	0.65	-	-	-	-	0.01	0.04		
1.0	1.0	2.5	0.47	0.40	106	39	0.69	0.67	0.65	0.62	-	-	-	-	0.02	0.03		
1.0	2.0	5.0	0.67	0.56	141	154	0.72	0.71	0.76	0.72	54.8	52.0	0.07	0.09	0.01	0.04	2.8	-0.01
1.0	5.0	5.0	0.39	0.33	71	154	0.73	0.71	0.71	0.68	50.0	47.6	0.09	0.14	0.02	0.03	2.4	-0.05
1.0	5.0	7.5	0.59	0.49	106	347	0.74	0.73	0.78	0.75	55.7	53.0	0.07	0.07	0.01	0.03	2.7	-0.01
2.0	0.1	2.0	0.45	0.39	161	12	0.69	0.67	0.65	0.61	-	-	-	-	0.02	0.04		
2.0	0.2	2.5	0.52	0.45	193	19	0.71	0.69	0.70	0.66	-	-	-	-	0.01	0.05		
2.0	0.5	2.5	0.44	0.38	169	19	0.69	0.68	0.67	0.63	-	-	-	-	0.01	0.04		
2.0	1.0	2.5	0.37	0.31	141	19	0.69	0.66	0.65	0.61	-	-	-	-	0.02	0.04		
2.0	2.0	5.0	0.56	0.47	212	77	0.74	0.72	0.77	0.73	54.5	51.6	0.07	0.09	0.02	0.03	2.9	-0.02
2.0	5.0	5.0	0.36	0.30	121	77	0.72	0.71	0.72	0.69	50.6	48.2	0.10	0.14	0.01	0.03	2.4	-0.04
2.0	5.0	7.5	0.54	0.45	182	173	0.73	0.73	0.78	0.76	56.1	53.4	0.06	0.07	0.00	0.02	2.7	-0.01
5.0	0.1	2.5	0.29	0.24	208	8	0.70	0.68	0.67	0.63	-	-	-	-	0.02	0.03		
5.0	0.2	2.5	0.28	0.24	204	8	0.69	0.67	0.66	0.63	-	-	-	-	0.02	0.03		
5.0	0.2	3.0	0.33	0.28	244	11	0.71	0.70	0.71	0.66	-	-	-	-	0.01	0.05		
5.0	2.0	5.0	0.40	0.33	303	31	0.73	0.72	0.76	0.71	54.1	50.6	0.08	0.10	0.01	0.05	3.5	-0.02
5.0	5.0	5.0	0.30	0.24	212	31	0.72	0.71	0.72	0.69	50.6	48.3	0.09	0.13	0.01	0.03	2.3	-0.04
5.0	5.0	7.5	0.45	0.37	318	69	0.73	0.73	0.77	0.75	55.9	53.2	0.07	0.07	0.00	0.02	2.7	0.00

Table 5.7: System 3 self-similar exponents and measured quantities. Quantities are h_o, r_s, ϕ_o, initial liquid apex E_o, Reynolds number $\mathsf{Re} = \sqrt{\rho\varepsilon_o/2}[\phi_o h_o/\mu(r_s + h_o)]$, electric Weber number $\mathsf{We} = \varepsilon_o\phi_o^2/2\gamma h_o$, protrusion apex r_f and z_f, β_M and β_C with fitting errors, t_f, $\tau(t_f) = t_* - t_f$ and number of decades in $t_* - t$ used for self-similar fitting n.

System 3: LMIS coronal mode

h_o (μm)	r_s	ϕ_o (kV)	E_o $\left(\frac{\text{GV}}{\text{m}}\right)$	Re	We	r_f (μm)	z_f (μm)	β_M^{S3}	β_C^{S3}	t_f (s)	$\tau(t_f)$ (ns)	n
2.0	0.1	3.5	0.67	282	38	1.3	3.1	$0.95 \pm 1.7\times10^{-3}$	$1.07 \pm 3.0\times10^{-3}$	1.6×10^{-7}	1.4	1.0
2.0	0.1	5.0	0.96	403	77	1.6	2.2	$0.86 \pm 7.4\times10^{-4}$	$1.03 \pm 4.2\times10^{-3}$	8.0×10^{-8}	0.4	1.0
2.0	0.2	5.0	0.89	385	77	1.4	2.5	$0.88 \pm 7.2\times10^{-4}$	$1.05 \pm 2.4\times10^{-3}$	9.7×10^{-8}	0.5	1.0
2.0	0.5	5.0	0.75	339	77	0.8	3.2	$0.86 \pm 1.2\times10^{-3}$	$0.99 \pm 3.6\times10^{-3}$	1.3×10^{-7}	0.4	1.0
5.0	0.1	4.0	0.39	332	20	3.4	8.7	$0.94 \pm 1.0\times10^{-3}$	$1.04 \pm 2.7\times10^{-3}$	7.8×10^{-7}	5.6	1.0
5.0	0.1	5.0	0.49	415	31	4.1	6.4	$0.89 \pm 9.3\times10^{-4}$	$0.94 \pm 1.3\times10^{-3}$	4.6×10^{-7}	1.2	1.0
5.0	0.1	6.0	0.58	498	44	4.4	5.1	$0.91 \pm 4.6\times10^{-4}$	$0.99 \pm 8.8\times10^{-4}$	3.2×10^{-7}	0.8	1.0
5.0	0.1	7.5	0.73	623	69	4.6	4.0	$0.90 \pm 6.4\times10^{-4}$	$1.02 \pm 1.7\times10^{-3}$	2.1×10^{-7}	0.6	1.0
5.0	0.2	4.0	0.38	326	20	2.7	9.6	$0.92 \pm 5.8\times10^{-4}$	$0.96 \pm 6.0\times10^{-4}$	8.4×10^{-7}	2.4	1.0
5.0	0.2	5.0	0.47	407	31	3.7	7.0	$0.93 \pm 3.5\times10^{-4}$	$1.04 \pm 1.7\times10^{-3}$	5.1×10^{-7}	1.4	1.5
5.0	0.2	6.0	0.56	489	44	4.0	5.7	$0.91 \pm 1.2\times10^{-3}$	$1.01 \pm 1.6\times10^{-3}$	3.6×10^{-7}	1.1	1.0
5.0	0.2	7.5	0.70	611	69	4.3	4.6	$0.86 \pm 1.9\times10^{-3}$	$1.01 \pm 3.3\times10^{-3}$	2.4×10^{-7}	0.8	1.0
5.0	0.2	8.5	0.80	692	89	4.4	4.2	$0.91 \pm 5.1\times10^{-4}$	$1.05 \pm 2.0\times10^{-3}$	1.9×10^{-7}	0.4	1.0
5.0	0.5	5.0	0.43	385	31	2.7	8.0	$0.90 \pm 1.3\times10^{-3}$	$0.99 \pm 1.2\times10^{-3}$	6.0×10^{-7}	1.9	1.0
5.0	0.5	7.5	0.65	578	69	3.6	5.8	$0.91 \pm 6.2\times10^{-4}$	$1.01 \pm 2.7\times10^{-3}$	3.0×10^{-7}	0.6	1.0
5.0	1.0	5.0	0.39	353	31	1.0	9.3	$0.88 \pm 2.5\times10^{-3}$	$1.01 \pm 3.2\times10^{-3}$	7.0×10^{-7}	1.2	1.0
5.0	1.0	7.5	0.58	529	69	2.7	6.9	$0.90 \pm 1.3\times10^{-3}$	$1.03 \pm 2.7\times10^{-3}$	3.7×10^{-7}	0.7	1.0
5.0	2.0	7.5	0.50	454	69	1.4	8.0	$0.87 \pm 6.0\times10^{-4}$	$1.03 \pm 3.6\times10^{-3}$	4.7×10^{-7}	0.5	1.5

Table 5.8: System 4.1 self-similar exponents and measured quantities for cases with $r_f = 0$. Quantities are h_o, r_s, ϕ_o, initial liquid apex E_o, Reynolds number $\mathsf{Re} = \sqrt{\rho\varepsilon_o/2}[\phi_o h_o/\mu(r_s + h_o)]$, electric Weber number $\mathsf{We} = \varepsilon_o\phi_o^2/2\gamma h_o$, protrusion apex z_f, β_M and β_C with fitting errors, t_f and $\tau(t_f) = t_* - t_f$. Last 1.0 decades in $t_* - t$ was used to extract β for each simulation.

System 4.1: LMIS instability mode with $r_f = 0$

h_o (μm)	r_s	ϕ_o (kV)	E_o $\left(\frac{\text{GV}}{\text{m}}\right)$	Re	We	z_f (μm)	β_M^{S4}	β_C^{S4}	t_f (s)	$\tau(t_f)$ (ns)
0.1	5.0	15.0	1.07	25	13900	0.20	$0.73 \pm 7.0\times10^{-4}$	$0.74 \pm 4.7\times10^{-3}$	1.2×10^{-7}	0.16
0.2	5.0	17.5	1.23	57	9440	0.31	$0.76 \pm 4.9\times10^{-4}$	$0.84 \pm 3.2\times10^{-3}$	5.3×10^{-8}	0.14
2.0	0.1	6.5	1.25	524	130	2.41	$0.74 \pm 6.7\times10^{-4}$	$0.80 \pm 7.5\times10^{-3}$	5.0×10^{-8}	0.15
5.0	0.1	12.5	1.21	1040	193	5.23	$0.75 \pm 5.1\times10^{-4}$	$0.81 \pm 7.0\times10^{-3}$	5.6×10^{-8}	0.15
5.0	0.5	10.0	0.86	770	123	5.97	$0.76 \pm 2.4\times10^{-4}$	$0.80 \pm 1.5\times10^{-3}$	1.7×10^{-7}	0.16
5.0	2.0	10.0	0.66	605	123	7.36	$0.75 \pm 5.4\times10^{-4}$	$0.76 \pm 2.2\times10^{-3}$	3.3×10^{-7}	0.16

Table 5.9: System 4.2 self-similar exponents and measured quantities for cases with $r_f > 0$. Quantities are h_o, r_s, ϕ_o, initial liquid apex E_o, Reynolds number $\mathsf{Re} = \sqrt{\rho\varepsilon_o/2}[\phi_o h_o/\mu(r_s + h_o)]$, electric Weber number $\mathsf{We} = \varepsilon_o\phi_o^2/2\gamma h_o$, protrusion apex r_f and z_f, β_M and β_C with fitting errors, t_f and $\tau(t_f) = t_* - t_f$. Last 1.0 decades in $t_* - t$ was used to extract β for each simulation.

System 4.2: LMIS instability mode with $r_f > 0$

h_o (μm)	r_s	ϕ_o (kV)	E_o $\left(\frac{\text{GV}}{\text{m}}\right)$	Re	We	r_f (μm)	z_f (μm)	β_M^{S4}	β_C^{S4}	t_f (s)	$\tau(t_f)$ (ns)
0.1	5.0	20.0	1.42	33	24700	0.24	0.17	$0.85 \pm 2.4\times10^{-3}$	$1.15 \pm 1.1\times10^{-2}$	4.1×10^{-8}	0.32
0.2	5.0	15.0	1.06	49	6940	0.27	0.41	$0.83 \pm 1.5\times10^{-3}$	$1.06 \pm 4.6\times10^{-3}$	9.8×10^{-8}	0.36
2.0	0.5	7.5	1.13	508	173	1.14	2.51	$0.80 \pm 1.4\times10^{-3}$	$1.05 \pm 6.4\times10^{-3}$	7.1×10^{-8}	0.27
2.0	0.5	10.0	1.50	678	308	0.25	2.23	$0.81 \pm 9.9\times10^{-4}$	$1.04 \pm 1.2\times10^{-2}$	2.8×10^{-8}	0.23
2.0	1.0	7.5	0.92	424	173	0.65	3.03	$0.82 \pm 1.7\times10^{-3}$	$1.04 \pm 9.0\times10^{-3}$	1.0×10^{-7}	0.25
2.0	2.0	10.0	0.94	424	308	0.38	2.63	$0.84 \pm 6.1\times10^{-4}$	$1.02 \pm 4.9\times10^{-3}$	8.3×10^{-8}	0.31
5.0	0.2	10.0	0.94	814	123	0.68	5.77	$0.89 \pm 1.3\times10^{-3}$	$1.08 \pm 5.2\times10^{-3}$	1.4×10^{-7}	0.54
5.0	0.2	12.5	1.17	1020	193	0.97	5.33	$0.85 \pm 9.0\times10^{-4}$	$0.99 \pm 4.0\times10^{-3}$	7.6×10^{-8}	0.35
5.0	1.0	10.0	0.78	706	123	0.87	6.45	$0.88 \pm 1.3\times10^{-3}$	$0.99 \pm 6.1\times10^{-3}$	2.2×10^{-7}	0.58

Chapter 6

CONCLUSION

The objective of this research was to bridge the gaps in the known details of EHD liquid metal distortion in geometries of relevance to LMIS systems. ALE-FEM simulations were conducted to track the entire liquid distortion in a realistic LMIS geometry prior to ion emission.

These simulations conducted in Chapter 3 revealed development of five different EHD modes categorized as drainage, axial, coronal, instability and dual characterized by the location and number of generated protrusions and modes. The multiplicity was cataloged just from variations in the key initial conditions in the applied electric potential, microemitter apex curvature radius and initial liquid thickness. It was found that all modes preferentially develop in the desirable liquid tip region given by the initial liquid apex curvature radius due to the curvature generated local pressure and pressure gradient enhancement. Correlations between the mode outcome and key initial conditions were further extracted from mode diagrams parameterized by the Reynolds and electric Weber numbers predominantly scaled by the applied electric potential, microemitter apex curvature radius and initial liquid thickness. In particular, the axial EHD mode, which is often the most desirable mode for applications, is found to be strongly correlated with low applied potential, large initial liquid apex curvature radius and thinly wetted liquid, which shows the importance of the often neglected liquid thickness for control over the excited mode.

In Chapter 4, we probed the influence of extractor aperture and microemitter curvature on the EHD instability from the classic flat liquid layer subject to a normal electric field. The effects of each component were isolated by sequentially adding the extractor aperture then the curved microemitter to the basic system and conducting simulations that tracked the instability development. The results indicated that the extractor aperture strongly suppresses instability growth inside the aperture by encoding bulk drainage generated by a nonuniform electric field distribution, whereas the microemitter curvature confined instability growth to within the initial liquid apex curvature radius by generating locally enhanced fields and capillary drainage. Despite the strong stabilization, the instability wavenumbers extracted from spectral analysis of LMIS free surface and capillary pressure evolution possessed a strong correlation with those predicted from known linear stability analysis about the flat, static liquid layer when the characteristic field value is taken as that generated at the

initial liquid apex. This was found to arise from the smallness of the instability wavelength compared to the initial liquid curvature radius, which allows the mode developing liquid tip region to be well approximated as a flat surface for the generated instability. The correlation offers a very simple estimate of the dominant wavelength encoded by the initial LMIS operating conditions and a criterion on instability observance when compared against the mode generating initial liquid apex curvature radius.

In Chapter 5, we examine the late time dynamic evolution of EHD modes that develop out of the realistic LMIS geometry modeled. The results show that the protrusion development indeed exhibits self-similar growth marked by power law growth of apex Maxwell and capillary pressures. This self similarity is crucially observed irrespective of the generated EHD mode, which can generate protrusions that no longer develop axially, possess symmetric profile about the apices and singularly develop without the presence of additional neighboring protrusions. This universality of self-similar dynamics is accompanied by a dichotomy of Maxwell and capillary self-similar exponent values, where those for the non-axial apices are found to be systematically larger than those for the axial counterparts. The axial mode exponents are additionally found to collapse in the parameter space constructed by the Reynolds and electric Weber numbers. These results show the robust presence of late time self-similar tip growth in a geometry possessing geometric components and field distributions strongly relevant to real LMIS systems. The assumptions of an axial, symmetric protrusion taken by the pioneering asymptotic analysis undertaken by Zubarev [165] are also shown to be not necessary for self-similar dynamics.

6.1 Pressing need for liquid thickness measurements in future studies of LMIS behavior

One of the most important recurring themes in the research undertaken is the critical influence of the liquid thickness on the ensuing EHD dynamics. In Chapter 3, it would have been much more difficult to access the EHD modes cataloged had the liquid thickness not been a controllable parameter. It sets not only the characteristic vertical scale but also the characteristic lateral scale described by the initial liquid apex radius (i.e. the addition of microemitter apex curvature radius and liquid thickness) that is shown to confine the ensuing EHD mode development. Construction of the Reynolds and electric Weber number and the resultant mode diagram would also have been impossible without the liquid thickness information. In Chapter 4, the liquid thickness is known to be a crucial parameter that contributes to the encoding of the dominant instability wavenumber and growth rate for the basic flat liquid layer subject to a normal electric field. Had the liquid thickness information been absent, the correlation between the LMIS instability mode and equivalent flat liquid

layer wavenumbers would also have been impossible to ascertain. In Chapter 5, the collapse of the axial EHD mode self-similar exponents would likewise have been difficult to extract as it would be impossible to construct the appropriate Reynolds and electric Weber numbers without the liquid thickness information. It is not an understatement to say that much, if not all, of the results offered by the presented research would simply have been inaccessible without the realization of the importance of liquid thickness wetted to the emitter substrates.

However, as already discussed in Chapter 3, the existing literature is almost entirely bereft of information and insight pertinent to the liquid thickness. Indeed, a literature search on the dimensions of key LMIS geometry components used to construct the table of relevant dimensions in Table 3.8 and ultimately motivate those applied to our simulations yielded no reported measurements of the applied liquid thicknesses. Though rough estimates may be derived from weighing or imaging the system prior and post wetting, measuring the thickness to the desired precision is made almost impossible due to the liquid metal opacity, which invalidate all visual techniques, and emitter substrate curvature, which make difficult to apply available nonvisual optical techniques such as ellipsometry [144]. It is the hope that the conducted research induces an interest in the development of experimental techniques for measuring such liquid metal thicknesses. Availability of such techniques is anticipated to not only allow greater reproducibility of future experimental investigations but also access to future enhancements in the LMIS design and operating paradigms.

BIBLIOGRAPHY

[1] A. M. Winslow, "An irregular triangle mesh generator," Report No. UCRL-7880. 1964 (cit. on p. 42).

[2] MATLAB R2020b, The MathWorks, Inc., Natick, MA, USA. 2020 (cit. on pp. 44, 101, 146).

[3] COMSOL Multiphysics, COMSOL, Inc., Burlington, MA, USA. 2022 (cit. on p. 42).

[4] T. G. Albertson. "Simulations of coniccusp formation, growth, and instability in electrified viscous liquid metals on flat and curved surfaces." PhD thesis. California Institute of Technology, 2020. DOI: 10.7907/thhf-5478 (cit. on p. 9).

[5] T. G. Albertson and S. M. Troian. "Electrified cone formation in perfectly conducting viscous liquids: self-similar growth irrespective of Reynolds numbers." In: *Phys. Fluids* 31 (2019), p. 102103. DOI: 10.1063/1.5123742 (cit. on pp. 9, 23, 36, 54, 138, 146, 148, 149, 151, 171, 173, 174).

[6] J. Asher, Z. Huang, C. Cui, and J. Wang. "Multi-scale modeling of ionic electrospray emission." In: *J. Appl. Phys.* 131 (2022), p. 014902. DOI: 10.1063/5.0071483 (cit. on pp. 45, 86).

[7] N. Baddour and U. Chouinard. "Theory and operational rules for the discrete Hankel transform." In: *J. Opt. Soc. Am. A* 32.4 (2015), pp. 611–622. DOI: 10.1364/JOSAA.32.000611 (cit. on p. 103).

[8] H.D. Beckey, H. Krone, and F. W. Roellgen. "Comparison of tips, thin wires and sharp metal edges as emitters for field ionization mass spectrometry." In: *J. Sci. Instr.* 2 (1968), pp. 118–120. DOI: 10.1088/0022-3735/1/2/308 (cit. on p. 46).

[9] A. E. Bell, K. Rao, G. A. Schwind, and L. W. Swanson. "A low-current liquid metal ion source." In: *J. Vac. Sci. Technol. B* 6 (1988), pp. 927–930. DOI: 10.1116/1.584325 (cit. on p. 8).

[10] A. E. Bell and L. W. Swanson. "The influence of substrate geometry on the emission properties of a liquid metal ion source." In: *Appl. Phys. A* 41 (1986), pp. 335–346. DOI: 10.1007/BF00616057 (cit. on pp. 6, 8, 79, 82).

[11] O. M. Belotserkovskii, V. A. Gushchin, and V. N. Kon'shin. "The splitting method for investigating flows of a stratified liquid with a free surface." In: *U.S.S.R. Comput. Maths. Math. Phys.* 27.2 (1987), pp. 181–191. DOI: 10.1016/0041-5553(87)90175-3 (cit. on p. 9).

[12] G. Ben Assayag and P. Sudraud. "LMIS energy broadening interpretation supported by HV-TEM observations." In: *J. Phys. Colloq.* 45.C9 (1984), pp. 223–226. DOI: 10.1051/jphyscol:1984937 (cit. on pp. 4, 35).

[13] G. Ben Assayag, P. Sudraud, and B. Jouffrey. “In situ high voltage TEM observation of an electrohydrodynamic (EHD) ion source.” In: *Ultramicroscopy* 16 (1985), pp. 1–8. DOI: 10.1016/S0304-3991(85)80002-4 (cit. on pp. 4, 35).

[14] S. I. Betelu, M. A. Fontelos, U. Kindelan, and O. Vantzos. “Singularities on charged viscous droplets.” In: *Physics of Fluids* 18.5 (2006), p. 051706. DOI: 10.1063/1.2204044 (cit. on pp. 9, 138).

[15] R. B. Blackman and J. W. Tukey. “The measurement of power spectra from the point of view of communications engineering - Part I.” In: *Bell Syst. Tech. J.* 37.1 (1958), pp. 185–282. DOI: 10.1002/j.1538-7305.1958.tb03874.x (cit. on p. 104).

[16] R. K. Brayton, F. G. Gustavson, and G. D. Hachtel. “A new efficient algorithm for solving differential-algebraic systems using implicit backward differentiation formulas.” In: *Proc. of the IEEE* 60 (1972), pp. 98–108. DOI: 10.1109/PROC.1972.8562 (cit. on p. 42).

[17] N. Buldrini, L. Bettiol, B. Seifert, F. Plesescu, J. G. del Amo, and L. Massotti. “Results of the successful 48000 h endurance test of a FEEP multi-emitter.” In: *74th International Astronautical Congress*. 2023 (cit. on pp. 8, 65).

[18] J. C. Burton and P. Taborek. “Simulations of coulombic fission of charged inviscid drops.” In: *Phys. Rev. Lett.* 106.14 (2011), p. 144501. DOI: 10.1103/PhysRevLett.106.144501 (cit. on pp. 9, 138).

[19] G. S. Cho, D. E. Kim, and S. O. Kang. “Electric field solutions between an emitter tip and a plane extractor in LMIS.” In: *J. Phys. D: Appl. Phys.* 23 (1990), pp. 85–89. DOI: 10.1088/0022-3727/23/1/014 (cit. on p. 46).

[20] U. Chouinard and N. Baddour. “Matlab code for the discrete Hankel transform.” In: *J. Open Res. Softw.* 5.1 (2017), p. 4. DOI: 10.5334/jors.82 (cit. on p. 103).

[21] X. L. Chu, M. G. Velarde, and A. Castellanos. “Dissipative hydrodynamic oscillators.” In: *Il Nuovo Cimento D* 11.5 (1989), pp. 727–737. DOI: 10.1007/BF02451559 (cit. on p. 7).

[22] R. Clampitt, K. L. Aitken, and D. K. Jefferies. “Abstract: Intense field-emission ion source of liquid metals.” In: *J. Vac. Sci. Technol.* 12 (1975), pp. 1208–1208. DOI: 10.1116/1.568496 (cit. on pp. 2, 35, 96, 137).

[23] M. Cloupeau and B. Prunet-Foch. “Electrohydrodynamic spraying functioning modes: a critical review.” In: *J. Aerosol Sci.* 25.6 (1994), pp. 1021–1036. DOI: 10.1016/0021-8502(94)90199-6 (cit. on p. 3).

[24] R. T. Collins, J. J. Jones, M. T. Harris, and O. A. Basaran. “Electrohydrodynamic tip streaming and emission of charged drops from liquid cones.” In: *Nat. Phys.* 4 (2008), pp. 149–154. DOI: 10.1038/nphys807 (cit. on pp. 3, 9, 35, 36).

[25] H. Conrad, Y. Li, and Y. Chen. “The temperature dependence of the electrorheology and related electrical properties of corn starch/corn oil suspensions.” In: *J. Rheol.* 39.5 (1995), pp. 1041–1057. DOI: 10.1122/1.550616 (cit. on p. 3).

[26] Z. Cui and L. Tong. "A new approach to simulating the operation of liquid metal ion sources." In: *J. Vac. Sci. Technol. B* 6.6 (1988), pp. 2104–2107. DOI: 10.1116/1.584131 (cit. on p. 8).

[27] R. J. Culbertson, T. Sakurai, and G. H. Robertson. "Ionization of liquid metals, gallium." In: *J. Vac. Sci. Technol.* 16.2 (1979), pp. 574–576. DOI: 10.1116/1.570001 (cit. on p. 43).

[28] S. Dandavino, C. Ataman, S. Chakraborty, H. Shea, C. Ryan, and J. Stark. "Design and fabrication of the thruster heads for the MicroThrust MEMS electrospray propulsion system." In: *Proc. 33rd International Electric Propulsion Conference*. 2011 (cit. on pp. 45, 86).

[29] W. M. Deen. *Analysis of transport phenomena*. Vol. 1. Oxford University Press, 1998 (cit. on p. 12).

[30] P. Deshpande, L. F. Pease III, L. Chen, S. Y. Chou, and W. B. Russel. "Cylindrically symmetric electrohydrodynamic patterning." In: *Phys. Rev. E* 70.4 (2004), p. 041601. DOI: 10.1103/PhysRevE.70.041601 (cit. on p. 27).

[31] P. Deuflhard. "A modified Newton method for the solution of ill-conditioned systems of nonlinear equations with applications to multiple shooting." In: *Numer. Math.* 22 (1974), pp. 289–315. DOI: 10.1007/BF01406969 (cit. on p. 42).

[32] J. Donea, P. Fasoli-Stella, and S. Giuliani. "Lagrangian and Eulerian finite element techniques for transient fluid-structure interaction problems." In: *Trans. 4th Int. Conf. on Structural Mechanics in Reactor Technology*. 1977 (cit. on pp. 9, 10, 36, 42, 97, 138).

[33] W. Driesel. "Low-energy ion optical system with a liquid-metal ion source for imaging and processing solid structures." In: *Ultramicroscopy* 52 (1993), pp. 65–72. DOI: 10.1016/0304-3991(93)90022-P (cit. on p. 2).

[34] W. Driesel, Ch. Dietszsch, E. Hesse, L. Bischoff, and J. Teichert. "In situ observation of the tip shape of Co-Ge liquid alloy ion sources in a high-voltage transmission electron microscope." In: *J. Vac. Sci. Technol. B* 14.3 (1996), pp. 1621–1629. DOI: 10.1116/1.589201 (cit. on pp. 4, 60).

[35] W. Driesel, Ch. Dietszsch, and M. Moser. "In situ observation of the tip shape of lead liquid metal ion sources." In: *J. Phys. D: Appl. Phys.* 29.5 (1996), pp. 2492–2500. DOI: 10.1088/0022-3727/29/9/039 (cit. on pp. 4, 35, 82).

[36] W. Driesel, Ch. Dietszsch, and R. Muhle. "In situ observation of the tip shape of AuGe liquid alloy ion sources using a high voltage transmission electron microscope." In: *J. Vac. Sci. Technol. B* 14.5 (1996), pp. 3367–3380. DOI: 10.1116/1.588537 (cit. on p. 4).

[37] W. Driesel, Ch. Dietszsch, and R. Muhle. "Tip-shape investigation of a Au-Si alloy liquid metal ion source using a high voltage transmission electron microscope." In: *J. Phys. D: Appl. Phys.* 28 (1995), pp. 787–793. DOI: 10.1088/0022-3727/28/4/025 (cit. on p. 4).

[38] W. Driesel, Ch. Dietszsch, H. Niedrig, and B. Praprotnik. "HV TEM in situ investigations of the tip shape of a gallium liquid-metal ion/electron emitter." In: *Ultramicroscopy* 57 (1995), pp. 47–58. DOI: 10.1016/0304-3991(94)00165-J (cit. on pp. 2, 4, 5, 35, 60, 82).

[39] W. Driesel and Ch. Dietzsch. "In situ HVTEM observation of the tip shape of tin liquid metal ion sourcess." In: *Appl. Surf. Sci.* 93 (1996), pp. 179–190. DOI: 10.1016/0169-4332(95)00326-6 (cit. on pp. 4, 35, 60, 82).

[40] C. F. Eyring, S. S. Mackeown, and R. A. Millikan. "Field currents from points." In: *Phys. Rev.* 31 (1928), pp. 900–909. DOI: 10.1103/PhysRev.31.900 (cit. on p. 46).

[41] R. T. Farouki. "The approximation of non-degenerate offset surfaces." In: *Comput. Aided. Geom. Des.* 3 (1986), pp. 15–43. DOI: 10.1016/0167-8396(86)90022-1 (cit. on pp. 37, 40, 41).

[42] R. P. Feynman. *There's plenty of room at the bottom - an invitation to enter a new field of physics*. 1959. URL: http://www.zyvex.com/nanotech/feynman.html (cit. on p. 2).

[43] H. Fisk Johnson. "An improved method for computing a discrete Hankel transform." In: *Comput. Phys. Commun.* 43 (1987), pp. 181–202. DOI: 10.1016/0010-4655(87)90204-9 (cit. on pp. 103, 104).

[44] M. A. Fontelos, U. Kindelan, and O. Vantzos. "Evolution of neutral and charged droplets in an electric field." In: *Phys. Fluids* 20.9 (2008), p. 092110. DOI: 10.1063/1.2980030 (cit. on pp. 9, 138, 168).

[45] R. G. Forbes. "Field evaporation theory: a review of basic ideas." In: *Appl. Surf. Sci.* 87 (1995), pp. 1–11. DOI: 10.1016/0169-4332(94)00526-5 (cit. on p. 2).

[46] R. G. Forbes and G. L. R. Mair. "Arguments about emitter shape for a liquid-metal field-ion emission source." In: *J. Phys. D: Appl. Phys.* 15 (1982), pp. L153–L158. DOI: 10.1088/0022-3727/15/11/006 (cit. on p. 6).

[47] Y. I. Frenkel. "On Tonks' theory of liquid surface rupture by a uniform electric field." In: *Zh. Eksp. Teor. Fiz* 6 (1935), pp. 347–350 (cit. on pp. 7, 96, 126, 137).

[48] A. M. Ganan-Calvo. "Cone-jet analytical extension of Taylor's electrostatic solution and the asymptotic universal scaling laws in electrospraying." In: *Phys. Rev. Lett.* 79.2 (1997), pp. 217–220. DOI: 10.1103/PhysRevLett.79.217 (cit. on p. 3).

[49] M. Garzon, L. J. Gray, and J. A. Sethian. "Numerical simulations of electrostatically driven jets from nonviscous droplets." In: *Phys. Rev. E* 89 (2014), p. 033011. DOI: 10.1103/PhysRevE.89.033011 (cit. on pp. 9, 138).

[50] J. Gierak. "Focused ion beam technology and ultimate applications." In: *Semicond. Sci. Technol.* 24.4 (2009), p. 043001. DOI: 10.1088/0268-1242/24/4/043001 (cit. on p. 3).

[51] W. Gilbert. *de Magnete*. Ed. by P. F. Mottelay. Trans. by P. Bothorel and E.J. Dufourc. Vol. 2. Dover, 1958 (cit. on p. 5).

[52] R. Gomer. "On the mechanism of liquid metal electron and ion sources." In: *Appl. Phys.* 19 (1979), pp. 365–375. DOI: 10.1007/BF00930099 (cit. on pp. 6, 48).

[53] H. Gonzalez, G. N. de Surgy, and J. P. Chabrerie. "Electrocapillary instability in annular geometry." In: *Phys. Fluids* 9.9 (1997), pp. 2542–2549. DOI: 10.1063/1.869371 (cit. on pp. 96, 128).

[54] H. Gonzalez, G. N. de Surgy, and J. P. Chabrerie. "Influence of bounded geometry on electrocapillary instability." In: *Phys. Rev. B* 50.4 (1994), pp. 2520–2528. DOI: 10.1103/PhysRevB.50.2520 (cit. on pp. 96, 128).

[55] C. Guerra-Garcia, D. Krejci, and P. Lozano. "Spatial uniformity of the current emitted by an array of passively fed electrospray porous emitters." In: *J. Phys. D: Appl. Phys.* 49 (2016), p. 115503. DOI: 10.1088/0022-3727/49/11/115503 (cit. on pp. 45, 86).

[56] Y. G. Guezennec, R. S. Brodkey, N. Trigui, and J. C. Kent. "Algorithms for fully automated three-dimensional particle tracking velocimetry." In: *Exp. Fluids* 17.4 (1994), pp. 209–219. DOI: 10.1007/BF00203039 (cit. on p. 4).

[57] D. Guo, X. Kang, J. Hu, X. Liu, and W. He. "Note: Fabrication of roughened tips for liquid metal ion sources." In: *Rev. Sci. Instrum.* 88 (2017), p. 066107. DOI: 10.1063/1.4985635 (cit. on p. 1).

[58] F. H. Harlow and J. E. Welch. "Numerical calculation of time-dependent viscous incompressible flow of fluid with free surface." In: *Phys. Fluids* 8.12 (1965), pp. 2182–2189. DOI: 10.1063/1.1761178 (cit. on pp. 8, 9).

[59] K. Hata, Y. Saito, A. Ohshita, M. Takeda, C. Morita, and T. Noda. "In situ HV-TEM observation of the liquid cone formation process in a liquid metal field emission gun." In: *Appl. Surf. Sci.* 76 (1994), pp. 36–40. DOI: 10.1016/0169-4332(94)90320-4 (cit. on p. 2).

[60] J. He, N. M. Miskovsky, P. H Cutler, and M. Chung. "Effects of viscosity on capillary wave instabilities of a planar liquid-metal surface in an electric field." In: *J. Appl. Phys.* 68.4 (1990), pp. 1475–1482. DOI: 10.1063/1.346676 (cit. on p. 7).

[61] P. J. Heard, J. R. A. Cleaver, and H. Ahmed. "Application of a focused ion beam system to defect repair of VLSI masks." In: *J. Vac. Sci. Technol. B* 3 (1985), pp. 87–90. DOI: 10.1116/1.583297 (cit. on p. 3).

[62] E. Hesse, W. Driesel, Ch. Dietszsch, L. Bischoff, and J. Teichert. "Shape of a Co-Nd liquid alloy ion source." In: *Jpn. J. Appl. Phys.* 35 (1996), pp. 5564–5570. DOI: 10.1143/JJAP.35.5564 (cit. on pp. 4, 60).

[63] K. Hoflich et al. "Roadmap for focused ion beam technologies." In: *Appl. Phys. Rev.* 10.4 (2023), p. 041311. DOI: 10.1063/5.0162597 (cit. on p. 3).

[64] P. W. Holland and R. E. Welsch. “Robust regression using iteratively reweighted least-squares.” In: *Commun. Stat - Theory Methods* 6.9 (1977), pp. 813–827. DOI: 10.1080/03610927708827533 (cit. on p. 147).

[65] C. G. Hopkins. “The Oil of Corn.” In: *J. Am. Chem. Soc.* 20.12 (1898), pp. 948–961 (cit. on p. 3).

[66] T. S. Huang. “Two-dimensional windows.” In: *IEEE Trans. on Audio and Electroacoustics* 20.1 (1972), pp. 88–89. DOI: 10.1109/TAU.1972.1162331 (cit. on p. 104).

[67] M. C. Hung and C. D. Andereck. “Transitions in convection driven by a horizontal temperature gradient.” In: *Phys. Lett. A* 132.5 (1988), pp. 253–258. DOI: 10.1016/0375-9601(88)90560-9 (cit. on p. 4).

[68] J. P. Ibe, P. P. Bey Jr., S. L. Brandow, R. A. Brizzolara, N. A. Burnham, D. P. Dilella, K. P. Lee, C. R. K. Marrian, and R. J. Colton. “On the electrochemical etching of tips for scanning tunneling microscopy.” In: *J. Vac. Sci. Technol. A* 8 (1990), pp. 3570–3575. DOI: 10.1116/1.576509 (cit. on pp. 2, 82).

[69] T. Iida and R. I. L. Guthrie. *The physical properties of liquid metals*. Oxford University Press, 1993 (cit. on pp. 3, 44, 98, 144).

[70] J. D. Jackson. *Classical electrodynamics*. 3rd ed. John Wiley and Sons, Inc., 1999 (cit. on p. 6).

[71] N. K. Kang and L. W. Swanson. “Computer simulation of liquid metal ion source optics.” In: *Appl. Phys. A* 30 (1983), pp. 95–104. DOI: 10.1007/BF00614910 (cit. on p. 6).

[72] J. Kiefer. “Sequential minimax search for a maximum.” In: *Proc. Amer. Math. Soc.* 4.3 (1953), pp. 502–506. DOI: 10.2307/2032161 (cit. on pp. 102, 146).

[73] H. Kim, S. G. Bankoff, and M. J. Miksis. “The effect of an electrostatic field on film flow down an inclined plane.” In: *Phys. Fluids A* 4 (1992), pp. 2117–2130. DOI: 10.1063/1.858508 (cit. on p. 97).

[74] D. R. Kingham and L. W. Swanson. “Shape of a liquid metal ion source: a dynamic model including fluid flow and space-charge effects.” In: *Appl. Phys. A* 34 (1984), pp. 123–132. DOI: 10.1007/BF00614764 (cit. on p. 6).

[75] M. Komuro, H. Hiroshima, H. Tanoue, and T. Kanayama. “Maskless etching of a nanometer structure by focused ion beams.” In: *J. Vac. Sci. Technol. B* 1 (1983), pp. 985–989. DOI: 10.1116/1.582719 (cit. on p. 3).

[76] L. O. Kornum and H. K. Raaschou Nielsen. “Surface defects in drying paint films.” In: *Prog. Org. Coat.* 8.3 (1980), pp. 275–324. DOI: 10.1016/0300-9440(80)80019-1 (cit. on p. 51).

[77] D. Krejci, I. Vasiljevich, V. Hugonnaud, Q. Koch, B. Little, A. Goswami, A. Reissner, and B. Seifert. "FEEP extractor electrode clogging and in-space cleaning demonstration." In: *AIAA SciTech 2025 Forum*. 2025. DOI: 10.2514/6.2025-2382 (cit. on pp. 8, 65).

[78] V. E. Krohn. "Liquid metal droplets for heavy particle propulsion." In: *Prog. Astro. Aero.* 5 (1961), pp. 73–80 (cit. on pp. 2, 35, 96, 137).

[79] V. E. Krohn and G. R. Ringo. "Ion source of high brightness using liquid metal." In: *Appl. Phys. Lett.* 27 (1975), pp. 479–481. DOI: 10.1063/1.88540 (cit. on p. 2).

[80] V. E. Krohn and G. R. Ringo. "Microprobe design using a liquid gallium ion source." In: *Int. J. Mass Spectrom. Ion Processes* 22 (1976), pp. 307–308. DOI: 10.1016/0020-7381(76)80089-7 (cit. on p. 2).

[81] V. E. Krohn and G. R. Ringo. "Possible applications of a high brightness gallium source to ion microprobes." In: *Nuc. Instr. Meth. Phys. Res.* 149 (1978), pp. 735–737. DOI: 10.1016/0029-554X(78)90960-6 (cit. on p. 2).

[82] V. E. Krohn and G. R. Ringo. "Some proposed improvements in the scanning ion microprobe." In: *J. Microscopy* 110 (1977), pp. 59–64. DOI: 10.1111/j.1365-2818.1977.tb00013.x (cit. on p. 2).

[83] R. L. Kubena, C. L. Anderson, R. L. Seliger, R. A. Jullens, and E. H. Stevens. "FET fabrication using maskless ion implantation." In: *J. Vac. Sci. Technol.* 19 (1981), pp. 916–920. DOI: 10.1116/1.571189 (cit. on p. 3).

[84] W. L. Lama and C. F. Gallo. "Systematic study of the electrical characteristics of the 'Trichel' current pulses from negative needle-to-plane coronas." In: *J. Appl. Phys.* 45 (1974), pp. 103–113. DOI: 10.1063/1.1662943 (cit. on pp. 46, 82).

[85] L. Landau and E. Lifshitz. *Electrodynamics Of Continuous Media*. 1st ed. Vol. 8. Butterworth-Heinemann, 1960. Chap. 1, pp. 35–35 (cit. on pp. 7, 34).

[86] G. Lenguito, J. Fernandez de la Mora, and A. Gomez. "Scaling up the power of an electrospray microthruster." In: *J. Micromech. Microeng.* 24 (2014), p. 055003. DOI: 10.1088/0960-1317/24/5/055003 (cit. on pp. 45, 86).

[87] K. Levenberg. "A method for the solution of certain problems in least squares." In: *Quart. Appl. Math.* 2 (1944), pp. 164–168. URL: https://www.jstor.org/stable/43633451 (cit. on p. 101).

[88] R. Levi-Setti, G. Crow, and Y. L. Wang. "Progress in high resolution scanning ion microscopy and secondary ion mass spectrometry imaging microanalysis." In: *Scan Electron Microsc.* 1985.2 (1985), pp. 535–551 (cit. on p. 3).

[89] R. Levi-Setti and T. R. Fox. "High resolution scanning ion probes: applications to physics and biology." In: *Nuc. Instr. Meth. Phys. Res.* 168 (1980), pp. 139–149. DOI: 10.1016/0029-554X(80)91244-6 (cit. on p. 3).

[90] H. Q. Li, D. G. Courtney, P. Diaz Gomez Maquero, and P. Lozano. "Fabrication and testing of an ionic electrospray propulsion system with a porous metal tip array." In: *Proc. 16th IEEE Int. Conf. Solid-State Sens., Actuators, Microsys. Conf.* 2011. DOI: 10.1109/TRANSDUCERS.2011.5969199 (cit. on pp. 45, 86).

[91] L. B. Loeb, A. F. Kip, and G. G. Hudson. "Pulses in negative point-to-plane corona." In: *Phys. Rev.* 60 (1941), pp. 714–722. DOI: 10.1103/PhysRev.60.714 (cit. on p. 46).

[92] R. D. Lord. "The use of the Hankel transform in statistics: I. General theory and examples." In: *Biometrika* 41.1/2 (1954), pp. 44–55. DOI: 10.2307/2333004 (cit. on p. 103).

[93] G. L. R. Mair. "Emission from liquid metal ion sources." In: *Nuc. Instr. Meth. Phys. Res.* 172 (1980), pp. 567–576. DOI: 10.1016/0029-554X(80)90350-X (cit. on p. 6).

[94] G. L. R. Mair. "On the onset voltage of liquid metal ion sources." In: *Nuc. Instr. Meth. Phys. Res. B* 43 (1989), pp. 240–242. DOI: 10.1016/0168-583X(89)90044-X (cit. on p. 6).

[95] C. G. Malmberg and A. A. Maryott. "Dielectric constant of water from 0 to 100 C." In: *J Res Natl Bur Stand* 56.1 (1956), pp. 1–8 (cit. on p. 3).

[96] D. Marquardt. "An algorithm for least-squares estimation of nonlinear parameters." In: *SIAM J. Appl. Math.* 11 (1963), pp. 431–441. URL: https://www.jstor.org/stable/2098941 (cit. on p. 101).

[97] C. M. Marrese-Reading, J. Anderson, C. Jung-Kubiak, F. Greer, N. Rouhi, D. Wilson, V. White, M. Dickie, R. Mueller, V. Singh, W. Mackie, R. Wirz, and M. Gamero-Castano. "Silicon emitter needle and array design for indium electrospray arrays for spacecraft propulsion." In: *52nd AIAA/SAE/ASEE Joint Propulsion Conference*. 2016. DOI: 10.2514/6.2016-4547 (cit. on pp. 3, 45, 86).

[98] C. M. Marrese-Reading, J. Anderson, C. Jung-Kubiak, J. Polk, V. Singh, K. Yee, V. White, D. Wilson, P. Bruneau, N. Rouhi, F. Greer, J. P. Borgonia, M. Dickie, R. Muller, J. Ziemer, A. Gray, J. Mueller, R. Wirz, and M. Gamero-Castano. "Microfluidic electrospray propulsion (MEP) thruster performance with microfabricated emitter arrays for indium propellant." In: *52nd AIAA/SAE/ASEE Joint Propulsion Conference*. 2016. DOI: 10.2514/6.2016-4738 (cit. on pp. 1, 3, 45, 86).

[99] S. Matsui, T. Kaito, J. Fujita, M. Komuro, K. Kanda, and Y. Haruyama. "Three-dimensional nanostructure fabrication by focused-ion-beam chemical vapor deposition." In: *J. Vac. Sci. Technol. B* 18.6 (2000), pp. 3181–3184. DOI: 10.1116/1.1319689 (cit. on p. 3).

[100] J. R. Melcher and G. I. Taylor. "Electrohydrodynamics: a review of the role of interfacial shear stresses." In: *Annu. Rev. Fluid Mech.* 1 (1969), pp. 111–146. DOI: 10.1146/annurev.fl.01.010169.000551 (cit. on pp. 3, 35).

[101] J. Melngailis. “Focused ion beam technology and applications.” In: *J. Vac. Sci. Technol. B* 5.2 (1987), pp. 469–495. DOI: 10.1088/0268-1242/24/4/043001 (cit. on p. 3).

[102] N. M. Miskovsky, J. He, P. H Cutler, and M. Chung. “Electrohydrodynamical study of the instability of a thin liquid metal film: application to planar liquid metal ion sources.” In: *J. Appl. Phys.* 69 (1991), pp. 1956–1961. DOI: 10.1063/1.348767 (cit. on p. 7).

[103] J. Mitterauer. “Miniaturized liquid metal ion sources (MILMIS).” In: *Surf. Sci.* 246 (1991), pp. 107–112. DOI: 10.1109/27.108416 (cit. on pp. 3, 35, 96, 137).

[104] N. S. Muhlich, B. Seifert, and F. Aumayr. “IFM Nano Thruster performance studied by experiments and numerical simulations.” In: *J. Phys. D: Appl. Phys.* 54 (2021), p. 095203. DOI: 10.1088/1361-6463/abc84c (cit. on p. 6).

[105] E. W. Muller. “Field desorption.” In: *Phys. Rev.* 102 (1956), pp. 618–624. DOI: 10.1103/PhysRev.102.618 (cit. on p. 2).

[106] M. R. Natisin, H. L. Zamora, and W. A. McGehee. “Fabrication and characterization of a fully conventionally machined, high-performance porous-media electrospray thruster.” In: *J. Micromech. Microeng.* 30 (2020), p. 115021. DOI: 10.1088/1361-6439/abb8c3 (cit. on pp. 45, 86).

[107] V. A. Nevrovskii. “Instability of molten-metal film in an electric field.” In: *Fluid Dyn.* 12.4 (1977), pp. 505–511. DOI: 10.1007/BF01089666 (cit. on p. 7).

[108] J. Orloff. *Handbook of charged particle optics*. 2nd ed. CRC Press, 2008. Chap. 2, pp. 29–87 (cit. on pp. 2, 3, 35, 43, 79, 81, 96, 137, 167).

[109] J. Orloff. “High-resolution focused ion beams.” In: *Rev. Sci. Instrum.* 64.5 (1993), pp. 1105–1130. DOI: 10.1063/1.1144104 (cit. on p. 3).

[110] N. M. Patrikalakis and T. Maekawa. *Shape interrogation for computer aided design and manufacturing*. 1st ed. Springer, 2002. Chap. 11, pp. 316–317 (cit. on pp. 37, 40).

[111] E. M. Petro, X. Gallud, S. K. Hampl, M. Schroeder, C. Geiger, and P. C. Lozano. “Multiscale modeling of electrospray ion emission.” In: *J. Appl. Phys.* 131 (2022), p. 193301. DOI: 10.1063/5.0065615 (cit. on pp. 3, 45, 86).

[112] M. Pokorny and H. U. Astrom. “Temperature dependence of the electrical resistivity of liquid gallium between its freezing point (29.75 degrees C) and 752 degrees C.” In: *J. Phys. F.* 6.4 (1976), pp. 559–565. DOI: 10.1088/0305-4608/6/4/015 (cit. on p. 3).

[113] B. Praprotnik, W. Driesel, Ch. Dietzsch, and H. Niedrig. “HV-TEM in-situ investigations of the tip shape of indium liquid metal ion emitter.” In: *Surf. Sci.* 314 (1994), pp. 353–364. DOI: 10.1016/0039-6028(94)90237-2 (cit. on pp. 4, 35, 60, 82).

[114] A. L. Pregenzer. "Electrohydrodynamically driven large-area liquid-metal ion sources." In: *J. Appl. Phys.* 58.12 (1985), pp. 4509–4511. DOI: 10.1063/1.336263 (cit. on p. 3).

[115] A. L. Pregenzer. "Electrohydrodynamically driven, large-area liquid metal ion source for inertial confinement fusion." In: *Rev. Sci. Instrum.* 61.1 (1990), pp. 571–573. DOI: 10.1063/1.1141920 (cit. on p. 3).

[116] A. L. Pregenzer and B. M. Marder. "Liquid lithium ion source: Nonlinear behavior of liquid surface in electric field." In: *J. Appl. Phys.* 60.11 (1986), pp. 3821–3824. DOI: 10.1063/1.337551 (cit. on p. 3).

[117] P. D. Prewett and G. L. R. Mair. *Focused ion beams from liquid metal ion sources*. Taunton: Research Studies Press, 1991 (cit. on p. 3).

[118] N. V. Priezjev, A. A. Darhuber, and S. M. Troian. "Slip behavior in liquid films on surfaces of patterned wettability: comparison between continuum and molecular dynamics simulations." In: *Phys. Rev. E* 71 (2005), p. 041608. DOI: 10.1103/PhysRevE.71.041608 (cit. on pp. 43, 168).

[119] N. Rouhi, C. Jung-Kubiak, V. White, D. Wilson, J. Anderson, C. Marrese-Reading, and S. Forouhar. "Fabrication of 3-D silicon microneedles using a single-step DRIE process." In: *J. Microelectromech. Syst.* 24.5 (2015), pp. 1409–1414. DOI: 10.1109/JMEMS.2015.2406878 (cit. on pp. 79, 82).

[120] S. N. Sahasrabudhe, V. Rodriguez-Martinez, M. O'Meara, and B. E. Farkas. "Density, viscosity, and surface tension of five vegetable oils at elevated temperatures: measurement and modeling." In: *Int. J. Food Prop.* 20 (2017), pp. 1965–1981. DOI: 10.1080/10942912.2017.1360905 (cit. on p. 3).

[121] T. Sakamoto and M. Komuro. "High impurity doping in Si-MBE using liquid Ga ion source." In: *Jpn. J. Appl. Phys.* 22.12A (1983), p. L760. DOI: 10.1143/JJAP.22.L760 (cit. on p. 3).

[122] J. G. Santiago, S. T. Wereley, C. D. Meinhart, D. J. Beebe, and R. J. Adrian. "A particle image velocimetry system for microfluidics." In: *Exp. Fluids* 25.4 (1998), pp. 316–319. DOI: 10.1007/s003480050235 (cit. on p. 4).

[123] D. A. Saville. "Electrohydrodynamics: the Taylor-Melcher leaky dielectric model." In: *Annu. Rev. Fluid Mech.* 29 (1997), pp. 27–64. DOI: 10.1146/annurev.fluid.29.1.27 (cit. on pp. 3, 12, 35).

[124] O. Schenk and K. Gartner. "Solving unsymmetric sparse systems of linear equations with PARDISO." In: *Future Gener. Comput. Syst.* 20 (2004), pp. 475–487. DOI: 10.1016/j.future.2003.07.011 (cit. on p. 42).

[125] L. W. Schwartz and D. E. Weidner. "Modeling of coating flows on curved surfaces." In: *J. Eng. Math.* 29.1 (1995), pp. 91–103. DOI: 10.1007/BF00046385 (cit. on p. 51).

[126] R. L Seliger, J. W. Ward, V. Wang, and R. L. Kubena. "A high-intensity scanning ion probe with submicrometer spot size." In: *Appl. Phys. Lett.* 34.5 (1979), pp. 310–312. DOI: 10.1063/1.90786 (cit. on p. 2).

[127] R. L. Seliger, R. L. Kubena, R. D. Olney, J. W. Ward, and V. Wang. "High-resolution, ion-beam processes for microstructure fabrication." In: *J. Vac. Sci. Technol.* 16 (1979), pp. 1610–1612. DOI: 10.1116/1.570253 (cit. on p. 2).

[128] J. C. Slater. "Atomic radii in crystals." In: *J. Chem. Phys.* 41 (1964), pp. 3199–3204. DOI: 10.1063/1.1725697 (cit. on p. 43).

[129] F. M. Stein. "The curve parallel to a parabola is not a parabola: parallel curves." In: *The Two-Year Coll. Math. J.* 11 (1980), pp. 239–246 (cit. on p. 40).

[130] J. J. Stoker. *Water waves*. Interscience Publishers, 1957. Chap. 3, pp. 41–45 (cit. on p. 27).

[131] G. N. de Surgy, J. P. Chabrerie, O. Denoux, and J. E. Wesfried. "Linear growth of instabilities on a liquid metal under normal electric field." In: *J. Phys. II* 3 (1993), pp. 1201–1225. DOI: 10.1051/jp2:1993192 (cit. on pp. 7, 10–12, 24, 34, 43, 60, 96, 98, 110, 126, 128, 148).

[132] G. N. de Surgy, J. P. Chabrerie, and J. E. Wesfreid. "Emission of liquid metal in vacuum." In: *IEEE Trans. Dielectr. Electr. Insul.* 2 (1995), pp. 184–189. DOI: 10.1109/94.388238 (cit. on pp. 7, 10–12, 24, 33, 34, 43, 60, 62, 63, 96, 98, 110, 126, 128, 148).

[133] G. N. de Surgy, H. Gonzalez, and J. P. Chabrerie. "Influence of bounded geometry on the initial growth of electrocapillary instability for a liquid metal under electric field." In: *Appl. Surf. Sci.* 87 (1995), pp. 91–98. DOI: 10.1016/0169-4332(94)00523-0 (cit. on pp. 96, 128).

[134] V. G. Suvorov. "Numerical analysis of liquid metal flow in the presence of an electric field: application to liquid metal ion source." In: *Surf. Interface Anal.* 36 (2004), pp. 421–425. DOI: 10.1002/sia.1700 (cit. on pp. 9, 36, 138, 148, 153, 154, 158, 159, 169–173).

[135] V. G. Suvorov and E. A. Litvinov. "Dynamic Taylor cone formation on liquid metal surface: numerical modelling." In: *J. Phys. D: Appl. Phys.* 33 (2000), pp. 1245–1251. DOI: 10.1088/0022-3727/33/11/301 (cit. on pp. 9, 36, 54, 151).

[136] V. G. Suvorov and N. M. Zubarev. "Formation of the Taylor cone on the surface of liquid metal in the presence of an electric field." In: *J. Phys. D: Appl. Phys.* 37 (2004), pp. 289–297. DOI: 10.1088/0022-3727/37/2/019 (cit. on pp. 9, 36, 54, 55, 138, 143, 151).

[137] L. W. Swanson and J. Z. Li. "The influence of electrode geometry on liquid metal ion source performance." In: *J. Vac. Sci. Technol. B* 6.4 (1988), pp. 1062–1065. DOI: 10.1116/1.584298 (cit. on pp. 79, 82).

[138] M. Tajmar, C. Scharlemann, A. Genovese, N. Buldrini, W. Steiger, and I. Vasiljevich. "Liquid-metal-ion source development for space propulsion at ARC." In: *Ultramicroscopy* 109 (2009), pp. 442–446. DOI: 10.1016/j.ultramic.2008.10.009 (cit. on p. 3).

[139] M. Tajmar, W. Steiger, and A. Genovese. "Micronewton indium FEEP thrusters." In: *Proc. 3rd Int. Conf. Spacecraft Propulsion*. Vol. 465. 2000, pp. 475–481 (cit. on p. 3).

[140] Y. Takeda. "Measurement of velocity profile of mercury flow by ultrasound Doppler shift method." In: *Nucl. Technol.* 79.1 (1987), pp. 120–124. DOI: 10.13182/NT87-A16010 (cit. on p. 4).

[141] G. Taylor. "Disintegration of water drops in an electric field." In: *Proc. R. Soc. Lond. A* 280 (1964), pp. 383–397. DOI: 10.1098/rspa.1964.0151 (cit. on pp. 5, 53, 54, 143, 150, 151, 156, 170, 172–174).

[142] S. G. Teodorescu, R. A. Overfelt, and S. I. Bakhtiyarov. "An inductive technique for electrical conductivity measurements on molten metals." In: *Int. J. Thermophys.* 22 (2001), pp. 1521–1535. DOI: 10.1023/A:1012809524286 (cit. on p. 3).

[143] R. D. Thornton and T. S. Light. "A new approach to accurate resistivity measurement of high purity water." In: *Ultrapure Water* 7 (1989), pp. 14–21 (cit. on p. 3).

[144] H. Tompkins and E. A. Irene. *Handbook of ellipsometry*. Vol. 1. William Andrew Publishing, Springer-Verlag GmbH, and Co. KG, 2005 (cit. on p. 183).

[145] L. Tonks. "A theory of liquid surface rupture by a uniform electric field." In: *Phys. Rev.* 48 (1935), pp. 562–568. DOI: 10.1103/PhysRev.48.562 (cit. on pp. 7, 96, 126, 137).

[146] D. Tseluiko, M. G. Blyth, D. T. Papageorgiou, and J. M. Vanden-Broeck. "Electrified viscous thin film flow over topography." In: *J. Fluid Mech.* 597 (2008), pp. 449–475. DOI: 10.1017/S002211200700986X (cit. on p. 97).

[147] D. Tseluiko, M. G. Blyth, D. T. Papageorgiou, and J. M. Vanden-Broeck. "Viscous electrified film flow over step topography." In: *SIAM J. Appl. Math.* 70.3 (2009), pp. 845–865. DOI: 10.1137/080721674 (cit. on p. 97).

[148] D. Tseluiko and D. T. Papageorgiou. "Wave evolution on electrified falling films." In: *J. Fluid Mech.* 556 (2006), pp. 361–386. DOI: 10.1017/S0022112006009712 (cit. on p. 97).

[149] J. J. Van Es, J. Gierak, R. G. Forbes, V. G. Suvorov, T. Van den Berghe, Ph. Dubuisson, I. Monnet, and A. Septier. "An improved gallium liquid metal ion source geometry for nanotechnology." In: *Microelectron. Eng.* 73 (2004), pp. 132–138. DOI: 10.1016/j.mee.2004.02.029 (cit. on pp. 4, 35).

[150] C. A. Volkert and A. M. Minor. "Focused ion beam microscopy and micromachining." In: *MRS Bull* 32.5 (2007), pp. 389–399. DOI: 10.1557/mrs2007.62 (cit. on p. 6).

[151] A. Wagner. "The hydrodynamics of liquid metal ion sources." In: *Appl. Phys. Lett.* 40 (1982), pp. 440–442. DOI: 10.1063/1.93100 (cit. on p. 6).

[152] A. Wagner and T. M. Hall. "Liquid gold ion source." In: *J. Vac. Sci. Technol.* 16.6 (1979), pp. 1871–1874. DOI: 10.1116/1.570316 (cit. on pp. 8, 79, 82).

[153] A. Wagner, T. Venkatesan, P. M. Petroff, and D. Barr. "Droplet emission in liquid metal ion sources." In: *J. Vac. Sci. Technol.* 19 (1981), pp. 1186–1189. DOI: 10.1116/1.571240 (cit. on p. 4).

[154] J. W. Ward and R. L. Seliger. "Trajectory calculations of the extraction region of a liquid-metal ion source." In: *J. Vac. Sci. Technol.* 19.4 (1981), pp. 1082–1086. DOI: 10.1116/1.571173 (cit. on p. 6).

[155] A. R. Waugh, S. Payne, G. M. Worrall, and G. D. W. Smith. "In situ ion milling of field ion specimens using a liquid metal ion source." In: *J. Phys. Colloq.* 45 (1984), pp. 207–209. DOI: 10.1051/jphyscol:1984934 (cit. on p. 3).

[156] N. C. White. "Nonlinear dynamics and stability of viscous free-surface microcapillary flows in V-shaped channels and on curved surfaces." PhD thesis. California Institute of Technology, 2022. DOI: 10.7907/yd3w-ck87 (cit. on p. 9).

[157] W. Widada. "Two dimensional window functions." PhD thesis. Naval Postgraduate School, 1979 (cit. on p. 104).

[158] D. Xu, K. M. Liechti, and K. Ravi-Chandar. "Mesoscale scanning probe tips with subnanometer rms roughness." In: *Rev. Sci. Instrum.* 78 (2007), p. 073707. DOI: 10.1063/1.2756997 (cit. on p. 82).

[159] Y. Yeh and H. Z. Cummins. "Localized fluid flow measurements with an He-Ne laser spectrometer." In: *Appl. Phys. Lett.* 4.10 (1964), pp. 176–178. DOI: 10.1063/1.1753925 (cit. on p. 4).

[160] J. Zeleny. "Instability of electrified liquid surfaces." In: *Phys. Rev.* 10.1 (1917), pp. 1–6. DOI: 10.1103/PhysRev.10.1 (cit. on p. 35).

[161] J. Zeleny. "The electrical discharge from liquid points, and a hydrostatic method of measuring the electric intensity at their surfaces." In: *Phys. Rev.* 3.2 (1914), pp. 69–91. DOI: 10.1103/PhysRev.3.69 (cit. on p. 35).

[162] J. Zeleny. "The role of surface instability in electrical discharges from drops of alcohol and water in air at atmospheric pressure." In: *J. Franklin Inst.* 219.6 (1935), pp. 659–675. DOI: 10.1016/S0016-0032(35)91985-8 (cit. on p. 35).

[163] C. Zhou. "Collection of solved nonlinear problems for remote shaping and patterning of liquid structures on flat and curved substrates by electric and thermal fields." PhD thesis. California Institute of Technology, 2020. DOI: 10.7907/PEJ5-1626 (cit. on p. 9).

[164] C. Zhou and S. M. Troian. “Multiplicity of inertial self-similar conical shapes in an electrified liquid metal.” In: *Phys. Rev. Appl.* 15 (2021), p. 044001. DOI: 10.1103/PhysRevApplied.15.044001 (cit. on pp. 7, 9, 54, 55, 138, 139, 143, 151).

[165] N. M. Zubarev. “Formation of conic cusps at the surface of liquid metal in electric field.” In: *JETP Lett.* 73 (2001), pp. 544–548. DOI: 10.1134/1.1387524 (cit. on pp. 7, 9, 36, 55, 70, 73, 83, 108, 137–139, 145, 147–149, 154, 173, 182).

[166] N. M. Zubarev. “The effect of viscosity on the self-similar growth of conic cusps on the surface of a conducting liquid in an electric field: limiting cone angle.” In: *Phys. Fluids* 36.4 (2024). DOI: 10.1063/5.0200820 (cit. on pp. 7, 81, 138, 143, 148, 149, 154, 161, 167, 168, 174).